



HAL
open science

Elaboration and characterization of organic semiconducting thin films for optoelectronics

Xiao Liu

► **To cite this version:**

Xiao Liu. Elaboration and characterization of organic semiconducting thin films for optoelectronics. Material chemistry. Sorbonne Université, 2020. English. NNT : 2020SORUS205 . tel-03850561

HAL Id: tel-03850561

<https://theses.hal.science/tel-03850561v1>

Submitted on 14 Nov 2022

HAL is a multi-disciplinary open access archive for the deposit and dissemination of scientific research documents, whether they are published or not. The documents may come from teaching and research institutions in France or abroad, or from public or private research centers.

L'archive ouverte pluridisciplinaire **HAL**, est destinée au dépôt et à la diffusion de documents scientifiques de niveau recherche, publiés ou non, émanant des établissements d'enseignement et de recherche français ou étrangers, des laboratoires publics ou privés.

Sorbonne Université

Ecole doctorale Physique et Chimie des Matériaux (ED397)

Institut Parisien de Chimie Moléculaire (CNRS-UMR 8232)

Institut des NanoSciences de Paris (CNRS-UMR 7588)

Elaboration and Characterization of Organic Semiconducting Thin Films for Optoelectronics

Par Xiao LIU

Thèse de doctorat de Physique et Chimie des Matériaux

Dirigé par Dr. LACAZE Emmanuelle et Dr. MATHEVET Fabrice

Présentée et soutenue publiquement le 13 Novembre 2020

Devant un jury composé de :

M. BATTAGLINI Nicolas	Maître de conférence HDR ITODYS, Université de Paris	Rapporteur
M. WANTZ Guillaume	Maître de conférence HDR IMS, Université de Bordeaux	Rapporteur
Mme MAITRE Agnès	Professeure INSP, Sorbonne Université	Examineur
M. HEISER Thomas	Professeur ICube, Université de Strasbourg	Examineur
M. KREHER David	Professeur ILV, Paris-Saclay Université	Invité
Mme LACAZE Emmanuelle	Directeur de Recherche INSP, Sorbonne Université	Directeur de thèse
M. MATHEVET Fabrice	Chargé de Recherche CNRS IPCM, Sorbonne Université	Co-Encadrant

Acknowledgement

Firstly, I would like to express my sincerest appreciation to my two supervisors, Dr. Emmanuelle Lacaze at *INSP* and Dr. Fabrice Mathevet at *IPCM*, for their impressive teaching and patient help during last four years. Dr. Emmanuelle Lacaze always stresses that I should think before I do. For example, when I performed AFM at the very beginning, I tended to mechanically memorize what to do now and what to do next. I really didn't have the habit to think why I did like this. But She reminded me that I should figure out the purpose of each step. Similarly, during my PhD thesis writing, she also suggested that it was important to explain why we started this PhD work, what still needed to be improved concerning the organic materials with respect to the work already made in the literatures, and what scientific questions we have addressed. Indeed, only after you figure out why you do something, you can better understand it. My co-supervisor, Dr. Fabrice Mathevet, also impresses me with his enthusiasm to scientific research. Sometimes, when I met some difficulties during the experiments and asked him for help, he always showed great curiosity and interest to solve those problems. He is a workaholic. When he is busy, he could work until very late and doesn't sleep. In addition, he keeps good collaborations with his colleagues in France, China, Korea, Japan, and so on. Thanks to this, most of the PhD students in our lab have the chance to perform a research internship in the group of Prof. Chihaya Adachi at *Kyushu University* in Japan and improve our scientific skills.

Secondly, I would like to express my gratitude to our collaborators Dr. D'Aléo Anthony and Prof. Frédéric Fages at *CINAM* in Marseille, Dr. Xiaolu Su and Dr. Teng Teng at *IPCM* for their providing of small molecular organic semiconductors studied in this PhD project. I appreciate Mme Lise-Marie Chamoreau for her performing of X-ray diffraction. I also would like to thank Dr. Jean-Louis Fave and the group of Dr. Emmanuel Lhuillier for their help concerning the vacuum thermal evaporation of materials and the characterization of charge transport properties.

Thirdly, I acknowledge the support of *China Scholarship Council (CSC)*, *Japan Society for the Promotion of Science (JSPS) core-to-core program*, and *Projet international de coopération scientifique (PICS) CNRS* for my study abroad and the completion of this PhD project.

In addition, I would like to express my gratitude to my colleagues at *IPCM* and *INSP* including David, Lydia, Quentin, Yiming, Xiaolu, Morgan, Teng Teng, Ting Liang, Dizheng, Haixia,

Weiwei Du, Haiqin, Yan Li, Shuaiyuan, Weiwei Fang, and so on. Everyone is nice and be ready to help others to solve either experimental problems or daily difficulties. What really surprised me was that they ordered food and presents on the internet and delivered to my room after my online PhD defense during this special period of lockdown due to the epidemic of Coronavirus disease (COVID-19)!

Meanwhile, I would like to thank my neighbors Yang Luo, Sunbin Huang, Weixian Wang, Zheng Han, Fen Zhao and her three lovely cats. In 2020, we already spend about one third of the time at home and can't go to school. The life without them would be so lonely and boring. This March, I broke my new computer carelessly and I was very worried about my PhD thesis writing. Fortunately, Yang Luo lent her computer to me and let me use it for two months until I took my old computer back in May when France lifted lockdown. What's more, to my surprise, Sunbin Huang, was able to repair my new computer! How lucky I am to live close with them.

Finally, I appreciate the accompany of my family and my friends, which makes my life richer and happier in France. I enjoyed visiting different places of interest, various museums and beautiful parks, drinking coffee at cafe, and walking along Seine River with them on weekends. I love colorful houses in Colmar, the firework of Eiffel Tower and the lavender of Provence.....

Content

Acknowledgement.....	1
Content	3
Glossary	7
General introduction	9
Résumé en français.....	11
Chapter 1 Introduction and background	17
1.1 Organic semiconductors.....	19
1.1.1 Π -conjugated small molecules and polymers toward high charge mobility....	20
1.1.2 Applications for organic optoelectronics.....	24
1.1.2.1 Organic photovoltaic (OPV).....	24
1.1.2.2 Organic field-effect transistor (OFET)	26
1.1.2.3 Organic light emitting diode (OLED).....	31
1.2 Elaboration of semiconducting thin films	36
1.2.1 Solution-processing methods	37
1.2.1.1 Drop coating	37
1.2.1.2 Dip coating	38
1.2.1.3 Blade coating	39
1.2.1.4 Spin coating	39
1.2.1.5 Inkjet printing	41
1.2.1.6 Roll-to-roll techniques	42
1.2.2 Solution-free methods	43
1.2.2.1 Vacuum thermal evaporation	44
1.2.2.2 Physical vapor transport deposition.....	45
1.2.2.3 Melt processing.....	46
1.3 Characterization of semiconducting thin films	48
1.3.1 Characterization of charge transport properties	48
1.3.1.1 Organic field-effect transistor (OFET)	50
1.3.1.2 Time of flight (TOF).....	51
1.3.2 Characterization of self-organized materials.....	52
1.3.2.1 Polarized optical microscope (POM).....	53
1.3.2.2 Grazing incidence X-ray scattering (GIXS)	54

1.3.2.3 Atomic force microscope (AFM).....	56
1.4 Aim of work.....	59
Chapter 2 A solvent-free and vacuum-free melt-processing method to fabricate organic semiconducting layers with large crystal size for organic electronic applications	63
2.1 Thermal properties of DAL1.....	66
2.2 Structure of DAL1 single crystal prepared by slow solvent evaporation	67
2.3 Powder X-ray scattering	68
2.4 Preparation of DAL1 thin films by solution deposition and melt-processing method.....	70
2.5 Structure and morphology of DAL1 thin films.....	72
2.5.1 Grazing incidence X-ray scattering (GIXS).....	72
2.5.2 Atomic force microscope (AFM)	74
2.6 Charge transport properties of DAL1 thin films	75
2.7 Photophysical properties of DAL1 thin films	81
2.8 Conclusion	83
2.9 Experimental section.....	83
2.9.1 Materials.....	83
2.9.2 DSC	83
2.9.3 POM	84
2.9.4 XRD, SAXS and GIXS	84
2.9.5 AFM	84
2.9.6 Characterization of OFET devices	84
2.9.7 Photophysical properties	85
Chapter 3 Investigation of charge transport properties of [1]Benzo[thieno[3,2-b][1]-benzothiophene derivatives in field-effect transistor configuration.....	87
3.1 Thermal properties of BTBT.....	90
3.2 Preparation of BTBT single crystals by physical vapor transport deposition.....	91
3.3 Structure of BTBT single crystals prepared by physical vapor transport deposition.....	92
3.3.1 Single-crystal X-ray diffraction.....	92
3.3.2 Polarized optical microscope (POM) and Scanning electron microscope (SEM)	94
3.3.3 Atomic force microscope (AFM)	95
3.4 Charge transport properties of single crystal BTBT	96
3.4.1 Fabrication of BTBT single crystal OFETs.....	96
3.4.2 Charge carrier mobility of BTBT single crystal transistors	97

3.5 Charge transport properties of C ₈ -BTBT-C ₈ melt-processed thin films.....	101
3.5.1 Fabrication of C ₈ -BTBT-C ₈ melt-processed thin film and transistors	102
3.5.2 Charge carrier mobility of C ₈ -BTBT-C ₈ melt-processed thin film.....	103
3.6 Conclusion	104
3.7 Experimental section.....	105
3.7.1 Materials.....	105
3.7.2 DSC	105
3.7.3 XRD	105
3.7.4 POM, SEM and AFM.....	106
3.7.5 Characterization of OFET devices	106

Chapter 4 Investigation of photo- and electro-luminescence properties of the fluorescent materials C10-PBT **107**

4.1 Thermal properties of C10-PBT	110
4.2 Film morphology analysis.....	110
4.3 Photophysical properties of C10-PBT in solution	111
4.4 Electronic properties of C10-PBT	113
4.5 Photophysical properties of C10-PBT in solid-state film	113
4.5.1 Neat film properties.....	114
4.5.2 CBP/C10-PBT host-guest system properties.....	115
4.6 Electroluminescence properties of C10-PBT.....	118
4.6.1 Neat film as the emitting layer	119
4.6.2 Host-guest emitting layer	121
4.7 Conclusion	123
4.8 Experimental section.....	124
4.8.1 Materials.....	124
4.8.2 DSC	124
4.8.3 POM	125
4.8.4 AFM	125
4.8.5 Photophysical properties in solution and in solid-state film	125
4.8.6 Fabrication and characterization of OLED devices.....	125

Chapter 5 Investigation of charge transport properties of isoindigo-based oligothiophenes in field-effect transistor configuration **127**

5.1 Thermal properties of iI(T2) ₂	130
5.2 Structure and morphology of iI(T2) ₂ thin films	131

5.2.1 Polarized optical microscope (POM)	131
5.2.2 Grazing incidence X-ray scattering (GIXS)	132
5.2.3 Atomic force microscope (AFM)	133
5.3 Electronic properties of iI(T2)_2 thin films	135
5.4 Charge transport properties of iI(T2)_2 thin films and annealing effect	135
5.4.1 Time of flight (TOF)	135
5.4.2 Organic field-effect transistor (OFET)	137
5.5 Conclusion	142
5.6 Experimental section	143
5.6.1 Materials	143
5.6.2 TGA and DSC	143
5.6.3 POM	143
5.6.4 GIXS	143
5.6.5 AFM	143
5.6.6 Photoelectron spectroscopy	144
5.6.7 TOF	144
5.6.8 Fabrication and characterization of OFET devices	144
Conclusions and Perspectives	147
References	151

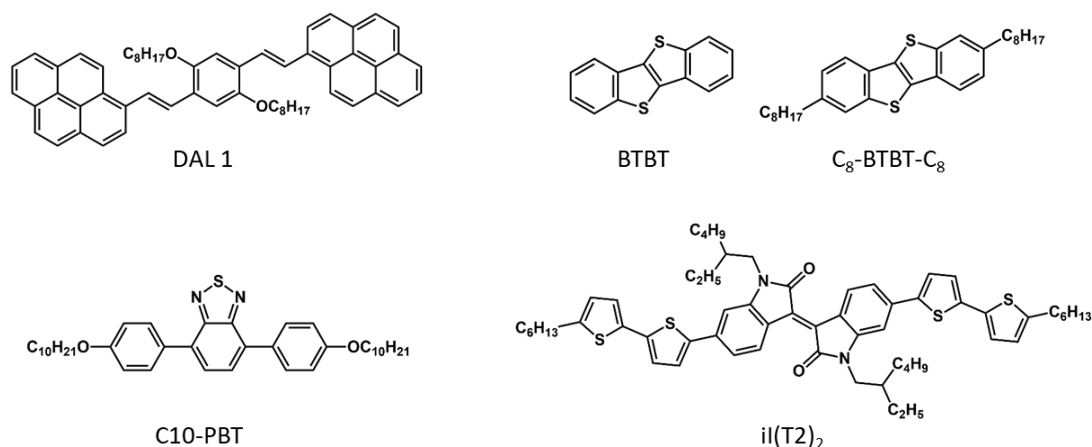
Glossary

AFM	Atomic force microscope
BG/BC	Bottom gate/bottom contact
BG/TC	Bottom gate/top contact
BTBT	[1]Benzothieno[3,2-b][1]-benzothiophene
D-A	Donor-acceptor
DSC	Differential scanning calorimetry
EBL	Electron blocking layer
EIL	Electron injection layer
EL	Electroluminescence
EML	Emitting layer
EQE	External quantum efficiency
ETL	Electron transport layer
FET	Field-effect transistor
FI-TRMC	Field-induced time-resolved microwave conductivity
FRET	Förster resonant energy transfer
GIXS	Grazing incidence X-ray scattering
HBL	Hole blocking layer
HIL	Hole injection layer
HOMO	Highest occupied molecular orbital
HTL	Hole transport layer
IQE	Internal quantum efficiency
ISC	Intersystem crossing
LCD	Liquid crystal display
LUMO	Lowest unoccupied molecular orbital
OFET	Organic field-effect transistor
OLED	Organic light emitting diode
OLET	Organic light emitting transistor
OPV	Organic photovoltaic
OSCs	Organic semiconductors
OTFT	Organic thin film transistor
OTS	N-octadecyltrichlorosilane
PCE	Power conversion efficiency
PL	Photoluminescence

PLQY	Photoluminescence quantum yield
POM	Polarized optical microscope
R2R	Roll-to-roll
RISC	Reverse intersystem crossing
RTP	Room-temperature phosphorescence
S ₀	Ground state
S ₁	Singlet first electronic state
S ₂	Singlet second electronic state
SAXS	Small-angle X-ray scattering
SCLC	Space charge limited current
SEM	Scanning electron microscope
T ₁	First triplet state
TADF	Thermally active delayed fluorescence
TDM	Transition dipole moment
TEM	Transmission electron microscope
TGA	Thermogravimetric analysis
TG/BC	Top gate/bottom contact
TG/TC	Top gate/top contact
TOF	Time of flight
VTP	Vapor transport deposition
XRD	X-ray diffraction
WAXS	Wide-angle X-ray scattering

General introduction

During this PhD work, we were interested in the elaboration and characterization of organic semiconducting thin films of different π -conjugated semiconducting materials for optoelectronic applications such as organic field-effect transistors (OFETs) and organic light-emitting diodes (OLEDs). We conducted four projects based on DAL1, BTBT derivatives, C10-PBT and $il(T2)_2$, respectively, whose molecular structures are presented below.



The first project is centered on a new method to produce single-crystalline thin films of a Pyrene derivative DAL1 synthesized by our colleagues Dr. D'Aléo Anthony and Prof. Frédéric Fages at Center Interdisciplinaire de Nanoscience de Marseille (CINAM), for the optimization of charge transport and photophysical properties. The second project focuses on the fabrication of organic field-effect transistors based on single crystals of BTBT derivatives prepared in our laboratory at Institut Parisien de Chimie Moléculaire (IPCM) by the Dr. Xiaolu Su. The third project deals with the study of photo- and electro-luminescence of a new liquid crystalline fluorescent material C10-PBT emitter also synthesized in our laboratory by the Dr. Teng Teng. The OLED devices incorporating C10-PBT emitter were fabricated in collaboration with Prof. Chihaya Adachi's group at Center for Organic Photonics and Electronics Research (OPERA) at Kyushu University in Japan. Finally, the last project is about the study of charge transport properties of thin films based on a narrow-bandgap isoindigo derivative $il(T2)_2$ synthesized by our colleague Dr. D'Aléo Anthony at Ewha Womans university in Seoul.

More generally, this PhD work wants to show the importance of the morphology optimization of semiconducting active layers in the field of the optoelectronics to achieve high charge transport and/or photophysical properties, and consequently, to take full advantage of the intrinsic potential of organic semiconductors.

Résumé en français

Les récentes avancées sur les matériaux organiques semi-conducteurs (petites molécules ou polymères) ont permis de faire émerger cette classe de matériaux comme une alternative aux matériaux semiconducteurs inorganiques tel que le silicium. Ces matériaux organiques, présentant des propriétés de conduction électrique, ont été découverts vers la fin des années 70 par les chercheurs A. J Heeger, A. G. MacDiarmid and H. Shirakawa. Cette découverte leur a valu de recevoir le prix Nobel de Chimie 2000. Ces matériaux dit « π -conjugués » sont à la base de ce qu'on appelle « l'électronique organique » qui connaît un essor considérable depuis une vingtaine d'années. Ces matériaux π -conjugués peuvent être utilisés en tant que couche active dans différents types de composants optoélectroniques tels les cellules photovoltaïques (PV), les transistors à effet de champs (OFETs) ou les diodes électroluminescentes (OLEDs), dont les performances viennent aujourd'hui concurrencer leurs équivalents en silicium.

Dans ce travail de thèse, nous nous sommes intéressés à l'élaboration et la caractérisation de films minces semi-conducteurs préparés à partir de différents matériaux π -conjugués (DAL1, BTBT, C₈-BTBT-C₈, C10-PBT, il(T2)₂) pour des applications en OFETs et OLEDs. Sachant que les performances de ces dispositifs électroniques dépendent grandement de l'arrangement moléculaire, de la structure et de la morphologie des couches semiconductrices utilisées, nous avons cherché à optimiser les méthodes de fabrication de ces couches actives en développant ou comparant différentes méthodes de dépôt à notre disposition.

Ainsi, dans un premier chapitre, nous proposons une nouvelle méthode de mise en forme de films minces ne nécessitant ni solvant, ni ultraviolet appelée « melt-processing ». Cette méthode, adaptée de la mise en forme des films de cristaux liquides, permet de préparer des couches semiconductrices du composé DAL1 de quelques centaines de nanomètre d'épaisseur et présentant de larges domaines monocristallins (voir **Figures Ia et Ib**). Ces couches, obtenues depuis l'état liquide isotrope du matériau, présentent une cristallinité supérieure aux films spin-coatés polycristallins et par conséquent, permettent d'avoir des propriétés de transport de charges améliorées avec des mobilités de l'ordre de $5 \times 10^{-2} \text{ cm}^2 \text{ V}^{-1} \text{ s}^{-1}$ en configuration transistor à effet de champs (voir **Figure Ic**). De plus, la présence de ces larges domaines monocristallins améliore notablement les propriétés photophysiques du matériau à l'état solide avec des rendements de photoluminescence (PLQY) multipliés par deux par rapport aux films spin-

coatés. Cette étude, nous a permis de démontrer que la technique de dépôt de matériaux semiconducteurs moléculaires par melt-process constitue une alternative intéressante aux techniques par voie solution ou par évaporation sous ultravide pour la réalisation de dispositifs en optoélectronique. Cette approche peut être étendue à de nombreux autres semiconducteurs moléculaires et plusieurs études en ce sens sont actuellement en cours dans notre groupe.

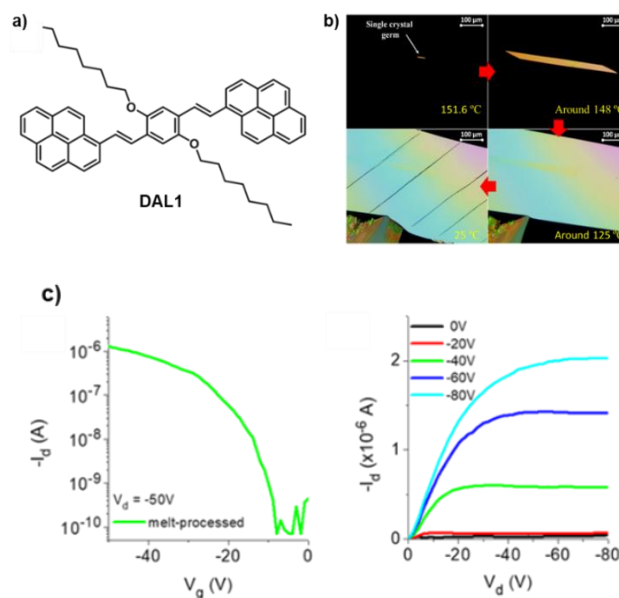


Figure I a) Structure moléculaire du composé DAL1. b) Images POM montrant la croissance d'un large domaine monocristallin à partir d'un germe dispersé dans la phase liquide isotrope de DAL1. c) Courbes de transfert et output d'un transistor obtenu à partir d'un film de DAL1 melt-processé.

Dans un deuxième chapitre, nous avons étudié les propriétés de transport de charges dans des cristaux de cœur [1]benzothieno[3,2-b][1]benzothiophene BTBT (voir Figure IIa). Pour ce faire, nous avons préparé des monocristaux du matériau par vapor transport deposition et l'organisation moléculaire dans ces cristaux, ainsi que leur morphologie ont été étudiées en détails. Ces monocristaux de cœur BTBT ont été ensuite transférés sur des structures transistor (bottom/gate-bottom/contact) et une mobilité de trous de l'ordre de $0.032 \text{ cm}^2\text{V}^{-1}\text{s}^{-1}$ a été mesurée (voir Figures IIb et IIc). En parallèle, les propriétés de transport de charges ont été également mesurées sur un dérivé de BTBT substitué par deux chaînes aliphatiques (voir Figure II d). Pour ce faire, des transistors à effet de champs ont été fabriqués à partir de films minces de C_8 -BTBT- C_8 préparés par melt-processing et une mobilité de charges de l'ordre de $1.1 \text{ cm}^2\text{V}^{-1}\text{s}^{-1}$ a été enregistrée (voir Figures IIe et II f). Cette étude correspond à la première caractérisation des propriétés de transport de charges en configuration transistor d'un simple cœur de BTBT et confirme le rôle important de la substitution par des chaînes aliphatiques pour atteindre de bonnes mobilités des porteurs de charge.

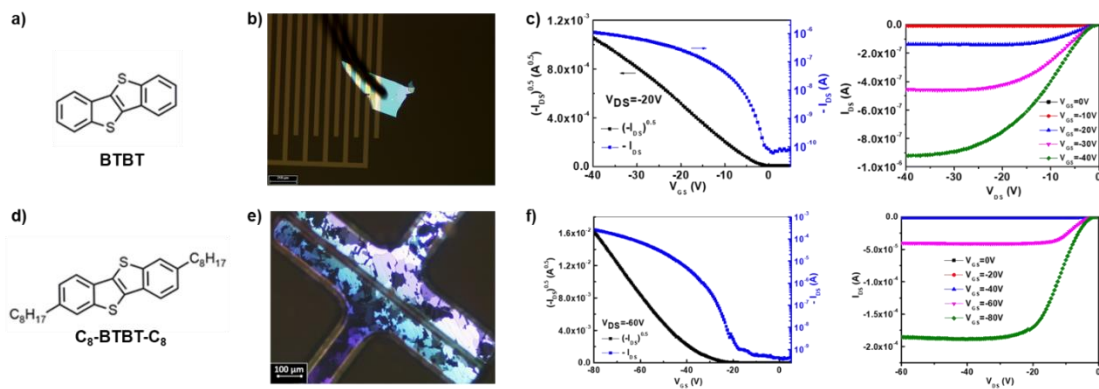


Figure II a) Structure moléculaire du composé BTBT. b) Image POM montrant le dépôt d'un monocristal obtenu par vapor transport deposition sur une structure transistor (electrodes d'or interdigitées). c) Courbes de transfert et output d'un transistor obtenu à partir d'un monocristal de BTBT. d) Structure moléculaire du composé C₈-BTBT-C₈. e) Image POM montrant le positionnement d'un shadow mask sur un film mince de C₈-BTBT-C₈ melt-processé avant le dépôt des électrodes d'or. f) Courbes de transfert et output d'un transistor obtenu avec un film melt-processé de C₈-BTBT-C₈.

Dans un troisième chapitre, nous avons étudié un nouveau matériau donneur-accepteur auto-organisé fluorescent (C10-PBT) pour la réalisation de dispositifs électroluminescents (voir Figure IIIa). Ce composé possède un riche polymorphisme avec deux phases cristallines lamellaires (transition de phase autour de 70°C) et une phase cristal liquide de type smectique A entre 94°C et 135°C (voir Figure IIIb). Ce matériau présente également de forts rendements de photoluminescence à l'état solide avec un PLQY de plus de 80% dans sa phase cristalline après recuit à 80°C. Ceci indique un faible quenching de la fluorescence à l'état. Dispersé dans une matrice, C10-PBT présente également de grands PLQYs pouvant atteindre 91% pour un mélange de 2% en masse dans du CBP (voir Figure IIIc).

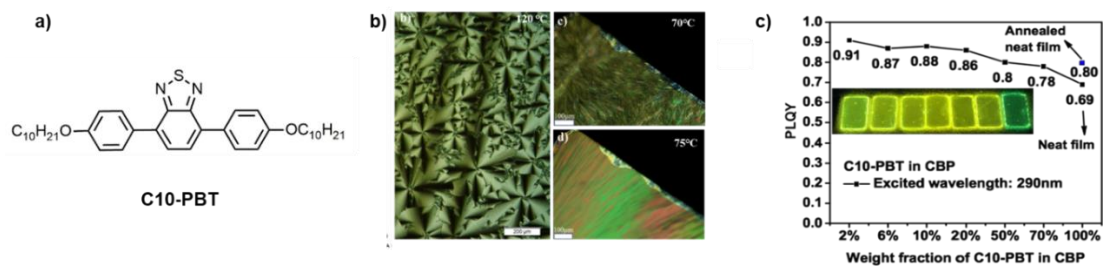


Figure III a) Structure moléculaire du composé C10-PBT. b) Image POMs montrant (gauche) la texture optique « conique-focale » de la phase smectique A et (droite/haut/bas) la texture optique observer pour les phases cristallines à 70°C et à 75°C. c) PLQYs à l'état solide en fonction de la concentration en C10-PBT dans une matrice de CBP et (image insérée) photo des films observés sous irradiation UV.

Les OLEDs préparées avec une couche émettrice (EML) spin-coaté de 6% de C10-PBT dans du CBP montrent une efficacité quantique externe (EQE) de 3%, ce qui représente une

valeur élevée compte tenu de l'EQE théorique maximum escomptée pour ce type de fluorophore (voir **Figure IV**). Cependant, ces OLEDs peuvent encore être optimisées notamment par l'utilisation de méthodes de dépôt des couches par évaporation sous vide. Des premiers essais à partir d'EMLs évaporées ont montré des résultats prometteurs avec des EQEs similaires aux OLEDs spin-coatées, mais fonctionnant à de plus faibles tensions.

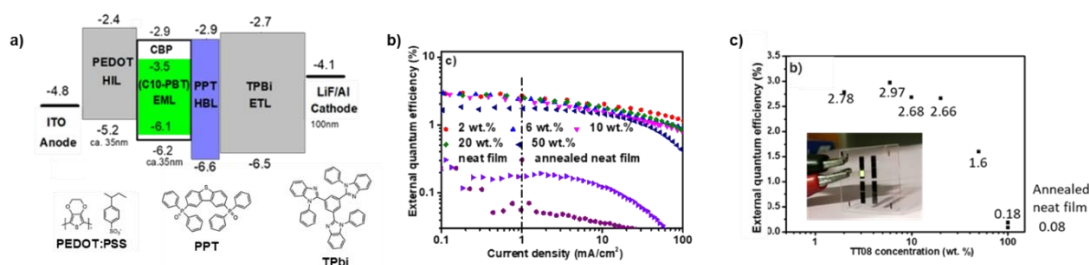


Figure IV a) Structure des OLEDs préparées avec une EML spin-coatée de 6% de C10-PBT dans du CBP. b) EQEs des OLEDs fabriquées avec une EML spin-coatées suivant la concentration en C10-PBT dans du CBP. c) EQEs des OLEDs fabriquées avec une EML spin-coatées en fonction de la concentration en C10-PBT dans du CBP et illustration (image) d'une diode en fonctionnement.

De plus, le design de structures plus complexes incluant des couches injectrices de trou ou bloqueuses d'électron, ou encore l'optimisation de l'épaisseur de toutes les couches actives pourraient encore améliorer les performances de ces dispositifs. En conclusion, cette étude montre que le composé de C10-PBT est un fluorophore prometteur pour la réalisation de dispositifs électroluminescents. Outre les OLEDs, des transistors électroluminescents (OLETs) pourrait également être envisagés ; des expériences en ce sens sont actuellement en cours de réalisation en collaboration avec le groupe du Prof. Ebinazar Namdas à l'Université du Queensland en Australie.

Dans un quatrième et dernier chapitre, nous nous sommes intéressé à l'étude de films minces d'un composé à faible gap optique, nommé $iI(T2)_2$. Ce dérivé oligothiophene, incorporant une unité isoindigo, présente une structure de type donneur-accepteur-donneur et un transfert de charge intramoléculaire expliquant son faible gap optique (voir **Figure IVa**). La relation structure/propriétés de transport de charges des films préparés à partir de ce dérivé à été étudiée en détails, notamment en fonction de la température de recuit. Une mobilité de trous maximale de $0.011 \text{ cm}^2\text{V}^{-1}\text{s}^{-1}$ a été évaluée en configuration transistor pour des films minces spin-coatés recuit à 160°C sur des substrats SiO_2 , démontrant l'impact bénéfique de l'accroissement de la température de recuits sur la morphologie des films en diminuant la densité de joints de grain (voir **Figures IVb et IVc**). De plus, une bonne stabilité des propriétés de transport de charge suite à une exposition à l'air a été démontrée pour ce matériau et un

transport de charge ambipolaire a également été observé pour des films d' $iI(T2)_2$ déposés sur des substrats traités au préalable par une couches d'octadecyltrichlorosilane (OTS).

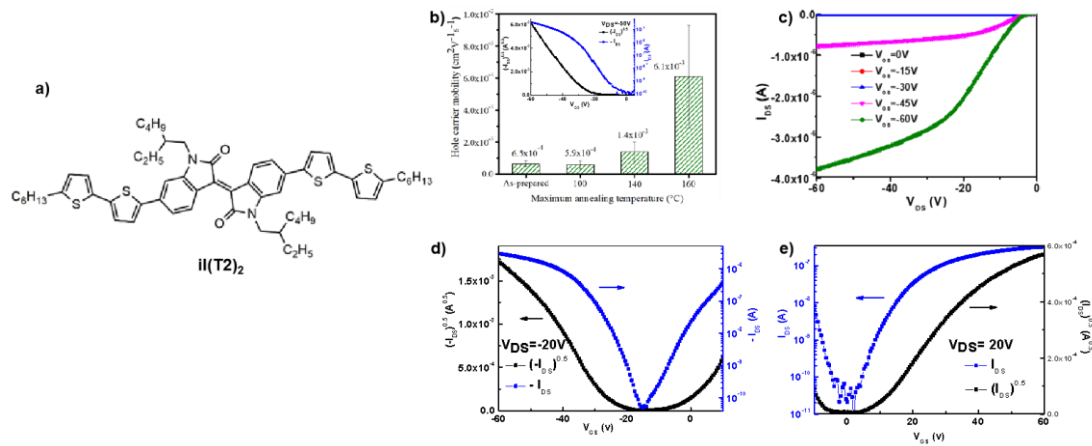


Figure 5 a) Structure moléculaire du composé $iI(T2)_2$. b) mobilité de trous mesurée en fonction de la température de recuit du film de $iI(T2)_2$ (insertion : courbe de transfert de l'OFET recuit à 160°C). c) courbe de output du transistor obtenu avec un film de $iI(T2)_2$ recuit à 160°C. d) et e) courbes de transfert pour les trous (gauche) et les électrons (droite) d'un transistor préparé avec un film de $iI(T2)_2$ sur un substrat traité OTS et recuit à 160°C.

En conclusion, ce travail de thèse permet de confirmer l'importance de l'optimisation de la structure et morphologie des couches actives semiconductrices dans le domaine de l'optoélectronique pour obtenir notamment de bonnes propriétés de transport de charges ou photophysiques. Il souligne également, que cette optimisation peut se faire en jouant sur plusieurs paramètres, tels que les méthodes de dépôt (voie solution, évaporation,...), les post-traitements appliqués (modification de surface, température de recuit,...) et la nature du matériau étudié (synthèse organique,...). Cependant, il apparait évident que tous ces paramètres doivent être pris en compte de façon concomitante pour espérer obtenir la meilleur configuration et les meilleurs performances possibles, nécessitant ainsi une approche pluridisciplinaire.

Chapter 1 Introduction and background

1.1 Organic semiconductors

A semiconductor has an electrical conductivity between that of a conductor, such as metallic copper, and an insulator, such as glass. In general, organic solids are electrical insulators, but become semiconductors when charges are either injected from appropriate electrodes, upon doping or by photoexcitation.

The discovery of ‘organic semiconductors (OSCs)’ could date back to 1948 when D. D. Eley examined the electrical conductivity of two phthalocyanines which were found to be semiconductors ¹. Particularly in 1977, the high conductivity of conducting polymer polyacetylene was reported by Heeger, MacDiarmid, Shirakawa et al. ^{2,3}, and they were awarded the Nobel Prize in Chemistry in 2000 for their revolutionary discovery that plastic can, after certain modifications, be made electrically conductive ⁴. Their findings yielded remarkable interest of OSCs in both basic scientific research and industrial application in organic optoelectronics such as organic photovoltaic (OPV), organic field-effect transistor (OFET), and organic light emitting diode (OLED).

Compared with their widely known inorganic counterparts (mainly silicon, germanium, and metal oxide semiconductors), OSCs offer some intrinsic advantages. Firstly, they are solution-processible on lightweight, very-low-cost and large-area substrates such as glass, plastic or metal foils which can be used under low processing temperature ⁵. Secondly, the mechanical flexibility of organic materials opens the door to flexible, foldable and stretchable organic electronics including flexible OLED displays ⁶, flexible batteries, electronic circuits fabricated in clothing and biomedical devices ⁷. Thirdly, organic compounds are almost endless in number and range from small molecules to macromolecules, which increases the range of screening and design possibilities for OSCs ⁸. However, there is a big challenge. These devices performances depend significantly on the fabrication methods of the semiconducting films and the control of the film morphology. Therefore, during my PhD, we were interested in the elaboration and characterization of several semiconducting materials. The appropriate elaborating method for each material was investigated in order to figure out the structure/property relationships and maximize the performances of the corresponding semiconducting film in optoelectronic devices (OFETs or OLEDs). Next, we will introduce some organic semiconducting materials in the literatures (small molecules and polymers) and their applications in organic optoelectronics such as OPVs, OFETs and OLEDs.

1.1.1 π -conjugated small molecules and polymers toward high charge mobility

Like all organic materials, OSCs are carbon-rich compounds whose structures are normally tailored to optimize a special function such as charge transport or luminescent properties. According to whether the molecular weight is well-defined, OSCs can be usually divided into π -conjugated small molecules (low-generation dendrimers⁹ and other oligomers included) and π -conjugated polymers consisting of an indeterminate number of molecular repeat units. **Figure 1.1** gives some examples of the chemical structures of typical π -conjugated small molecules and polymers: Anthracene, Pentacene, TIPS-Pentacene, Rubrene, Phthalocyanine, [1]Benzothieno[3,2-b][1]-benzothiophene (BTBT), 2,7-Dioctyl[1]benzothieno[3,2-b][1]benzothiophene (C₈-BTBT-C₈), Dinaphtho[2,3-b:2',3'-f]thieno[3,2-b]thiophene (DNTT) and C₁₀-DNTT-C₁₀ as small molecules; Polyacetylene (PA), Polypyrrole (PPy), Poly(3-alkylthiophene) (P3HT), Poly(p-phenylene vinylene) (PPV) and Oligothiophene as polymers.

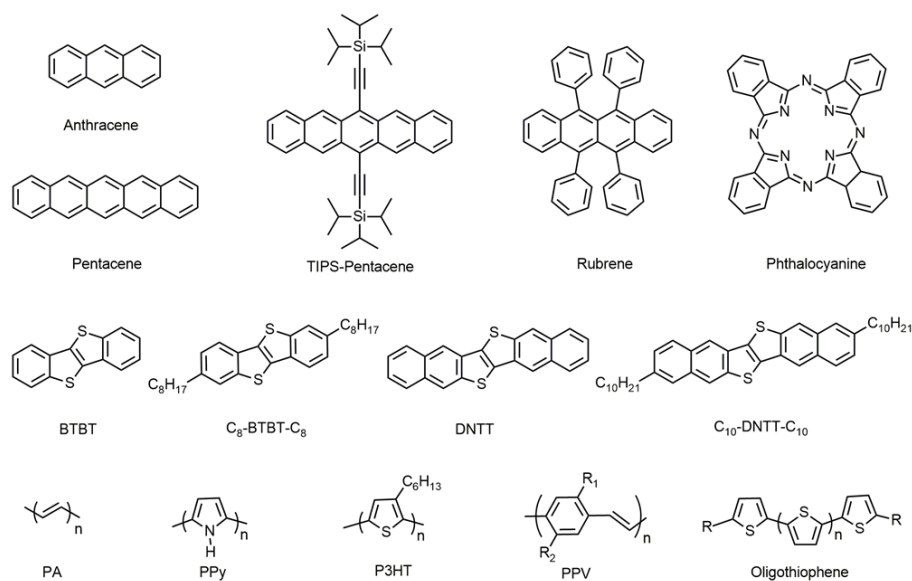


Figure 1.1 Chemical structures of typical π -conjugated small molecules and polymers.

Molecular structure of OSC dramatically influences the charge carrier mobility which is one of the important parameters for OPV, OFET and OLED devices. In solid-state physics, charge mobility of a semiconductor characterizes how quickly a carrier (electron or hole) can move through the semiconductor when pulled by an electric field (E). When E is applied across a piece of material, the charges respond by moving with an average velocity called the drift velocity, v_d . Charge mobility, μ , is defined as the ratio of the mean drift velocity to the applied electric field (See equation below)¹⁰. Its unit is $\text{cm}^2\text{V}^{-1}\text{s}^{-1}$.

$$\mu = v_d / E$$

Mobility is a very important parameter for semiconductor materials. Almost always, higher mobility leads to better device performance, with other things equal. In OFETs, for clean switching behavior, the “on” current (the source-drain current in the on-state at a particular gate voltage) should be as large as possible. It mainly depends on the charge mobility^{10,11}. In OLEDs, good charge mobility is critical for achieving high efficiency and high brightness. In OPVs, balanced charge transport can reduce current losses of recombination¹².

For small molecular OSCs, an ideal conjugated backbone is the basic requirement for high mobility. Linear fused acene rings are promising building block systems for conjugated backbone, and the extension of π -conjugation is an effective approach to enhance their intermolecular couplings for high charge carrier mobility. However, the modification on the conjugated backbone with suitable substituents at the appropriate places will be necessary to control the solubility and stability problem accompanied with further π -conjugation extension of larger acenes or heteroatoms incorporation⁸. In addition to the basic principles (ideal conjugated backbone, suitable substituents) to achieve high mobility for small molecular OSCs, conjugated polymers designing has other principles such as high molecular regioregularity, high molecular weight, narrow molecular weight distribution, appropriate rotational freedom along the conjugated chain, the construction of donor-acceptor (D-A) system and π -conjugation extension to two-dimensional sheets.

Small molecular semiconductors

Although the molecular structure of the small molecular semiconductors plays an important role, it is the packing of individual moiety inside the solid-state that mainly determines the overlap of neighbor orbitals and defines pathways for charge transport¹³. Currently, there are four frequently observed packing motifs adopted by organic molecules (See Figure 1.2): the slipped-stack (molecular orientation in adjacent columns is the same), slipped π -stack (molecular orientation in adjacent columns is rotated), the brick-wall packing and herringbone packing. The dominant transfer integrals (J) in the x - y plane between adjacent molecules in such prototypical molecular structures are also displayed in Figure 1.2 and constitute an important parameter for charge transport properties.

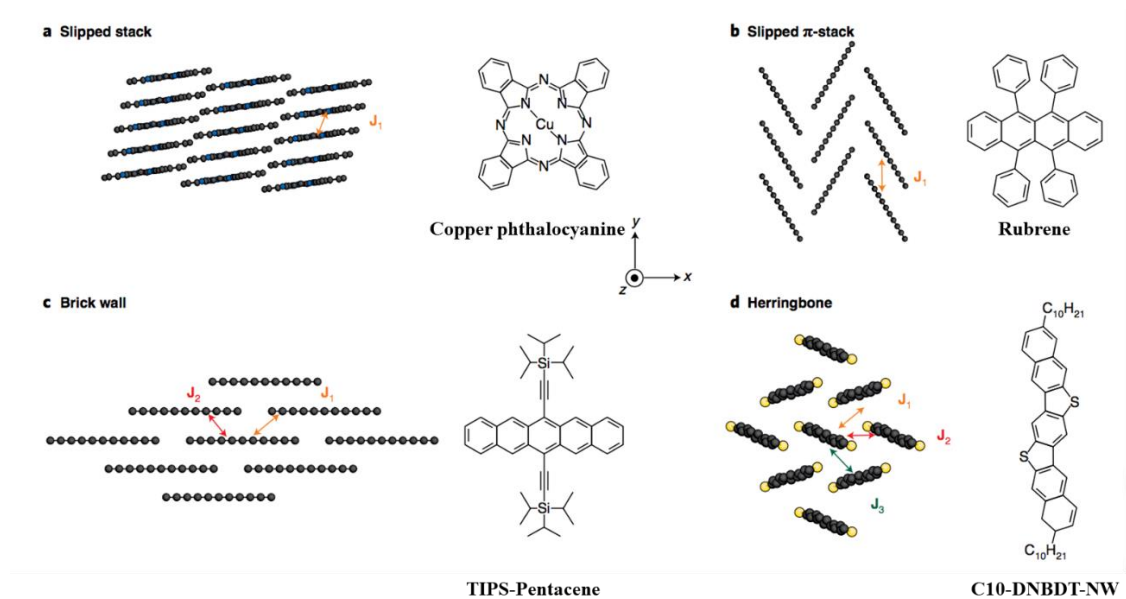


Figure 1.2 Four frequently observed packing motifs adopted by organic small molecules and prototypical molecules¹³.

The first two packing motifs offer only one large J and display strongly anisotropic transport, whereas the herringbone packing with three large transfer integrals provides isotropic transport on condition that the three values of J are equal or very similar. Charge carrier mobilities are commonly found to be the highest among OSCs with herringbone packing motifs, such as C_n -BTBT- C_n ($n=0,2,8,10,12$)^{14,15} and pentacene¹⁶. For example, C_{12} -BTBT- C_{12} achieved unprecedented mobility of $170 \text{ cm}^2\text{V}^{-1}\text{s}^{-1}$ measured by field-induced time-resolved microwave conductivity (FI-TRMC) technique¹⁷. Indeed, to optimize the transport of hole carriers, one should aim for structures with intermolecular transfer integrals that are isotropic in the different directions and for which the product of signs of the different transfer integrals is positive¹⁸.

Polymer semiconductors

Different from small molecules, design of conjugated polymers is harder due to their inherently disordered nature and lack of clear structure/property relationship. Their synthesis and purification are more difficult. In spite of this, in the past few years, hole mobility of high performance conjugated alternating D-A polymer such as PDTT- C_8C_{10} (See Figure 1.3a) could achieve a benchmark value of $10.5 \text{ cm}^2\text{V}^{-1}\text{s}^{-1}$ ¹⁹. The intrachain hole mobility along isolated chain of ladder-type poly(p-phenylenes) (See Figure 1.3b) on dilute solution measured by time resolved microwave conductivity (TRMC) achieved $600 \text{ cm}^2\text{V}^{-1}\text{s}^{-1}$ ²⁰.

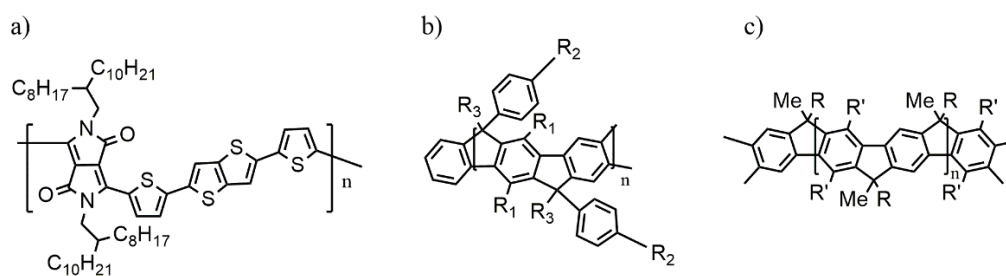


Figure 1.3 Molecular structure of a) PDTT-C₈C₁₀, b) poly(*p*-phenylenes) and c) MeLPPP.

U. Scherf et al. had shown that the intrachain mobility for methyl-substituted poly(*p*-phenylene) (MeLPPP) (See [Figure 1.3c](#)) is more than 3 orders of magnitude higher than the interchain mobility measured by time of flight (TOF) ²¹. Carrier mobility in polymers is significantly dependent on time as shown in [Figure 1.4](#) ¹³. Thus, it's critical to understand charge transport in conjugated polymers from the perspective of multiple scales. In OPV operation, this conception also helps to understand the importance of on-chain, short-timescale transport for charge generation and then charge separation by moving only a few nanometers away at the D-A interface.

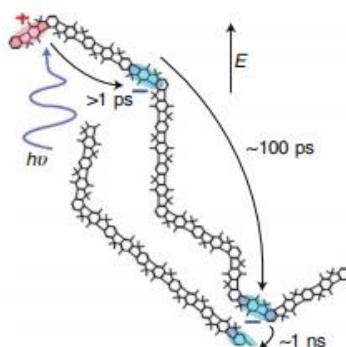


Figure 1.4 Sketch of 3 time domains governing charge transport. These are identified as ultrafast motion inside a conjugated segment and along a single polymer chain, respectively, while the slow motion phase involves interchain jumps ¹³.

There are two typical molecular packing modes adopted by polymer backbones in solid-state (See [Figure 1.5](#)): face-on and edge-on packing of conjugated backbone plane relative to the substrate, which could be tuned by the methods of thin-film deposition, substrate treatment and post thermal treatment of the film ²². For example, after mechanical rubbing, polymer chains of P3HT align parallel to the rubbing direction and subsequently, crystalline domains undergo orientation changes from edge-on to face-on orientation ²³. The highest field-effect mobility was measured along the rubbing direction in the oriented face-on films, i.e., along the long axis of polymer chain.

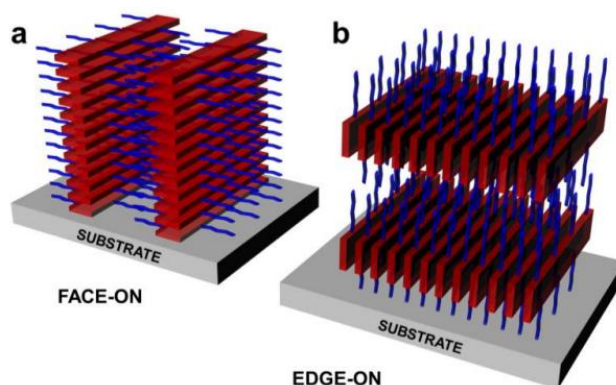


Figure 1.5 Schematic representations of (a) face-on and (b) edge-on orientations with red color symbolizing the conjugated backbone and blue arms symbolizing the polymer side chains ²².

However, for a given organic semiconducting material, large variations of charge transport properties from device to device usually exist since the device performance is not only affected by molecular packing and orientation, but also by morphological defects, amount of grain boundaries, crystal size, misalignment of crystalline grains and crystal defects, etc... which could be modified by the film deposition methods. The different processing methods that are applied for semiconducting thin film fabrication will be introduced and discussed in detail in § 1.2.

1.1.2 Applications for organic optoelectronics

As OFETs and OLEDs were mainly studied during the PhD work, they will be more discussed hereafter, while OPV will be just introduced briefly.

1.1.2.1 Organic photovoltaic (OPV)

Solar energy, as one of the cleanest and most abundant novel energies, has been attracting considerable interest of the scientists committed to convert it to the electrical energy so as to solve the global energy crisis and environmental problem due to the consumption of traditional nonrenewable energy such as coal, oil and natural gas. One approach is to employ the organic solar cells based on the organic semiconducting small molecules or polymers to achieve photoelectron conversion. Low-temperature processing of organic small molecules by vacuum thermal evaporation or polymers by low-cost and large-scale solution-processed methods endows the OPV with critical advantages over its inorganic counterparts, since the high-temperature processing of the latter limits the range of substrates on which they can be

deposited.

Considering the bulk-heterojunction organic solar cells as an example, the photoconversion mechanism can be divided into five steps: light absorption, exciton diffusion, charge separation, charge transport and charge extraction, which can be seen in Figure 1.6. Excitons (electron-hole pairs) bounded by the Coulomb attractive forces are generated from the HOMO into the LUMO after the photoactive layer absorbs the photons of the solar energy. They must diffuse toward an adjacent D-A interface to dissociate into free charges. If an exciton is not separated within its lifetime, it will easily recombine. To maximize charge separation, a large heterointerface is required. Under the effect of the chemical potential difference between the two organic semiconductors, electron transfer from the donor to the acceptor, or hole transfer from the acceptor to the donor, at the heterointerface, can both result in charge separation. Subsequently, the free electrons and holes are transported through their respective domains (holes hop through p-type material and electrons hop through n-type material) to induce a photocurrent.

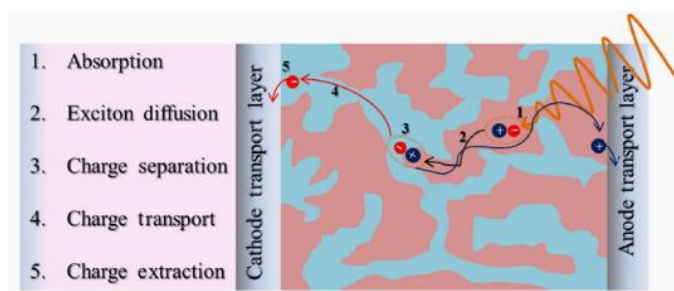


Figure 1.6 Overview of the photoconversion mechanism in bulk-heterojunction organic solar cells²⁴.

External quantum efficiency (η) defines the percentage of incident photons at a given wavelength that are converted into photocurrent²⁵. The overall η is determined by the efficiency of photoconversion processes through $\eta = \eta_{abs} \times \eta_{exdis} \times \eta_{ce}$, where η_{abs} is the light absorption efficiency, η_{exdis} the exciton diffusion and charge separation efficiency, and η_{ce} the charge extraction efficiency. Power conversion efficiency (PCE) is also another key parameter to evaluate solar cell performance and an efficiency of at least 10% is necessary for organic solar cells to establish a viable market²⁵. PCE is proportional to short circuit current density (J_{sc}), open-circuit voltage (V_{oc}), and fill factor (FF), as shown by the formula $PCE = (J_{sc} \times V_{oc} \times FF) / P_{in}$, where P_{in} is the input light power²⁶.

The development of the device structures of organic solar cells experienced an improvement from single layer, bilayer, bulk heterojunction (BHJ) and ordered heterojunction²⁴, with the motivation being to enlarge donor/acceptor interface (see Figure 1.7) and to increase charge separation and transport efficiency.

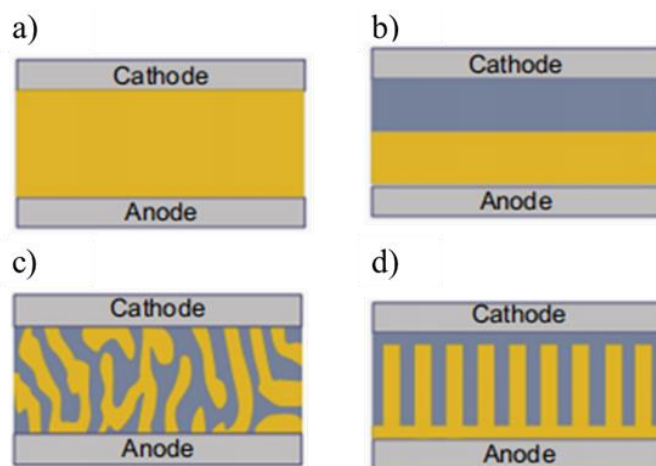


Figure 1.7 Schematic representations of device structures of organic solar cells: a) single-layer, b) bilayer, c) bulk heterojunction, and d) ordered-heterojunction ²⁴.

1.1.2.2 Organic field-effect transistor (OFET)

A FET is an electronic device that amplifies and switches electrical signals by modulating the semiconductor channel conductance through the gate voltage. OFETs with π -conjugated small molecules or polymers as the active layers, have attracted particular attention for the promising applications in low-cost radiofrequency identification (RFID) tags, flexible, active-matrix electronic-paper displays and liquid crystal or OLED displays (See Figure 1.8). However, OFETs require a transistor performance with charge mobility exceeding $1 \text{ cm}^2\text{V}^{-1}\text{s}^{-1}$ for practical applications ²⁷. There is clear evidence that the mobility of the best OSCs now exceeds that of thin films of traditional amorphous silicon. For example, Rubrene achieved a high record mobility of $43 \text{ cm}^2\text{V}^{-1}\text{s}^{-1}$ for its single-crystal transistor ²⁸.



Figure 1.8 Applications of OFETs.

OFET mainly consists of substrate, gate electrode, dielectric layer, source/drain electrodes and organic semiconducting layer. The gate can be a metal or a conducting polymer, but very often, highly doped silicon serves as substrate and gate electrode simultaneously ¹¹. Inorganic insulators such as thermally grown SiO_2 on Si, Al_2O_3 , Si_3N_4 or polymeric insulators like poly(methyl methacrylate) (PMMA) are commonly employed depending on the transistor

structure. The source/drain electrodes, which inject charges into the semiconductor, are generally high work function metals such as gold, Pd, and Ag, but conducting polymers like printable PEDOT:PSS are adopted as well. According to the carriers transported by the semiconducting materials in the channel, OFETs can be classified into 3 kinds: p-type, n-type and ambipolar. P-type OFETs, or more precisely p-type materials, transport holes in the channel; n-type materials transport electrons in the channel; while ambipolar ones can transport holes or electrons in the active layer. OFETs can be divided into four configurations according to the relative positions of the semiconducting layer with respect to the electrodes: bottom gate/bottom contact (BG/BC), bottom gate/top contact (BG/TC), top gate/ bottom contact (TG/BC) and top gate/top contact (TG/TC), as shown in Figure 1.9a, b, c and d, respectively. Generally, p-type materials adopt bottom-gate OFET structures, while n-type or ambipolar materials employ top-gate structures which could, to some extent, overcome the sensitivity of these materials to ambient oxygen and water, thus improving the device stability.

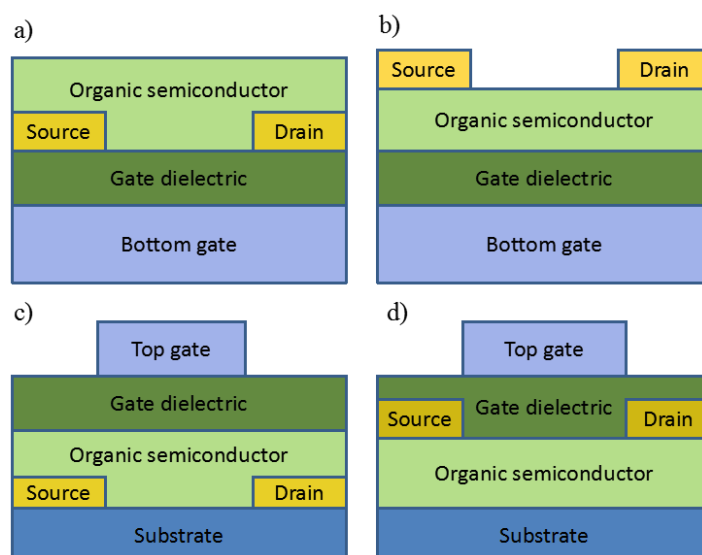


Figure 1.9 Four basic OFET device configurations: a) BGBC, b) BGTC, c) TGBC and d) TGTC.

When a voltage (V_{DS}) is applied between the source and drain, and the source-gate voltage (V_{GS}) is zero, the source-drain current (I_{DS}) is very low and the device is “off”; when V_{GS} is negative or positive, holes or electrons will accumulate at the semiconductor/dielectric interface, then the device is “on”. However, not all accumulated charges are mobile and contribute to the I_{DS} . Thus, V_{GS} higher than a threshold voltage (V_{th} : the minimum $V_{GS(th)}$ that is needed to create a conducting path between the source and drain) is necessary to fill first the deep traps and induce mobile charges. The key parameters to evaluate the OFETs performance include V_{th} , on/off current ratio (I_{on}/I_{off}) (the ratio of I_{DS} in “on” state at a particular V_{GS} and the I_{DS} in “off” state), and hole or electron carrier mobility (μ_{h+} or μ_{e-}). The essential prerequisites for OFETs are (1) near zero V_{th} , (2) large I_{on}/I_{off} , (3) large field-effect mobility (up to $1 \text{ cm}^2\text{V}^{-1}\text{s}^{-1}$)²⁹. Near zero

V_{th} reduces the power consumption of an integrated circuit. V_{th} usually results from built-in dipoles, impurities, interface states, and in particular, charge traps. It can be reduced by increasing the gate capacitance and thus inducing more charges at lower applied voltages. Another important parameter of FETs is I_{on}/I_{off} . Large I_{on}/I_{off} promotes clean switching behavior of the transistor. I_{off} is generally determined by gate leakage; whereas, I_{on} mainly depends on the charge mobility. High mobility is the key to obtaining a large I_{on} for a given device geometry and gate dielectric.

Charge carrier mobilities of OFETs are severely influenced by the charges injection which would be more efficient if the work function of the source/drain electrodes match well with the highest occupied molecular orbital (HOMO) level for p-type material or lowest unoccupied molecular orbital (LUMO) level for n-type material. HOMO and LUMO are associated respectively to the ionization potential and electronic affinity of the organic semiconducting materials. In OLEDs, the work function match of the anode (or the cathode) to the HOMO of the hole injection material (or the LUMO of the electron injection material) is also very important for an effective charge injection³⁰, which will be discussed in chapter 4.

Small molecular OFETs

Typical small molecular semiconductors of high field-effect mobility include pentacene¹⁶ (15-40 $\text{cm}^2\text{V}^{-1}\text{s}^{-1}$, herringbone packing), rubrene²⁸ (43 $\text{cm}^2\text{V}^{-1}\text{s}^{-1}$, slipped π -stack), TIPS-pentacene³¹ (1.8 $\text{cm}^2\text{V}^{-1}\text{s}^{-1}$, brick-wall packing), C₈-BTBT-C₈³² (16.4 $\text{cm}^2\text{V}^{-1}\text{s}^{-1}$, herringbone packing), DNNT³³ (10 $\text{cm}^2\text{V}^{-1}\text{s}^{-1}$, herringbone packing) and C₁₀-DNNT-C₁₀³⁴ (3.4 $\text{cm}^2\text{V}^{-1}\text{s}^{-1}$, herringbone packing), as shown in **Figure 1.1** and **Figure 1.2** in § 1.1.1. More recent developments of p-type OFETs (See **Figure 1.10a** and **b**) involve liquid crystalline derivatives^{35,36} (Ph-BTBT-C₁₀, 13.9 $\text{cm}^2\text{V}^{-1}\text{s}^{-1}$, herringbone packing), thienoacenes with V or N shaped core³⁷⁻³⁹ (C₁₀-DNT-VW, 6.5 $\text{cm}^2\text{V}^{-1}\text{s}^{-1}$; C₆-DNT-VW, 9.5 $\text{cm}^2\text{V}^{-1}\text{s}^{-1}$; C₁₀-DNBDT-NW, 16 $\text{cm}^2\text{V}^{-1}\text{s}^{-1}$; C₈-DNBDT-NW, 13 $\text{cm}^2\text{V}^{-1}\text{s}^{-1}$).

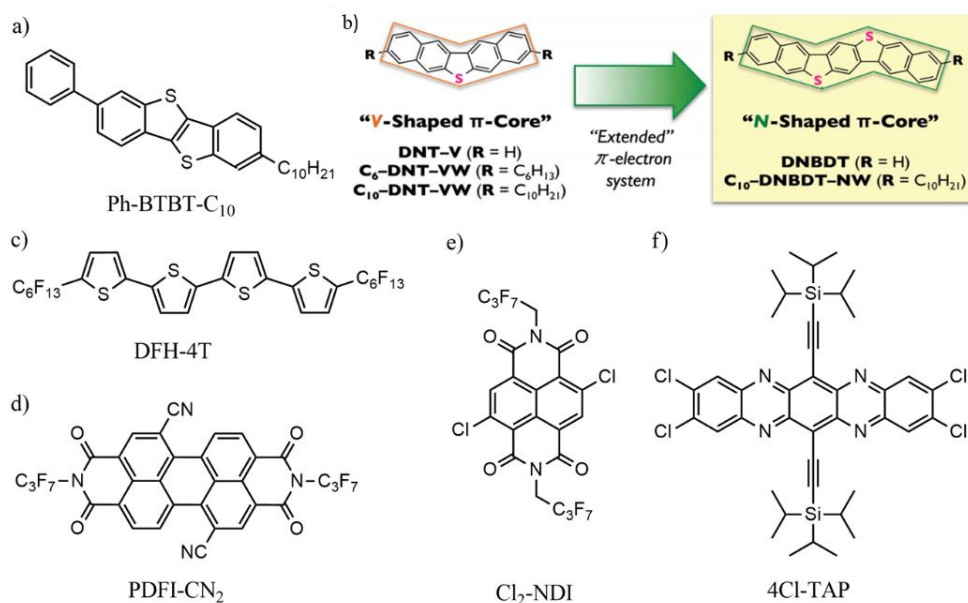


Figure 1.10 Chemical structures of recent high-mobility small-molecule p-type materials: a) Ph-BTBT-C₁₀, b) thienoacenes; and n-type materials: c) Functionalizing oligothiophene, d) PDIF-CN₂, e) Cl₂-NDI and f) 4Cl-TAP.

However, the development of n-type materials, needed for complementary circuits, lags behind due to challenges such as instability in air and large barriers to electron injection. N-type OFETs molecules should have deeper LUMO, and they can be realized for example by functionalizing oligothiophene cores with electron-withdrawing perfluorinated groups (e.g. DFH-4T in Figure 1.10c), or via functionalizing perylene-based and naphthalene OFETs materials with electron-withdrawing imide substituents (NDI and PDI)⁴⁰. To date, the best performing n-type materials include molecules exhibiting a brick-wall packing (PDIF-CN₂ in Figure 1.10d, 10.8 cm²V⁻¹s⁻¹; 4Cl-TAP in Figure 1.10f, 27.8 cm²V⁻¹s⁻¹)^{41,42}, slipped π -stack (Cl₂-NDI in Figure 1.10e, 8.6 cm²V⁻¹s⁻¹)⁴³.

However, there are several problems needed to be solved concerning this research field.

(1) Modern electronics require the integration of many devices with various function (such as organic light emitting transistor (OLET)⁴⁴ combining the function of OFET and OLED in a single device). If fewer materials are used to realize multifunctionality, then the fabrication cost will be evidently decreased⁴⁵. To date, only a few molecules were reported with bifunctionality, such as the integration of high mobility and photoemission in organic single crystals. Thus, in chapter 2 and 4, both the charge transport properties and the photophysical properties of the organic semiconducting materials will be investigated.

(2) Side-chain substitution are usually used to introduce the solubility of the semiconducting material. However, care must be taken when introducing solubilizing side chains that these substituents do not significantly disrupt the formation of an ordered solid-state structure which are critical for charge carrier transport in electronic devices. Therefore, in chapter 3, the effect

of side chain on the charge mobility of BTBT derivatives will be investigated.

(3) The development of n-type materials, needed for complementary circuits, lags behind due to challenges such as instability in air and large barriers to electron injection. In chapter 5, the dependence of the n-type behavior of the semiconducting material on substrate surface treatment will be introduced.

Polymer OFETs

In terms of polymer OFETs, developments have occurred from simple polythiophene conjugated polymers to D-A copolymers with alternating electron-donating and electron-withdrawing units along the backbone. There is now a wide range of these D-A polymers, combining acceptor moieties such as Diketopyrrolopyrrole (DPP), naphthalene Diimides (NDI), Perylenetetracarboxylic diimides (PDI), Benzothiadiazole (BTZ), Pyridalithiadiazole (PT) and isoindigo (ii), with donor moieties like Thiophene (T), Thieno[3,4-b]thiophene (TT), Cyclopentadithiophene (CDT) and so on. Chemical structures of current high-performance p-type, n-type and ambipolar polymers are respectively shown in [Figure 1.11](#). C. Luo, A. J. Heeger, et al. employed sandwich casting to create unidirectional alignment and achieve efficient charge transport for self-assembled PCDTPT ⁴⁶ ([See Figure 1.11](#)) film, with a high hole mobility of $36.3 \text{ cm}^2\text{V}^{-1}\text{s}^{-1}$ measured in OFET device. The PCDTPT incorporates the donor blocking CDT and the acceptor blocking PT, resulting in higher electron affinity in the backbone and narrower optical gap. In 2016, Yunqi Liu and coworkers reported the high-performance, air-stable FETs based on heteroatom-substituted NDI-BTZ copolymers PNBS ⁴⁷ ([See Figure 1.11](#)) exhibiting ultrahigh electron mobility up to $8.5 \text{ cm}^2\text{V}^{-1}\text{s}^{-1}$. Selenophene (Se) heterocycles were introduced into the polymer main chains, leading to strong Se-Se and π - π interactions between neighboring chains. Regarding the ambipolar polymer presenting both p-type and n-type operations, D-A polymer PTDPPSe-SiC5 ⁴⁸ ([See Figure 1.11](#)) using DPP-Se copolymer with hybrid siloxane-solubilizing groups achieved unprecedentedly high hole and electron mobilities of 8.84 and $4.34 \text{ cm}^2\text{V}^{-1}\text{s}^{-1}$ respectively. These results provide new insight into the design of printed and flexible polymer. However, compared to p-type material, both n-type and ambipolar materials are lagging behind. This is due to the few types of acceptor units that strongly accept electrons. Therefore, designing and synthesizing new acceptor units is an important task in this field.

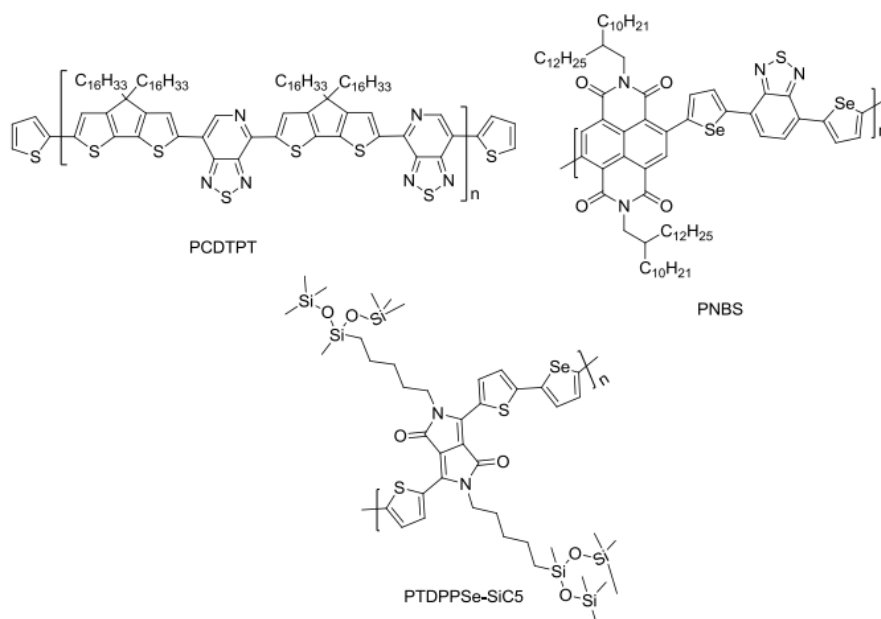


Figure 1.11 Chemical structures of current high-performance p-type, n-type and ambipolar polymers.

1.1.2.3 Organic light emitting diode (OLED)

OLED is a device with a film of organic semiconductor corresponding to an electroluminescent layer which emits light in response to an electric current. Since OLEDs share the advantages of organic semiconducting materials such as flexibility and foldability over large-area, low-cost fabrication and high-performance optoelectronic properties, their potential is high for novel optoelectronic devices, for example, lighting applications and flat-panel displays free of backlight. As a result, OLED displays are generally thinner and more efficient than conventional liquid crystal displays (LCDs), while the latter need a white backlight. Additionally, OLED displays provide improved image quality (better contrast, higher brightness, wider viewing angle, wider color range and much faster refresh rates) and better durability in a broader temperature range. Small and medium size OLED panels have been successfully applied to portable devices, such as mobile phones, digital cameras, mp3 players, and so on. Large size OLED TVs are now also available from Samsung and LG ⁴⁹.

The phenomenon of electroluminescence (EL) can be traced back to Pope's early work ⁵⁰ in 1960s, when he used 10-20 μm thick single crystals of Anthracene (molecular structure: See Figure 1.12a) as electroluminescent material. The luminescence was first observed above 400 V. The current through the crystal was more than 1 μA ; this represents a current density near the small electrode of about 100 $\mu\text{A}/\text{cm}^2$. In 1982, Vincett ⁵¹ obtained the lighting at applied voltage of only about 30 V (Typical current density ~ voltage curve is shown in Figure 1.12b) from vacuum-deposited 600 nm thick Anthracene film, which significantly reduced the driving voltage and improved the efficiency.

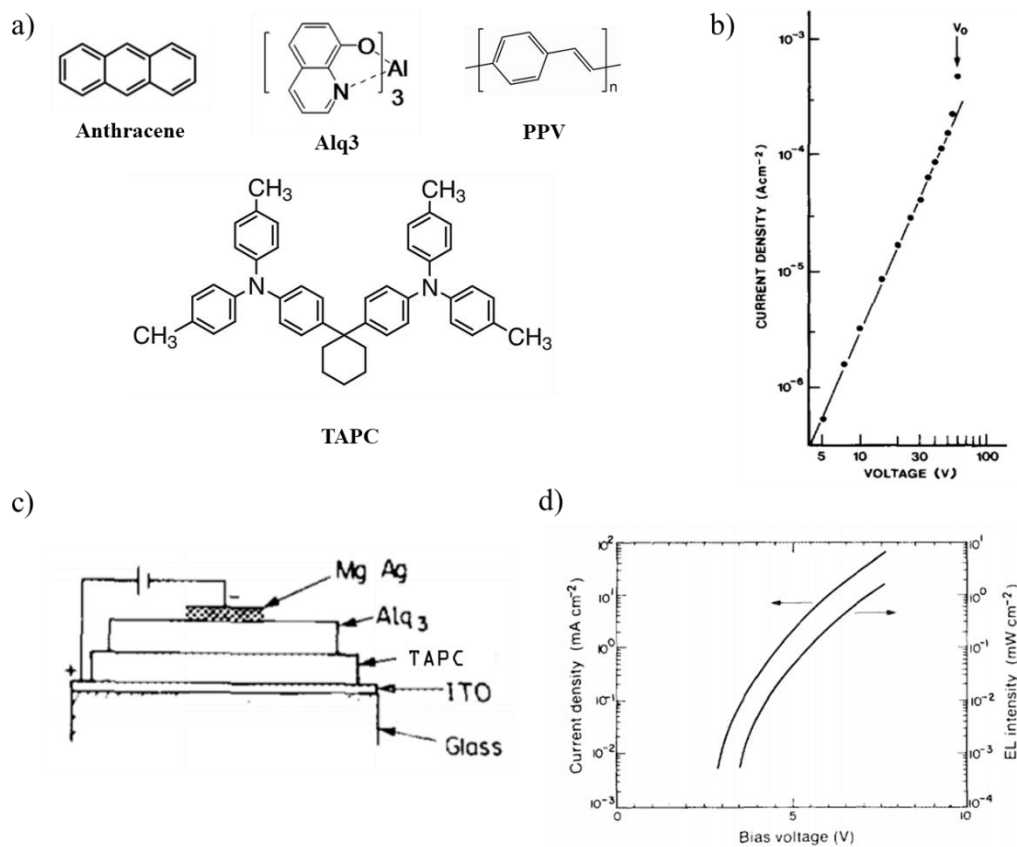


Figure 1.12 a) Chemical structures of Anthracene, Alq3, PPV and TAPC. b) Typical $\log J$ vs. $\log V$ plot obtained at lower voltages after long-time application of a higher voltage V_0 (arrowed) (nominal film thickness about 600nm)⁵¹. c) Schematic representation and d) Brightness-current-voltage characteristics of the first practical OLED structure⁵².

The first practical OLED with luminance above 1000 cd m⁻², a driving voltage about 10 V and an external quantum efficiency (EQE) of 1% was developed by Ching W. Tang and Steven Van Slyke at Kodak in 1987⁵². (Internal and external quantum efficiency (IQE and EQE) are two important parameters that evaluate the OLEDs performance. The former is defined as the number of photons generated per number of injected carriers, while the latter is defined as the number of photons emitted per number of injected carriers.) The structure of this first practical OLED (See Figure 1.12c) was ITO/TAPC/Alq3/Mg/Ag (ITO: indium tin oxide; TAPC: 1,1-bis{4-[di(p-tolyl)amino]-n phenyl}cyclohexane; Alq3: tris(8-quinolinolato)aluminum) (molecular structures of TAPC and Alq3: See Figure 1.12a). TAPC played the role of hole transport layer (HTL), while Alq3 was vacuum thermal evaporated and served as electron transport layer (ETL) and emitting layer (EML). The strategy of each material with its own function has become the basic rule for high-performance OLED designing. The light output from the OLED is linearly proportional to the input current in the current range from 10²-10⁵ μ A/cm². (See Figure 1.12d) Soon after, in 1990⁵³, the first polymer OLED, with structure of

ITO/PPV/Al (PPV: poly(*p*-phenylene vinylene); molecular structure: See Figure 1.12a), was reported by Richard Friend et al., and PPV was spin-coated, holding prospect for a large-area, low-cost solution-processable commercial application.

OLED devices structures and work mechanism

At first, there was only one organic emitting layer (EML: the layer where the electrical energy is directly converted into light in response to an electric current) between the cathode (negatively charged to inject electrons into the organic layers) and the anode (positively charged to inject holes into the organic layers), which was the simplest OLED structure (See Figure 1.13a). However, in this simplest OLED configuration, the luminescent efficiency was very low due to bad charge injection and the unbalance transport of holes and electrons. In order to improve the EL efficiency, scientists keep optimizing the structure. Now more layers are inserted, such as hole injection layer (HIL: this layer receives holes from the anode and injects them deeper into the device), hole transport layer (HTL: this layer supports the transport of holes across it so they can reach the emissive layer), electron injection layer (EIL: this layer receives electrons from the cathode and injects them deeper into the device) and electron transport layer (ETL: this layer supports the transport of electrons across it so they can reach the emissive layer), as shown in Figure 1.13b. Sometimes, HTL or ETL can simultaneously be used as electron or hole blocking layer (EBL or HBL: this layer is used to improve OLED technology by confining electrons or holes to the emissive layer) respectively, or additional EBL or HBL are incorporated.

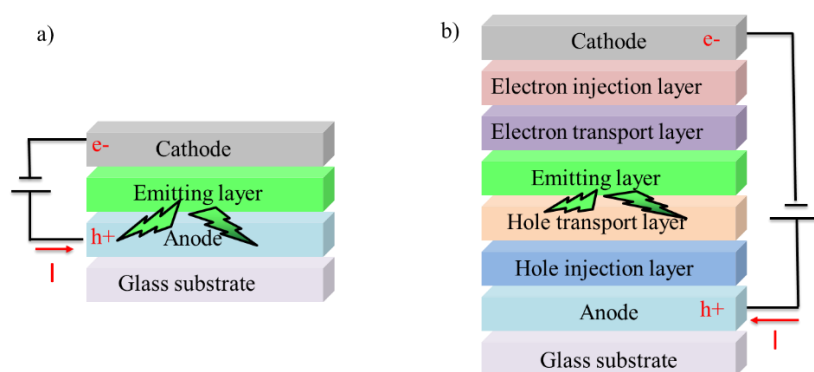


Figure 1.13 Schematic representation of the OLED device structures. a) The simplest OLED structure with only EML between the cathode and the anode; b) The optimized OLED structure with EIL, ETL, EML HTL and HIL between the cathode and the anode.

After an external bias is applied to the device, holes and electrons are injected from the anode and the cathode respectively into the adjacent organic semiconducting layer. Recombination of holes and electrons in the EML results in the creation of excitons that radiatively decay to the

ground state (S_0) and emit light.

Development of the organic electroluminescent materials

In OLEDs, the emitters play a vital role in the devices⁵⁴. According to the electroluminescent mechanism of the EML, organic electroluminescent materials have been developed in three generations⁵⁵. The first generation corresponded to fluorescent materials with a maximum IQE of 25% due to the creation of only 25% singlet excitons (S_1) accompanied with 75% non-radiative triplet excitons (T_1) (See Figure 1.14a). Emission from S_1 to S_0 and from T_1 to S_0 are called fluorescences and phosphorescence, respectively.

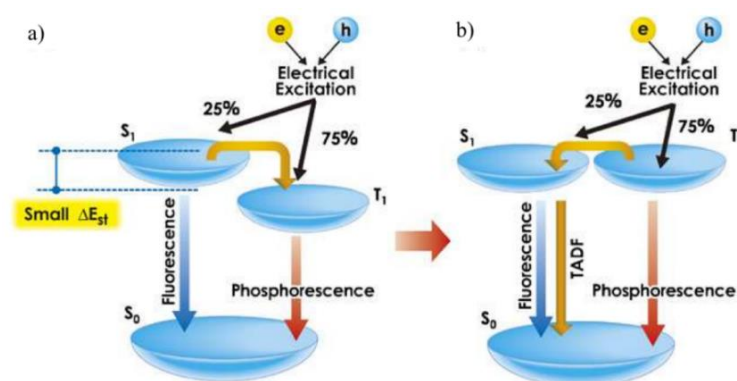


Figure 1.14 Diagram for the processes of a) fluorescence and phosphorescence, and b) thermally active delayed fluorescence (TADF)⁵⁵.

In S_1 , the electrons in the excited orbital is paired to the second electron in S_0 orbital by opposite spin (See Figure 1.15). As a result, return to S_0 involves no spin change and it is spin allowed and occurs rapidly by emission of a photon. A typical fluorescence lifetime is near 10 nanoseconds (ns). (The lifetime determines the time available for the luminescent materials to interact with or diffuse in its environment. It is the average time the molecule spends in the excited state before returning to S_0) However, in T_1 , the electrons in the excited orbital is paired to the ground-state electron by the same spin orientation (See Figure 1.15). Therefore, return from T_1 to S_0 is “forbidden” with a slow rate of emission and typical phosphorescent lifetime of milliseconds (ms) to seconds (s). (Allowed transitions are those that have high probability of occurring. Forbidden transitions are those that have a high probability of not occurring. Strictly forbidden transition is one that cannot occur at all.)

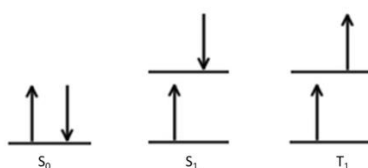


Figure 1.15 Singlet and triplet levels.

Figure 1.16 presents some typical fluorescent materials with light emission from UV to red. In 1998, the Thompson and Forrest groups⁵⁶ boosted OLED IQE from 25% to 100% by using phosphorescent materials, constituting the second-generation organic electroluminescent materials. Heavy metal atoms were widely used in phosphorescent materials with the purpose being to mix the triplet and singlet excitons, thus making the direct radiative decay possible from T_1 to S_0 (See Figure 1.14a). Initially, the only phosphorescent emitters found to be practically useful were iridium (Ir) and platinum (Pt) complexes. Phosphorescent materials were thus limited due to the high cost, high toxicity and instability of Ir and Pt. Figure 1.17 presents the molecular structures of some typical phosphorescent materials^{57–59}.

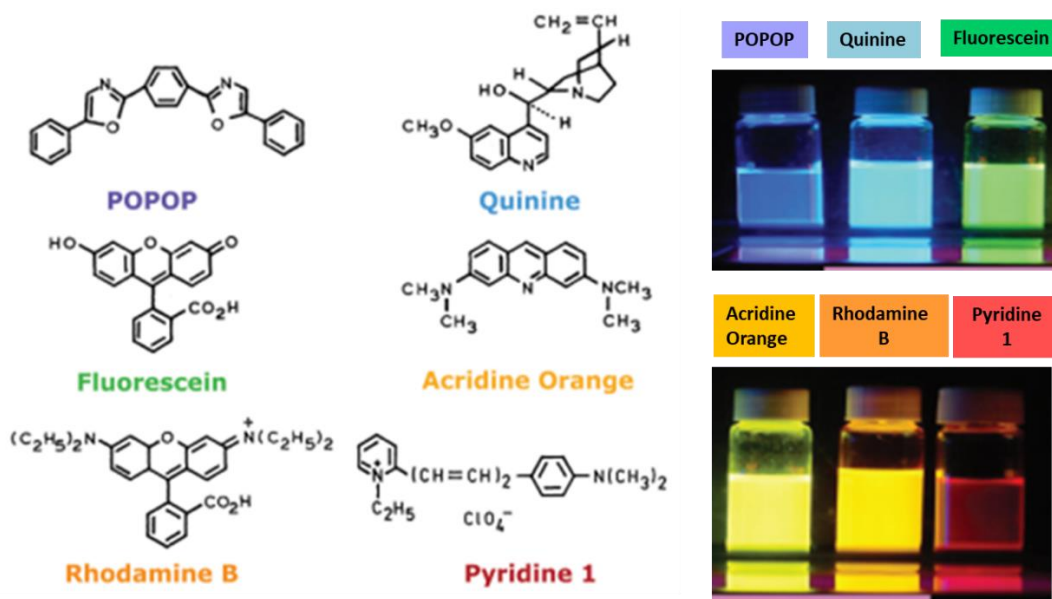


Figure 1.16 Molecular structures of typical fluorescent materials and fluorescence of their solution under UV⁶⁰.

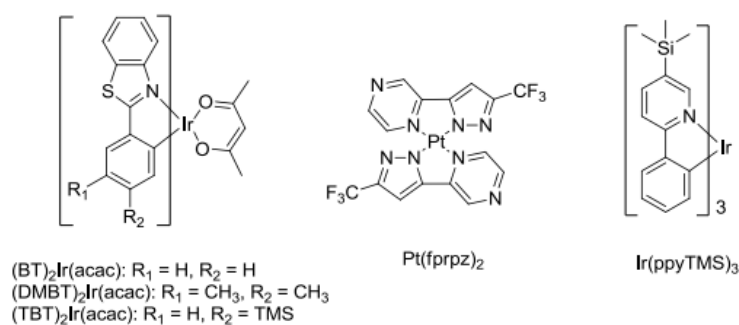


Figure 1.17 Chemical structures of typical phosphorescent materials^{57–59}.

In comparison, pure organic room-temperature phosphorescence (RTP) emitters don't have those drawbacks of traditional phosphorescent materials, and they are attracting rising interest in optoelectronic devices. Recently, Benzhong Tang's group⁶¹ synthesized a series of metal-free carbazole-based emitters without heavy atoms and carbonyl groups. They realized tunable molecular emission from fluorescence to phosphorescence by gradually tuning the substituent

from fluoro to hydrogen and then to hydroxyl group. After removing the excitation light source, commercial TCz-F (See [Figure 1.18](#)) led to a lifetime of 727 ms benefiting from an existing isomer in the commercial carbazole, while the lab-synthesized TCz-F only led to a lifetime of 48.6 ms. The small energy gap between S_1 and T_1 and the low reorganization energy helped to enhance intersystem crossing (ISC) from S_1 to T_1 and contributed to a more competitive radiative decay from T_1 to S_0 .

Another kind of emitters that can theoretically realize an IQE of 100% are thermally active delayed fluorescence (TADF) emitters^{62,63}, the third-generation of organic electroluminescent materials. In 2009, Adachi's group^{64,65} from Kyushu University proposed potential mechanisms to achieve capability of harvesting both singlet and triplet excitons by the use of TADF without the utilization of heavy metal chelate. TADF emitters, such as 4CzIPN (see [Figure 1.18](#)), have a very small energy gap between S_1 and T_1 , which allows the reverse intersystem crossing (RISC) from T_1 to S_1 (see [Figure 1.14b](#)).

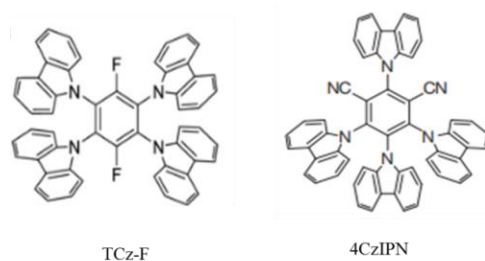


Figure 1.18 Chemical structure of TCz-F and 4CzIPN.

However, like charge mobility, the photoluminescence (PL) and electroluminescence (EL) properties of the emitting materials in OLED devices depend greatly on the film morphology formed during different deposition methods such as spin coating and vacuum thermal evaporation. In the next [§ 1.2](#), a systematic introduction of the different elaboration methods of the semiconducting thin film will be presented. Moreover, their advantages and disadvantages will also be discussed.

1.2 Elaboration of semiconducting thin films

Generally, for a given organic semiconducting material, large variations of performance from device to device usually exist. This is because the performance of semiconducting thin film is affected a lot by molecular alignments, morphological defects, amount of grain boundaries, crystal size, misalignment of crystalline grains and crystal defects, etc.... which could be modified by carefully choosing deposition methods. As a result, if the deposition method is successful, the theoretical intrinsic charge carrier mobility of OSCs can be measured.

1.2.1 Solution-processing methods

Solution-processing methods are widely applied to deposit organic thin films mainly due to their low cost and the possibility of obtaining films of large areas. In particular, if either decomposition or degradation happens during the vacuum thermal evaporation, the solution-processing methods will worth to be tried. Deposition parameters such as solvent type, solution concentration, solution and substrate temperature, substrate surface treatment as well as the organic semiconductor itself can influence the thin film quality and the final device performance. Solution-processing methods for elaboration of semiconducting thin films include drop coating, dip coating, blade coating, spin coating, inkjet printing, roll-to-roll techniques, and so on. The first four methods are lab-scale and commonly applied to investigate the property of the semiconducting materials in academic research field such as universities and institutes, while the last two methods are more industrial-scale and widely employed, having great potential for industrial production.

1.2.1.1 Drop coating

Drop coating is the simplest method to fabricate semiconducting thin films. Usually the solution is dropped on the substrate and the solvent evaporates quickly, forming a thin film on the substrate surface, as displayed in [Figure 1.19](#). This method is very simple and doesn't waste material. However, it is just applicative for small-area deposition and small-scale device fabrication. In addition, relatively longer evaporation time generally leads to bigger crystals with radial alignment instead of directional character which is crucial for charge transport in OFETs ⁶⁶. A number of modifications have been developed to improve the quality of drop coated films, such as vibration with unidirectional sound waves during evaporation ⁶⁷ as well as using sealed chambers ⁶⁸, and inert gas purging ⁶⁹ to control the solvent evaporation. It should also be noted that drop coating may be a good method to prepare single crystals as active layers in OFETs. Li et al. ⁷⁰ obtained the single crystals of TIPS-Pentacene (Molecular structure: [See Figure 1.1](#)) with dimension up to millimetres by utilizing the drop coating from azeotropic binary solvent. The TIPS-PEN single crystals exhibit enhanced charge mobility by a factor of four compared to that of the polycrystalline-films.

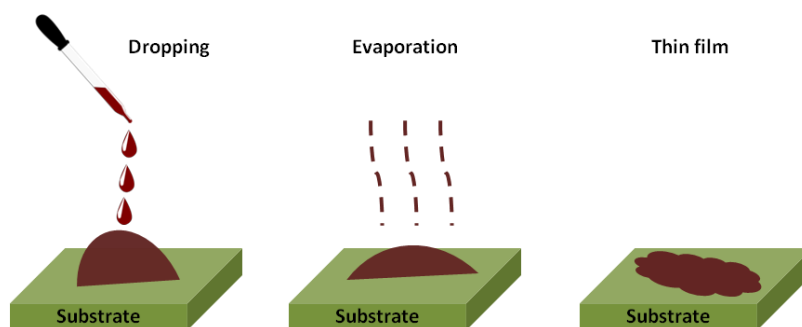


Figure 1.19 Schematic representation of the stages of drop coating.

1.2.1.2 Dip coating

Dip coating is another simple method to fabricate semiconducting thin films. During this process, as sketched in [Figure 1.20](#), a substrate is withdrawn vertically at a constant speed from the solution of the OSCs after it has been immersed inside the solution for a while. Excess liquid drains from the surface and the solvent evaporates, forming a thin-layer film on the substrate surface. Films with varied thickness and aligned crystalline domains can be achieved by modifying withdrawn speed, solvent evaporating rate, solution concentration, solution viscosity and reservoir temperature^{71,72}. Rogowski et al.⁶⁶ precisely controlled the crystalline size of the organic semiconductor via the speed of dip coating of an azeotropic binary solvent mixture. They manufactured high-performance OFETs with charge mobility up to $1\text{ cm}^2\text{V}^{-1}\text{s}^{-1}$ for TIPS-Pentacene. Nam et al.⁷³ used a programmed dip-coating technique with low-boiling-point solvent to induce the self-assembly of TIPS-Pentacene film, which induced highly crystalline grains, favourable morphology and molecular ordering for efficient charge transport in OFETs. Indeed, the dip coating method can fabricate very thin and large area films with good uniformity. However, a few drawbacks are waste of material, time consuming and double side coverage.

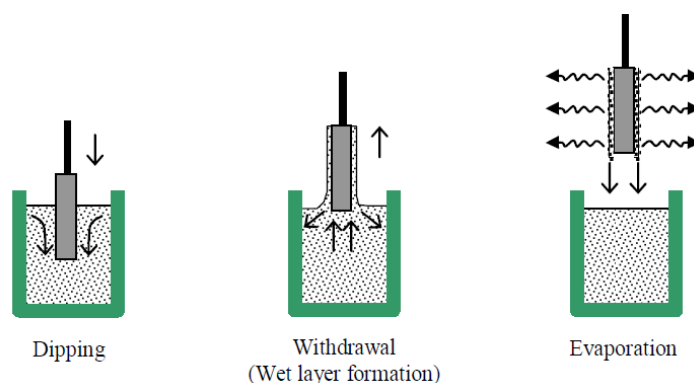


Figure 1.20 Schematic representation of the different stages of dip coating⁷⁴.

1.2.1.3 Blade coating

From a fluid mechanical perspective, blade coating is a horizontal dip coating⁷¹. A variety of techniques (doctor blading, bar coating and knife-over-edge methods, and so on) in which a solid edge is passed over a bead of solution can be classified as “blade coating” methods. Typically, a sharp blade (a knife’s edge or a needle, for example) is passed over a solution droplet and then the solvent evaporation occurs, leaving a layer of film⁷². This method induces low material waste and can fabricate large-area film with good uniformity and low cost. In addition, as a facile way to simply spread and deposit a film over a substrate, it has been employed in roll-to-roll processes^{75,76}. Chun-Yu Chen and coworkers successfully applied the continuous roll-to-roll blade-only method to a wide range of multi-layer structures for OLED involving HTL, EML and ETL. This method is applicable both for polymers and small molecules. The authors applied top-hot wind and bottom heating plate (Figure 1.21) to assure immediate evaporation of the solvent and achieve uniform film. However, compared to spin coating, solvent evaporation during blade coating is relatively slow and the solutes tend to aggregate or crystallize at high concentration^{77,78}. R. Mens et al. focused on the influence of the casting methods on the resulting phase morphology of polymer blend films. They found that there was a higher degree of crystallized PC₆₀BM in doctor-bladed films as compared to spin-coated films using the same solutions⁷⁹. On the other hand, the thickness of the blade coated film is mainly determined by the gap between the blade coater and the substrate, with film thickness control limited at micrometric level.

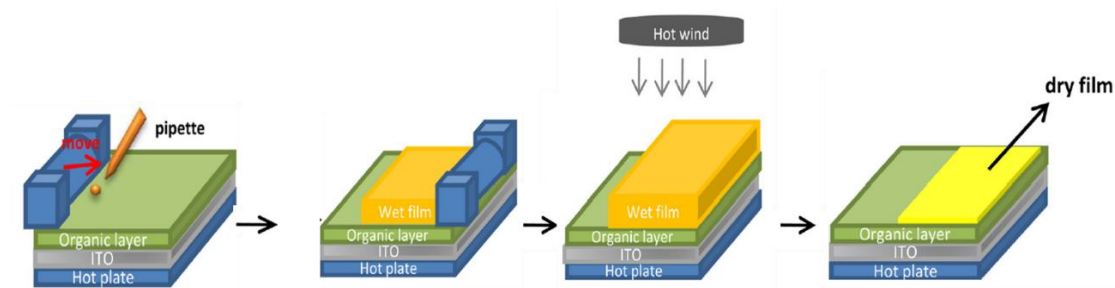


Figure 1.21 The procedure of the blade-only method⁷⁵.

1.2.1.4 Spin coating

Conventional on-centre spin coating is the most commonly adopted solution-processing method. Schematic representations of its different stages are shown in Figure 1.22⁸⁰. Spin coating involves depositing the solution onto a substrate, followed by acceleration of the substrate to a set rotational speed⁷⁷. The solvent then evaporates soon after deposition, leaving a thin and homogenous film on the substrate. For both the polymers and some small molecules, it can

provide very uniform thin films ($\sim 100\text{nm}$), as required in most devices such as OFETs and OLEDs. The film thickness and morphology depend on the solution concentration, solvent type⁸¹, rotational speed, substrate surface treatment, substrate temperature, and post thermal treatment⁸² of the film. Advantages such as good control of thickness and efficient deposition of large-area semiconducting thin films over large-scale optoelectronics devices are conceivable. However, there are also some shortcomings. Primarily, fast rotation of the substrate results in the ejection of most of the applied solution and thereby a waste of material. Secondly, molecules have less time to align due to quick dry of the film.

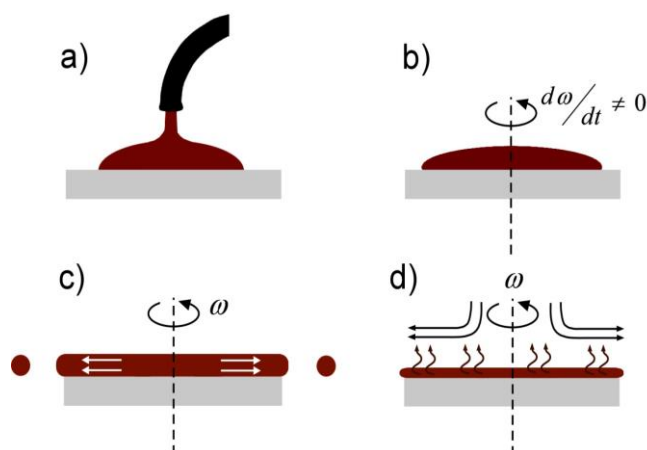


Figure 1.22 Schematic representations of the different stages of conventional on-centre spin coating⁸⁰.

However, Bao Zhenan and coworkers⁸³ demonstrated a new spin coating method, off-centre spin coating (Figure 1.23), to enhance the performance of organic thin film transistors (OTFTs) (maximum hole mobility $43\text{cm}^2\text{V}^{-1}\text{s}^{-1}$ for $\text{C}_8\text{-BTBT-C}_8$ (molecular structure: See Figure 1.1)). They compared the $\text{C}_8\text{-BTBT-C}_8\text{:PS}$ blend film morphology fabricated by conventional on-centre and new off-centre spin coating; the former film showed randomly oriented crystals, while the latter showed highly aligned $\text{C}_8\text{-BTBT-C}_8$ crystals due to the unidirectional centrifugal force over the whole substrate in the off-centre spin coating process. The third shortcoming is solvents used for one polymer layer often damage the layers below, thereby limiting the complexity and performance of the device structure that can be achieved⁸⁴. An even more serious concern is that full-surface deposition hampers the locally patterning of the optoelectronic device such as red, green, and blue polymer OLEDs⁸⁵.

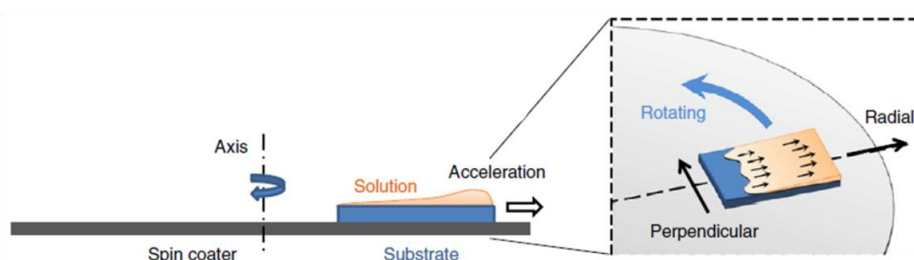


Figure 1.23 Schematic representation of the off-centre spin coating⁸³.

1.2.1.5 Inkjet printing

The working principle of inkjet printing is to eject inks from fine nozzles to a specified position on a treated substrate under the control of a computer. Generally, the ink droplets are ejected in a continuous or drop-on-demand manner (Figure 1.24)⁸⁶. In the continuous mode, the droplets are electrostatically charged by the nozzles. These charged droplets are divided into two parts according to the amount of charge carried under an external electric field. Some droplets involved in the patterning arrive at the specified position of the substrate, whereas the other ones go into the recycling system. Generally, the inks are required to be of low viscosity (4-30 cP) with high surface tension (typically $> 35\text{mN/m}$) in order to easily generate a stream of droplets⁸⁷. Inkjet printing is considered to be a promising candidate to fabricate low-cost, flexible, large optoelectronic devices, such as OFETs, OLEDs and OPVs⁸⁸, owing to its low wastage of inks⁸⁹, quite high resolution, tight control of deposited volume, additive character (that enables material usage minimization and process flow simplicity) and non-contact nature⁹⁰. Moreover, due to the digital and maskless character, the number, layout, and arrangement of the fabricated devices are easily customized by modifying the digital file input to the printer. However, ink jet printers typically use small nozzle size to enable high resolution and controlled deposition, with the potential drawback of nozzle clogging. Inkjet printing suffers from the coffee ring effect, and it is not suitable for dielectric ink and low throughput⁹¹. The characteristics of ink, such as viscosity, surface tension, suspended particle size, and concentration affect its printability, film reliability and device performance thereafter⁸⁶.

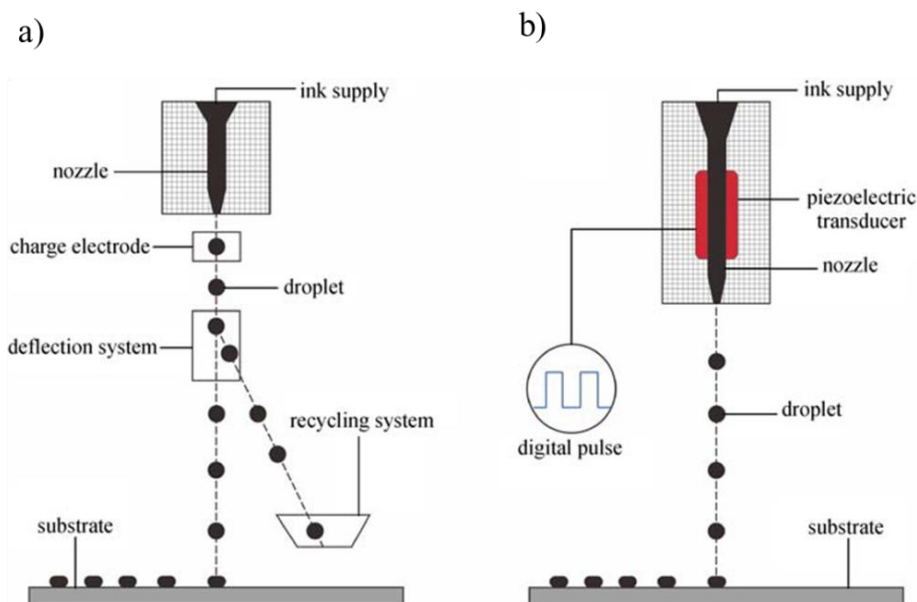


Figure 1.24 Schematic representations of inkjet printing⁸⁶. (a) Continuous mode; (b) Drop-on-demand mode.

1.2.1.6 Roll-to-roll techniques

The most efficient way to fabricate the thin film of a conductive material is using only additive steps through defined printing or coating processes. In this case, the functional material is only deposited where it is necessary and material waste can be fully avoided or minimized to a very low fraction relative to fabrication volume. The highest output is expected through fast roll-to-roll (R2R) processes⁹². R2R techniques, offering the advantages of large-scale⁹³ and low-cost process and high output with high-quality films, have been developed to fabricate OPVs⁹⁴, OFETs⁹⁵ and OLEDs⁹⁶. Obtaining organic semiconducting thin films on flexible substrates has been the goal of organic optoelectronic researchers to be able to transfer the laboratory small-scale devices to industrial large-scale production. In contrast to the abovementioned methods including drop coating, dip coating, blade coating, spin coating and inkjet printing, all being operated on a single device, R2R techniques involve a substrate in the form of a very long sheet that is wound on a roll (See Figure 1.25). The substrate is referred to as the web and is required to be flexible. During printing or coating, the web is unwound from the roll and passed through the printer or coater followed by a rewind to another roll. Along with the printing or coating, there may be heating, drying, UV-curing, and so on. This is appealing in industry where one strives to process in such an integrated manner as the manually operational damages are significantly avoided. Figure 1.25 reveals the schematic representations of R2R processing of a three-layer polymer solar cell in an integrated process.

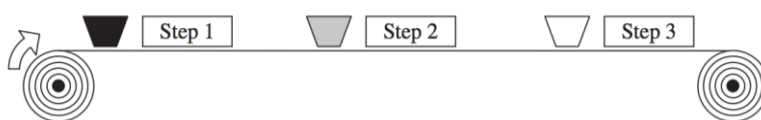


Figure 1.25 Schematic representation of R2R processing of a three-layer polymer solar cell in an integrated process⁹⁶.

There are some R2R compatible methods, such as knife-over-edge, slot die, gravure, meniscus (See Figure 1.26), curtain, multiple slot and multiple slide coating (See Figure 1.27). The last three techniques were expected to coat three layers simultaneously on top of each other and fabricate low-cost multilayers polymer solar cells in a single coating step⁷⁷. However, each layer in the organic electronic device has its own requirements for the deposition techniques (for example, viscosity of the ink)⁹⁷. In addition, if processing of large-area organic semiconducting films is achieved via large-scale production, the currently-used toxic and chlorinated solvents must be replaced with something less harmful to the environment. Furthermore, processing procedures at very high speeds and new materials which are stable in the ambient condition need to be developed⁹⁶.

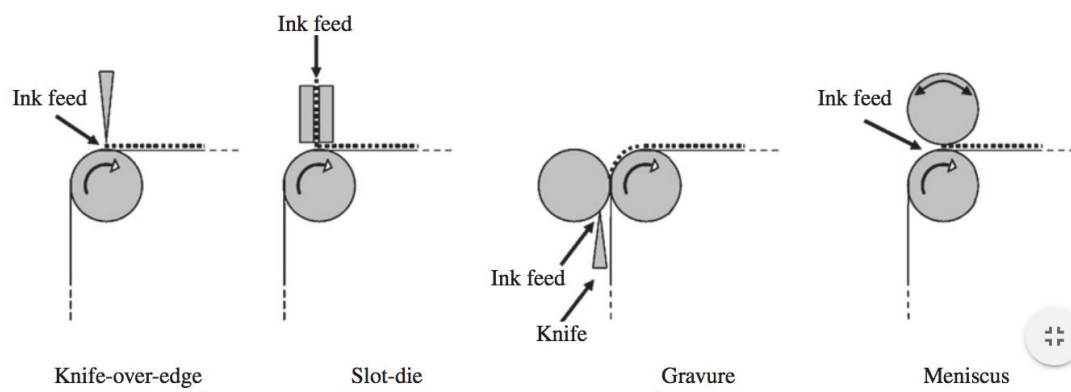


Figure 1.26 Schematic representations of several R2R compatible methods ⁷⁷.

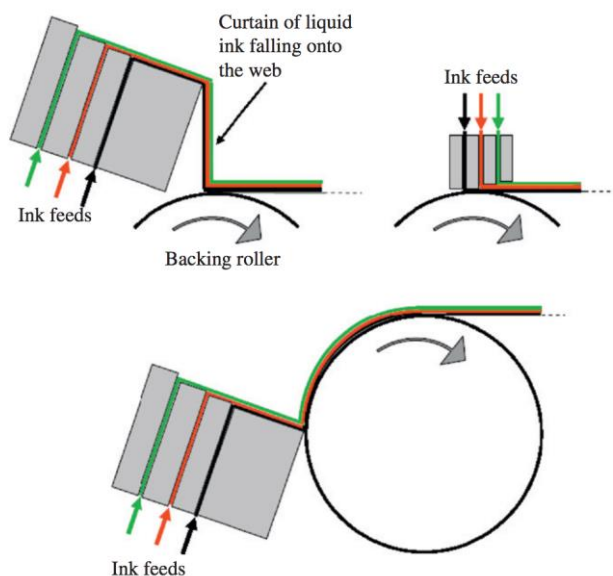


Figure 1.27 An illustration of curtain (top left), multiple slot (top right) and slide coating (bottom) for the simultaneous coating of three layer ⁷⁷.

1.2.2 Solution-free methods

While scientific research and industrial application of OSCs benefit a lot from the solution-processing methods abovementioned, there are some other organic semiconducting compounds, especially some small molecular candidates (pentacene, rubrene...) which are not soluble in common solvents or can't achieve good device performance through solution processing. Hence, solution-free methods such as vacuum thermal evaporation, physical vapor transport deposition and melt-processing are also quite popular in organic optoelectronics fabrication.

1.2.2.1 Vacuum thermal evaporation

The vacuum thermal evaporation method has been widely applied for the fabrication of organic optoelectronics based on small molecules, while polymers devices are generally solution processed. This method involves the heating of the organic compounds in the sublimation boat at the bottom of the vacuum chamber, with the substrate located at the top of the chamber. Usually, shadow masks are needed to limit the place of evaporated organic layers or the electrode layer and to design the device structures (See Figure 1.28).

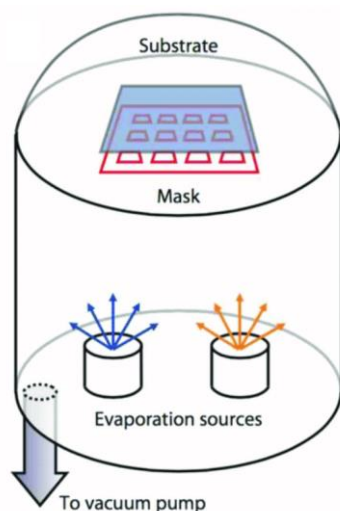


Figure 1.28 Schematic representation of a vacuum thermal evaporation chamber ⁹⁸.

Deposition parameters such as evaporating temperature, evaporating rate, substrate temperature, substrate surface treatment and film thickness have a critical effect on the thin film morphology and device performance. Hakan Usta and coworkers ⁹⁹ firstly synthesized a new n-type BTBT based semiconductor D(Ph_FCO)-BTBT, and the electron mobility of corresponding OFET device fabricated by vacuum thermal evaporation increased from 0.45 to 0.57 cm²V⁻¹s⁻¹ when the substrate temperature increased from 70°C to 100°C during the deposition. There are several advantages concerning this method. Firstly, it usually results in high-quality thin film due to the absence of solvent (for example, high hole mobility about 17.2 cm²V⁻¹s⁻¹ based on evaporated film of mono-substituted C₁₃-BTBT in FET configuration was obtained ¹⁰⁰). Secondly, multi-layer evaporation could be achieved for optimized device structure and performance, basically without physical inter-layer interaction and contamination ⁵, whereas in terms of the solution processing, the solvent used in the preparation of one component may dissolve or affect the previously deposited components ¹⁰¹. Regarding the vacuum thermal evaporation method, one can grow an unlimited number of layers, each optimized for a special function such as the HIL, HTL, HBL and ETL in an OLED device. Nevertheless, masked evaporation leads to material

waste and prevents efficient upscaling. It is also difficult to maintain a uniform evaporation rate as the organic materials are intrinsically thermally insulating ⁵. In addition, to avoid decomposition and degradation of small molecular semiconductors during the sublimation process, high vacuum typically lower than 10^{-4} Pa should be adopted. Therefore, it may be demanding for high-cost equipment such as efficient evaporator.

1.2.2.2 Physical vapor transport deposition

To avoid the drawbacks of the vacuum thermal evaporation, an alternative technique for deposition of organic small molecules called physical vapor transport deposition (VTD) has been developed. Unlike the vacuum thermal evaporation, this method is realized in a hot walled reactor vessel filled with high-temperature inert carrier gas such as nitrogen or argon which induces the evaporation of the source material (See Figure 1.29). The organic vapor is carried downstream to the cooled substrate and forms film with different morphology and crystal structures dependent on the pressure and temperature inside the reactor ⁵. For example, crystallite size of the pentacene grown by VTD deposition varies from a few tens of nanometers when the molecular partial pressure is lower or the gas flow rate is higher, to several micrometers when the molecules arrive at the surface slowly and can form an ordered crystal structure ¹⁰². This technique is able to control the crystalline morphology and use the material efficiently because molecules adsorption only occurs at the cold substrates. In addition, it can achieve uniform and equivalent evaporation independent of the thermal conductivity of the source material ⁵.

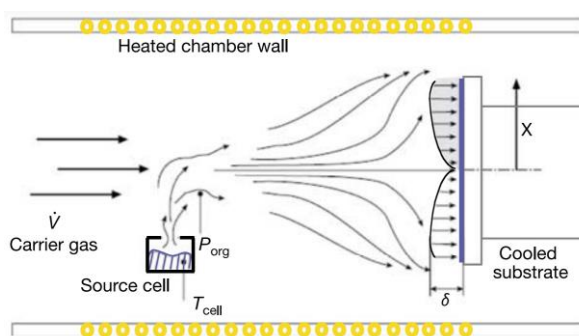


Figure 1.29 Schematic representation of the cross-section of a physical vapor transport deposition reactor ⁵.

Recently, method named micro-spacing in-air sublimation ¹⁰³, actually updated VTD deposition which I prefer to call, has been further developed by researchers to prepare cocrystals. This technique can be conducted totally in air, thus avoiding costly vacuum system and time-consuming procedure in common VTD. The apparatus merely consist of a hot-stage and two silicon wafers as the bottom and top substrates (See Figure 1.30), with the former locating the

organic powder and the latter absorbing physically the formed molecular crystals. Coincidentally, our laboratory also succeeded to fabricate **BTBT** single crystals¹⁰⁴ in air through VTD, which will be discussed in detail in **chapter 3** of this thesis.

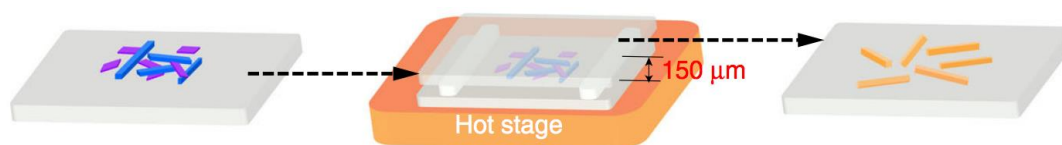


Figure 1.30 Schematic representation of micro-spacing in air sublimation¹⁰³.

1.2.2.3 Melt processing

Thermal treatment is widely used to improve the film morphology and corresponding device performances of organic semiconducting materials. However, heating of unconstrained spin-coated or evaporated film easily results in dewetting of the thin film, especially on hydrophobic n-octadecyltrichlorosilane (OTS)-treated surface. Jonathan and coworkers¹⁰⁵ overcame the problem of dewetting of the material from the OTS-treated surface by confining and melt-processing the material between the substrate and the OTS-treated glass cover (See Figure 1.31). They obtained large domain and favorable morphology for the liquid crystal semiconductor DH-PTTP (5,5'-bis(4-hexylphenyl)-2,2'-bithiophene) in the channel of an OFET with hole mobility up to $2.6 \times 10^{-2} \text{ cm}^2 \text{ V}^{-1} \text{ s}^{-1}$ (five times higher than those of the evaporated devices). DH-PTTP powder was either put under the glass cover or along the edge of the glass cover under the N_2 atmosphere. The powder was heated above the melting point ($233 \text{ }^\circ\text{C}$) and filled the gap of the two substrates. A slow cooling down to the room temperature then occurred.

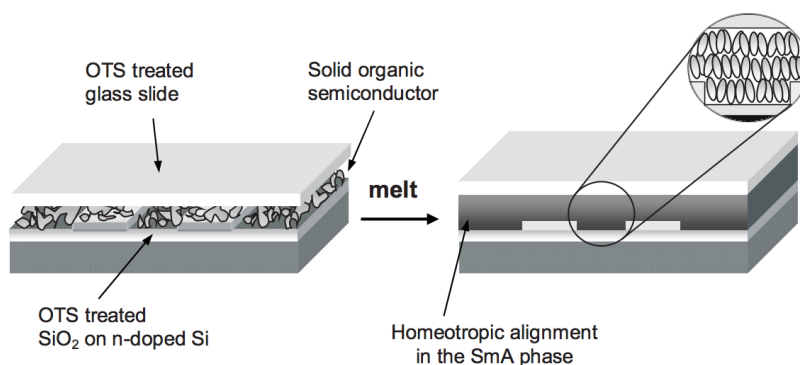


Figure 1.31 Fabrication of an OFET by using a melting process¹⁰⁵.

Another research group¹⁰⁶ also fabricated highly ordered liquid crystal semiconductor film of C_{10} -BTBT- C_{10} by a method they called template-assisted self-assembly (See Figure 1.32), and the OFET based on this highly ordered small molecule micropatterns achieved a hole mobility of $\sim 1.7 \text{ cm}^2 \text{ V}^{-1} \text{ s}^{-1}$. When the PDMS template was carefully detached, the semiconducting lines were formed in a negative copy of the mold with a thickness of 800nm.

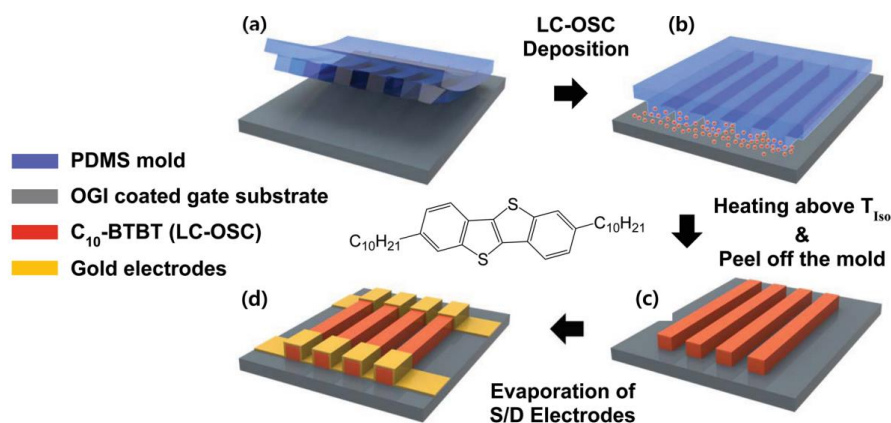


Figure 1.32 A schematic illustration of the micropattern and OFET fabrication process ¹⁰⁶.

According to the above descriptions about melt-processing method, its advantages such as materials saving, solvent free and vacuum free are quite visible. Recently, our laboratory and colleagues ¹⁰⁷ also proposed an improved melt-processing method for the fabrication of DAL1 single-crystalline thin films. This part of work will be introduced in detail in chapter 2 of this thesis. Concerning the drawbacks of melt-processing method, it seems that the devices fabricated by this method are generally limited to p-type materials. Indeed, this method is usually manipulated in ambient condition where the devices made with n-type materials are unstable. The n-type devices suffer large barrier of electron injection since electrons can be easily trapped by the oxygen and water (contains H⁺ and OH⁻) around.

Solution-processing methods such as spin coating and roll-to-roll techniques are generally applied for device fabrication of polymer semiconducting thin films, while solution-free methods like vacuum thermal evaporation, physical vapor transport deposition and melt-processing are the most common methods for depositing the small-molecule semiconducting thin films. In some cases, small molecules can also be processed with solution-processing methods if solubilizing long alkyl chains can have been incorporated ³⁵. Depending on elaboration processes, semiconducting films can be roughly categorized into 3 groups: small-molecule solution-processed films, small-molecule solution-free processed films and polymer solution-processed films. The relative advantages and disadvantages of each type of film at present are summarized in [Table 1.1](#) below ^{108,109}.

Table 1.1 Advantages and disadvantages of semiconducting films depending on elaboration processes.

Type of film	Advantages	Disadvantages
Small-molecule solution-free processed films	Ease of stacking an ideal multilayer structure (vacuum thermal evaporation), High thermal stability, High material purity, Highly-ordered molecular orientation	High cost of fabrication processes, Difficulty in fabricating large-area devices
Small-molecule solution-processed films	Low cost of fabrication processes, Ease of fabricating large-area devices	Low thermal stability, Not well-ordered molecular orientation, Difficulty in stacking an ideal multilayer structure
Polymer solution-processed films	Low cost of fabrication processes, Ease of fabricating large-area devices, High thermal stability, Good horizontal molecular orientation	Low material purity, Low solubility, Difficulty in stacking an ideal multilayer structure

1.3 Characterization of semiconducting thin films

1.3.1 Characterization of charge transport properties

As discussed before, charge transport property is one of the most important properties of the semiconducting thin film and determines the final performance of the corresponding optoelectronic devices including OFETs, OLEDs, OPVs.

The exact nature of charge transport in OSCs is still controversial due to its complexity. However, in terms of charge transport models, there is a clear distinction between disordered amorphous films such as polymer films and highly ordered organic single crystals. One way to highlight the problem is to compare two key parameters of charge transport at the microscopic scale: the electronic coupling or transfer integral (J , in meV) and the reorganization energy (λ , in meV), consists of inner reorganization (λ_{in}) and outer reorganization (λ_{out}), $\lambda_{out} \ll \lambda_{in}$ ¹¹⁰. J refers to the wave function overlap of the orbitals of neighboring molecules, while λ_{in} corresponds to the sum of geometry relaxation energies of the molecule upon going from the neutral-state geometry to the charged-state geometry. As shown in [Figure 1.33](#), if $J \ll \lambda$ (weak coupling regime), the charge wave function is localized on individual molecule and transport proceeds through incoherent hopping; by contrast, if $J \gg \lambda$ (strong coupling regime), charge wave function is delocalized over several molecules and transport takes place via diffusion.

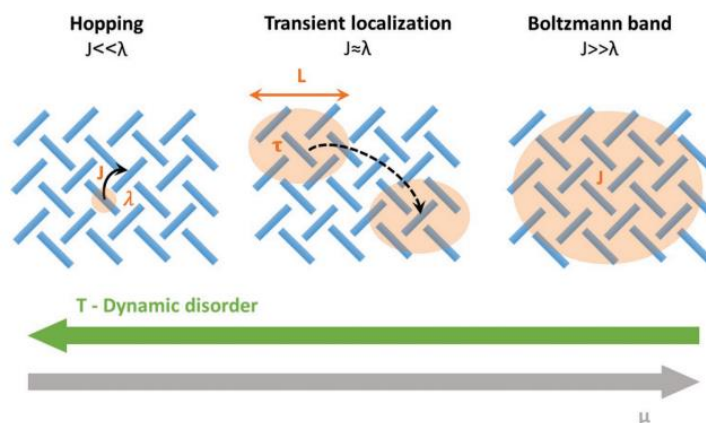


Figure 1.33 Schematic representation of the charge transport mechanism of hopping, transient localization and Boltzmann band model. The orange areas depict the charge delocalization. T is the temperature ¹¹⁰.

Charge transport in amorphous semiconducting films is usually explained by thermally activated hopping of charges via a distribution of localized states, and the transport of charge carriers improves with increasing temperature because strongly localized charges require energy to perform a hopping. This energy is given by the lattice vibrations which will be enhanced at higher temperature. In contrast, charge transport in ordered single crystals is generally described by band-like transport whose feature is the charge mobility increase with decreasing temperature since lattice vibrations will mostly break down the formation of bands. Models for charge transport in polycrystalline thin films of small molecules and microcrystalline polymers which lie in between these two extreme cases, have been proposed as well ¹¹¹. However, in all cases, J is a crucial parameter to determine the probability of charge transport from one molecule to the adjacent molecule and depends strongly on the particular molecule and the relative position of the interacting units ¹¹. For example, as we discussed in § 1.1.1, the slipped-stack and slipped π -stack packing motifs offer only one large J in the x - y plane, while the herringbone packing has three large J and enables the charge carrier mobility of the corresponding semiconductors to be the highest.

While the molecular packing ordering of semiconducting films affects the charge transport property, the methods how the films are processed have a dramatic effect on the performance of optoelectronic devices incorporating them. In some cases, morphological defects, amount of grain boundaries, crystal size, misalignment of crystalline grains and crystal defect, etc... can completely obscure the materials' intrinsic charge transport properties. Fortunately, these parameters could be modified by carefully choosing the film elaboration methods, thus the theoretical intrinsic charge carrier mobility of OSCs can be measured.

There are different methods to evaluate the charge carrier mobility of OSCs, such as OFET method, TOF technology, space-charge limited current (SCLC) method and field-induced time-

resolved microwave conductivity (FI-TRMC), which will thus give valuable information and direction for upstream molecular structure design and subsequent device fabrication. Next, OFET method and TOF technique will be introduced in detail since they were mostly used during this PhD work.

1.3.1.1 Organic field-effect transistor (OFET)

The working mechanism of an OFET has been described in § 1.1.2.2. When source/drain voltage (V_{DS}) is applied, negative or positive source-gate voltage (V_{GS}) will induce accumulation of holes or electrons at the semiconductor/dielectric interface of the OFET. As a result, there will be a current flow (I_{DS}) in the channel from the source to the drain. By recording these voltage and current data, two electrical characteristics can be obtained. One is the output curve showing the relationship of I_{DS} versus V_{DS} for different constant V_{GS} ; another is the transfer curve which presents the relationship of I_{DS} versus V_{GS} at constant V_{DS} . When a small V_{DS} is applied ($V_{DS} \ll V_{GS}$), a linear gradient of charge density (from the carrier injecting source to the carrier extracting drain) forms and I_{DS} along the channel is directly proportional to V_{DS} , indicating that the device operates in the linear regime. When $V_{DS} = V_{GS} - V_{th}$, the channel is pinched off, and I_{DS} cannot increase significantly anymore with further increase of the V_{DS} and saturates. Typical transfer and output curves of a n-type OFET are shown below in Figure 1.34.

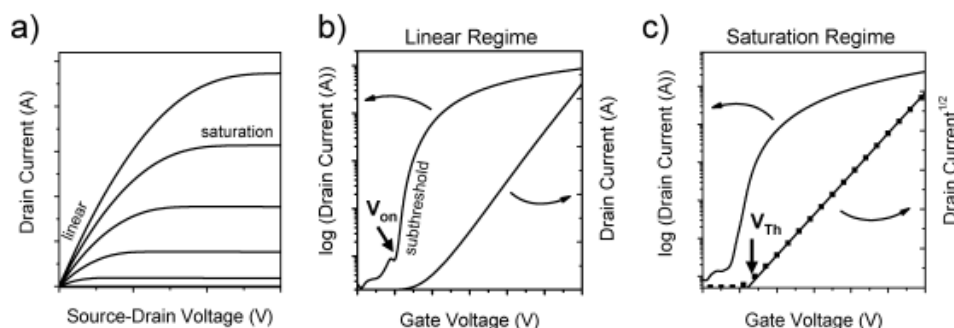


Figure 1.34 Typical transfer and output curves of a n-type OFET. a) output curves indicating the linear and saturated regimes; b) transfer curves in the linear regime, indicating the onset voltage (V_{on}) when the I_{DS} starts increases abruptly; c) transfer curves in the saturated regime, indicating the V_{th} , where the linear fit to the square root of the I_{DS} intersects with x-axis¹¹.

From the left curves ($\log I_{DS} \sim V_{GS}$) in Figure 1.34b and c, values of I_{on} and I_{off} can be extracted. I_{on} is I_{DS} in “on” state at a particular V_{GS} and I_{off} is the I_{DS} in “off” state. The right curve ($I_{DS} \sim V_{GS}$) in Figure 1.34b and right curve ($I_{DS}^{1/2} \sim V_{GS}$) in Figure 1.34c are used for extracting the threshold voltage (V_{th}) and the charge mobility. More precisely, the charge mobility value in the linear-regime, μ_{lin} , could be extracted from the slope of the curve of $I_{DS} \sim V_{GS}$ (right curve of Figure 1.34b) according to equation 1. The slope value equals to “ $(W/L) \mu_{lin} C_i V_{DS}$ ”, thus μ_{lin} could be

extracted from equation 2. The charge mobility value in the saturation-regime, μ_{sat} , could be extracted from the slope of the curve of $I_{\text{DS}}^{1/2} \sim V_{\text{GS}}$ (right curve of Figure 1.34c) according to equation 3. The slope value equals to “[$(W/2L) \mu_{\text{sat}} C_i$] $^{1/2}$ ”, thus μ_{sat} could be extracted from equation 4^{11,112}.

$$I_{\text{DS,lin}} = (W/L) \mu_{\text{lin}} C_i (V_{\text{GS}} - V_{\text{th}}) V_{\text{DS}} \quad (1)$$

$$\mu_{\text{lin}} = (L/W C_i V_{\text{DS}}) (\partial I_{\text{DS,lin}} / \partial V_{\text{GS}}) \quad (2)$$

$$I_{\text{DS,sat}} = (W/2L) \mu_{\text{sat}} C_i (V_{\text{GS}} - V_{\text{th}})^2 \quad (3)$$

$$\mu_{\text{sat}} = (2L/W C_i) (\partial I_{\text{DS,sat}}^{1/2} / \partial V_{\text{GS}})^2 \quad (4)$$

Where $I_{\text{DS,lin}}$ is the source-drain current in the linear regime, $I_{\text{DS,sat}}$ is the source-drain current in the saturation regime, W is the channel width, L is the channel length, μ_{lin} is linear mobility, μ_{sat} is saturation mobility, C_i is the capacitance per unit area of the dielectric layer, and V_{th} is the threshold voltage. Details about these equations deduction can be found in the reference¹¹.

1.3.1.2 Time of flight (TOF)

The first application of TOF in the measurement of charge carrier mobility of OSCs could date back to 1960, when Kepler¹¹³ and Leblanc¹¹⁴ investigated the drift mobilities of both holes and electrons of very high purity anthracene with a pulsed photoconductivity technique. TOF is a quite suitable setup for obtaining the charge transport properties of organic semiconducting materials with low mobilities. The principle is depicted in Figure 1.35¹¹⁵.

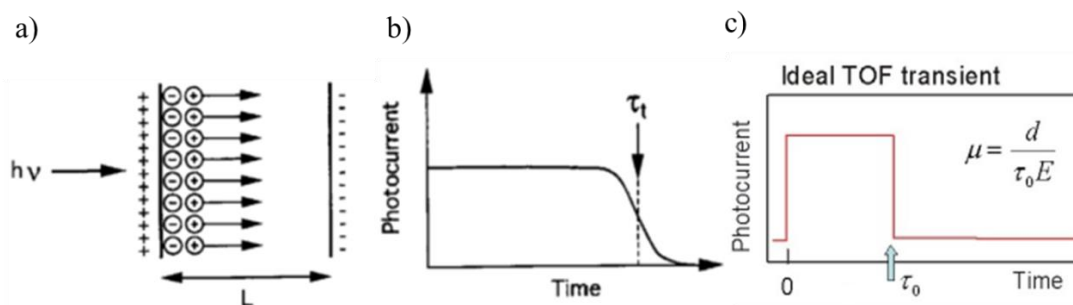


Figure 1.35 a) Principle representation of a Time-of-Flight technique; b) Resulting time dependent current; c) Ideal curve of photocurrent as a function of time¹¹⁵.

The organic film or crystal is sandwiched between two conducting electrodes connected to a resistor and an external electric field. The electrode on which the laser is incident should be semitransparent or transparent to allow the laser pulse to photogenerate electron-hole pairs in the vicinity. When the electric field is positive (negative), electrons (holes) will discharge at this electrode, whereas holes (electrons) will travel across the sample and reach the rear electrode. This charge transport leads to a constant photocurrent which can be recorded by the

external circuit. The current decreases to zero at the time τ_0 when the charge sheet arrives at the rear electrode. The transit time τ_0 is related to the mobility μ through the equation below:

$$\mu = d/(\tau_0 E) = d^2/(\tau_0 V)$$

Where d is the distance between the electrodes, E the electric field and V the external voltage across the sample. In theory, the TOF signal should present a step shape (See [Figure 1.35c](#)) corresponding to the charge sheet arriving to the rear electrode and the current falling off. However, the charges may experience diffusion and trapping during the trip from the first electrode to the second one. For this reason, TOF measurements for OSCs require highly pure and flawless samples. TOF technology is generally suitable for organic semiconducting materials with low mobilities.

In my PhD work, I mainly used OFET method to investigate the threshold voltages, on/off current ratios and charge mobilities of several organic materials. Combined with the structure characterizations with polarized optical microscope (POM), grazing incidence X-ray scattering (GIXS) and atomic force microscope (AFM), the effects of different parameters such as fabrication methods, crystals structures, film morphologies, substrate surface treatment and even the device geometry on the charge mobilities of the semiconducting films could be investigated. Therefore, the potential application of certain semiconducting material in OFET or OLED devices can be evaluated.

1.3.2 Characterization of self-organized materials

We have discussed that charge carrier mobility of the semiconducting thin films depends significantly on the molecular packing, crystal structure and film morphology. Π -conjugated small molecules and polymers can present the self-organization capability, through intermolecular force such as van der Waals force (π - π conjugation included) and hydrogen bond, to assemble molecules into a specific solid-state arrangement and achieve desired highly ordered crystalline or liquid crystalline structures with subsequent good film morphology. This unique self-organized feature generally endows the OSCs with high charge carrier mobility owing to π -orbital overlap between neighboring molecules ¹¹⁶.

The characterizations of molecular packing, crystal structure and film morphology rely greatly on different techniques such as polarized optical microscope (POM), X-ray diffraction (XRD), grazing incidence X-ray scattering (GIXS), scanning electron microscope (SEM), transmission electron microscope (TEM) and atomic force microscope (AFM). As POM, GIXS and AFM were frequently performed during this PhD work, they will be introduced in detail below.

1.3.2.1 Polarized optical microscope (POM)

POM is a technique that employs polarized light to study the microstructures of materials. POM works by converting depolarized light to linear polarized light¹¹⁷, which is achieved by the 1st linear polarizer located between the light source and the specimen, as shown in Figure 1.36a. Then, the linear polarized light passes through the sample and will become circular polarized light (See Figure 1.36b) if there is crystalline composition in the sample (such as crystals, fibers and liquid crystals) which typically show birefringence. In contrast, if the sample is isotropic (such as ordinary gases, liquids and amorphous solid), the linear polarized light will conserve its original characteristics. The circular polarized light can pass through the 2nd linear polarizer (located between the sample and human eyes) whose direction is perpendicular to the 1st linear polarizer, while the linear polarized light can't pass through the 2nd linear polarizer. Therefore, only the light penetrating into crystalline material can be detected by the observers.

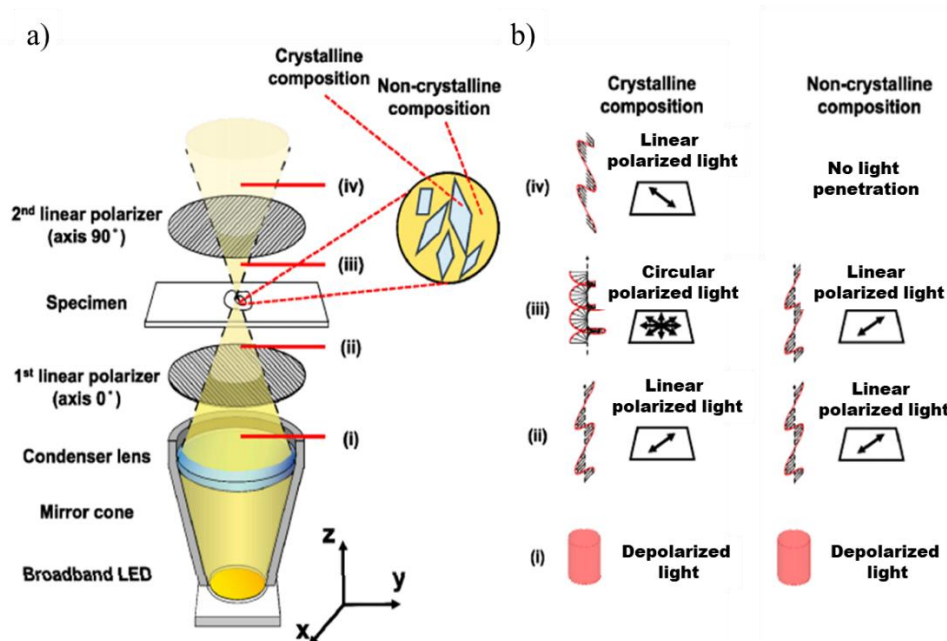


Figure 1.36 The (a) schematic representation and (b) principle of a polarized optical microscope¹¹⁷.

Particularly, POM is one of the techniques to investigate the characterization of liquid crystal organization thanks to the liquid crystal birefringence. Different liquid crystal phases exhibit different characteristic patterns. The typical schlieren texture of nematic phase, cholesteric texture of chiral nematic phase and focal conic texture of smectic A phase are shown in Figure 1.37.

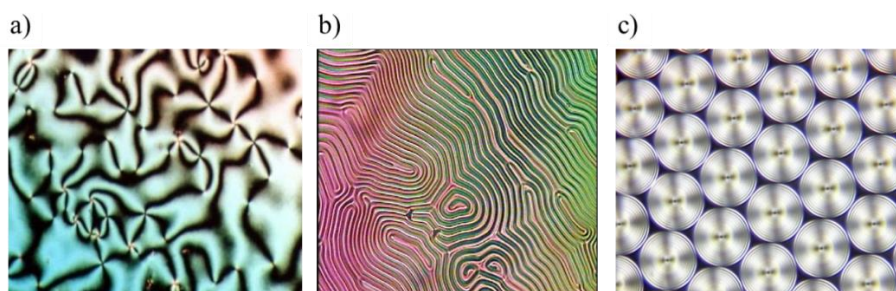


Figure 1.37 a) Typical schlieren texture of nematic phase; b) Typical cholesteric texture of chiral nematic phase; and c) Typical focal conic texture of smectic A phase.

1.3.2.2 Grazing incidence X-ray scattering (GIXS)

GIXS is demonstrated to be a powerful tool to characterize thin film microstructures, subtly identifying different film phases and accurately measuring the unit cell structure and dimensions ¹¹⁸. It is particularly appropriate for investigating the structure/property relationships in terms of charge carrier transport in OFETs because it can probe the first few monolayers above the dielectric layer where carrier transport predominantly occurs ¹¹⁹. It is well known that the molecular packing in thin films may be different from that in bulk, especially near the substrate surface ¹²⁰. Examples for this are tetracene where the molecular packing motifs in thin film state and bulk single-crystal state are different ¹²¹.

A graphical representation of X-ray diffracting from crystal planes is shown in Figure 1.38. Diffracted beams interfere constructively when the following Bragg's law is satisfied:

$$2d\sin\theta = n\lambda$$

Where n is an integer, λ the wavelength of incident wave, d the spacing between the planes of the atomic lattice, and θ the angle between the incident ray and the scattering planes. The angle between the incident beam and the diffracted beam is 2θ .

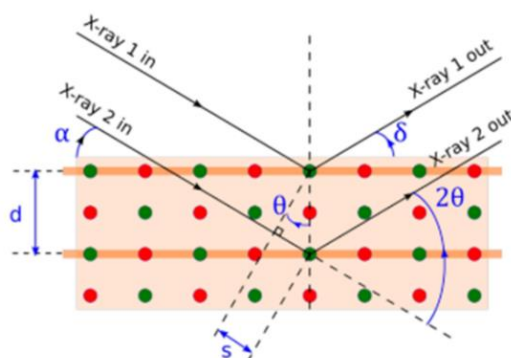


Figure 1.38 Graphical representation of X-ray diffracting from crystal planes ¹²².

There is no clear delineation between wide-angle X-ray scattering (WAXS) and small-angle X-ray scattering (SAXS); generally speaking, WAXS corresponds to X-ray incident angles α from

about 1° to 45° . When the X-ray is incident at a high angle (see Figure 1.39a), potentially most of the X-ray is absorbed by the substrate rather than the sample, leading to signal loss. In contrast, reducing the incident angle (see Figure 1.39b) will allow more X-rays to be absorbed by the sample instead of the substrate and to be spread over a large sample area, thus increasing signal yield. Another point that should be taken into account is that by setting the incident angle below the critical angle of the substrate, scattering of X-rays from the substrate is eliminated and most of the beam intensity is focused into a surface-near region of the sample¹²⁰, which allows for independent analysis of the diffraction signal of a crystalline organic film¹²³.

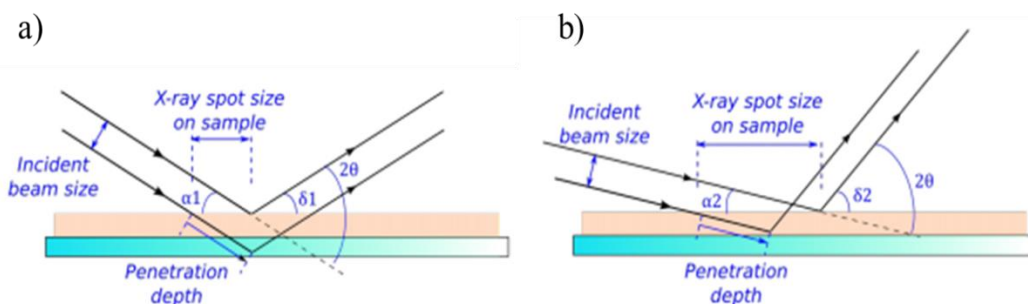


Figure 1.39 Illustration of XRD performed at a) high and b) low incident angle¹²².

The geometry of the classical GIXS measurement on thin films is presented in Figure 1.40. Organic molecules are weak X-ray scatterers, and only the use of incident synchrotron beam can produce enough scattered intensity. The synchrotron X-ray beam, \mathbf{K}_0 , strikes the sample surface under a grazing incidence angle α . The scattered intensity (wave vector \mathbf{K}) is detected by two-dimensional (2D) image plate detector (distance L). The intensity, $I(\mathbf{q}_{xy}, \mathbf{q}_z)$, in 2D GIXS is acquired versus in-plane (\mathbf{q}_{xy}) and out-of-plane (\mathbf{q}_z) components of the scattered vector \mathbf{q} ($\vec{q} = \vec{k} - \vec{k}_0$). Bragg's law is used to analyse GIXS patterns. In three-dimensional (3D) crystals, diffraction from a set of h,k,l (Miller indices) crystal planes with an interplanar spacing \mathbf{d} occurs only when the Bragg's law is satisfied. A given \mathbf{q} value in reciprocal-space corresponds to a real-space \mathbf{d} of

$$q = 2\pi/d$$

Therefore, from a peak position in scattering, one can calculate the real space repeat-structure distance:

$$d = 2\pi/q$$

As a result, because of the inverse nature of reciprocal-space, the large \mathbf{q} value corresponds to small \mathbf{d} .

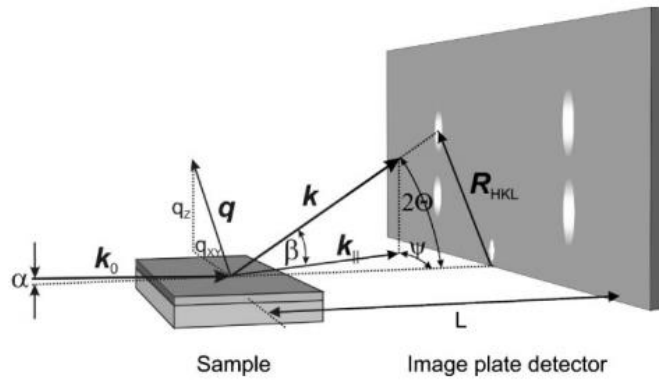


Figure 1.40 Geometry of the GIXS setup. The incident beam k_0 forms an angle α with the sample surface. The scattered beam k is registered by an image plate detector at a distance L . The in-plane component of the momentum transfer vector q is q_{xy} and the vertical component q_z ¹²⁴.

Sample textures are readily assessed from 2D GIXS data in Figure 1.41. An amorphous film shows no special feature. A perfect non-oriented polycrystalline film displays full Debye rings. Single crystals with well-oriented structures relative to the substrate appear as dots. Likewise, data from samples with texture somewhere in-between these extremes will appear as partial rings. Macrostrains readily result in a shifted dot or a stretched ring in the 2D XRD data. Sharp peaks indicate large crystalline domains. Usually, the region close to the origin of the detectors is covered by beam stops to prevent damage from the direct X-ray radiation, leaving a small hole in the data which is not shown here.

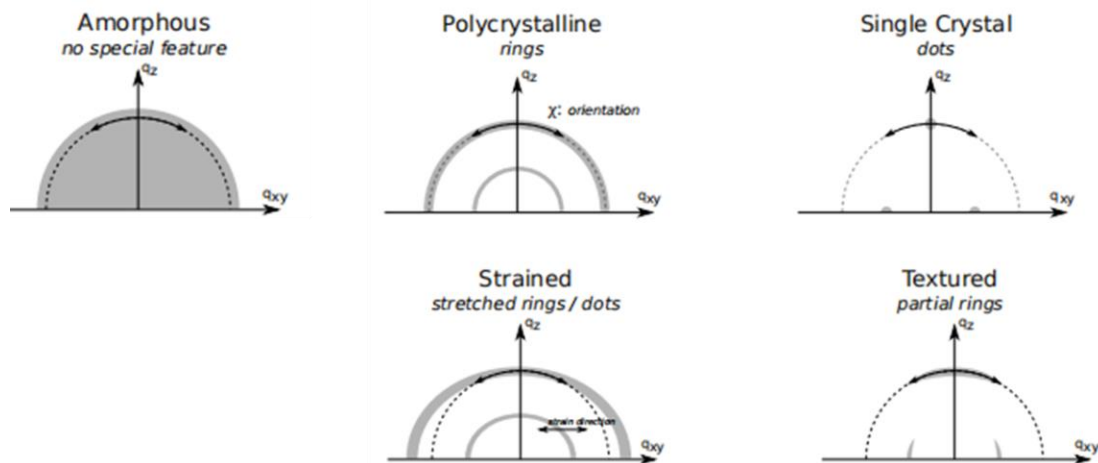


Figure 1.41 GIXS images illustrations of data from samples with different textures.

1.3.2.3 Atomic force microscope (AFM)

AFM can offer images of the sample surface with high spatial resolution (as high as 0.1 nm for the vertical resolution, and 1 nm for the lateral resolution), which helps the worldwide researchers to figure out the structure/property relationship of the semiconducting films and

achieve property optimization of optoelectronic devices. As AFM were frequently performed during this PhD work, it will be introduced in detail below.

AFM was invented in 1986 by C. F. Quate, G. Binnig and Ch. Gerber¹²⁵ on the basis of the scanning tunneling microscope (STM), and G. Binnig et al. were awarded the Nobel Prize in Physics that year. AFM overcomes the drawback of STM which is inherently limited to conductors. It not only allows to image the surface topography, but also to quantitatively map the physicochemical properties (for example, the Young's modulus) of a wide range of materials including insulators such as organic small molecules, polymers and living cells¹²⁶. Moreover, AFM can measure a number of properties of the materials in addition to offer an image, while other microscopes like POM, TEM and SEM can only provide images. In addition, it can operate at various conditions from vacuum to air to liquid over temperature ranging from sub-ambient to high temperatures, and generally don't damage the sample¹²⁷.

AFM involves the detection of atomic forces between the sharp probe and the sample surface. As shown in [Figure 1.42](#), the scan unit includes: a) a scanner base, b) a cantilever holder mounted on c) optical head, and d) piezo positioner. The sample is attached to the sample stage located on the top of the piezo positioner.

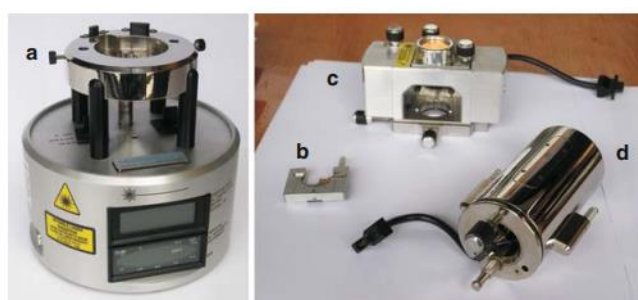


Figure 1.42 Photographs of the basic components of a sample scanning AFM: a) scanner base, b) cantilever holder, c) optical head, and d) piezo positioner¹²⁸.

The scanner base contains electronic circuit and serves as the connection between the controller and actual force microscope¹²⁸. As for the optical head, it comprises the cantilever-tip assembly, laser diode, mirror and position-sensitive photodiode consisting of four-segmented photodiodes ([See Figure 1.43](#)). One end of the cantilever is fixed on the cantilever holder, while the other side with a tip is freely suspended ([See notes in Figure 1.43](#)). Interactions between the sharp tip and the sample surface induce moving up and down of the tip and subsequent deflection of the cantilever. A laser beam is applied to record the vertical movement of the cantilever. It is reflected onto the photodiode by the back of the cantilever and the mirror, which allows the diode detector to monitor the light signal change and thus the cantilever bending. Since the cantilever obeys Hooke's Law for small displacement, the interaction between the tip and the sample surface can be measured. The utilization of four-segmented photodiodes enables the

detection of both normal and lateral forces. The movement of the sample is performed using the extremely precise piezo positioner with sub-angstrom resolution in x-, y-, and z-direction.

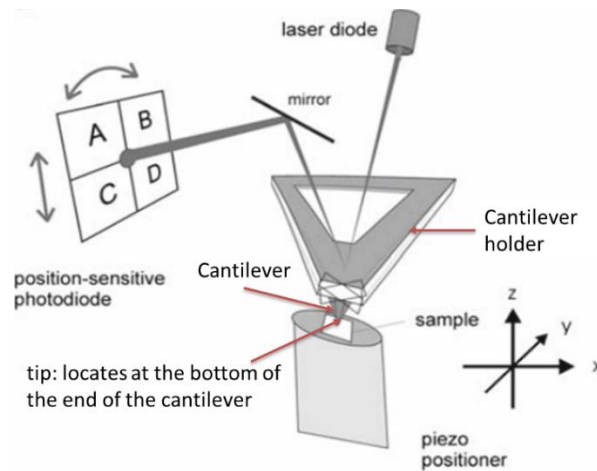


Figure 1.43 Schematic diagram of the optical head of the AFM ¹²⁹.

There are different working modes in AFM operation. The three widely-used modes are contact mode, non-contact mode and tapping mode, as shown in Figure 1.44, and we mostly used tapping mode. Tapping mode AFM was first described in 1993¹³⁰. It is a key advancement in the history of AFM development, which enables researchers to image samples too fragile to withstand the lateral force of contact mode, and use scan speeds much higher than the one obtained in non-contact mode.

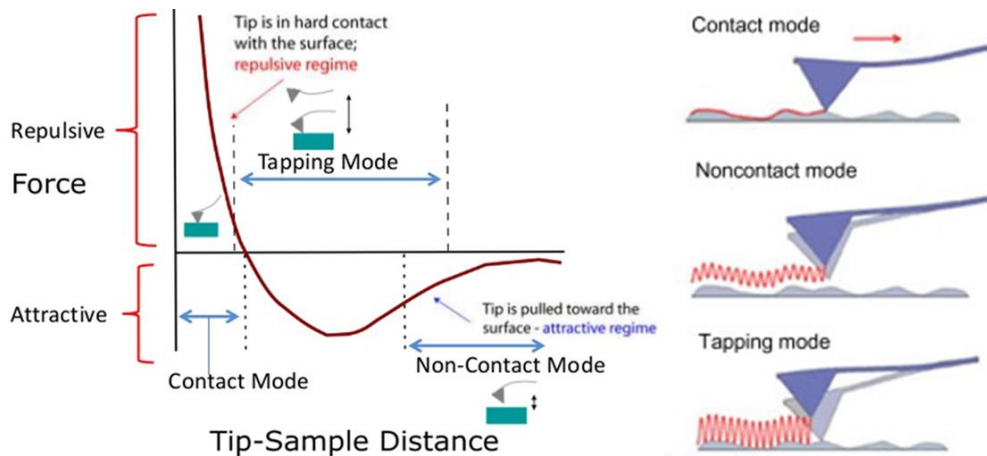


Figure 1.44 The repulsive and attractive force regimes as the AFM tip approaches the sample (left) and movement route of the tip (right) in contact mode, tapping mode and non-contact mode ¹³¹.

In tapping mode imaging, the tip is driven by an oscillator near its resonance frequency, and strikes the surface at each oscillation. When the tip strikes the sample surface, part of the energy in the oscillating system is transferred to the sample, resulting in a reduced vibrational amplitude. The control system maps the sample surface by regulating the piezo positioner to adjust the tip-sample separation and keep a constant amplitude ¹³². In the tapping mode, when

the tip contacts the surface, it has sufficient oscillation amplitude to overcome the tip-sample adhesion force ¹³³. The tapping force exerted by the tip on the surface is very small ranging approximately from 0.2 to 5 nN, which is much smaller than the one in contact mode, hence minimizing the sample deformation and tip radius change. On the other hand, the lateral shear force is also essentially eliminated, since the tip is no longer dragged along the surface. The tip taps the surface many times before it moves to the next place, which assures the high resolution of the image. However, despite the small vertical compressive force and absence of the laterally shear force, too high amplitude or too low set point may lead to damages to the sample or the tip as well.

In my PhD work however, I mostly used AFM in its topographic mode in order to investigate the surface structure of the organic film in relation with the employed preparation methods.

1.4 Aim of work

In this work, during my PhD, we were interested in the elaboration and characterization of self-organized organic semiconducting thin film based on different semiconducting materials (See Table 1.2) for organic optoelectronic applications such as OFETs and OLEDs. As outlined previously in this chapter, the device performances based on the semiconducting thin films depend greatly on the molecular packing motifs, crystal structures and morphological defects which could be tuned and optimized by carefully choosing deposition methods (solution-processing methods or solution-free methods). Moreover, the appropriate coating technique is quite different from molecule to molecule because each molecule has its specific characteristics. Thus, in this PhD project, we have studied how to optimize the fabrication methods of semiconducting thin films based on different π -conjugated molecules in order to maximize their device performances of the corresponding optoelectronic devices (OFETs or OLEDs).

Table 1.2 Main semiconducting materials used in this PhD work and our collaborators.

Materials	Collaborators	Institution
DAL1	Dr. D'Aléo Anthony and Prof. Frédéric Fages	CINAM, Marseille (France)
BTBT	Dr. Xiaolu Su	IPCM, Paris (France)
C ₈ -BTBT-C ₈	Dr. Teng Teng	IPCM, Paris (France)
C10-PBT	Dr. Teng Teng	IPCM, Paris (France)
iI(T2) ₂	Dr. D'Aléo Anthony	EWHA, Seoul (Korea)

In the next chapter (chapter 2), we will first investigate the charge transport properties of crystalline organic semiconducting layers of the DAL1 semiconductor (See Figure 1.45)

prepared with a solvent-free, vacuum-free, simple and versatile method, so-called “melt-processing”. This method is an alternative method to i) the classical solution-processing techniques (such as spin coating) requiring large amounts of organic solvent or ii) the vacuum thermal evaporation technique requiring complex and expensive facilities. Adapted from the template-assisted self-assembly process ¹⁰⁶ (See [Figure 1.32 in §1.2.2.3](#)), which has been developed to prepare a homogeneous and high optical-quality organic liquid crystalline thin films, this melt-processing method was not employed so far to fabricate high quality single-crystalline thin films. In this work we will utilize melt-processed DAL1 thin films to fabricate OFETs and demonstrate how this processing method can enhance charge carrier mobilities in comparison to other processing methods. This part of work has been published in *Journal of materials chemistry C in 2019* ¹⁰⁷.

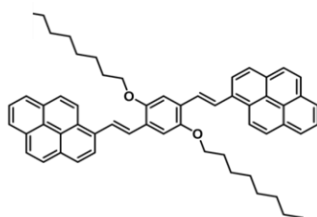


Figure 1.45 Molecular structure of DAL1
(collaboration with Dr. D'Aléo Anthony and Prof. Frédéric Fages at CINAM, Marseille).

Secondly, in the chapter 3, we will study the charge transport properties of single crystals of BTBT core ([See Figure 1.46](#)). As introduced in [§1.1.1](#), thienoacenes such as BTBT derivatives have emerged as promising materials for the fabrication of efficient OFETs. These derivatives are composed of fused thiophenes and benzene rings, leading to a rigid and planar π -conjugated system. Such chemical structure induces a large intermolecular orbital overlap in solid state explaining their high charge carrier mobility. The charge transport properties of substituted BTBT derivatives were widely studied in thin film transistors (TFTs), but no field-effect mobility had been reported for an unsubstituted BTBT core before this part of work was began and published in ‘*Organic electronics*’ in December 2019 ¹⁰⁴. In this work, we will describe the BTBT single crystal preparation and characterization, their integration in transistor configuration, and their charge transport properties. In addition, charge mobility of OFET based on melt-processed C₈-BTBT-C₈ ([See Figure 1.46](#)) will be also investigated to study the influences of the side-chain substitutions.

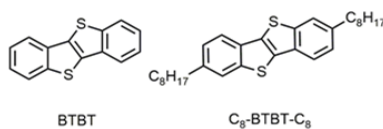


Figure 1.46 Molecular structures of unsubstituted BTBT core and C₈-BTBT-C₈
(collaboration with Dr. Xiaolu Su and Dr. Teng Teng at IPCM).

Thirdly, in the chapter 4, we will study the photo- and electro-luminescence properties, of spin coated thin film of a new liquid crystalline fluorescent material C10-PBT (See Figure 1.47). Contrary to typical fluorophores that often present an aggregation-caused quenching problem in solid state^{134,135} limiting their practical application in optoelectronics, this C10-PBT material presents highly efficient luminescent properties in its crystalline phase. These interesting properties turn C10-PBT into a promising candidate for the fabrication of light emitting devices such as OLED or OLET. In this work, we will briefly study the thermal properties of C10-PBT and its thin film morphology. Then we will deeply investigate its PL properties in solution and solid state, and its EL properties in OLED devices based on different type of emitting layer (neat and host/guest system).

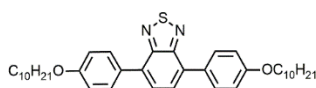


Figure 1.47 Molecular structure of C10-PBT (collaboration with Dr. Teng Teng at IPCM).

Finally, in the chapter 5, we will investigate the charge transport properties of thin film of a D-A molecule $il(T2)_2$ based on Isoindigo (*il*) acceptor units (See Figure 1.48). Semiconducting materials based on D-A macro- or molecular architectures, alternating electron-donating and electron-withdrawing units, are promising materials in OPV and ambipolar FETs due to their absorption in the near-IR range and small bandgap (<1.6 eV)¹³⁶⁻¹³⁸. The use of *il* as strong electron-withdrawing units is now very popular in D-A semiconductors due to its fully conjugated structure¹³⁹. *il* was utilized in 2010 for the first time as building block to prepare the conjugated p-type materials ($il(T2)_2$) for solar cells fabrication¹⁴⁰. However, to the best of our knowledge, no investigation of the charge transport properties of $il(T2)_2$ has been reported so far. In this work, we will study the structure of $il(T2)_2$ thin films and the effect of annealing process on film morphology. The charge transport properties of these films will be also investigated in detail in FET devices. This work represents the first investigation of charge carrier mobility of $il(T2)_2$ in transistor configuration.

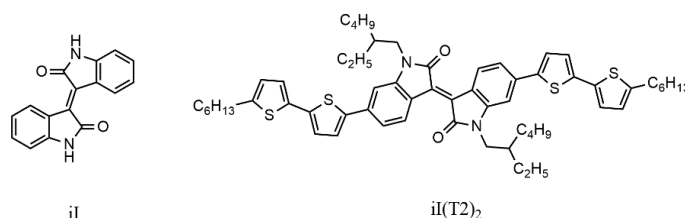


Figure 1.48 Molecular structures of *il* and $il(T2)_2$ derivative (collaboration with Dr. D'Aléo Anthony at EWHA, Seoul (Korea)).

Chapter 2 A solvent-free and vacuum-free melt-processing method to fabricate organic semiconducting layers with large crystal size for organic electronic applications

As introduced in the chapter 1 (§ 1.2.1 and 1.2.2.1), two kinds of methods based on solution processing and vacuum thermal evaporation are generally used for the fabrication of the organic layers of OFETs. Solution-processing techniques such as spin-coating, dip-coating and ink-jet printing are very promising for the industrial production of large area organic electronic devices but require large amount of organic solvents^{32,83}. In parallel, vacuum thermal evaporation has been extensively used for the realization of high performance organic electronic devices but is not necessarily well-adapted for large-scale production due to its cost and the waste of organic compounds during the evaporation process. To sort out these issues, several methods to fabricate organic thin films under solvent-free and vacuum-free conditions have been proposed including the friction-transfer method¹⁴¹, organic vapor jet printing¹⁴², and more recently cold and hot isostatic pressure techniques¹⁴³. Another interesting approach based on a template-assisted self-assembly process (also introduced in Figure 1.32 in chapter 1) has been developed to prepare organic liquid crystalline thin films in OFET devices¹⁰⁶. In this method, powder of materials presenting liquid crystalline properties is melted above its isotropic phase temperature, fills by capillarity the active area of the organic electronic devices, and the sample is finally cooled down at room temperature, leading to the formation of a homogeneous and high optical-quality organic liquid crystalline layer with homeotropic alignment and good charge carrier mobilities. Surprisingly, this method has not been employed so far to fabricate high mobility OFETs based on crystalline organic semiconductors able to form organic single crystals *via* conventional techniques such as physical vapor transport deposition or solution-processing. This melt-processing route has only been used to form highly crystalline organic layers in light-emitting organic microcavities showing polariton lasing under optical pumping¹⁴⁴.

In this chapter, we thus propose and investigate a melt-processing method to prepare highly crystalline organic semiconducting layers with millimetric single crystal monodomains and enhanced charge transport and photophysical properties. As shown in Figure 2.1, the organic compound used in this study is a solution-processable oligo(*p*-phenylene vinylene) derivative substituted at both ends with pyrene moieties DAL1 (collaboration with Dr. D'Aléo Anthony and Prof. Frédéric Fages at CINAM, Marseille). The melt-processed thin film is described in detail as well as the morphology and structure of such films. The charge transport properties of DAL1 are investigated with OFET configurations based on spin-coated films and melt-processed films. In addition, the photophysical properties of these films are also discussed.

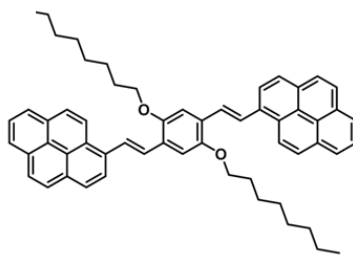


Figure 2.1 Molecular structure of DAL1

(collaboration with Dr. D'Aléo Anthony and Prof. Frédéric Fages at CINAM, Marseille).

2.1 Thermal properties of DAL1

The thermal behavior of the material was investigated by DSC at different rates on heating and cooling and the thermogram at $2^{\circ}\text{C min}^{-1}$ is displayed in Figure 2.2. The DSC trace upon heating shows a small endothermic peak at around 84.6°C ($\Delta H \approx 2.4 \text{ J g}^{-1}$), which is attributed to a crystal-to-crystal phase transition related to a slight reorganization of the lattice, and a sharp endothermic peak at around 151.6°C ($\Delta H \approx 47 \text{ J g}^{-1}$), which corresponds to the melting to isotropic liquid phase transition. On cooling, these thermal transitions are reversible with the crystallization observed at 119.7°C and the crystal-to-crystal transition occurring at 85.8°C . The transition temperatures, phase sequence, and transition enthalpies of DAL1 are listed in Table 2.1.

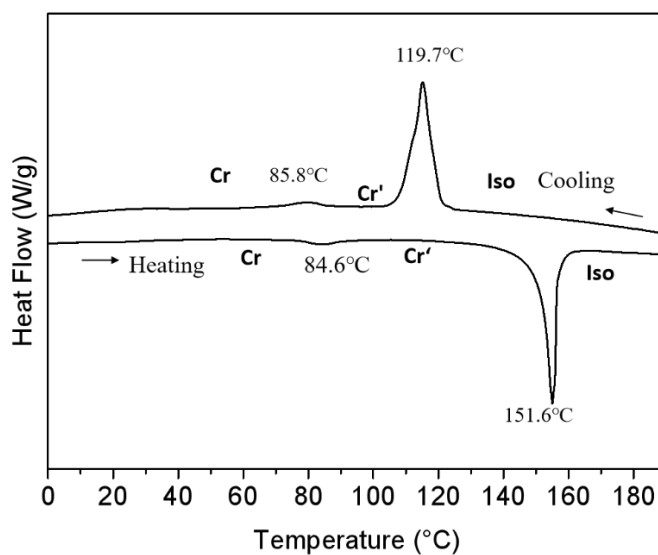


Figure 2.2 DSC traces of DAL1 derivative recorded at 2°C/min .

Table 2.1 Phase transition temperatures and enthalpy of DAL1.

compound	transition	T^b (°C)	ΔH (J g ⁻¹)	transition	T^b (°C)	ΔH (J g ⁻¹)
ligo(<i>p</i> -phenylene vinylene) DAL1	Cr→Cr'	84.6 ^c	2.4	Cr'→Iso	151.6 ^c	47
	Iso→Cr'	119.7 ^d	54.7	Cr'→Cr	85.8 ^d	2.6

Cr = Crystalline phase 1, Cr' = Crystalline phase 2, Iso = Isotropic phase. ^b Indicated temperatures are the onsets of the peaks on heating and on cooling. ^c Temperature transition determined during 2nd heating (rate 2°C/min). ^d Temperature transition determined during 2nd cooling (rate 2°C/min).

2.2 Structure of DAL1 single crystal prepared by slow solvent evaporation

X-ray quality single-crystals of DAL1 were grown by slow evaporation of dichloromethane in a mixture of dichloromethane/methanol. A single crystal was mounted on a glass fiber and diffraction data were acquired using a Mo K α radiation source ($\lambda = 0.71073$ Å). Table 2.2 presents the detailed crystallographic parameters of DAL1 single crystal prepared by slow solvent evaporation. This derivative crystallizes in a monoclinic crystal system (C2/c, Z = 4). The molecule is non-planar with a tilt of the pyrene units of 35.57° compared to the central phenyl unit (see below Figure 2.3 a and b). The details of the crystal structure are summarized in the table 2.2.

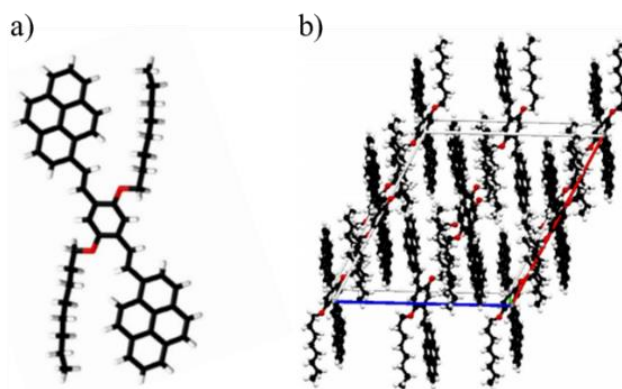


Figure 2.3 a) Crystalline structure of DAL 1; b) Representation of the lattice structure of DAL 1 single crystal prepared by slow solvent evaporation.

Table 2.2 Crystal structure data for single crystal of DAL1 prepared by slow solvent evaporation.

Compound	
Formula	C ₅₈ H ₅₈ O ₂
Molecular weight (g mol ⁻¹)	787.04
Size (mm)	0.3 x 0.24 x 0.06
Crystal lattice	monoclinic
Space group	C2/c
a [Å]	25.0499(5)
b [Å]	8.3917(2)
c [Å]	23.4363(6)
β	116.997(2)
V [Å ³]	4389.73(19)
ρ _{calcd} (g cm ⁻³)	1.191
Z	4
λ(Mo/Kα) / Å	0.71073
T / K	293(2)
θrange / deg	1.825-27.483
<i>hkl</i> ranges	0 < h < 32 0 < k < 10 -30 < l < 26
Variable	289
Refln measured	34085
Refln I > 2σ(I)	4995
R1 I > 2σ(I)	0.057
R1 all data	0.1241
wR2 I > 2σ(I)	0.1585
wR2 all data	0.1977
Δρ (+/-) / e. Å ⁻³	0.473 / -0.396

2.3 Powder X-ray scattering

Small angle X-ray scattering (SAXS) measurements were carried out on DAL1, in powder state and as a function of temperature. As shown in **Figure 2.4**, the crystalline structure in the powder state (black curve) is completely different from the arrangement of the single crystals (purple curve) obtained by slow solvent evaporation. As shown by the black curve, the pristine powder presents two reflections at the small angle region characteristic of a lamellar (See yellow arrows in **Figure 2.4**) organization of periodicity 22.8 Å (According to the relationship between q and d, $d=2\pi/q$ introduced in §1.3.2.2, $d=2\pi/0.27=22.8$ Å), which is maintained after thermal treatments (blue curve in **Figure 2.5**). The powder crystallized from the molten state presents a similar lamellar structure indicating a similar molecular organization (red curve in **Figure 2.5**).

The crystal-to-crystal phase transition observed by DSC at 85°C (See Figure 2.2) corresponds to slight change of the molecular packing as revealed by small shifts of some wide-angle reflections in the powder XRD pattern of DAL1 at 100°C. Note that this transition is also completely reversible on cooling, consistently with DSC measurements (Figure 2.6).

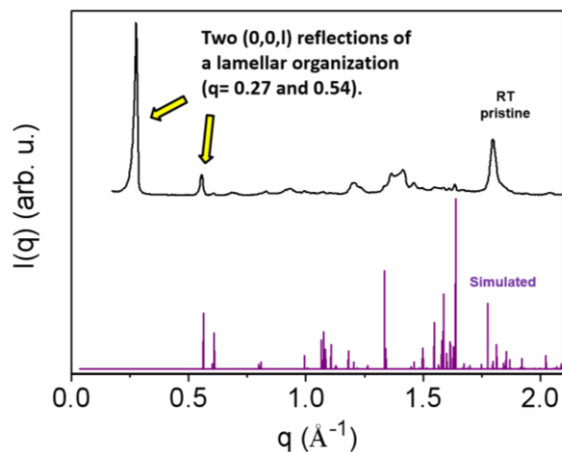


Figure 2.4 SAXS pattern of DAL1 pristine powder (black curve) and simulated SAXS pattern calculated from single crystal structure resolved from single-crystals prepared by slow solvent evaporation (purple curve).

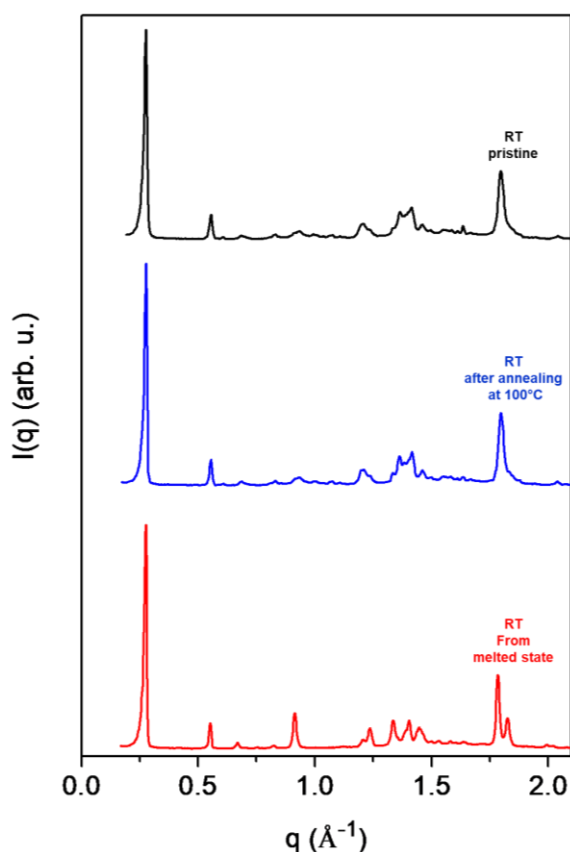


Figure 2.5 SAXS patterns of DAL1 derivative at room temperature (RT) in the pristine powder state (black), at RT after annealing at 100°C (blue) and at RT after melting in the isotropic liquid phase and cooling (red)

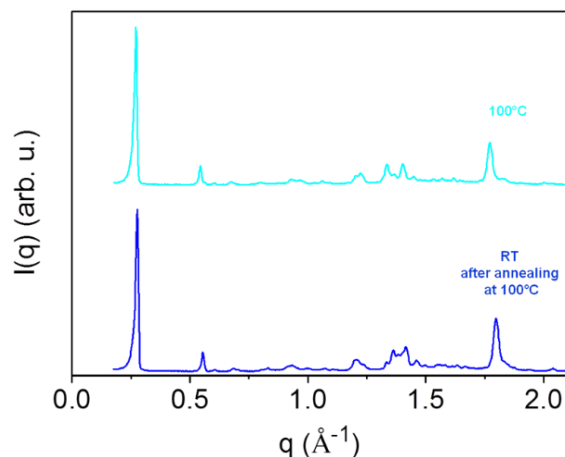


Figure 2.6 SAXS patterns of DAL1 derivative powder at 100°C (sky blue) and at RT after the annealing at 100°C (blue).

2.4 Preparation of DAL1 thin films by solution deposition and melt-processing method

Herein, three kinds of DAL1 films (as-spin-coated film, annealed spin-coated film and melt-processed film) will be prepared for further structures and morphology characterization. The preparation process for each film will be described in detail below.

Solution deposition

Before the spin coating, the SiO_2 substrates were sonicated in ethanol, acetone and chloroform successively, followed by a cleaning in the UV-Ozone cleaner for 30 min. Then, the organic thin films were deposited by spin-coating at 2000rpm from a 5 mg/ml tetrahydrofuran (THF) solution in ambient condition with a spin coater (See Figure 2.7) for GIXS and AFM measurements. Annealing of the spin-coated films was carried out on a hot plate for 1h at 100°C which is between the crystal-to-crystal transition temperature and the melting point of DAL1 compound.

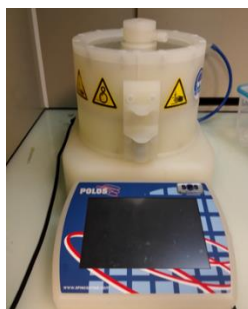


Figure 2.7 One photo of the spin coater.

Melt-processing method

Processing of the crystalline thin layer was carried out in several steps. As shown in [Figure 2.8](#), firstly, a glass substrate treated with a self-assembled monolayer (SAM) of n-octadecyltrichlorosilane (OTS) was placed on top of a silicon wafer substrate. The cover glass was previously treated with an OTS SAM as the procedures described in the literature ¹⁴⁵. After the OTS treatment, the hydrophilic surface will be grafted alkylsilane monolayers shown in [Figure 2.9](#) and become hydrophobic. As a result, the surface energy and adherence with the final organic film of the cover glass will be reduced.

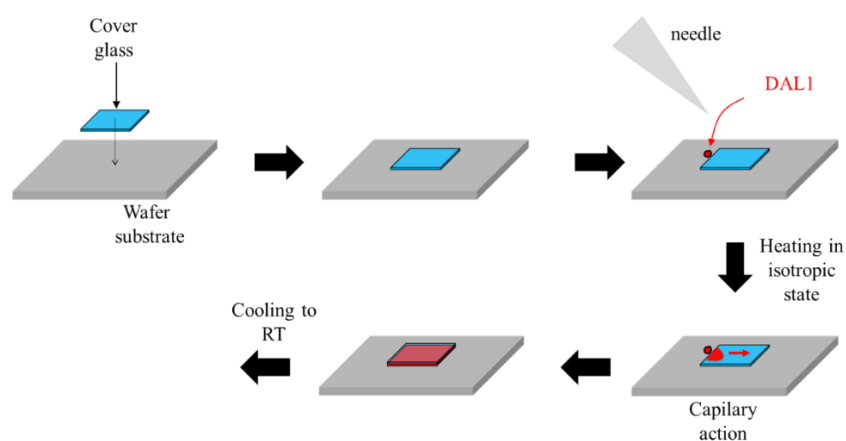


Figure 2.8 Steps of the processing of the crystalline thin layer prepared by the melt-processing.

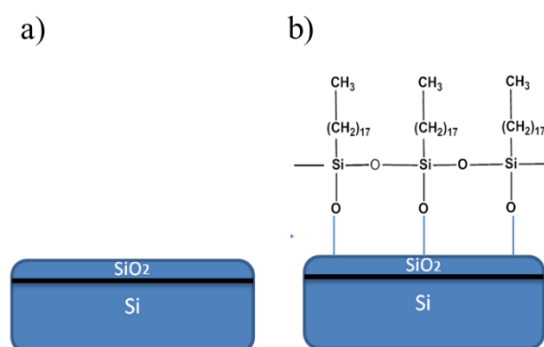


Figure 2.9 Schematic representations of substrate surface a) before and b) after OTS treatment.

Secondly, a very small amount of organic crystalline powder was placed at one edge of the empty space separating the two substrates and the sample was heated above the melting temperature of the compound in a Linkam THMS 350 heating plate under a nitrogen flow. Then, the organic semiconductor in the isotropic liquid phase filled the empty space by capillary action ^{146–148} to form a thin liquid film between the two substrates. Third step consists in a rapid cooling down to room temperature, in order to obtain a fine polycrystalline texture. Then, the film was heated again carefully around melting temperature ($T = 151.6\text{ }^{\circ}\text{C}$) and POM was used

to monitor the process (See Figure 2.10). When almost the entire polycrystalline film had been molten, except few isolated crystals surrounded by the isotropic liquid, the sample was cooled down again upon very slow rate ($< 0.1 \text{ }^\circ\text{C min}^{-1}$) to room temperature. The small residual crystals acted then as crystallization germs and grew to millimetric single monodomains (see Figure 2.10). In the last step, the weakly adhering OTS-treated cover glass was removed. This method therefore proved to be very efficient to process thin films with large single-crystalline domains on top of silicon or fused silica substrates.

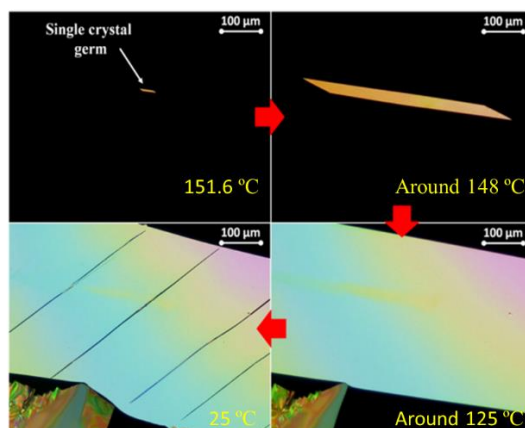


Figure 2.10 POM images showing the growth of a large single crystal monodomain from a single crystal germ during the melt-processing.

2.5 Structure and morphology of DAL1 thin films

2.5.1 Grazing incidence X-ray scattering (GIXS)

GIXS measurements were carried out at room temperature on DAL1 spin-coated (as-prepared and annealed at 100°C), and melt-processed films. The GIXS patterns of the two former, spin-coated films and the melt-processed film exhibit a lamellar structure with the same periodicity (about 22.3 \AA) (See the vertical red spots in the black dotted frame in Figure 2.11), similar to powder samples (See yellow arrows in Figure 2.4). In the three cases, the lamellar systems are oriented parallel to the substrates as shown by the concentration of the lamellar reflections on the meridian (See the vertical red spots in the black dotted frame in Figure 2.11. If the lamellae are perpendicular to the substrate, the red spots will be horizontal and in the equator of GIXS; if there is no orientation for the polycrystalline film, the GIXS only shows Debye rings).

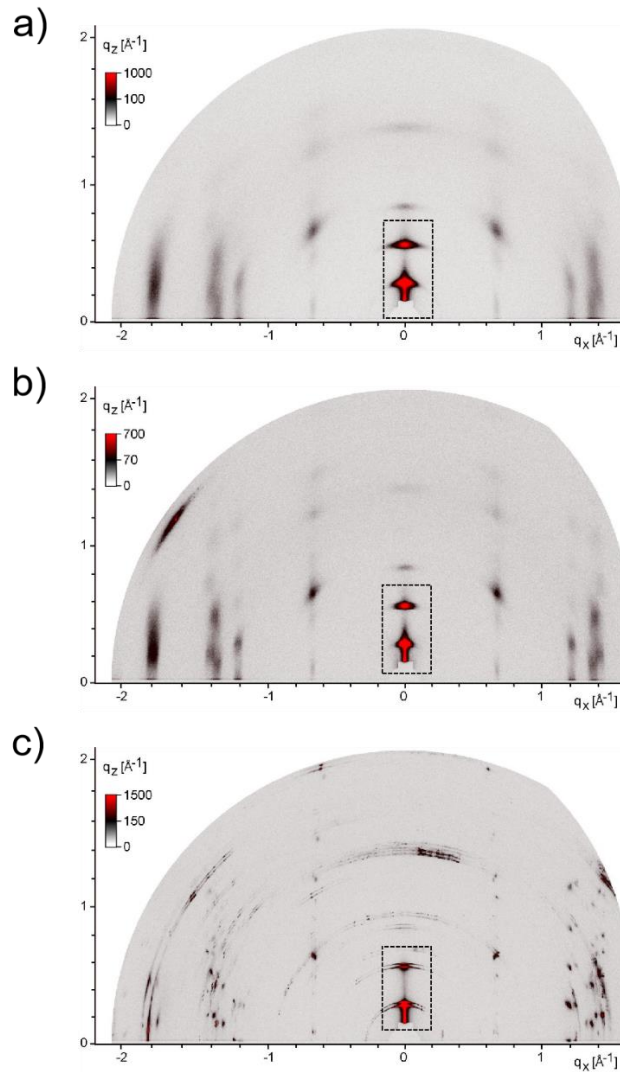


Figure 2.11 Grazing incidence X-ray scattering patterns of DALI in a) as-prepared and b) annealed at 100 °C spin-coated films, and c) melt-processed thin film. Two red spots are (0,0,l) reflections. Other black spots on the meridian are (h,k,l) miller index reflections.

The three films only differ significantly in the size of the crystallites. For the spin-coated films, the crystallites are mesoscopic and give substantially broadened reflections spots (Figure 2.11a and b). The spot width allows in turn the determination of the average crystallize size from the Scherrer equation below (with shape factor $K = 0.9$)¹⁴⁹.

$$D = K\lambda / \beta \cos\theta$$

Where D is the mean size of the ordered crystalline domains; K is a dimensionless shape factor; λ is the X-ray wavelength; β is the line broadening at half the maximum intensity (FWHM); θ is the Bragg angle. Thus, sharp peaks (smaller β) indicate large crystalline domains (large D). The average crystallize sizes were found to be 10-15 nm and 15-20 nm, for as prepared and annealed films, respectively. For the melt-processed films, crystallites are larger than 200 nm, due to the absence of measurable spot broadening. The speckled pattern shape, with

discontinuous spots/rings and saturated dots (See Figure 2.11c), even suggests very large micrometer-sized crystals, which is indeed in accordance with the optical microscopy observations in Figure 2.10. As a matter of fact, the population of crystallites in conditions of reflection drastically decreases when the size increases and some domain orientations become then missing while some others get over-represented, resulting in a characteristic speckled pattern. This is consistent with POM observations made during the melt-processing procedure.

2.5.2 Atomic force microscope (AFM)

The morphology of spin-coated (as-prepared and annealed) and melt-processed thin films of DAL1 was also studied using tapping mode AFM. The AFM topography images are shown in Figure 2.12. The as-prepared spin-coated thin film (Figure 2.12a) shows a granular texture that may be accompanied by a large number of small-sized crystallites along with a large density of grain boundaries. The spin-coated film annealed at 100°C shows a higher crystallinity (Figure 2.12b), which is consistent with GIXS observations. Indeed, it consists of larger grains where a terrace-and-step morphology is clearly noticed. The average value (or multiples) of 2.4 nm being determined from the step height is further consistent with the d-spacings obtained from GIXS in case of a lamellar structure with an orientation of lamellae parallel to the substrate. The melt-processed thin film (Figure 2.12c) shows very flat, smooth and large domains (above micrometric scale), and molecular steps of around 2.4 nm. Overall, these results demonstrate that the improved melt-processing method yields thin films with very large single-crystalline monodomains and a similar orientation of molecular packing (lamellae oriented parallel to the substrate).

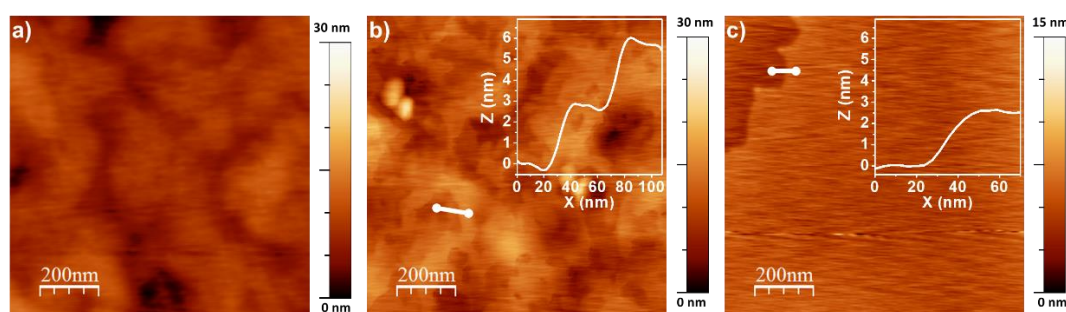


Figure 2.12 Topography AFM images of DAL1 thin films prepared a) by spin-coating (as-prepared), b) by spin-coating after annealing at 100°C for 1h, and c) by melt-processing method. The white insets in b) and c) show the terrace step profiles on the surface of thin films along the white lines.

2.6 Charge transport properties of DAL1 thin films

The OFET based on abovementioned three kinds of DAL1 films will be fabricated. For the spin-coated films, the corresponding solution will be spin-coated on interdigitated source/drain electrodes on the SiO₂ substrates. The device structure will be bottom gate/bottom contact (Figure 2.13a). For the melt-processed film, gold electrodes will be evaporated on the top of the film, resulting in bottom gate/top contact (Figure 2.13b) device structure.

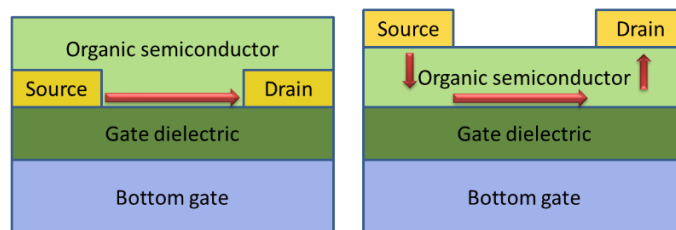


Figure 2.13 Device architecture for the a) spin-coated and b) melt-processed OFETs.

Fabrication of bottom gate/bottom contact transistors based on spin-coated films

The spin-coated OFET devices were fabricated onto silicon wafer substrates with a thermally-grown 300 nm thick SiO₂ layer. Interdigitated source/drain electrodes were deposited on top of the substrates and were achieved by the sequential thermal evaporation of a 5 nm thick adhesion layer of Cr and a 50 nm thick Au layer. The channel width and length of these BG/BC devices were 76000 and 25 μm , respectively. The organic thin films were then deposited by spin-coating from a 5 mg/ml tetrahydrofuran (THF) solution in inert atmosphere. Annealing of the spin-coated devices was carried out at 100°C on a hot plate in inert atmosphere.

Fabrication of bottom gate/top contact transistors based on melt-processed film

The fabrication of the melt-processed devices is more unique and special. To fabricate the melt-processed devices, after removing the top glass substrate mentioned in § 2.4, an array of source/drain gold electrodes was deposited (See Figure 2.14a) by thermal evaporation through a shadow mask. Note that the location of the shadow mask was carefully chosen under POM in order to find the best active areas with the largest single crystalline monodomains. In case of the melt-processed devices, a BG/TC configuration was used for the devices to minimize the effects of the cracks (See Figure 2.14b) on the electrical properties of the film. Channel width and length were in this case equal to 150 and 50 μm , respectively. And from the red curve in Figure 2.14b, a thickness of 100 to 150nm can be determined for the single crystal film.

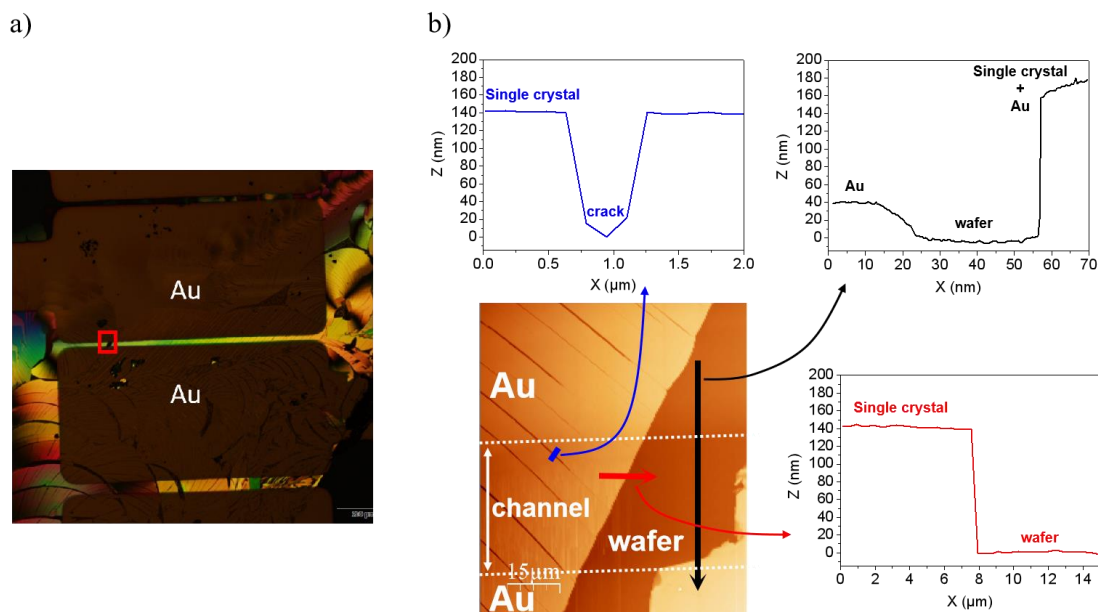


Figure 2.14 a) Picture of a transistor prepared with a melt-processed thin film of DAL1. b) AFM image of the transistor channel area localized in the red square shown in a), and height profiles along the red, black and blue lines showing the typical melt-processed thin film thickness and the crack depth.

Charge transport properties in field-effect transistor configuration

The charge transport properties of the spin-coated and melt-processed organic layers were investigated using a field-effect transistor configuration. Cyclic voltammetry measurements (in collaboration with our colleague at CINAM in Marseille, See Figure 2.15) indicated that HOMO and LUMO energy levels of the oligomer are around 5.21 and 2.64eV, respectively. Due to its work function matching well with the HOMO energy level of the oligomer, gold was chosen for the source/drain electrodes in order to investigate the hole transport properties of the organic thin films.

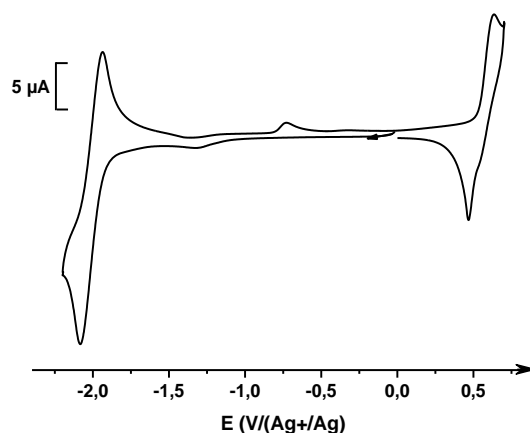


Figure 2.15 Cyclic voltammogram of a 1M solution of DAL1 in THF using TBAPF6 as the supporting electrolyte and a vitreous carbon working electrodes at a rate of $50 \text{ mV}\cdot\text{s}^{-1}$ (from CINAM, Marseille).

Figure 2.16 shows typical transfer and output characteristics measured in the devices based on spin-coated films before and after a thermal annealing at 100 °C. The square roots of the source/drain current versus gate voltage are also displayed in Figure 2.17. The results indicate that the spin-coated films operate as p-type semiconductor layers^{150, 151}. The output characteristics exhibit clear saturation and linear regimes for negative applied voltages (See Figure 2.16b and c), which means a higher I_{on}/I_{off} ratio and lower power consumption¹⁵². However, it can be seen from their behavior at low V_d that contact resistance effects (the curvature at small V_d and “S” shape of the output curve of the OFETs indicate significant contact resistance¹⁵³), which seem to be negligible in the as-prepared spin-coated device, are slightly increased after the thermal treatment. This effect upon annealing is accompanied by a decrease of the source/drain current. A plausible explanation is that thermal annealing modified not only the crystallite size but also the interface between the metal injecting bottom contact and the active organic layer, causing some changes in the contact resistance of the devices. Hole field-effect mobilities were calculated from the transfer characteristics in the saturation regime, using the standard method¹¹ described in chapter 1 (§1.3.1.1).

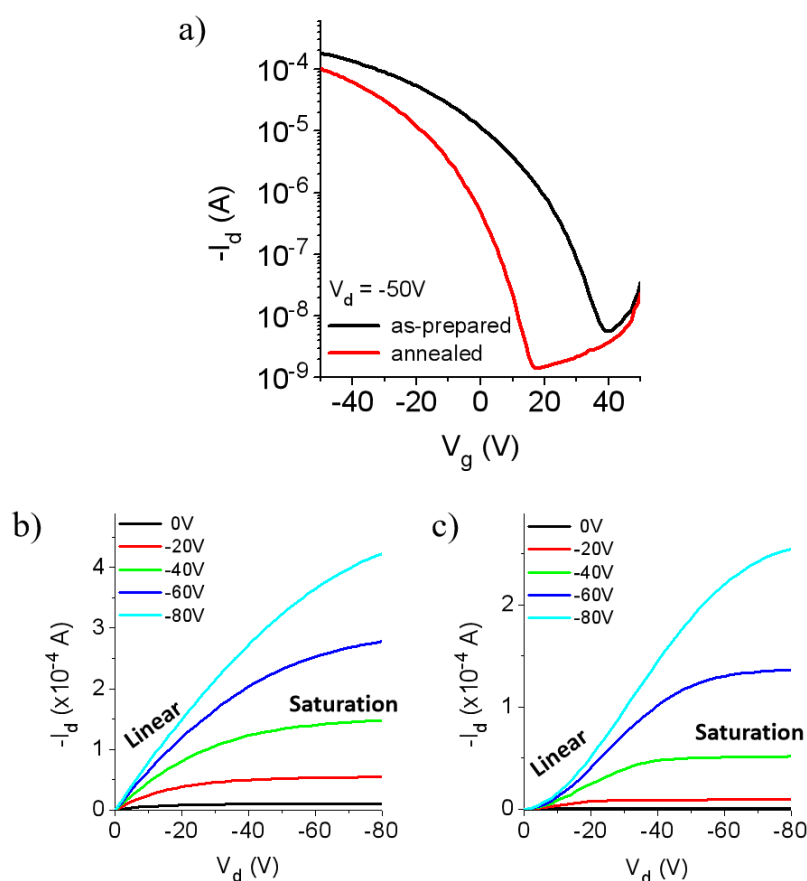


Figure 2.16 a) Transfer characteristics of OFETs based on as-prepared and annealed spin-coated films. b) and c) shows the output characteristics of the devices before and after annealing, respectively. Annealing was performed at 100 °C.

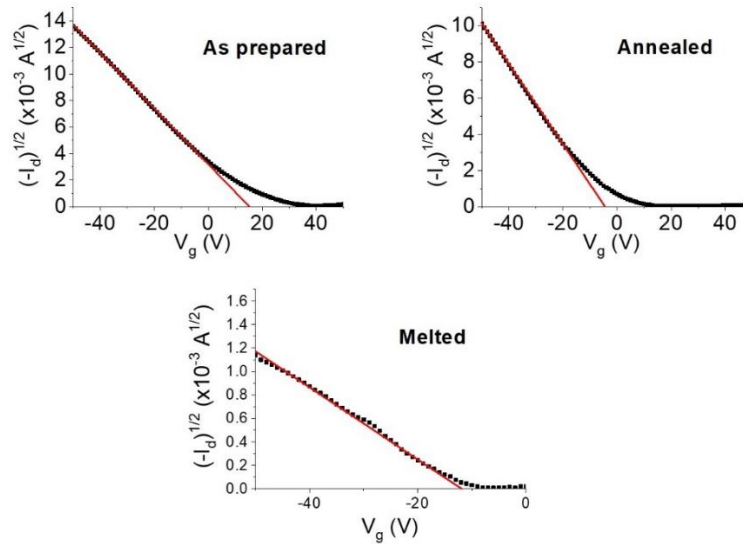


Figure 2.17 Square root of the s/d current versus the gate voltage in as-prepared, annealed, and melted OFETs.

The average mobility values were determined by testing 10 devices (before and after annealing) prepared from 2 different solutions. The excellent repeatability of the device properties is also illustrated by the histograms in Figure 2.18 (Due to limited amount of DAL1 compound, number of OFET devices based on annealed spin-coated film and melt-processed film are not enough. Therefore, only histograms of the OFET device properties based on as-prepared spin-coated film are presented here).

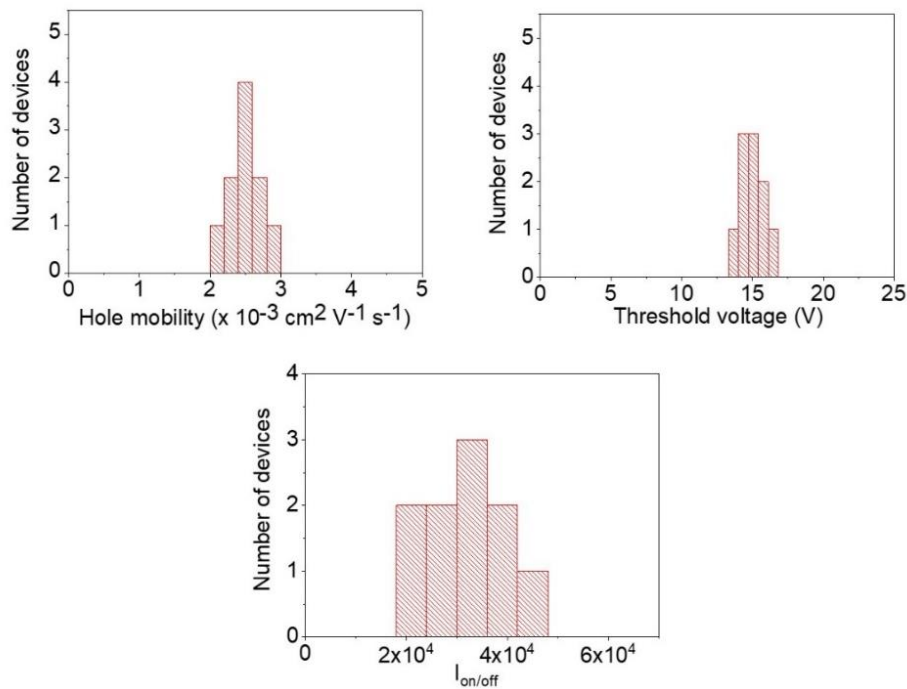


Figure 2.18 Summary of the OFET properties measured in the as-prepared device. These data show the excellent repeatability of the device performance.

As shown in [Table 2.3](#), the average hole field-effect mobility of the spin-coated films was found to slightly increase upon annealing at 100 °C from 2.4×10^{-3} to $3.5 \times 10^{-3} \text{ cm}^2\text{V}^{-1}\text{s}^{-1}$. The thermal treatment is also found to modify the threshold voltage (V_{th}) from 15 V to -5 V, suggesting an effect of the annealing on the surface states at the interfaces of the organic semiconductor layer. In other words, although the annealed devices show lower I_{DS} than the as-prepared devices, we found that the hole mobility of the annealed OFET is higher. This can be understood by looking at the significant changes in V_{th} and in the slopes of the square root of the source/drain current versus gate voltage (See [Figure 2.17](#)).

Table 2.3 Summary of the OFET properties.

Film	Hole mobility ($\text{cm}^2\text{V}^{-1}\text{s}^{-1}$)	$I_{\text{on/off}}$	V_{th} (V)
As-prepared	$(2.4 \pm 0.4) \times 10^{-3}$	$(3 \pm 1.2) \times 10^4$	15 ± 1
Annealed	$(3.5 \pm 0.4) \times 10^{-3}$	$(7.5 \pm 2) \times 10^4$	-5 ± 2
Melt-processed	$(5 \pm 1) \times 10^{-2}$	$(3 \pm 2) \times 10^4$	-12 ± 5

To gain further insights into the role of annealing on the charge transport of the spin-coated films, we plotted in [Figure 2.19](#) the hole mobility determined in the saturation regime versus gate voltage. As the V_g bias increases, hole mobilities of the three kinds of films in OFET configurations keep relatively constant. These results are useful to exclude any potential issues in field-effect mobility overestimation due to contact resistance problems ^{148,154}.

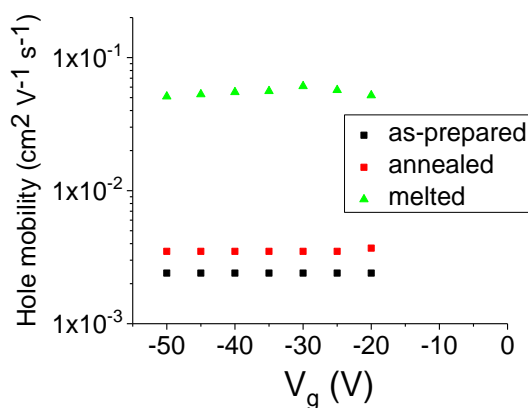


Figure 2.19 Gate voltage dependence of the hole mobility in representative as-prepared, annealed and melted OFETs.

[Figure 2.20](#) displays the transfer and output characteristics of a representative device based on a melt-processed organic layer. Similar to the spin-coated polycrystalline thin films, the melt-processed devices exhibit a unipolar p-type conduction with clear linear and saturation regimes in their output characteristics. Noticeably, no significant contact resistance effects (no curvature of the curve at low V_d) can be seen from the behaviour of the output characteristics at low V_d

in Figure 2.20b.

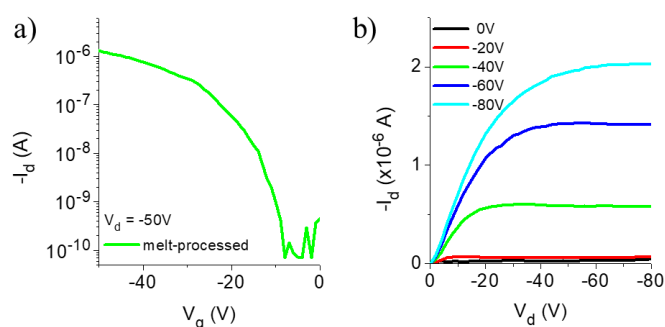


Figure 2.20 a) Transfer and b) output characteristics of an OFET based on a melt-processed film.

It is worth pointing out that, compared to the bottom gate/bottom contact devices (See Figure 2.13a), when using bottom gate/top contact devices (See Figure 2.13b), charge injection extends further away from the channel area between the contact electrodes and gate dielectrics (See short red arrow in Figure 2.13b), thereby reducing the contact resistance and boosting the injection¹⁵⁵. In other words, the use of a bottom gate/top contact configuration in the melt-processed devices is certainly helpful to minimize contact resistance effects.

It is important to emphasize here that the device architecture for the spin-coated and melt-processed OFETs is different. The conventional interdigitated bottom source/drain electrodes were not used for the melt-processed devices in order to minimize the effects of the cracks on the electrical properties of the film and thus their potential impact on the determination of the field-effect charge carrier mobilities. We should also mention that the position of the shadow mask used for the evaporation of the top source/drain electrodes was carefully selected using an optical microscope. This aspect was indeed essential to fabricate melt-processed devices with the cracks in the direction parallel to the transistor channel (See Figure 2.14). Although these values (See table 2.3) cannot be directly compared with those obtained in the spin-coated devices due to their different architectures, the threshold voltage and the on/off current ratio deduced from the transfer characteristics of the melt-processed devices were typically around -12 V and over 10^4 , respectively.

Looking at Figures 2.16 and 2.20, it can also be seen that the flowing source-drain current in the device prepared by the melt-processing method is reduced to around 10^{-6} A with respect to about 10^{-4} A when using spin-coated films and interdigitated electrodes. Taking into account the channel length and width of the device structures and using the standard method to determine the charge carrier mobility in the saturation regime, the hole mobility of the melt-processed device is found to be $5 \times 10^{-2} \text{ cm}^2\text{V}^{-1}\text{s}^{-1}$, which is more than one order of magnitude higher than the values measured in spin-coated polycrystalline thin films. Although the use of different device architectures certainly affects, to some extent, the determination of the charge

carrier mobility, these results are fully consistent with the increase of the crystal size evidenced by the XRD diffraction results and film morphology shown in Figures 2.11 and 2.12, respectively. Although the field-effect mobility of the melted film of DAL1 is not increased by several orders of magnitude, the improved melt-processing method described in the present work is found to be suitable for the fabrication of organic electronic devices based on highly crystalline organic materials without using any solvent or vacuum.

2.7 Photophysical properties of DAL1 thin films

There are many semiconducting polycyclic aromatic hydrocarbons that can be used in OLEDs as emitters including naphthalene, anthracene, fluorene, and pyrene¹⁵⁶. Pyrene derivatives are generally highly fluorescent. DAL1 is an oligo(*p*-phenylene vinylene) derivative substituted at both ends with pyrene moieties. Thus, we would like to investigate the photophysical properties of the three kinds of films (as-prepared spin-coated film, annealed spin-coated film and melt-processed film) and study the impact of melt-processing technique. Figure 2.21a shows the steady-state PL spectra of the as-prepared, annealed and melted oligomer films.

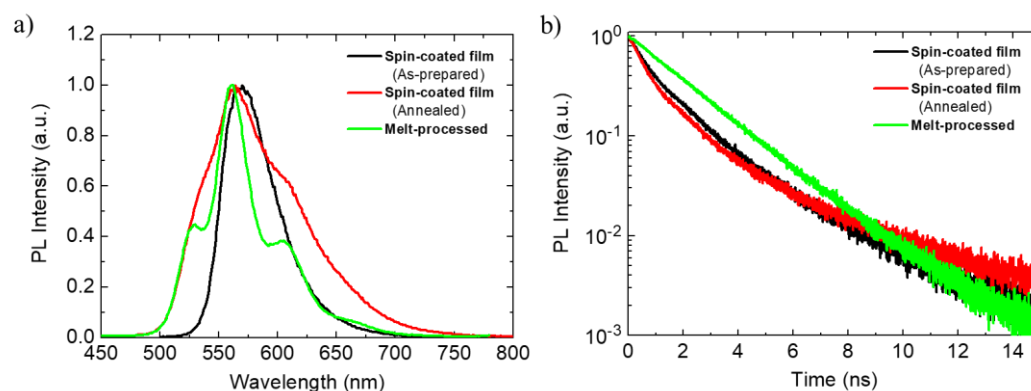


Figure 2.21 a) Steady-state photoluminescence spectra of the pristine, annealed and melted films. Excitation wavelength was 400 nm. b) Photoluminescence decays measured at room temperature in pristine, annealed and melted films.

The spectrum of the pristine film displays only one main peak with no vibronic progression, which has a maximum emission wavelength at 569 nm. Annealing of the film at 100 °C for one hour leads to a 5 nm blue-shift of the maximum emission wavelength and a substantial broadening of the spectrum. The full-width-at-half-maximum (FWHM) increases indeed from 51 to 94 nm (*i.e.* 1540 to 2862 cm^{-1}) upon the thermal treatment. It can also be seen that two shoulders appear at about 535 and 595 nm in the spectrum of the annealed sample. In clear contrast with the pristine film, the PL spectrum of the melted oligomer sample shows a well-

resolved vibronic structure with a maximum emission wavelength at 561 nm. Photoluminescence quantum yield (PLQY) values of 12, 22 and 30 % were obtained in the as-prepared, annealed and melted oligomer film, respectively, indicating a significant improvement of the light-emitting properties with the extent of crystallinity in this material.

The PL decays measured in the films are shown in [Figure 2.21b](#). While the PL dynamics in as-prepared and annealed film can be fitted by the sum of two exponential decay functions, the transient curve measured in the melted film follows a single exponential decay with a PL lifetime of 2 ns. It is worth noting that we did not observe any significant emission wavelength dependence of the PL dynamics in the three different films, indicating the presence of only one light-emitting specie in the films. This suggests that changes in molecular configuration are not responsible for the observed variations of PLQY upon thermal treatment. Instead, the GIXS data provided evidence that the crystalline structure of the as-prepared, annealed and melted films was identical and that the morphology of these films only varied by the size of the crystallites. This implies that the observed changes in PLQY cannot be explained by a modification of the molecular arrangement/packing in the film upon thermal treatment.

Exciton diffusion is an important process in OSCs and plays a critical role on the properties of OLEDs and organic solar cells¹⁵⁷⁻¹⁶¹. Singlet excitons in these materials can migrate by a Förster-type dipole-dipole coupling and their diffusion length in the films is typically around 5-10 nm¹⁶²⁻¹⁶⁸. Interestingly, a few studies have investigated the influence of the crystallinity on the exciton diffusion length in organic thin films^{169,170}. In particular, photophysical measurements in 3,4,9,10 - perylenetetracarboxylic dianhydride (PTCDA) polycrystalline thin films showed that singlet exciton diffusion length was strongly improved by an increase in the extent of crystalline order¹⁶⁷. This effect was accompanied by a substantial reduction of the PL quenching at the grain boundaries as the crystallite size in the film was increased. As mentioned above, the GIXS measurements carried out in the present study showed that the crystallite size in the as-prepared and annealed spin-coated oligomer films is around 10-15 and 15-20 nm, respectively. While the exciton diffusion length is several orders of magnitude smaller than the dimensions of the single crystal monodomains in the melt-processed film, its value is in the same order of magnitude as the crystallite sizes in the spin-coated thin films. This implies that a significant number of singlet excitons in the spin-coated films is able to migrate to the grain boundaries where they are more likely to decay non-radiatively. Based on these considerations, we attribute the lower PLQY values and the presence of two time constants in the PL decays of the spin-coated films to a quenching of the singlet excitons at the grain boundaries. Noticeably, the fact that the PL quenching of the spin-coated films is slightly reduced after annealing is consistent with the little increase of the crystallite size upon the thermal treatment. These results provide clear evidence that the melt-processing of highly crystalline organic semiconductor thin

films leading to millimetric single crystal monodomains enables to suppress PL quenching at grain boundaries and can thus significantly improve significantly their PL properties.

2.8 Conclusion

In summary, we propose an improved melt-processing method for the fabrication of crystalline organic semiconducting layers with millimetric single crystal monodomains. For this purpose, we used an oligo(*p*-phenylene vinylene) derivative substituted at both ends with a pyrene moiety which is solution-processable and shows a melting temperature around 150 °C. The organic film prepared by melting presents a much higher crystallinity than the spin-coated polycrystalline films, resulting in a significantly higher hole field-effect mobility value. The charge carrier mobility is found to increase indeed from $2.4 \times 10^{-3} \text{ cm}^2\text{V}^{-1}\text{s}^{-1}$ in the as-prepared spin-coated film to $5 \times 10^{-2} \text{ cm}^2\text{V}^{-1}\text{s}^{-1}$ in the melted sample. This improvement of the charge transport properties upon melting is accompanied by a substantial enhancement of the PLQY. Such a simultaneous optimization of the charge carrier mobility and photophysical properties has been proven to be quite elusive so far in organic semiconductors and can be explained here by the substantial improvement of the crystallinity and the reduction of the number of grain boundaries in the melt-processed sample. Overall, this study demonstrates that the solvent-free vacuum-free melt-processing method can be utilized to fabricate high performance organic electronic and light-emitting devices. This approach is suitable for a large variety of organic semiconductors and, as a consequence, should be of strong interest for future research in the field of organic electronics.

2.9 Experimental section

2.9.1 Materials

The oligo(*p*-phenylene vinylene) derivative used in this chapter was synthesized by Dr. D'Aléo and Prof. Frederic Fages at CINAM (Marseille) and the details of the synthesis was reported in the reference¹⁷¹.

2.9.2 DSC

The thermal phase transitions of the oligomer were analyzed by DSC using TA instruments Q2000 under a nitrogen flow on heating and cooling cycles at different rates (20°C/min, 10°C/min, 5°C/min,

and 2°C/min).

2.9.3 POM

POM was carried out using a Leica microscope equipped with a Linkan THMS 350 hot plate connected to a Linkam 93 temperature controller.

2.9.4 XRD, SAXS and GIXS

Regarding the characterization of the structural properties of powder state, the SAXS patterns were obtained with an experimental set-up composed with a linear monochromatic Cu-K α 1 beam ($\lambda = 1.5405 \text{ \AA}$) obtained using a sealed-tube generator (900 W) equipped with a bent quartz monochromator. The setup is based on the Guinier transmission geometry and the crude powder was filled in Lindemann capillaries of 1 mm diameter. Diffraction patterns were recorded with a curved Inel CPS 120 counter gas-filled detector linked to a data acquisition computer, and the sample temperature controlled to within $\pm 0.05 \text{ }^\circ\text{C}$ from the ambient up to 200°C (in collaboration with Dr. Benoit Heinrich, IPCMS, Strasbourg).

The characterization of the structural properties of the spin-coated and melt-processed thin films was performed by 2D GIXS experiments at PLS-II 9A U-SAXS beamline of Pohang Accelerator Laboratory in Korea. The thin films were studied on silicon substrates and the X-rays coming from the vacuum undulator (IVU) were monochromated using Si(111) double crystals and focused on a detector consisting in a 2D CCD detector (Rayonix SX165). The distance between sample and detector was around 225 mm and the beam energy was about 11.06 keV (1.121 \AA).

2.9.5 AFM

Atomic force microscope (AFM) experiments were performed in tapping mode, using an apparatus Bruker 3100 and silicon tips, with a resonance around 400kHz, allowing to specifically probe soft matter.

2.9.6 Characterization of OFET devices

For the OFET characterization, a semiconductor analyzer (Agilent Technologies, B1500A) and a probe station were used to measure the electrical characteristics of the devices in nitrogen atmosphere.

2.9.7 Photophysical properties

The PL properties of DAL1 were investigated in as-prepared, annealed (at 100 °C for 1 hour) and melted films. The steady-state PL spectra were measured using a spectrofluorometer (Fluoromax-4, Horiba Jobin Yvon) with an excitation wavelength of 400 nm. PLQY values were determined using an absolute PLQY spectrometer (C11347 Quantaaurus-QY, Hamamatsu, Japan). The transient PL characteristics of the films were recorded at room temperature using a Quantaaurus-Tau fluorescence lifetime measurement system (C11367-03, Hamamatsu Photonics Co., Japan).

**Chapter 3 Investigation of charge transport
properties of [1]Benzothieno[3,2-b][1]-
benzothiophene derivatives in field-effect transistor
configuration**

As introduced in the Chapter 1 (§ 1.1.1), thienoacenes such as [1]Benzothieno[3,2-b][1]-benzothiophene (BTBT) derivatives have emerged as promising materials for the fabrication of efficient OFETs ¹⁷². These derivatives are composed of fused thiophenes and benzene rings, leading to a rigid and planar π -conjugated system. Such chemical structure induces a large intermolecular orbital overlap in solid-state explaining their high charge-carrier mobility.

In pioneer works reported by Takimiya *et al.*, hole mobilities of end-capped BTBTs (either by two phenyl rings (DPh-BTBT) ¹⁷³ or two alkyl chains (C_n-BTBT-C_n) ¹⁴) OFETs showed promising values about 1-2 cm²V⁻¹s⁻¹ based on vacuum deposited and spin-coated thin films. Later on, the charge transport properties of alkyl-substituted BTBT derivatives were intensively studied in different FET configurations and highlighted the beneficial effect of the alkyl functionalization of the BTBT core on the charge transport properties. Hole mobilities as high as 31 cm²V⁻¹s⁻¹ were demonstrated based on single-crystalline thin films of C₈-BTBT-C₈ derivative ³². Moreover, alkyl-substitution of BTBT cores incorporating functional groups such as hydroxyl group (-OH) ¹⁷⁴ or organosilica (-Si(OEt)₃) ¹⁷⁵ were also investigated, which leads to efficient air stable transistors (hole mobilities of 0.17 cm²V⁻¹s⁻¹) or very robust cross-linked BTBT-based active for OFET fabrication. In the same way, asymmetrically alkyl-substituted BTBTs (C_n-BTBTs) and its derivatives were also widely investigated in FET configuration. For example, high mobilities about 14.7 cm²V⁻¹s⁻¹ based on liquid crystalline Ph-BTBT-C₁₀ spin-coated film ³⁵, or about 17.2 cm²V⁻¹s⁻¹ based on evaporated films of mono-substituted C₁₃-BTBT were obtained ¹⁷⁶.

To better understand the crucial role of alkyl substitution on BTBT derivative charge transport properties, Minemawari *et al.* investigated most recently the systematic chain-length dependence of the molecular packing for a series of symmetrically and asymmetrically alkyl-substituted BTBTs ¹⁷⁷. Based on crystal structure analysis and calculations of intermolecular interaction energies for C_n-BTBT-C_n derivatives, the authors demonstrated that substitutions with long alkyl chains stabilize the layered-herringbone packing of BTBT cores, and are consistent with the high charge carrier mobilities reported so far. In addition to these results, Yavuz *et al.* proposed to theoretically explore these structures and to rationalize the impact of alkyl substitution on bulk structure and charge-transport properties ¹⁵. Based on solid-state morphology predicted by molecular dynamics simulations from reported X-ray crystal structures, the authors modeled charge transport by both band and hopping type transport models for each C_n-BTBT-C_n derivative. They compared these calculated mobilities with the corresponding experimental ones reported in literatures ^{14, 172, 178}. In this latter work, the charge transport properties of the unsubstituted BTBT derivative (i.e. for n=0) was also calculated, and mobility values ranging from 10⁻³ to 10⁻¹ cm²V⁻¹s⁻¹ were determined depending on the transport models used. However, to the best of our knowledge, no comparison between experimental and theoretical field-effect mobility had been reported for BTBT core before this part of work was began and published in ‘*Organic electronics*’ in December 2019. (Note

that single-crystal OFETs (SC-OFETs) of BTBT core were reported by Takimiya et al. in May 2020¹⁷⁹) The absence of FET mobility values on the BTBT model until recently is mainly explained by the fact that homogeneous thin films of such a small heteroaromatic system cannot be obtained by vacuum vapor deposition as reported by Takimiya¹⁸⁰.

In this chapter, we will thus outline the investigation of the charge transport properties of a simple BTBT core (See Figure 3.1, collaboration with Dr. Xiaolu Su at IPCM) in OFET configuration. To overcome the inability to obtain homogeneous thin films by vacuum thermal evaporation, BTBT single crystals are fabricated by physical vapor transport deposition (VTD)¹⁸¹ and the molecular packing and morphologies of BTBT single-crystals are analyzed by XRD, POM, SEM and AFM. Then, BTBT single-crystal transistors are fabricated, and the charge transport properties are investigated. In addition, SC-OFETs with ion gels gate configuration will be also investigated for low voltage operation. On the other hand, the charge transport properties of alkyl-substituted C₈-BTBT-C₈ (See Figure 3.1, collaboration with Dr. Teng Teng at IPCM) are also briefly investigated by transistors based on melt-processed films to compare to the BTBT single-crystal results.

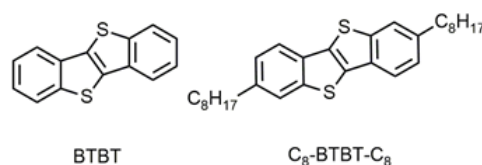


Figure 3.1 Chemical structures of unsubstituted BTBT core and C₈-BTBT-C₈ (collaboration with Drs Xiaolu Su and Teng Teng at IPCM).

3.1 Thermal properties of BTBT

The thermal behavior of BTBT was studied by DSC and the thermograms obtained are given in Figure 3.2. They present on heating and cooling only one transition at 219°C and 193°C, respectively, with similar transition enthalpies. On further heating, no additional peaks were observed, indicating that this reversible transition can be attributed to the melting point of the derivative.

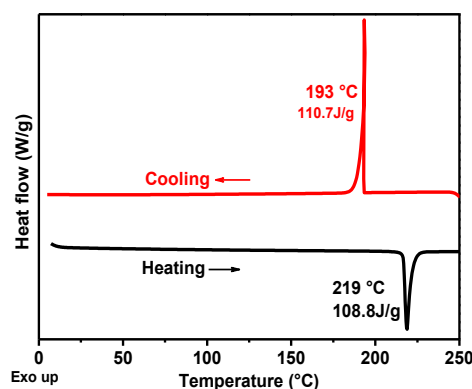


Figure 3.2 DSC curves of BTBT compound on heating and cooling at a rate of 20 °C/min.

3.2 Preparation of BTBT single crystals by physical vapor transport deposition

As introduced in the beginning of this chapter, FET mobility of BTBT core has never been reported due to the fact that homogeneous thin films of such a small heteroaromatic system cannot be obtained by vacuum thermal evaporation. However, we were able to prepared BTBT single crystal as the active layer of the OFET via physical vapor transport deposition (VTD) method (also introduced in § 1.2.2.2). The preparation of BTBT single crystals was adapted from the classical physical VTD method reported by Laudise¹⁸¹. As shown in Figure 3.3, several milligrams of freshly synthesized BTBT compound were placed on a clean glass substrate on the hot-stage of a POM (Linkan THMS 350) and topped with another glass substrate (about 2mm higher than the bottom glass substrate). The system was heated to 165 °C at the rate of 30 °C/min in nitrogen (N₂) flow condition, and kept at this temperature for 8 mins. This led to the rapid sublimation of the compound to form large, thin, single crystal platelets growing perpendicularly to the top (cold) glass substrate, as shown in Figure 3.4. With a size ranging from dozens to hundreds of micrometers, these platelet-like crystals are very flexible and can be easily bended (see insert of Figure 3.4), indicating a sub-micron thickness typically as thin as 150-300 nm¹⁸². The system was then cooled to room temperature at the rate of 30 °C /min. Next, the top glass was turned upside down, and the selected BTBT single crystals were carefully isolated with a microscale gold wire for structural studies or transferred onto the interdigitated electrodes of transistors with the help of the POM.

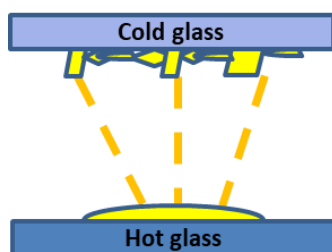


Figure 3.3 Schematic representation of the fabrication of BTBT single crystals by vapor transport deposition.

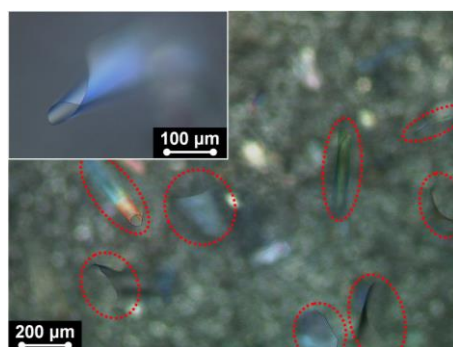


Figure 3.4 POM image of BTBT single crystals grown perpendicularly to the top glass substrate (red dashed circles) by vapor transport deposition method. (Insert: magnification of a flexible BTBT single crystal rolled up on itself)

3.3 Structure of BTBT single crystals prepared by physical vapor transport deposition

The crystal structure and film morphology of the BTBT single crystals is investigated by single-crystal XRD, POM, SEM and AFM, respectively.

3.3.1 Single-crystal X-ray diffraction

The single crystals of BTBT obtained by VTD method were studied by single-crystal XRD in collaboration with Ms Lise-Marie Chamoreau (X-ray platform, IPCM). The molecular structure of the unit cell is presented in [Figure 3.5a](#) and the crystallographic data are provided in [table 3.1](#). BTBT cores exhibit a layered-herringbone packing as shown in [Figure 3.5b](#). This packing is similar to the one reported previously for BTBT single crystals obtained from solutions by slow liquid/liquid diffusion¹⁸³. This indicates that the molecular packing of BTBT in the crystalline state is not, in that case, sensitive to the crystal growth conditions. This result is also consistent with the simple polymorphism observed by DSC and the absence of crystal-crystal transitions between room temperature and the melting point. This suggests strong van der Waals bonding between crystallized BTBT molecules and the existence of a single crystalline structure.

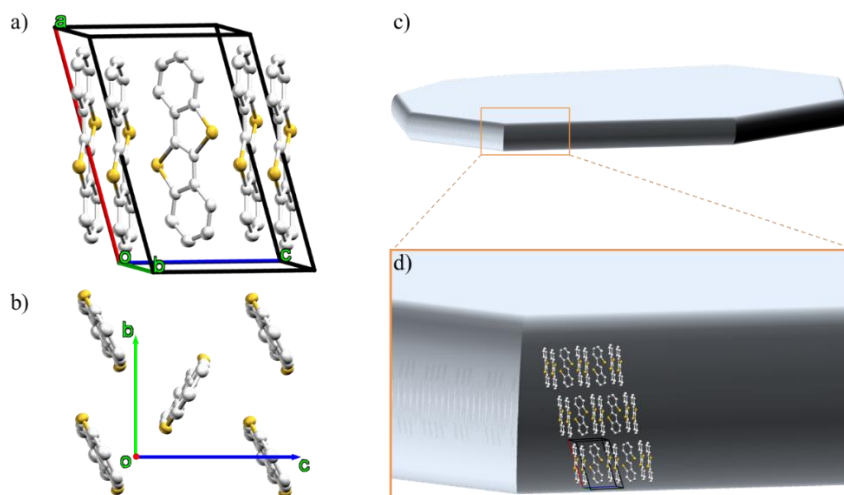
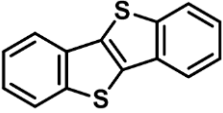


Figure 3.5 a) Perspective view of the BTBT crystal structure prepared by VTD method. b) Representation of the herringbone packing structure of BTBT along a axis. c) Schematic representation of the typical platelet-like single-crystals of BTBT obtained by VTD method and d) schematic representation of the lattice and molecular orientation of BTBT cores within the platelet-like crystal. b and c axis are in the plane of the crystal.

Table 3.1 Crystal data and structure refinement for BTBT.

 BTBT	
Empirical formula	C ₁₄ H ₈ S ₂
Formula weight	240.32
Temperature/K	200
Crystal system	monoclinic
Space group	P2 ₁ /c
a/Å	11.803(3)
b/Å	5.8805(12)
c/Å	8.0234(16)
α/°	90
β/°	106.269(13)
γ/°	90
Volume/Å ³	534.6(2)
Z	2
ρ _{calc} /cm ³	1.493
μ/mm ⁻¹	4.191
F(000)	248.0
Crystal size/mm ³	0.18 × 0.15 × 0.02
Radiation	CuKα (λ = 1.54178)
2θ range for data collection/°	15.642 to 137.912
Index ranges	-14 ≤ h ≤ 14, -7 ≤ k ≤ 4, -9 ≤ l ≤ 9
Reflections collected	5116
Independent reflections	962 [R _{int} = 0.0713, R _{sigma} = 0.0656]
Data/restraints/parameters	962/0/73
Goodness-of-fit on F ²	1.044
Final R indexes [I >= 2σ (I)]	R ₁ = 0.0540, wR ₂ = 0.1398
Final R indexes [all data]	R ₁ = 0.0724, wR ₂ = 0.1540
Largest diff. peak/hole / e Å ⁻³	0.50/-0.54

To go further into the description of the molecular packing of BTBT single crystals, XRD analysis of oriented crystals was performed. Large and thin crystals were illuminated with the incident X-ray beam either perpendicular or parallel (**Figure 3.6a or b**) to the larger facets of the crystals. This procedure gives precious information on the orientation of the unit cell within the crystal and the crystallographic axes can be correlated with the anisotropic shape of the crystals (**Figure 3.6c**). Therefore, the longest axis ($a = 11.80 \text{ \AA}$) of the unit cell was found to be perpendicular to the larger facets of the crystal, corresponding to the smallest dimension of the platelet, while b and c axis are in the plane. It can be inferred that BTBT molecules are oriented perpendicular to the larger facets of the crystal and that the layers formed by the herringbone packing of BTBT are in the plane (illustrated in **Figure 3.5d**). This molecular organization is typical for organic crystals obtained by VTD. During the growth process, the larger crystal dimension corresponds to the direction of the strongest molecular interactions which corresponds, in the present case, to the strong overlap between the π -conjugated systems of adjacent BTBT molecules. It is

important to notice that this molecular packing with the layered-herringbone packing in the plane of the crystals is perfectly suitable for the fabrication of single crystal FETs because in such devices the molecular packing will coincide with the direction of the highest mobility of field-induced carriers.

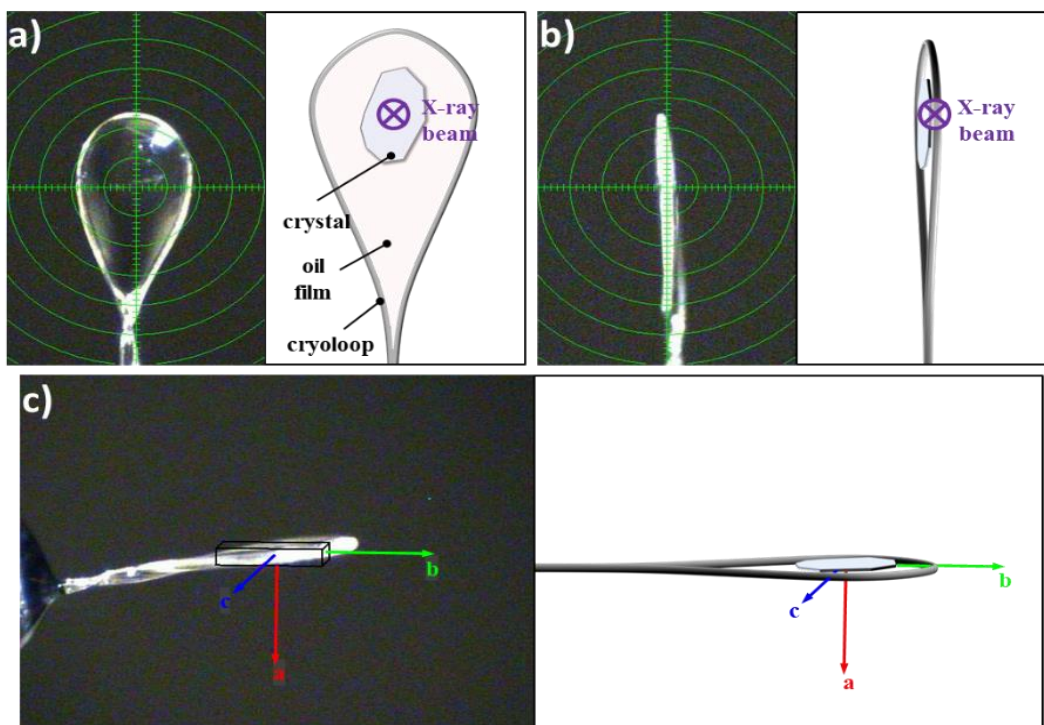


Figure 3.6 XRD measurements on oriented single crystal of BTBT. Optical image and schematic representation of a platelet-like single crystal mounted on a cryoloop with the X-ray beam a) perpendicular to the larger facets of the crystal and b) parallel to the larger facets of the crystal. c) Optical image and schematic representation of the crystal with its crystallographic axes. The longest axis *a* corresponds to the smallest dimension of the crystal and is perpendicular to the principal face. *b* and *c* axis are in the plane of the thin platelets.

3.3.2 Polarized optical microscope (POM) and Scanning electron microscope (SEM)

The quality of BTBT single crystals prepared by VTD method was investigated by POM. Based on this optical inspection, the largest birefringent crystals with uniform colors under the crossed polarized light were selected, transferred and deposited with micro-scale gold wire on interdigitated gold electrodes of prefabricated BG/BC FETs, as displayed in Figure 3.7a and b. The high flexibility of the BTBT single crystals induced a high quality of the electrostatic bonding to the electrodes and channels of the transistor as confirmed by the POM image in Figure 3.7b. The device structure and the adhesion of the crystal were also checked by SEM and no bends or folds were observed (Figure 3.7c).

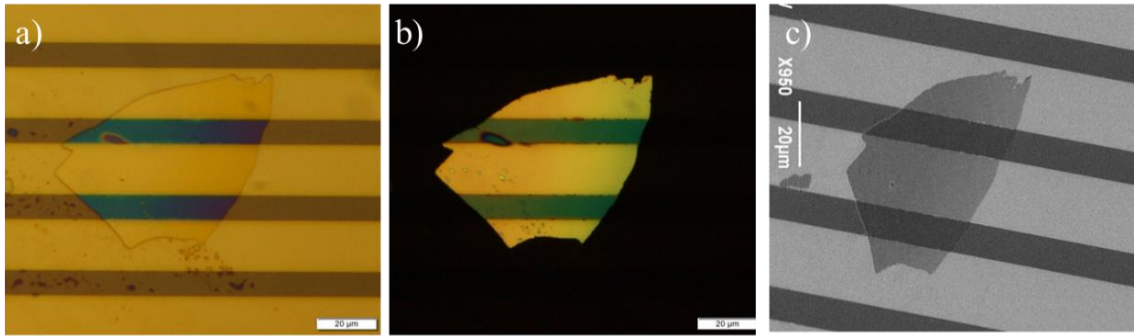


Figure 3.7 POM images of the single crystal on prefabricated BG/BC transistor a) under the natural light and b) under crossed polarized light. c) SEM image of the device structure.

3.3.3 Atomic force microscope (AFM)

The morphology of the single crystal deposited on the gold electrodes of the transistor was investigated by AFM. The 3D image given in **Figure 3.8a** shows the different components of the device: the crystal, the substrate and the gold electrode. In the 2D topography image of the crystal (**Figure 3.8b**), a 50nm thickness of the gold electrode and a 300nm thickness of the single crystal can be determined respectively from the first step and the second step of the height profile (shown by yellow arrow and white curve) of the crystal edge given in the inset of **Figure 3.8b**. Single crystals with a thickness of several hundreds of nanometer are usually very flexible and can be easily bended, which is consistent with the high flexibility observed by POM (**Figure 3.4**). At higher magnification (**Figure 3.8c**), the top of the crystal presents a layered structure with the presence of terraces. The height of these terraces is about 1.1 nm, or multiples of 1.1 nm, and corresponds to the length of standing molecules. Note that this observation is consistent with the molecular orientation determined by XRD with the layered-herringbone packing of BTBT in the plane of the crystals ($a = 11.8 \text{ \AA}$).

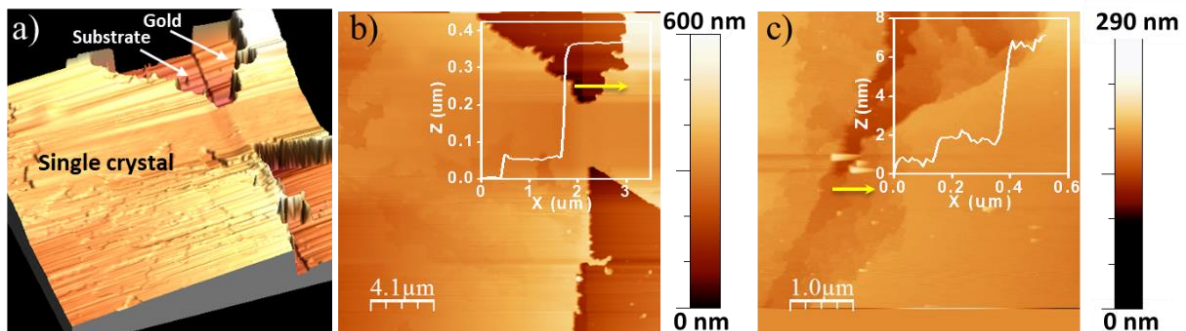


Figure 3.8 AFM images of BTBT single-crystal deposited on prefabricated BC/BG transistor: a) 3D topography image. b) 2D topography image (Inset: height profile of the crystal edge along the yellow arrow. c) 2D topography image at higher magnification of the top of the single crystal (Inset: terrace step profile along the yellow arrow).

3.4 Charge transport properties of single crystal BTBT

Below, four different OFET devices based on BTBT single crystals will be prepared: bottom gate/bottom contact (BG/BC) and ion gel top gate/bottom contact (TG/BC) configurations both on SiO₂ and OTS substrate surface. Their preparation processes will be introduced in detail. The charge transport properties of BTBT single crystals and the air stability of the devices were investigated with the BG/BC devices, while the TG/BC devices were prepared to evaluate the possibility of the BTBT OFETs to operate at low gate voltage, which is meaningful for the energy saving.

3.4.1 Fabrication of BTBT single crystal OFETs

Bottom gate/bottom contact transistors

BG/BC transistors (Figure 3.10a) were fabricated on heavily-doped Si wafer (i.e low bulk resistivity 0.01 Ω.cm) thermally oxidized by a 280nm-thick SiO₂ layer, purchased from MicroChemicals GmbH. SiO₂ was used here as gate dielectric (i.e Gate capacitance $C_i = 12 \text{ nF/cm}^2$) and the Si wafer as gate electrode in back contact. The interdigitated source and drain electrodes were patterned by photolithography process-flow through an MJB-4 (Karl Suss) mask-aligner in vacuum contact (in collaboration with Dr. Sebastien Sanaur, CMP, Gardanne), and completed by lift-off technique in acetone overnight. Previously, a sequential thermal evaporation of a 5 nm-thick adhesion layer of Chromium and a 100 nm-thick gold layer in a vacuum chamber at 10⁻⁷ Torr was achieved. The channel length (L) was 2.5, 5, 12.5, 25 or 50μm, while the channel width (W) depended on the size of each single crystal. The substrates were sonicated in ethanol, acetone and chloroform successively. Then they were cleaned for 30 min in a UV-Ozone cleaner. For the preparation of the OTS-treated surface, the substrates were further treated as the procedures described in the literature¹⁴⁵. Next, the largest birefringent crystals with uniform colors under the crossed polarized light were selected, transferred and deposited with micro-scale gold wire (See Figure 3.9) on the interdigitated gold electrodes.

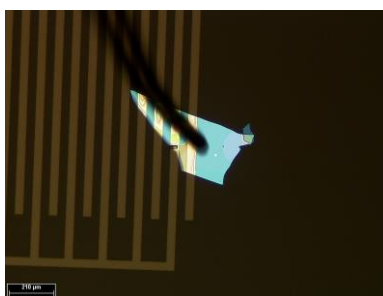


Figure 3.9 POM images showing the transfer and deposition of a large birefringent crystal on interdigitated gold electrodes with micro-scale gold wire (black).

Ion gel top gate/bottom contact transistors

For top gate studies, in collaboration with Dr. Emmanuel at INSP, we used ion gel electrolyte¹⁸⁴ which was obtained by mixing 50 mg of LiClO_4 with 230mg of polyethylene glycol (PEG, 6kg/mol) on a hot plate in an N_2 -filled glovebox at 175 °C for 90 min until the solution appears clear¹⁸⁵. Then, the mixture was cooled down and stored in the glove box to be used later. To prepare the top gate dielectric layer, the electrolyte was softened on a hot plate at 80 °C and brushed onto the channel and crystal area of the former BG/BC device on SiO_2 or OTS surface. It is important to point out that the active layer of the BG/BC (Figure 3.10a) and TG/BC (Figure 3.10b) OFET device was the same piece of BTBT single crystal; and the ion gel was deposited after the electrical measurement of the BGBC OFET had been performed. The device was finally cooled in the glove box first and then dried under vacuum in the transfer chamber. The PEG drops formed well-defined physical gels (See Figure 3.10c) through non-covalent association where ether crown surround the ion, with their reorganization ensuring the ion migration. A copper grid was then deposited on the top of the electrolyte gel drop to be used as the gate electrode during the current-voltage measurement in the glove box. A picture of a TG/BC transistor with ion gel drop on the top is given in Figure 3.10c.

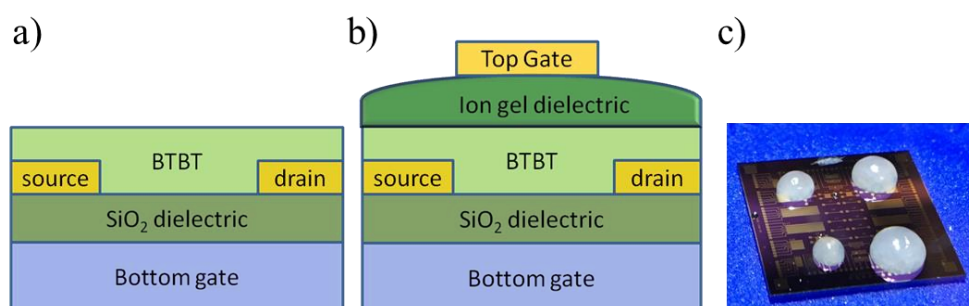


Figure 3.10 a) Schematic representation of the bottom gate/ bottom contact OFET structure. b) Schematic representation of the bottom contact/top gate OFET structure. c) Picture of ion gel drops on the top of BTBT single-crystal deposited on gold bottom contacts.

3.4.2 Charge carrier mobility of BTBT single crystal transistors

Bottom Gate/Bottom contact transistor configuration

Considering the energy of the HOMO of BTBT (5.5eV)⁸, gold contacts are well-suited for hole injection and charge transport investigation. Figure 3.11a and b show typical transfer and output characteristics of BTBT single crystal BG/BC devices with gold electrodes and SiO_2 gate dielectric. From these curves, it can be seen that the devices show a rise of conductance under hole injection (*i.e.* negative gate bias) consistent with a p-channel conduction. An average hole mobility about $2.9 \times 10^{-3} \text{ cm}^2 \text{ V}^{-1} \text{ s}^{-1}$ was extracted

from the saturation regime of a ten of transistors (Figure 3.12a). Charge mobilities and other device parameters such as the average threshold voltage (V_{th}) or average on/off current ratio (I_{on}/I_{off}) are given in Table 3.2.

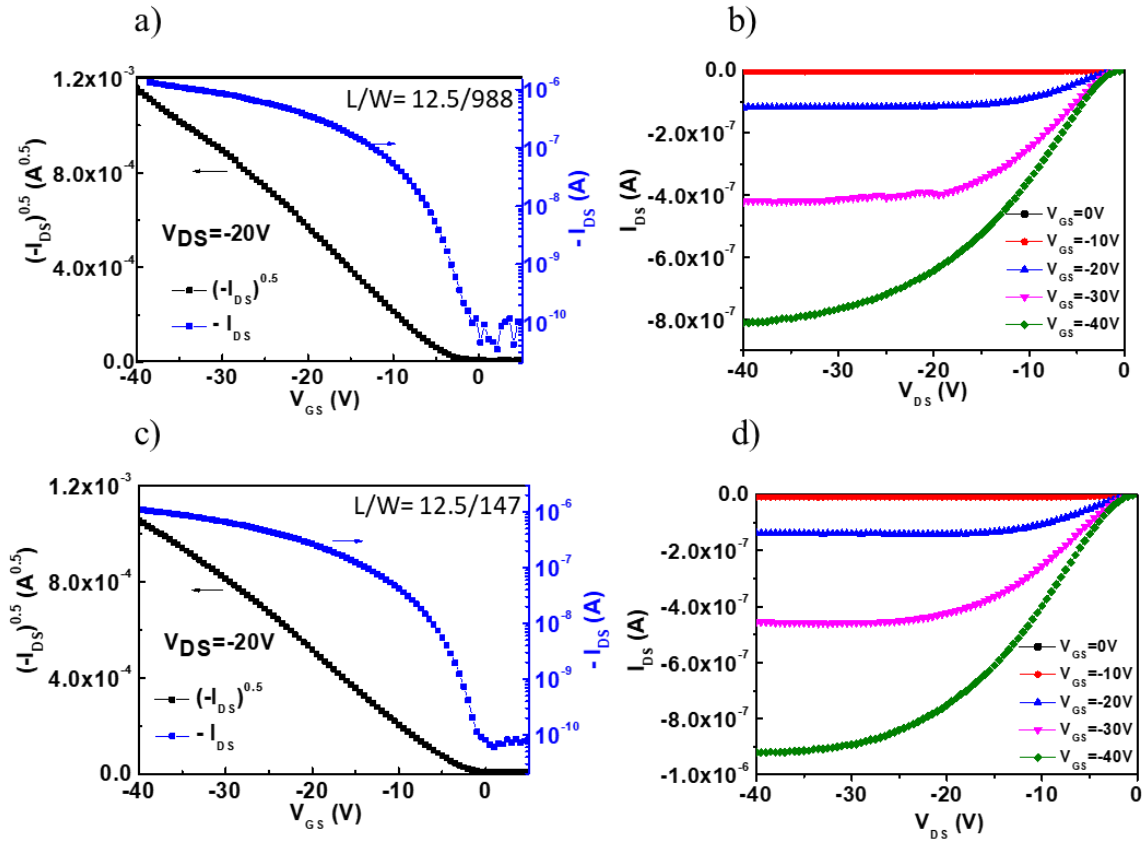


Figure 3.11 Transfer a) and output b) characteristics of BG/BC BTBT single crystal OFET with SiO_2 surface; Transfer c) and output d) characteristics of BG/BC BTBT single crystal OFET with OTS treated surface. (Insert: the channel width was determined from POM images, and we took care that the values chosen minimize the calculated mobility values.)

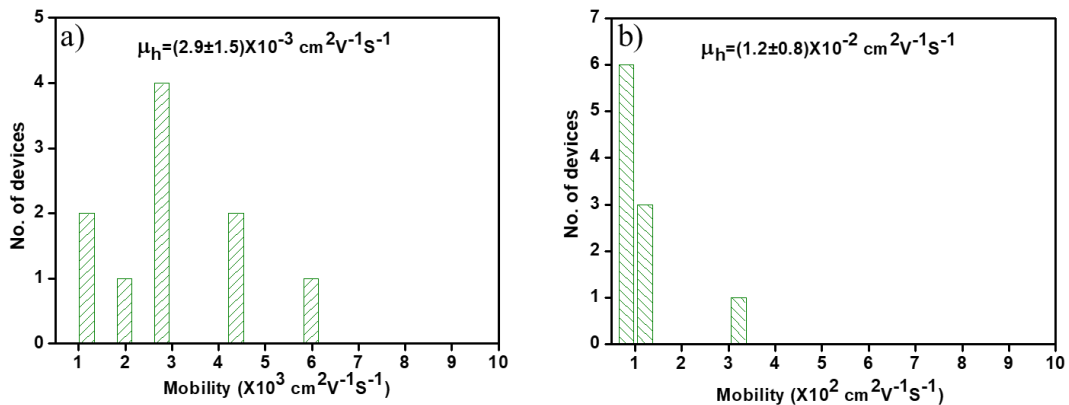


Figure 3.12 Histogram of hole mobility for 10 devices: a) BG/BC OFETs on SiO_2 surface b) BG/BC OFETs on OTS surface.

Table 3.2 Summary of the electrical characteristics of BG/BC BTBT SCOFETs.

Surface	μ_n (cm ² V ⁻¹ s ⁻¹) ^{a,b}	V_{th} (V) ^b	I_{ON}/I_{OFF} ($V_{DS}=-20V$) ^b
SiO ₂	(2.9±1.5)X10 ⁻³	-(3.1±2.5)	(4.1±2.5) X10 ³
OTS	(1.2±0.8) X10 ⁻²	-(5.7±1.8)	(2.7±2.6) X10 ⁴

^a From saturation regime. ^b Average values based on a ten of SCOFET devices.

We also investigated the devices performances of BTBT single-crystal transistors with OTS treated surfaces. The use of an OTS self-assembled monolayer (SAM) on the surface of SiO₂ gate dielectric generally enhances the overall performances in offering a lower surface energy¹⁸⁶, reducing the water adsorption¹⁸⁷ and decreasing the charge trap density at the interface between the crystal and the dielectric¹⁸⁸. **Figure 3.11c and d** show typical transfer and output characteristics of an OTS-modified BG/BC OFET. This surface treatment increased both the mobility and I_{on}/I_{off} by one order of magnitude leading to average values about $1.2 \times 10^{-2} \text{ cm}^2 \text{V}^{-1} \text{s}^{-1}$ and 2.7×10^4 , respectively. All the device parameters of OTS-modified SCOFETs are summarized in **Table 3.2**. Note that all the mobilities were also extracted from saturation regimes of a set of ten transistors (**Figure 3.12b**) and that a maximum value as high as $3.2 \times 10^{-2} \text{ cm}^2 \text{V}^{-1} \text{s}^{-1}$ was measured. Such FET values between 10^{-2} and $10^{-1} \text{ cm}^2 \text{V}^{-1} \text{s}^{-1}$ are in good agreement with BTBT calculated mobilities predicted from X-ray crystal structure and ranging from 10^{-3} to $10^{-1} \text{ cm}^2 \text{V}^{-1} \text{s}^{-1}$ ¹⁷⁸. They also confirm the good interfacial contact of single-crystals to the dielectric interface as suggested, for instance, by the POM and SEM observation (see **Figure 3.7**).

The air stability of the devices was also investigated. To this end, SCOFETs with OTS treated surfaces were removed from the glove box and electrical measurements were performed in ambient conditions. The devices measured in air present a significant degradation of their performances as illustrated in **Figure 3.13b**. The source-drain current flowing in the crystal is drastically reduced and the mobility is typically decreased by two or three orders of magnitude. The collapse of the mobility can be explained by the diffusion of water present in ambient air in the crystal lattice that is known to form trapping sites for injected charges¹⁸⁹. This assumption is also supported by the observation of the reversibility of the process since similar device performances can be restored by measuring again the transistors in glove box atmosphere after ambient air condition exposure (**Figure 3.13c**).

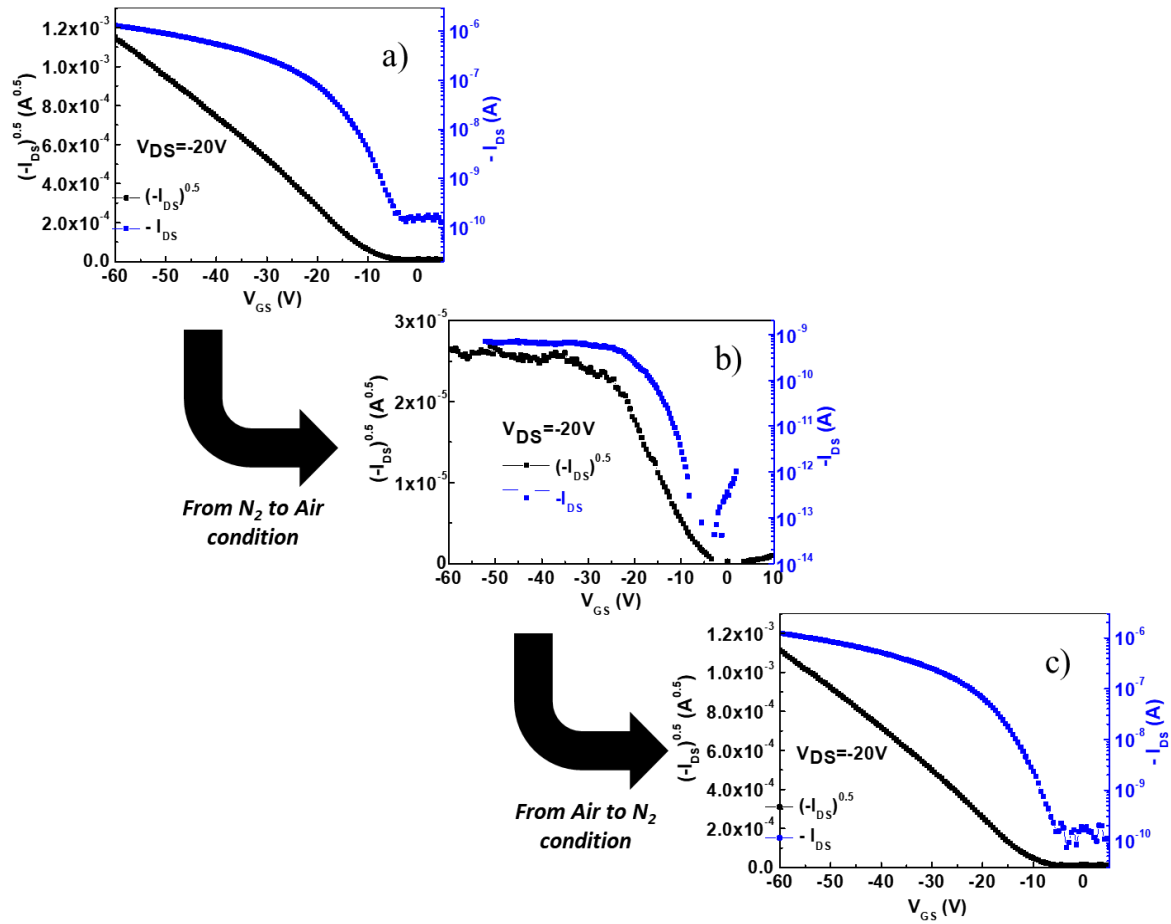


Figure 3.13 Typical transfer characteristics of BTBT single crystal OFET (OTS surface) under a) the Glove box N_2 atmosphere, b) the ambient air condition and c) the Glove box N_2 atmosphere after air exposure.

Ion gel top gate/bottom contact transistor configuration

SCOFETs with ion gels top gate (TG) configuration were mainly investigated to reduce voltage operation. Indeed, using electrolyte gating, the gate capacitance per unit area is no longer given by the ratio of the dielectric constant over the dielectric thickness but by the ratio of the dielectric constant divided by the ionic double layer thickness. Made of ions, the latter is typically 1 nm thick, leading to exceptionally high gate capacitance ($\mu\text{F}/\text{cm}^2$)^{189–191}. For that purpose, the BTBT single-crystals of BG/BC transistors previously fabricated with SiO_2 or OTS-modified gate dielectric were covered by an ion gel electrolyte (See Figure 3.10). Figure 3.14 shows typical transfer and output characteristics of the TG/BC transistors.

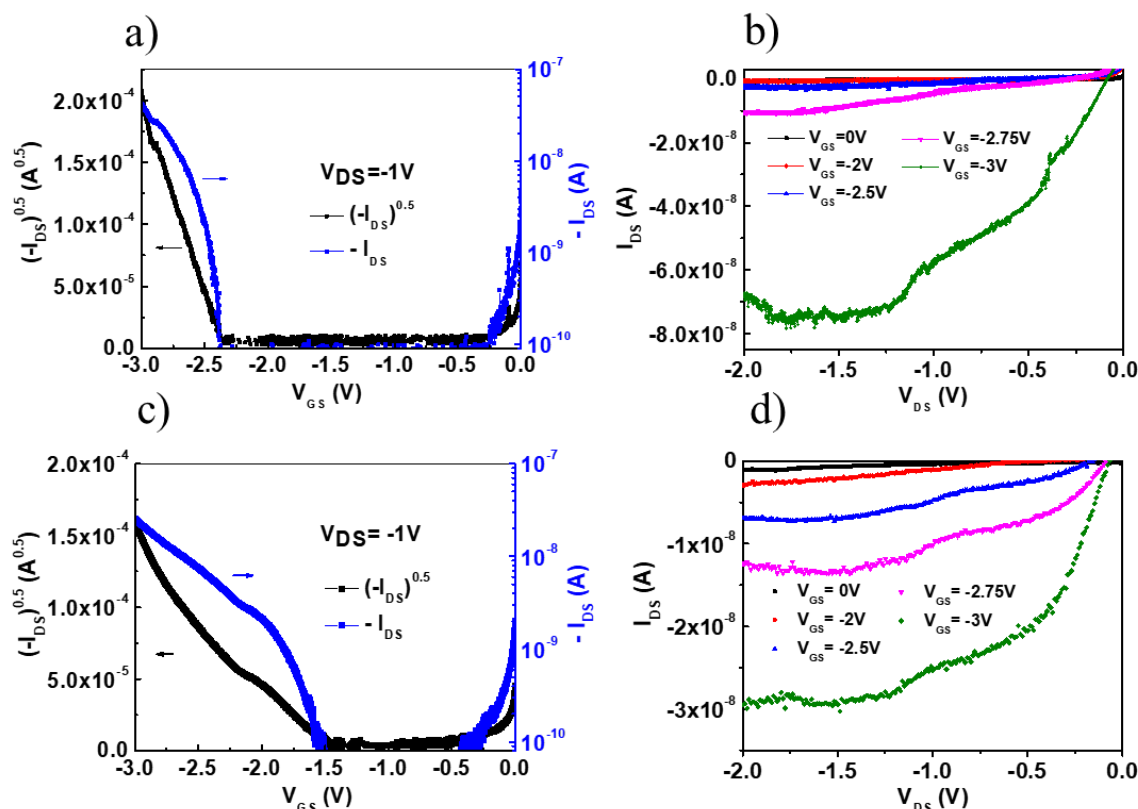


Figure 3.14 Transfer a) and output b) characteristics of BTBT TG single crystal OFET with SiO₂ surface. Transfer c) and output d) characteristics of BTBT TG single crystal OFET with OTS treated surface.

In spite of the larger gate capacitance, only a p-type conduction signal was measured. As observed in the output characteristics at five different gate voltage (V_{GS}) (Figure 3.14b and d), the devices show the gate modulation of the source-drain current (I_{DS}) in both the linear and saturation regimes. Thanks to the increase of the gate capacitance, the modulation of the drain source current over three order of magnitude (10^{-10} ~ 10^{-7} A) was achieved under 3 V of gate bias (Figure 3.14a and c), while 30 V was required using the conventional SiO₂ dielectric gating (Figure 3.11a and c). Note that we have been unable to accurately determine a field effect mobility in this ion gel top gate configuration since this will have required an accurate determination of the capacitance value and thus the introduction of a fourth electrode to uncouple the current and potential control.

3.5 Charge transport properties of C₈-BTBT-C₈ melt-processed thin films

The charge transport properties of the C₈-BTBT-C₈ melt-processed thin films were investigated with OFET configurations and compared with that of BTBT SCOFETs, in order to study the influences of

the side-chain substitutions.

3.5.1 Fabrication of C₈-BTBT-C₈ melt-processed thin film and transistors

The fabrication of C₈-BTBT-C₈ transistors by melt-processing was adapted from the one described for DAL1 derivative in § 2.4 of chapter 2. A very small amount of organic crystalline powder was placed at one edge of the empty space separating the two substrates and the sample was heated above the melting temperature (124 °C¹⁹² See Figure 3.15) of the compound under a nitrogen flow. Then, the organic semiconductor in the isotropic liquid phase filled the empty space by capillary action to form a thin liquid film between the two substrates. Second step consists in a rapid cooling down to room temperature, in order to obtain a fine polycrystalline texture. Third, the film was heated again carefully around melting temperature and POM was used to monitor the process in order to obtain almost the entire polycrystalline film being molten, except few isolated crystals surrounded by the isotropic liquid. The small residual crystals acted then as crystallization germs, and the sample was cooled down again slowly to liquid crystal state. After an annealing at 102 °C for 10mins, the germs crystallized to large domains. Then the film was cooled down to room temperature upon 0.5 °C min⁻¹. In the last step, the weakly adhering OTS-treated cover glass was removed.

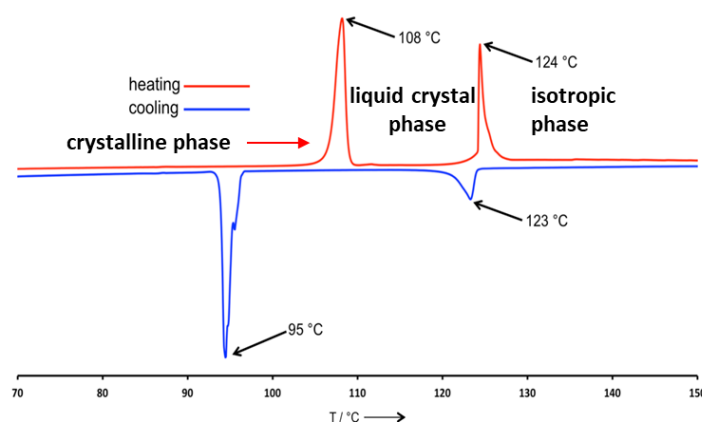


Figure 3.15 DSC for C₈-BTBT-C₈ powder¹⁹².

Concerning the fabrication of C₈-BTBT-C₈ OFETs, the gold top contacts were evaporated on the top of the film through a shadow mask. Compared to DAL1 OFET, the differences were that channel width and length here were 1mm and 30 μm respectively since another kind of shadow mask was used. Figure 3.16 shows the POM images of the shadow mask which was located carefully on the best active areas of the C₈-BTBT-C₈ melt-processed film. Like DAL1 OFET based on melt-processed film, a BGTC configuration was adopted to minimize the effects of the cracks on the electrical properties of the film.

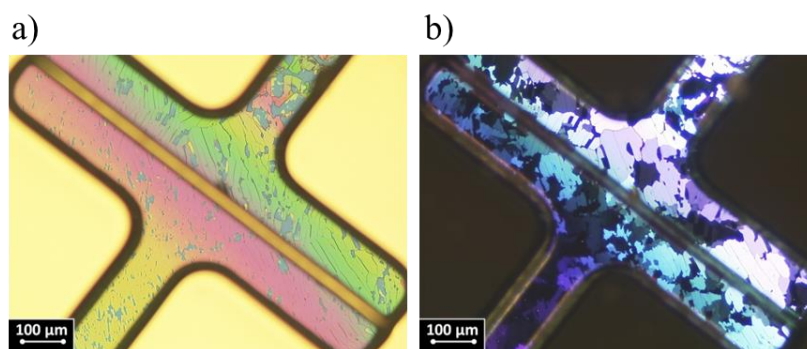


Figure 3.16 POM images of a shadow mask located on the C_8 -BTBT- C_8 single crystal surface a) under natural light and b) polarized light.

3.5.2 Charge carrier mobility of C_8 -BTBT- C_8 melt-processed thin film

The BG/TC OFET devices based on C_8 -BTBT- C_8 melt-processed thin film with gold electrodes and SiO_2 as gate dielectric were characterized in glove box under N_2 environment. Considering the energy of the HOMO of C_8 -BTBT- C_8 (5.4eV)¹⁹³, gold contacts are also well-suited for hole injection and charge transport investigation. Figure 3.17 a and b show the typical transfer and output curves of the melt-processed devices.

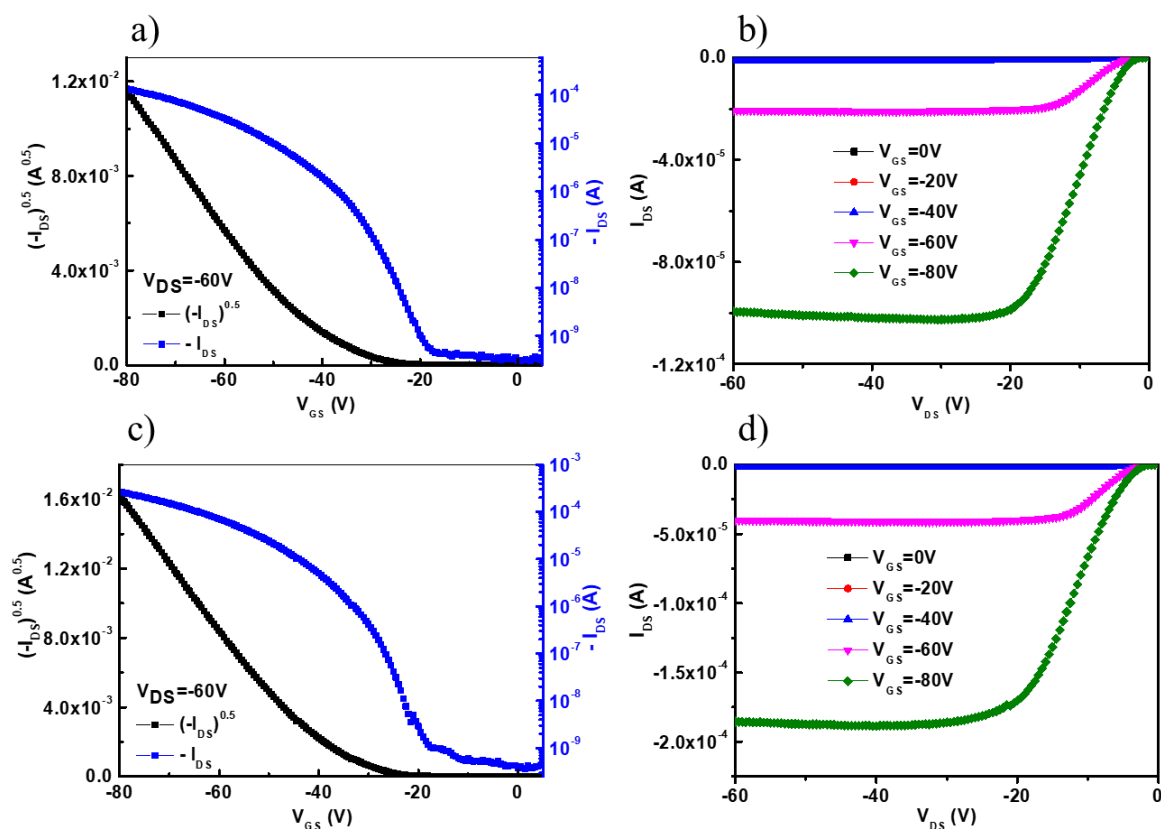


Figure 3.17 Transfer and output curves of as-prepared (a and b) and annealed (c and d, at $110^\circ C$ for 20 mins) C_8 -BTBT- C_8 OFETs.

As expected, C₈-BTBT-C₈ OFETs present a p-channel conduction, and a hole mobility about 0.6 cm²V⁻¹s⁻¹ was extracted from the saturation regime. The effect of the thermal treatment of the film on the hole mobility was investigated by annealing the same transistor at 110 °C for 20 mins, around the phase transition temperature from the crystalline phase to the liquid crystal phase¹⁹². After annealing, the hole mobility value is enhanced to 1.1 cm²V⁻¹s⁻¹ and the transfer and output curves of the annealed device are shown in **Figure 3.17c and d**. The increase of the hole mobility could be attributed to an increasing of the crystallite size and an improvement of the film morphology as already observed in chapter 2 for DAL1 derivative. Unfortunately, due to the limited time of my PhD works, no further investigations of the structure of C₈-BTBT-C₈ melt-processed thin films were performed and could be presented here. It is important to mention that, naturally, the hole mobilities of 0.032 cm²V⁻¹s⁻¹ for BTBT single crystals and 1.1 cm²V⁻¹s⁻¹ for C₈-BTBT-C₈ melt-processed films cannot be directly compared. Indeed, the device architectures are very different (BG/BC vs BG/TC, interdigitated vs simple source-drain electrodes...), and the film morphology is also very different (single crystals vs single-crystalline polydomain thin films). However, the trend of the mobility values observed for BTBT and C₈-BTBT-C₈ is in good agreement with the results reported in the literatures and highlight the essential role of the BTBT substitution in charge transport properties. Long side-chains enable C₈-BTBT-C₈ with well-ordered herringbone packing of BTBT cores and strong/balanced intermolecular charge-transfer¹⁷⁸. In addition, the mobility values about 0.6-1.1 cm²V⁻¹s⁻¹ obtained with C₈-BTBT-C₈ melt-processed thin films are comparable with the values reported by Takimiya's group¹⁹⁴ (0.30~0.74 cm²V⁻¹s⁻¹ with BG/TC OFETs based on 50nm-thick C₈-BTBT-C₈ thin film prepared by vacuum thermal evaporation on SiO₂ substrate). These results confirm once again that the solvent-free vacuum-free melt-processing method is an efficient method to fabricate high performance organic electronic devices.

3.6 Conclusion

In summary, in this chapter, we investigated for the first time the charge transport properties in field-effect transistor configuration of a simple [1]Benzothieno[3,2-b][1]-benzothiophene (BTBT) aromatic core. To this end, we prepared thin single crystals of unsubstituted BTBTs by physical vapor transport deposition technique. The structure and morphology analysis of these platelet-like crystals demonstrated that the BTBT aromatic cores are oriented perpendicular to the larger facets of the crystal and that they are organized in a layered herringbone packing in the plane. The charge transport properties of BTBT single-crystals were investigated by BG/BC OFET on both SiO₂ and OTS-treated gate dielectric, and a maximum hole mobility value of 0.032 cm²V⁻¹s⁻¹ was measured, in good agreement with calculated mobilities predicted from the BTBT crystal structure and reported in the literature. In addition, TG OFETs based on BTBT single crystals were also fabricated via using high-capacitance ion gel dielectrics,

enabling transistor operation at low gate voltages. On the other hand, the charge transport properties of C₈-BTBT-C₈ melt-processed thin films were also investigated by transistor, and a high mobility about 1.1 cm²V⁻¹s⁻¹ was obtained, highlighting the beneficial effect of the alkyl functionalization of the BTBT core on the charge transport properties. To date, this study presents experimentally the first investigation of the FET mobility of the unsubstituted BTBT aromatic core, which agrees well with the theoretical values.

3.7 Experimental section

3.7.1 Materials

All materials and solvents were purchased from Sigma Aldrich and were used without further purification. BTBT was synthesized by Dr. Xiaolu Su at IPCM in a one-step reaction from the commercially available 2-chlorobenzaldehyde according to the procedure described in the literature ¹⁹⁵. Yield: 35%. Mp=117-119 °C. ¹H NMR (CDCl₃, 200 MHz): δH = 7.95-7.87 ppm (4H, m, H_{arom}), 7.51-7.37 ppm (4H, m, H_{arom}). C₈-BTBT-C₈ was provided by Dr. Teng Teng at IPCM.

3.7.2 DSC

DSC was performed using TA instruments Q2000 under N₂ flow in aluminum hermetic pans. The DSC traces of BTBT compound on heating and cooling were recorded with a rate of 2.5 °C/min, 5 °C/min, 10 °C/min and 20 °C/min respectively.

3.7.3 XRD

A single crystal of BTBT was selected, mounted onto a cryoloop, and transferred under a cold nitrogen gas stream. Intensity data were collected with a BRUKER Kappa-APEXII diffractometer with micro-focused Cu-Kα radiation at 200 °K. APEX 3 suite and SAINT program (BRUKER) were used to carry out data collection, unit-cell parameters refinement, integration and data reduction. SADABS (BRUKER) was used for scaling and multi-scan absorption corrections. Despite large diffraction peaks in some direction due to the shape of crystal, in the Olex2 suite ¹⁹⁶, the structure were solved with SHELXT-14 ¹⁹⁷ program and refined by full-matrix least-squares methods using SHELXL-14 ¹⁹⁸. CCDC 1956856 contain the crystallographic data for this chapter. The data can be obtained free of charge from The Cambridge Crystallographic Data Centre via www.ccdc.cam.ac.uk/structures.

3.7.4 POM, SEM and AFM

POM was carried out using a Leica microscope equipped with a Linkan THMS 350 hot plate connected to a Linkam 93 temperature controller. The BG/BC SCOFET devices were observed with Hitachi SEM (SU8000). AFM experiments were carried out to examine the surface morphologies of BTBT single crystals. These measurements were performed in the tapping mode, with Bruker 3100 stand alone. Tips were in silicon, associated with a resonance around 300 kHz.

3.7.5 Characterization of OFET devices

For BTBT devices, current-voltage measurements of the BG/BC OFETs were collected in the glove box (N_2 environment) using two Keithley 2400 source units and a MS Tech probe station (MST 8000). Transfer characteristics of BG devices were acquired at $V_{DS} = -20$ V while V_{GS} was stepped from 5 V to -40 V in 0.5 V increments. Output characteristics of BG devices were taken at $V_{GS} = 0$ V to -40V in 10 V increments and V_{DS} was stepped from 0 V to -40 V in 0.5 V increments. Transfer characteristics of the electrolyte gated devices were acquired at $V_{DS} = -1$ V while V_{GS} was stepped from 0 V to -3 V in 1mV increments. This low gate bias range is chosen to avoid any electrochemical reaction within the electrolyte, while the slow sweep rate is required to let ion move within the viscous gel matrix. Hole field-effect mobilities were calculated from the transfer characteristics in the saturation regime, using the standard method described in chapter 1 (§1.3.1.1). On/Off current ratio (I_{on}/I_{off}) was determined from the transfer curves (I_{DS} at $V_{GS}=0V$ (I_{off}) and $V_{GS}=-40V$ (I_{on}) for BG devices; and I_{DS} at $V_{GS}=0V$ (I_{off}) and $V_{GS}=-3V$ (I_{on}) for TG devices).

Concerning the C_8 -BTBT- C_8 devices, OFETs characterization was carried out in the glovebox and with the same equipment with that for BTBT OFETs. Transfer characteristics of BG/TC devices were acquired at $V_{DS} = -60$ V while V_{GS} was stepped from 5 V to -80 V in 0.5 V increments. Output characteristics of BG devices were taken at $V_{GS} = 0$ V to -80V in 20 V increments and V_{DS} was stepped from 0 V to -60 V in 0.5 V increments.

Chapter 4 Investigation of photo- and electro-luminescence properties of the fluorescent materials C10-PBT

Combining supramolecular self-assembly and intrinsic light-emitting abilities, luminescent liquid crystals have gained a great deal of attention and considerable interest from both scientific and industrial organizations^{199,200}. However, the molecular design of highly efficient luminescent materials in ordered phases is still a big challenge. Indeed, when luminescent molecules aggregate into crystalline or liquid crystalline phases, the ordered stacking and strong intermolecular interactions of π - π bonds often induce an aggregation-caused quenching problem^{134,135}, which severely limits the practical applications of these materials for optoelectronic devices such as light emitting diodes. Fortunately, some materials presenting an aggregation-induced emission (AIE) can be designed to obtain ordered materials with unique solid-state luminescence properties^{201,202}. Briefly, scientists introduced active fluorophores/chromophores as mesogenic cores and decorated them with peripheral flexible long chains to synthesize highly luminescent discotic or calamitic LC molecules^{203–206}, whose light emissions could be dramatically enhanced or maintained by molecular aggregation and self-organization in their crystalline or liquid crystalline phases.

Thanks to this outstanding solid-state luminescence advantage, such materials have showed potential applications as one-dimensional semiconducting materials²⁰⁷ and organic light emitting diodes (OLEDs)²⁰⁸. Nevertheless, according to the literature studies, to date, all the known highly luminescent mesogenic molecules were based on very limited fluorophores including cyanostilbene²⁰³, tolane²⁰⁹, tetraphenylethene²¹⁰ and metallomesogen²⁰⁶, which greatly impedes the wide applications of these materials. In this context, the development of novel ordered materials presenting highly efficient luminescent properties in their crystalline and liquid crystalline condensed phases is still highly demanded and leaves us with plenty of opportunities for new molecular architectures.

In this chapter, in collaboration with Dr. Teng Teng at IPCM, we recently designed a new liquid crystalline fluorescent material C10-PBT (See Figure 4.1) presenting a donor-acceptor-donor (D-A-D) structure with O-alkylphenyl groups as donor units and benzothiadiazole unit as acceptor core. The benzothiadiazole is one of the most widely used moiety in photoluminescent compounds²¹¹ and in organic optoelectronic applications. Its derivatives have several desired characteristics such as electron withdrawing ability and effective fluorescent properties²¹². The liquid crystal properties of this material were already emphasized by Dr. Teng Teng. However, no investigation of its solid-state photoluminescence (PL) and electroluminescence (EL) properties have been performed yet. Therefore, in what follows, the thermal properties of C10-PBT are briefly described by POM and DSC; the film morphology of the C10-PBT melt-processed film is analyzed by AFM. Moreover, its PL properties in solid-state film and EL properties in OLED devices are investigated in details.

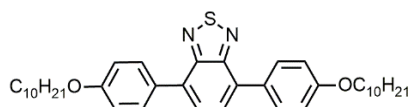


Figure 4.1 Molecular structure of C10-PBT (collaboration with Dr. Teng Teng at IPCM).

4.1 Thermal properties of C10-PBT

The DSC traces (Figure 4.2a) of C10-PBT on heating and cooling recorded at a rate of 5 °C/min present several transitions. On heating, we can observe two endothermic peaks: at 94 °C ($\Delta H = 104.7$ J/g) and 135 °C ($\Delta H = 9.6$ J/g) corresponding to the transition from the crystalline phase to a liquid crystal phase and from the liquid crystal phase to the isotropic phase of the material, respectively. On cooling, from the isotropic state, the first transition at 140 °C associated to a small enthalpy ($\Delta H = 11.3$ J/g) is consistent with the appearance of the liquid crystal phase, as proved by the typical fan-shape focal conic texture observed by POM and characteristic of lamellar (smectic) mesophase (Figure 4.2b). Upon further cooling, the second transition at 73 °C associated with a higher enthalpy ($\Delta H = 65.8$ J/g) is attributed to the transition to the crystalline phase. Interestingly, the POM textures at 70 °C and 75 °C upon heating is different (See Figure 4.2 c and d), which is consistent with the exothermic peak at 61 °C ($\Delta H = 34.9$ J/g) during heating (See Figure 4.2a). The exothermic peak is attributed to a possible reorganization of the molecular packing, resulting in transition from crystal phase 1 (Cr1) to crystal phase 2 (Cr2).

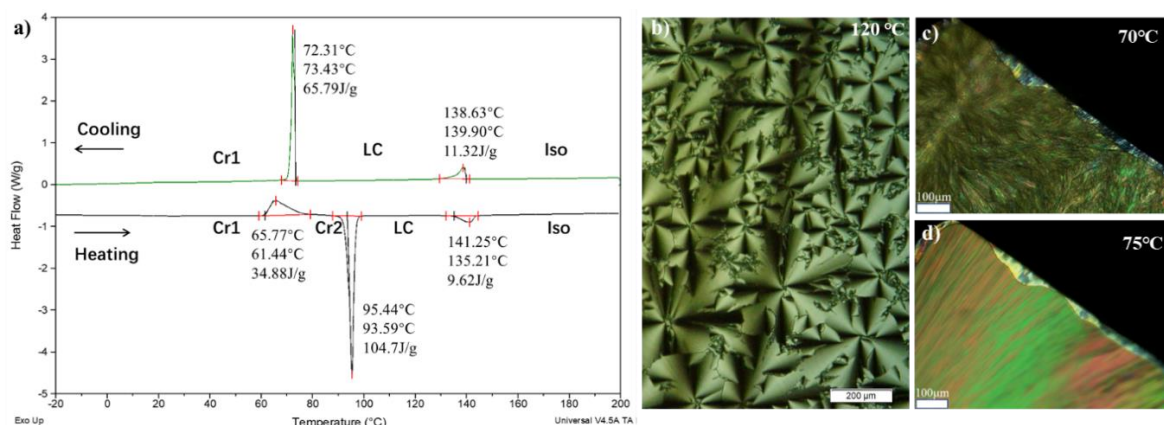


Figure 4.2 a) DSC curve of C10-PBT at 5°C/min on heating and cooling (3rd cycle); Optical texture observed by POM for C10-PBT thin film between glass and cover glass b) at 120°C: typical fan-shape focal conic texture of smectic mesophase; c) at 70°C and d) at 75°C upon heating.

4.2 Film morphology analysis

The morphology of C10-PBT thin film prepared by melt-processing between OTS treated substrates was studied by tapping-mode AFM. A typical topography image observed on the top of the film after removing the top substrate is given in Figure 4.3a and shows a clear nanostructured film with terraces. The heights of the terraces extracted from topographic profiles are 3.7-3.8 nm (See Figure 4.3b) or multiples of this value which is consistent with the length of a C10-PBT molecule (~3.7nm obtained by molecular modeling) and the preferential vertical orientation of the molecules within the film.

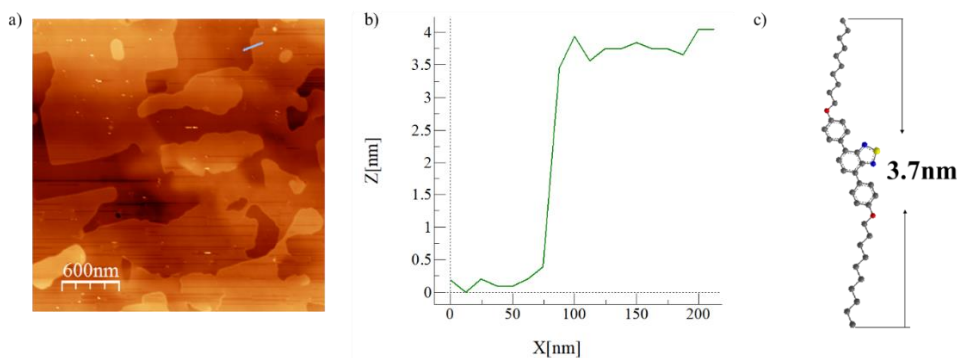


Figure 4.3 a) AFM topography image of C10-PBT melt-processed film; b) Terrace step profile along the blue line in image a); c) Representation of the chemical structure of C10-PBT with a molecular length of about 3.7nm.

4.3 Photophysical properties of C10-PBT in solution

The absorption and emission properties in solution were studied with low concentration solutions (ca. 10^{-5} M) and the measurements were performed at room temperature. In this condition, these molecules can be considered as adequately isolated, i.e. the aggregation and the intermolecular interactions can be ignored.

The absorption and emission spectra of C10-PBT in chloroform are shown in Figure 4.4. The C10-PBT absorption spectrum shows two absorption bands: a π - π^* transition in the 230-320 nm range and an intramolecular charge transfer band in the 330-500 nm range consistent with the D-A-D structure of the derivative. This compound is strongly fluorescent in chloroform solution with a maximum PL emission wavelength around 557 nm (in the range of yellow-green light wavelength) and a very high photoluminescence quantum yield (PLQY) around 89%.

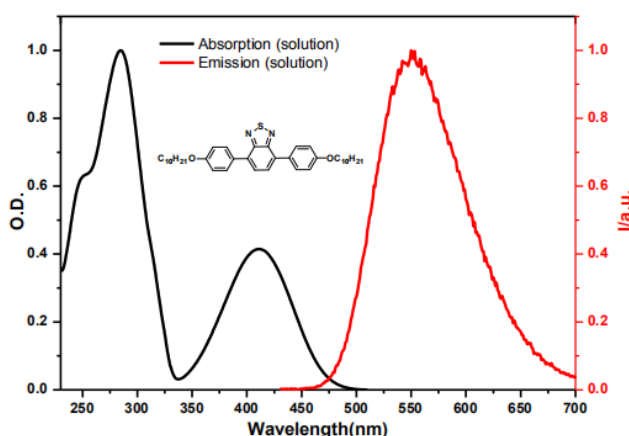


Figure 4.4 UV/Vis absorption and emission spectra of C10-PBT in $CHCl_3$ solution.

We also investigated the absorption and emission properties of C10-PBT in solution with different polarity solvents (Figure 4.5 and table 4.1). All solutions were also prepared with low concentrations

(10^{-5} M) in order to limit the potential aggregation effects. As the polarity of the solvent increases, the absorption spectra of C10-PBT show slight changes, with a maximum moving from 409 to 411 nm for the intramolecular charge transfer band (330-500 nm range) for instance. This result indicates a weak dipole moment of the molecule in the ground state. However, we can observe a significant solvatochromic shift of the fluorescence spectrum maxima from 523 nm in cyclohexane to 566 nm in acetonitrile. This red shift of emission spectra with the solvent polarity is classical for D-A systems and indicates the high polarity of the excited state (strong dipole moment) in comparison with its ground state^{213,214}.

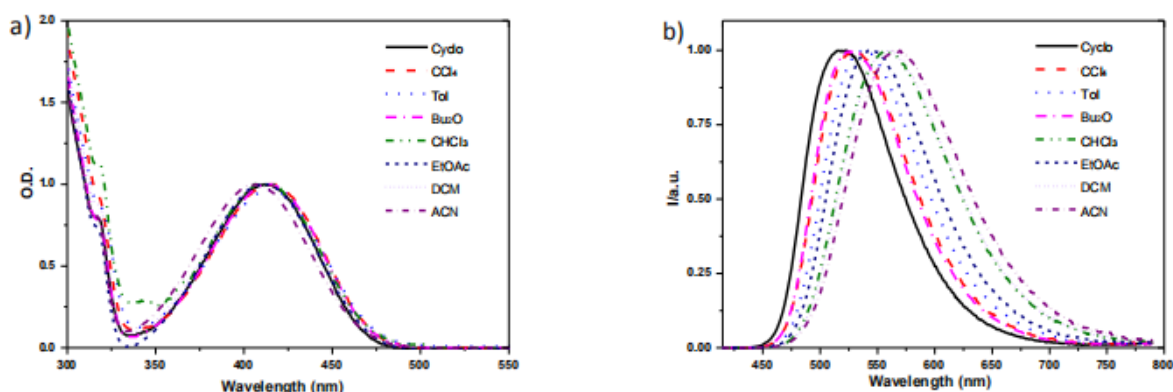


Figure 4.5 a) Absorption spectra of C10-PBT measured at room temperature in different solvents; b) Fluorescence spectra of C10-PBT at room temperature measured in different solvents (Cyclo: cyclohexane, CCl₄: tetrachloromethane, Tol: toluene, Bu₂O: dibutylether, CHCl₃: chloroform, EtOAc: ethyl acetate, DCM: dichloromethane, ACN: acetonitrile)

Table 4.1 Photophysical properties of C10-PBT in different solvents.

Solvent	$\lambda_{\text{abs}}^{\text{max}}$ (nm)	$\lambda_{\text{PL}}^{\text{max}}$ (nm)	Φ_f	τ_f (ns)
Cyclo	409	523	1	8.64
CCl ₄	411.5	530		
Tol	413.5	537	0.83	8.57
Bu ₂ O	412.5	531	0.88	9.5
CHCl ₃	415	557	0.89	11.48
EtOAc	413.5	544		
DCM	414.5	564	0.77	11.36
ACN	411.5	566		

The compound presents high PLQY in most of solvents with a maximum of 100% in very apolar solvent such as cyclohexane. The maximum absorption wavelength, $\lambda_{\text{abs}}^{\text{max}}$, maximum emission wavelength, $\lambda_{\text{PL}}^{\text{max}}$, photoluminescence quantum yield, Φ_f , and fluorescence lifetime, τ_f , in different solvents are given in Table 4.1. Although PLQYs are high in most of solvents, we can observe their slight decrease in very polar solvent (77% in DCM for instance). This phenomenon is generally explained by (i) the stabilization of the intramolecular charge transfer (ICT) state leading to a smaller energy gap between the excited and ground states and the deactivation of the excited state mainly via non-radiative pathways,

and/or (ii) the formation of a charge separated state which is non-emissive since the delocalized π -conjugated system is destroyed (the charges are localized) ²¹⁵.

4.4 Electronic properties of C10-PBT

The electronic properties of C10-PBT were investigated by photoelectron spectroscopy (Figure 4.6a). This measurement was performed with fresh spin-coated thin film samples and a HOMO level of -6.1eV was extracted (Reference of HOMO and LUMO level is the vacuum level (0 eV)). The optical energy gap E_g^{opt} , expressed in electronvolts, can be evaluated with the onset of the absorption spectrum in chloroform (See Figure 4.6b) according to the equation below:

$$E_g^{opt} = 1240/\lambda_{onset} \approx E_{LUMO} - E_{HOMO}$$

with λ_{onset} the wavelength value of the absorption spectrum onset in nm. Based on this equation and for an absorption onset of 473nm, E_g^{opt} is calculated around 2.62 eV. In neglecting the exciton binding energy ²¹⁶, E_g^{opt} can be also considered as the LUMO-HOMO energy gap. As a result, the LUMO level of C10-PBT was estimated at about -3.5eV.

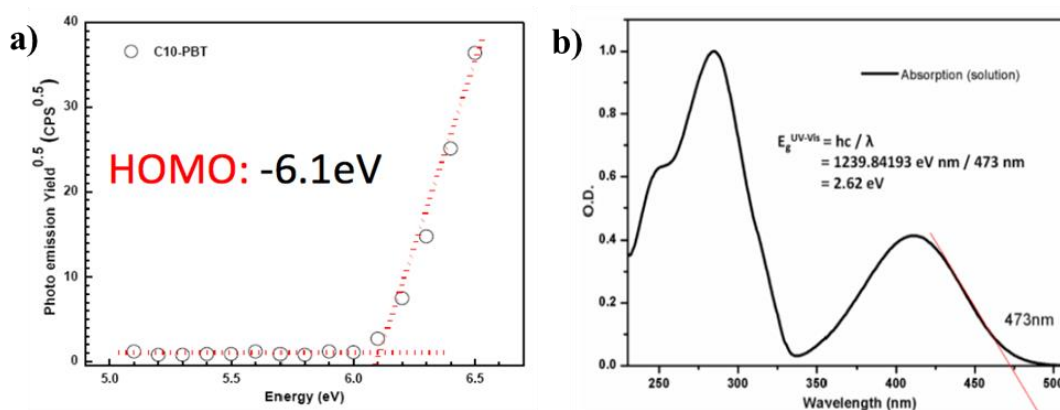


Figure 4.6 a) Photoelectron spectroscopy of a spin-coated C10-PBT thin film; b) Absorption spectrum of C10-PBT in chloroform and calculation of its optical band gap.

4.5 Photophysical properties of C10-PBT in solid-state film

In what follows, photophysical properties of the C10-PBT neat film and the CBP/C10-PBT blend films are investigated. The influence of guest concentration on the PL properties of CBP/C10-PBT blend films is also investigated.

4.5.1 Neat film properties

The absorption and emission properties of C10-PBT in solid-state were investigated based on spin-coated neat films with a thickness around one hundred nanometer. The absorption spectrum of as-spun C10-PBT film presents maximum absorption wavelengths at 266nm, 326nm and 389nm (See green curve in Figure 4.7a) which are slightly blue-shifted relative to the solution spectra (See Table 4.1). For the emission properties, the PL spectrum of the as-spun film exhibits also a blue shifted emission with a maxima at 542 nm, while the solution displays an emission with a maximum peak at 557 nm (chloroform, Figure 4.5b). The results of absorption and PL properties are summarized in Table 4.2.

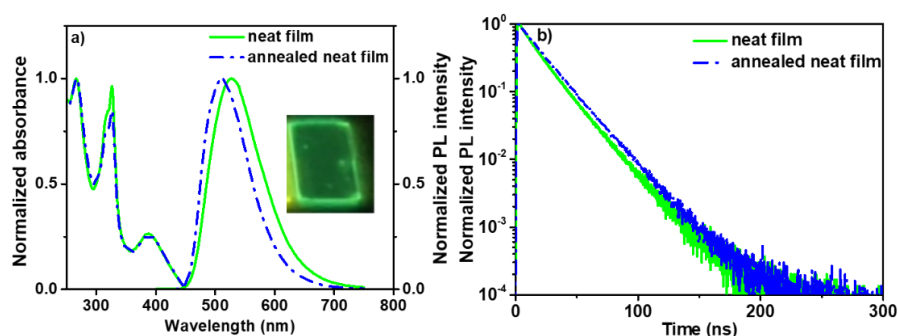


Figure 4.7 a) Absorption and emission spectra (ex. 400nm). The Insert in a) is picture of an as-spun C10-PBT film on glass substrate under UV lamp. b) PL lifetimes (recorded at 540nm) of spin-coated C10-PBT neat films (before and after annealing at 80°C for 15 mins).

Table 4.2 PL properties of the spin-coated C10-PBT neat film before and after annealing

Film	$\lambda_{\text{abs}}^{\text{max}}$ (nm)	$\lambda_{\text{PL}}^{\text{max}}$ (nm)	Φ_f	τ_f (ns)
Before annealing	266,326,389	542	0.69	16.4
After annealing	264,325,385	511	0.80	20

We also investigated the absorption and emission properties of C10-PBT neat films after annealing at 80°C. Typical absorption and emission spectra of a C10-PBT thin film after annealing are shown in Figure 4.7a (blue curves). Upon annealing at 80°C, the absorption spectra show slight changes. In terms of the emission spectra, upon annealing, the initial emission at 542 nm is blue shifted toward 511 nm. In addition, a significant increase of PLQY from 69% to 80% is observed (See Table 4.2). The change of emission spectrum after annealing at 80 °C, and the increase of PLQY suggest an important modification of the molecular packing after annealing which is consistent with the Cr1-Cr2 phase transition observed by DSC on heating around 61°C (§ 4.1). (In PhD thesis of Dr. Teng Teng, XRD results proved that after an annealing at 80 °C and cooling to room temperature, the Cr2 phase will stay. In contrast, a heating until the Smectic A phase (94 °C ~ 136 °C) and cooling to room temperature will lead to the re-obtaining of Cr1 phase.) Note that this molecular reorganization in C10-PBT neat film after annealing is also corroborated by the different PL lifetimes (16.4 ns vs 20 ns) observed before and

after annealing (See Figure 4.7b and Table 4.2) and by the significant change of the film appearance after annealing (See Figure 4.8).

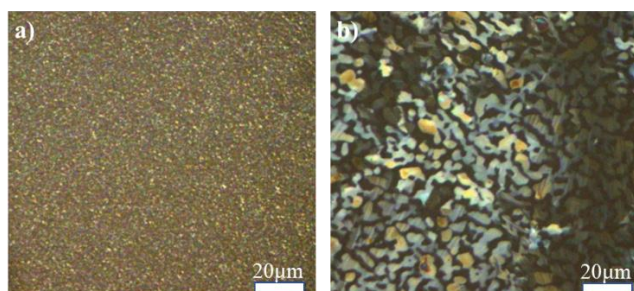


Figure 4.8 POM images of spin-coated neat films under crossed polarized light a) before annealing and b) after annealing at 80 °C for 15 mins.

In conclusion, it is worth to mention that the high PLQYs measured in neat films indicate that this material is not so sensitive to concentration quenching and it is potentially promising for light emitting device fabrication.

4.5.2 CBP/C10-PBT host-guest system properties

In addition to single emitting material, researchers often use a matrix (host) to disperse the emitting dopant (guest), which could reduce the degree of exciton quenching usually observed in neat film of either host or guest²¹⁷. Using this approach, one can take advantage of the large PLQY of the dispersed dopant molecules and achieve high quantum yields in composite materials²¹⁸. This could result in efficient Förster resonant energy transfer (FRET) from host to guest molecules²¹⁹. During the energy transfer, the exciton created in the host molecules either after absorption of a higher energy photon in the case of PL, or after recombination of an electron and a hole in the case of EL, delivers the excited-state energy to guest molecules and improve PL efficiency and stability²²⁰.

In the case of our emitter C10-PBT, we chose the 4,4'-Bis(N-carbazolyl)-1,1'-biphenyl (CBP) as host which is one of the most widely-used host materials for green, yellow and red emitters. Indeed, this host presents (i) a suitable HOMO/LUMO energy levels in confining the energy levels of the C10-PBT guest (Figure 4.9a) and avoiding a possible non-radiative deactivation by excimer formation²²¹, (ii) a perfect overlap between the emission spectrum of CBP host and the absorption spectrum of C10-PBT guest, leading to a possible efficient FRET (Figure 4.9b).

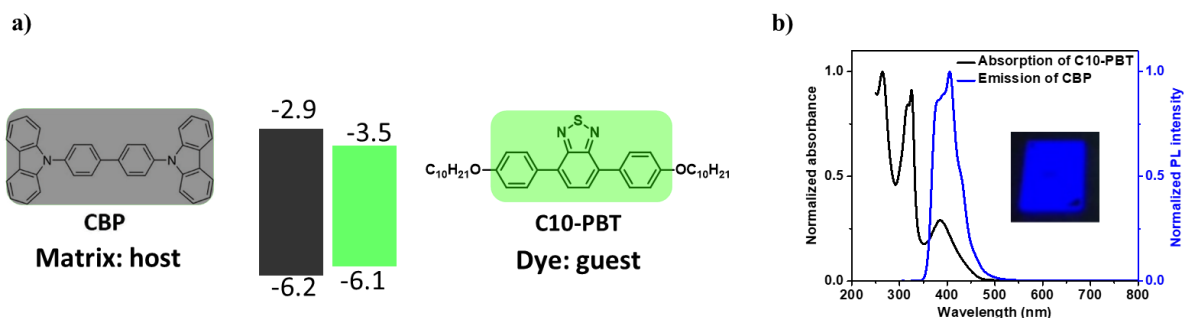


Figure 4.9 a) Schematic representations of energy levels of CBP host ²²² and C10-PBT guest (see § 4.4). b) Representation of the good overlap of the CBP emission spectrum and C10-PBT absorption spectrum favorable to an efficient Forster resonant energy transfer (insert: picture of CBP spin-coated film on quartz substrate under UV lamp)

Since the energy transfer from the host to the guest is dramatically affected by the guest concentration, we investigated the guest concentration dependence of the photophysical properties of the CBP/C10-PBT blend films with a guest concentration ranging from 2 to 70 wt%. As shown in [Figure 4.10a, b and Table 4.3](#), the absorption spectra of the blend films are mainly dominated by the host material (CBP: 297, 330, 344nm), with a small contribution from the guest (C10-PBT: 266, 326, 389nm). The optical intensity decreases as the guest concentration increases.

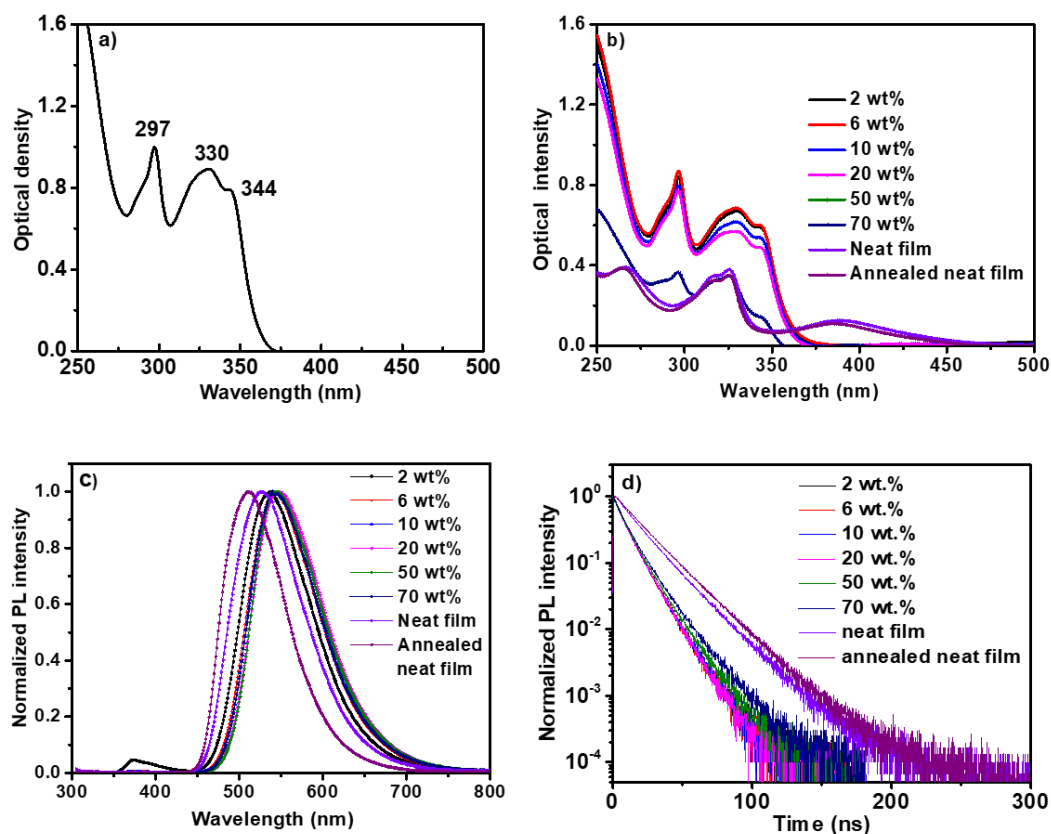


Figure 4.10 a) Absorption spectrum of CBP spin-coated film; b) Absorption spectra, c) PL spectra (excitation at 295nm) and d) Fluorescence lifetime of spin-coated CBP/C10-PBT blend films and C10-PBT neat films.

Table 4.3 Photophysical data measured with spin-coated CBP/C10-PBT blend and C10-PBT neat film.

C10-PBT concentration	$\lambda_{\text{abs}}^{\text{max}}$ (nm)	$\lambda_{\text{PL}}^{\text{max}}$ (nm)	Φ_{r}	τ_{r} (ns)
CBP neat film	297,330,344	405	0.61	/
2 wt%	297,330,342	537	0.91	10.8
6 wt%	296,330,343	543	0.87	11.1
10 wt%	297,329,343	544	0.88	11
20 wt%	296,329,343	548	0.86	11.4
50 wt%	297,325,344	545	0.8	12.3
70 wt%	296,325,394	540	0.78	12.3
Neat film	266,326,389	542	0.69	16.4
Annealed neat film	264,325,385	511	0.8	20

When excited at 295 nm (close to the absorption peak of CBP), the PL emissions of the blend films (See Figure 4.10c and Table 4.3) present almost exclusively the emission spectra of the C10-PBT guest, and only a residual emission of CBP host around 405nm is detected for the lowest concentration of 2 wt%. These results indicate that fast and efficient energy transfer from host to guest is the dominant process²¹⁸ in the PL of CBP/C10-PBT composites, confirming the right choice of CBP as host.

As shown in Table 4.3 and Figure 4.11, the PLQYs of the CBP/C10-PBT blend films are very high with values around 90% for doping concentrations of 2, 6 and 10 wt%. Interestingly, for higher guest concentrations (20, 50 and 70 wt%), the PLQYs remain also quite high with values ranging from 86-78%, attesting that C10-PBT is not very sensitive to concentration quenching and that Dexter energy transfer between aggregated C10-PBT is not very effective. These results are consistent with the high PLQY (69%) already observed in neat film. They also confirm that C10-PBT emitter is a promising dye for potential EL devices such as OLEDs and OLETs^{223,224}.

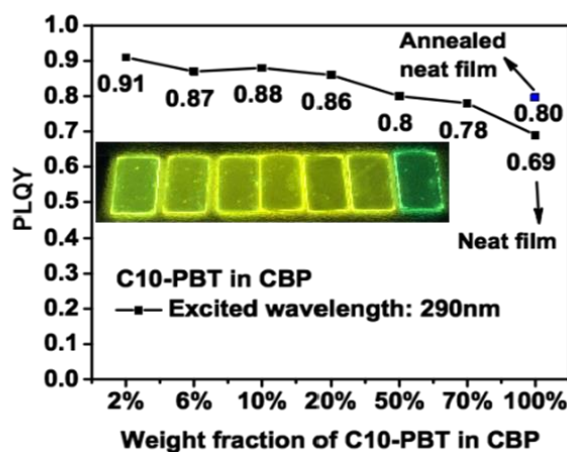


Figure 4.11 PLQYs of spin-coated CBP/C10-PBT blends and C10-PBT neat films. (insert: picture of spin-coated films on quartz substrates under UV lamp).

4.6 Electroluminescence properties of C10-PBT

Herein, the OLEDs based on both the C10-PBT neat film and the CBP/C10-PBT blend films are fabricated. Their EL properties are compared and discussed. The influence of guest concentration on the EL properties of CBP/C10-PBT blend films is also investigated.

Structure of the OLED devices

As shown in **Figure 4.12a**, the OLEDs device structure of devices based on the solution deposition of the emitting layer was ITO/PEDOT:PSS/emitting layer (EML)/PPT/TPBi/LiF/Al^{225–227}. Molecular structures of PEDOT:PSS, PPT and TPBi are displayed in **Figure 4.12b**. During the OLEDs fabrication, the PEDOT:PSS and emitting layers were spin-coated and the other layers were vacuum thermal evaporated. In this structure, ITO was used as anode, PEDOT:PSS as hole injection layer (HIL), PPT as the hole blocking layer (HBL), TPBi as electrons transport layer (ETL), and LiF/Al was finally utilized as the Cathode.

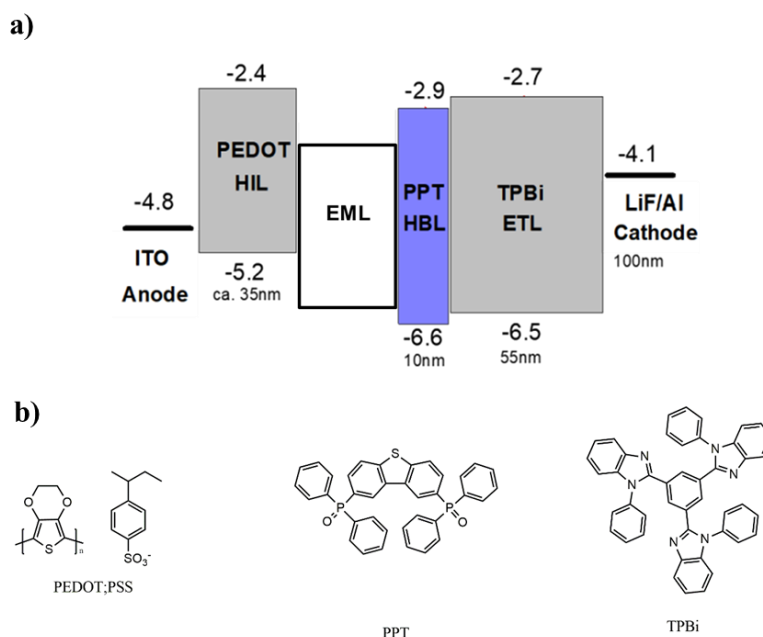


Figure 4.12 a) Schematic representations of the OLED device structure.

b) Molecular structures of hole injection, hole blocking and electrons transport layers used in the OLED devices.

ITO presents a good conductivity and is stable and highly transparent in the visible range²²⁸, thus it is widely applied as the anode material for OLEDs fabrication. However, work function of ITO (-4.8 eV) is still much higher than the HOMO of C10-PBT (-6.1 eV) or CBP (-6.2 eV). Therefore, PEDOT:PSS was spin-coated as the HIL before the deposition of the EML to assist the injection of holes from the

anode deeper into the EML. As a result, the insertion of this PEDOT:PSS layer leads to several improvements such as the increase of luminescence efficiency, the reduction of the turn on voltage and enhancement of the device lifetime²²⁹. The choice of PPT and TPBi as HBL and ETL respectively, was done due to their high electron affinities^{230–232} and appropriate energetic levels matching with CBP. In such combination, the thin HBL can improve OLED performance by confining holes to the emitting layer, while the ETL supports the electron transport from the cathode. Based on such an OLED structure, the EL properties of C10-PBT neat film or CBP/C10-PBT host-guest system as the emitting layer will be discussed hereafter.

4.6.1 Neat film as the emitting layer

Figure 4.13a presents the schematic representation of the structure, energy level diagram and thickness of each layer of the OLED devices based on spin-coated C10-PBT neat films. The external quantum efficiency (EQE: the number of photons emitted per number of injected carriers) of the fabricated OLEDs based on as-spun films is about 0.18% when the current density is 1mA/cm² (See Figure 4.13b and Table 4.4). This low EQE value, in comparison to its high PLQY (69%), could be explained by the polycrystalline nature of the spin-coated C10-PBT neat films as observed by POM in Figure 4.8a. This polycrystalline nature is normally associated with the spin-coating of crystalline materials¹⁰⁷. Such polycrystalline thin-films present small crystallite sizes and a large amount of grain boundaries that are detrimental for the charge injection/transport in the emitting layer and can quench a significant number of electrically created singlet excitons which can decay non-radiatively^{107,167,168}.

For devices prepared with annealed spin-coated films, the EQE decreases to 0.08%, which is not in agreement with the higher value of the PLQY already observed after annealing (PLQY of C10-PBT neat film increases from 69% to 80% after annealing). A possible explanation of this lower EQE could be the change of C10-PBT layer morphology during the annealing process. Indeed, as previously observed by POM (Figure 4.8b), the reorganization of the structure of the film at 80°C leads to a discontinuity of the film, which is damaging for the device performance. In addition, although larger crystallites can be also observed after annealing, the vertical reorientation of the molecules relative to the substrate can also occur during the annealing. This phenomenon is well known for materials presenting liquid crystalline properties¹⁰⁵. It is also consistent with the nanostructured films and the preferential vertical orientation of the C10-PBT molecules evidenced by AFM in thin films prepared by melt-processing (See § 4.2 and Figure 4.3). In film with such oriented structure, the transition dipole moments (TDMs) are oriented out-plane of the film since the direction of the TDMs is along the long axis of the molecules. This induced significant losses of the emitted light in the plane of the substrate which is not collected by the photon detector during the EQE measurement, leading to a decrease of the light outcoupling efficiency of the devices. Indeed, orientation of the molecules and TDMs of light-

emitting molecules are critical factors that influence the performance of OLEDs^{233–235}. Higher light outcoupling efficiency and EQE have been achieved when the emitters were oriented parallel to the substrates^{235,236}. It should be noted that all the thin-film PLQYs investigated in this work were measured with an integrated sphere which collects and integrates emitted light in all directions. Note also the further experiments such as ‘Angle dependence of PL intensity’, which studies the dependence of the PL intensity on the angle of incident light, or GIWAXS should be performed to definitively validate our assumption about the large reorientation of C10-PBT molecules during the thin film annealing process.

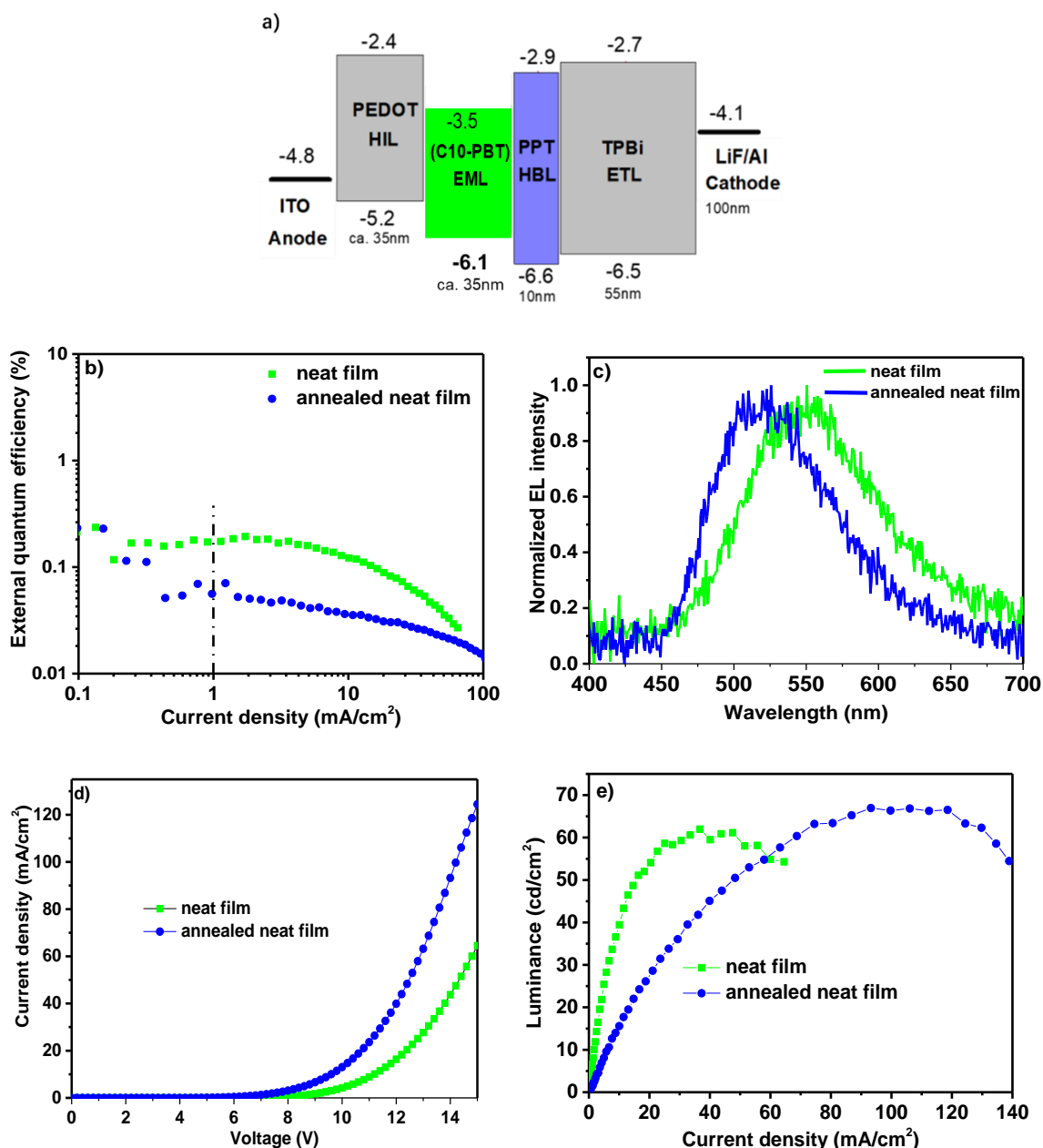


Figure 4.13 a) Schematic representation, energy level diagram and thickness of each layer of the OLED device based on C10-PBT neat film; b) External quantum efficiency versus current density, c) EL intensity spectra, d) Current density versus voltage, and e) Device luminance versus current density in OLEDs based on C10-PBT neat film before and after annealing.

Table 4.4 EL properties of the spin-coated C10-PBT neat film before and after annealing.

Film	$\lambda_{\text{EL}}^{\text{max}}$ (nm)	EQE (%)	Turn-on voltage (V)	L_{max} (cd/m ²)
Before annealing	550	0.18	7.4	62
After annealing	520	0.08	6.6	67

On the other hand, as shown in Figure 4.13c and table 4.4, the maximum EL emission wavelength of the as-spun neat film is around 550nm which corresponds to a green emission. After annealing at 80 °C, the maximum EL emission wavelength is significantly blue shifted toward 520nm that is consistent with the change of maximum PL emission wavelength from 542nm to 511nm previously observed. This phenomenon is attributed to the modification of the molecular packing and Cr1-Cr2 phase transition observed by DSC (See § 4.1). Note that this molecular reorganization in C10-PBT neat film after annealing is also corroborated by the different turn on voltage (The typical voltage required to turn the OLED on and to conduct current) of the device (7.4V vs 6.6V) observed before and after annealing (see Figure 4.13d) and by the change of the current density needed to reach the maximum EL luminance of the device (40 vs 100 mA/cm²) (See Figure 4.13e).

4.6.2 Host-guest emitting layer

According to Table 4.4, the OLED devices based on C10-PBT neat film present a modest EQE (0.18%), which drove us to study host-guest system to try to improve the EL efficiency. § 4.5.2 has introduced the host-guest system and the high PLQY values (above 78%) exhibited by all the CBP/C10-PBT blend films. Therefore, the dependence of the EL properties of the CBP/C10-PBT blend films on the C10-PBT concentration were investigated. Figure 4.14a presents the schematic representation of the structure, energy level diagram and thickness of each layer of the OLED devices based on CBP/C10-PBT blend films.

As expected (See Figure 4.14 b and c), the devices based on spin-coated CBP/C10-PBT host/guest systems present high EQE values above 2.7% for doping concentrations ranging from 2, 6, 10, and 20 wt%. The most efficient device is the OLED based on CBP/6 wt% C10-PBT blend film with an average EQE value of about 3% which is relatively good because it approaches the theoretical maximum EQE calculated from the equation²³⁷ below:

$$\eta_{\text{ext}} = \eta_{\text{int}} \eta_{\text{out}} = \gamma \eta_{\text{ST}} \phi_{\text{PL}} \eta_{\text{out}}$$

Where η_{ext} and η_{int} is the external and internal quantum efficiency, η_{out} is the light outcoupling efficiency (typically 0.2 because of the light losses in OLED), γ is the charge balance factor (ideally 1 if we consider that all the recombinations occur in the emitting layer), η_{ST} is the fraction of radiative excitons (0.25 for conventional fluorescence), and ϕ_{PL} is the PLQY. Considering the PLQY value of 87% for a CBP/6 wt% C10-PBT blend film, the theoretical maximum EQE can be estimated as η_{ext}

$=1*0.25*0.87*0.2 = 4.3\%$. High EQE value of about 3% is much higher than the one obtained with neat films of C10-PBT. This result can be explained by several concomitant effects such as i) a better film morphology of the emitting layer due to the amorphous character of CBP films (homogeneous films), ii) the dispersion of the dyes within the host layer limiting the concentration quenching phenomenon, iii) a better charge injection and transport in the CBP layer and iv) an efficient energy transfer from the electrically excited CBP host molecules to the dispersed guest emitters.

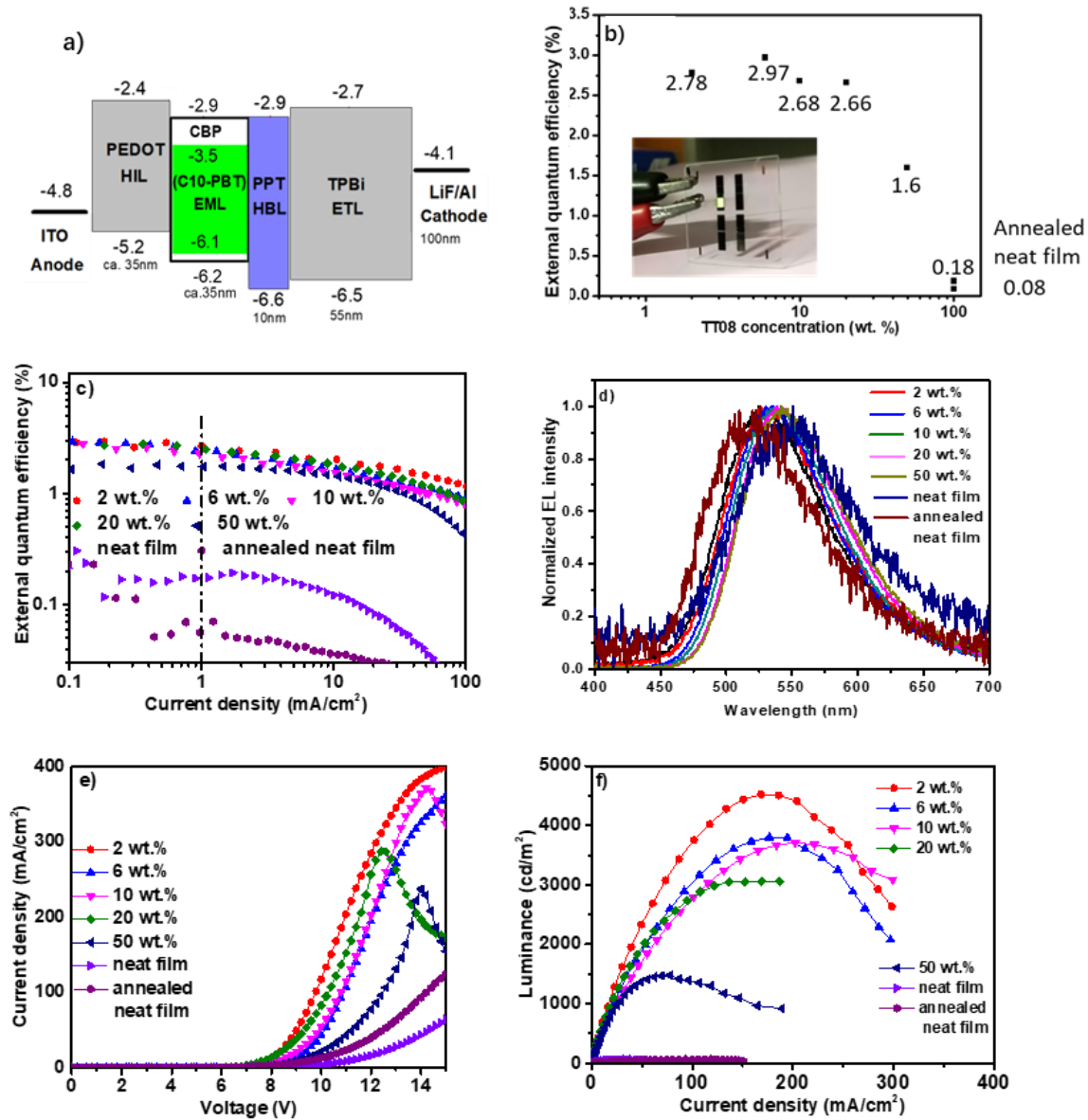


Figure 4.14 a) Schematic representation of the structure, energy level diagram and thickness of each layer of the OLED device based on CBP/C10-PBT blend films; b) Average external quantum efficiency of 4 devices when current density is 0.1 mA/cm² versus C10-PBT concentration; (insert: picture of an OLED device); c) External quantum efficiency versus current density, d) EL intensity spectra, e) Current density versus voltage, and f) Device luminance versus current density in OLEDs based on C10-PBT neat film and CBP/C10-PBT blend films as the emitting layer.

As shown in **Figure 4.14d**, the maximum EL emission wavelengths ($\lambda_{\text{EL}}^{\text{max}}$) of the blend films originate almost exclusively from C10-PBT and no residual EL of the CBP host can be detected. This implies that a fast and efficient energy transfer from host to guest is the dominant process in the EL of CBP/C10-PBT blend films, which is in good agreement with the previous observation (See **Figure 4.10c**) reported for the PL of CBP/C10-PBT blend films.

Figure 4.14 e and f present the current density ~ voltage characteristics and luminance ~ current density plots of the fabricated devices. It can be clearly observed that the devices incorporating a host/guest emitting layer present lower turn-on voltage values than those incorporating C10-PBT neat films, confirming the easier injection of charges into the EML. In addition, the maximum luminances are also much higher for host/guest-based devices than for C10-PBT neat film OLEDs (see also in **table 4.5**). These results confirm the reduction of the concentration quenching effect in host/guest-based devices. However, it is interesting to note that although maximum luminances (and EQEs) globally increase when the guest concentrations decrease, they remain of the same ranges indicating the limited effect of the concentration quenching for C10-PBT as also observed in PL.

Table 4.5 Maximum EL emission wavelength, turn on voltage and maximum luminance in OLEDs.

C10-PBT concentration	$\lambda_{\text{EL}}^{\text{max}}$ (nm)	V_{on} (V)	L_{max} (cd/m ²)
2 wt%	550	5.5	4521
6 wt%	551	5.3	3799
10 wt%	559	5.4	3707
20 wt%	555	5.2	3698
50 wt%	560	5.9	1479
Neat film	550	7.4	62
Annealed neat film	520	6.6	67

In conclusion of this paragraph, OLED devices based on spin-coated CBP/C10-PBT blend can present high performances (EQE up to 3%). However, further improvements of the EL and device efficiency could be still achieved by the optimization of the device structures such as the modification of the thickness of the HIL, EML, HBL and ETL, or the investigation of other HIL, HBL and ETL layers.

4.7 Conclusion

In summary, we studied a new fluorescent material C10-PBT presenting a donor-acceptor-donor (D-A-D) structure with O-alkylphenyl groups as donor units and benzothiadiazole unit as acceptor core. Its thermal behavior, thin film morphology and electronic properties were investigated. Its photoluminescence (PL) properties were examined in details in neat film (before and after annealing at 80°C) and CBP/C10-PBT host/guest systems. In neat film, C10-PBT presents a green emission which

is blue shifted from 542nm to 511nm and an increase of PLQY from 69% to 80% after annealing, suggesting a significant modification of the molecular packing after annealing. Blend films show high PLQY values from 78% to 91% for concentration ranging from 70 wt% to 2 wt%, attesting that C10-PBT is not very sensitive to concentration quenching and could be a promising dye for potential light emitting devices. The OLED with CBP/6 wt% C10-PBT host/guest system as EML showed the highest EQE (around 3%) which is relatively good considering the theoretical maximum EQE that could be expected with this type of fluorophore. EQE value of about 3% is much higher than the ones obtained with neat films of C10-PBT, which can be explained by several concomitant favorable effects such as a better film morphology, limited concentration quenching phenomenon, a better charge injection/transport and an efficient energy transfer. This study confirms the great potential of C10-PBT derivative as a promising dye for the fabrication of efficient light emitting devices and more generally for optoelectronic applications.

4.8 Experimental section

4.8.1 Materials

ITO on the glass substrates was used as anodes. Materials used in the OLED devices fabrication are summarized in [Table 4.6](#) below. C10-PBT was prepared by Dr. Teng Teng at IPCM. PEDOT:PSS was purchased from Heraeus Clevios. CBP, PPT and TPBi were supplied by TCI chemicals. LiF and Al were used as purchased.

Table 4.6 Materials used in the OLED devices fabrication.

ITO	Indium tin oxide
PEDOT:PSS	Poly(3,4-ethylenedioxy-thiophene):poly(styrene)
CBP	4,4'-bis(N-carbazolyl)-1,10-biphenyl
PPT	2,8-bis (diphenylphosphoryl)dibenzo-[b,d]thiophene
TPBi	2,2',2''-(1,3,5-benzinetriyl)-tris(1-phenyl-1-H-benzimidazole)
LiF	Lithium fluoride
Al	Aluminum

4.8.2 DSC

The thermal phase transitions of C10-PBT were analyzed by DSC using TA instruments Q2000 under a nitrogen flow on heating and cooling cycles at different rates (20°C/min, 10°C/min, 5°C/min, and 2°C/min).

4.8.3 POM

POM was carried out using a Leica microscope equipped with a Linkan THMS 350 hot plate connected to a Linkam 93 temperature controller.

4.8.4 AFM

AFM experiments were performed in tapping mode, using an apparatus Bruker 3100 and silicon tips, with a resonance around 400kHz, allowing to specifically probe soft matter.

4.8.5 Photophysical properties in solution and in solid-state film

For the characterization of photophysical properties in solution, C10-PBT was dissolved in solvents of different polarities at a concentration about 10^{-5} M and the solutions were placed in quartz cuvettes. All solvents used here were of spectroscopic grade. C10-PBT neat film and CBP neat film were prepared by spin coating at a rotating rate of 3000rpm for 60s from chloroform onto precleaned fused silica substrates at ambient atmosphere. In order to investigate the effect of C10-PBT concentration on the photophysical properties of the blend films, CBP/C10-PBT blend films with 2wt%, 6wt%, 10wt%, 20wt%, 50wt% and 70wt% of C10-PBT were prepared by spin coating (3000rpm, 60s) from chloroform solution. The concentration of each solution is 1wt%. All solutions were filtered with a $0.45\ \mu\text{m}$ (pore diameter) Acrodisc 13CR PTFE syringe filter (Pall Corp., East Hills, NY) before spin coating.

Absorption spectra of the solution and film were accumulated applying a Varian Cary 5000 spectrometer and UV-2550 spectrometer (Shimadzu) respectively. Steady-state PL spectra were recorded using a Fluoromax-4 spectrophotometer (Horiba Scientific). Absolute PLQYs were obtained using a Quantaaurus-QY measurement system (C11347-11, Hamamatsu Photonics). The transient photoluminescence decays were measured on a Quantaaurus-Tau C11367-03.

4.8.6 Fabrication and characterization of OLED devices

ITO-coated glass substrates were cleaned sequentially in ultrasonic bathes of detergent, deionized water, acetone, and 2-propanol, followed by the heating and boiling in 2-propanol before dried by compressed N_2 . Then all the substrates were put in the UV ozone cleaner for 20 mins to remove remaining organic contaminants and enhance hole injection ability of ITO²²⁰.

Before the deposition of the PEDOT:PSS film, the substrates were preheated at 120°C for a while to facilitate the form of the film with good morphology. PEDOT:PSS thin films (with thickness of about

35nm) were then deposited onto the ITO-coated glass substrates by spin-coating (3000rpm, 60s) followed by a heating of the film at 150°C for 20min to remove residual water. EML consisting of neat C10-PBT or CBP/C10-PBT blend with different C10-PBT concentration (2wt%, 6wt%, 10wt%, 20wt%, and 50wt%) were spin-coated (3000rpm, 60s) from their chloroform solution onto the PEDOT:PSS layer. Next, substrates were covered with shadow masks (See **Figure 4.15 a and b**) for further evaporation of HBL, ETL under a pressure of 3×10^{-4} Pa in the evaporating chamber. Then, all the substrates were transformed from the evaporator chamber to the glove box for a quick replacement of the shadow masks. The substrates were transformed back to the evaporator chamber for the deposition of the cathode (LiF: 0.8 nm; Al: 100 nm). The active area of each device was designed to be 4 mm². **Figure 4.15c** shows the location of 4 OLED devices, namely a, b, c and d, on each substrate.

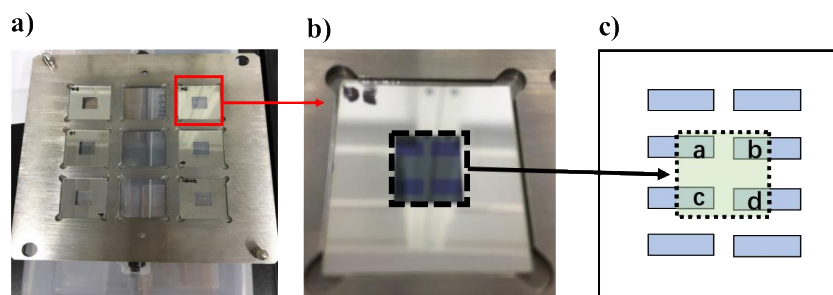


Figure 4.15 a) Photo of six substrates covered by six shadow masks. b) Zoom photo of a substrate with shadow mask on the top. c) Schematic representation of the ITO-coated glass substrate and green square is where the OLED device located.

For OLED characterization, external quantum efficiency (EQE) measurement were performed applying a C9920-12 Hamamatsu Photonics detector. The EL spectra were recorded by an optical fiber connected to a spectrometer (PMA-12, Hamamatsu Photonics). All measurements were performed in air under ambient condition without encapsulation.

**Chapter 5 Investigation of charge transport properties of
isoindigo-based oligothiophenes in field-effect transistor
configuration**

As mentioned in §1.1.2.2, the development of semiconducting materials based on donor-acceptor (D-A) macro- or molecular architectures, alternating electron-donating and electron-withdrawing units, have attracted wide attention these last two decades¹³⁶. These materials, absorbing in the near-IR range and typically having a bandgap smaller than 1.6 eV, are particularly attractive in organic photovoltaics (OPV), photodetectors (PDs), and ambipolar field-effect transistors (FETs)^{137,138}. Generally, thiophene, bithiophene, thieno[3,2-b]thiophene, benzodithiophene (BDT) or dithienopyrrole are commonly used as strong electron-donating units¹³⁶. The choice of strong electron-withdrawing units is generally more limited and chemical moieties such as naphthalene diimide (NDI), perylene diimide (PDI)⁴⁰, 2,1,3-benzothiadiazole²³⁸, quinoxaline²³⁹, thieno[3,4-c]pyrrole-4,6-dione (TPD)²⁴⁰, or isoindigo (iI) are mainly used.

Among all the existing strong electron-withdrawing units, iI is now very popular in D-A semiconductors and it is mainly utilized for both OPV and OFET applications¹³⁹. This unit contains two five-membered lactam rings joined by an exocyclic double bond at the 3 and 3' positions; each lactam is fused to a benzene ring, forming a fully conjugated structure²⁴¹ (See Figure 5.1). iI was utilized for the first time as building block to prepare conjugated p-type materials for solar cells in 2010 by J. Reynolds et al. In this work, the authors reported a donor-acceptor-donor small molecule, named iI(T2)₂, (See Figure 5.1), consisting of one iI as the acceptor unit and two bithiophene as the donor units¹⁴⁰. The bulk heterojunction solar cells based on iI(T2)₂/PC₆₀BM(1:1) blend films showed a power conversion efficiency of 1.76%¹⁴⁰. In 2012, Pei and coworkers reported a series of alternating copolymer based on iI/thiophene repeat unit (P(iI-T2)₂, 3 and 4, See Figure 5.1)²⁴², and high hole mobility of 3.62 cm²V⁻¹s⁻¹ was achieved with P(iI-T2)₃ OFET.

Considering the intrinsic drawbacks of polymers such as end-group contaminants and batch-to-batch variations, new small molecules based on iI unit were also developed recently for OFET application. Such molecular architectures possess indeed several inherent advantages including more well-defined chemical structures, simpler purification methods, easier modification and functionalization, and more reproducible synthesis¹⁴⁰. For example, Diphenyl thienoisindigo (Dph-TiI, See Figure 5.1) was synthesized by Matsumoto and coworkers²⁴³, and the authors demonstrated ambipolar transistor properties with a maximum hole and electron mobility of 0.12 cm²V⁻¹s⁻¹ and 0.13 cm²V⁻¹s⁻¹ respectively.

Although iI(T2)₂ has been extensively studied in solar cells due to its strong absorption in the visible spectrum²⁴⁴, to the best of our knowledge, no investigation of the charge transport properties of this iI-based molecular materials has been reported so far. In this chapter, we thus propose to study the morphology of spin-coated thin films of iI(T2)₂ (See Figure 5.1) and its

annealing temperature dependence by DSC, POM, GIXS and AFM. Then, the charge transport properties of $iI(T2)_2$ thin films will be investigated in FET configuration and the device air stability and surface treatment effect will be also discussed. This work represents the first investigation of charge carrier mobility of $iI(T2)_2$ in transistor configuration.

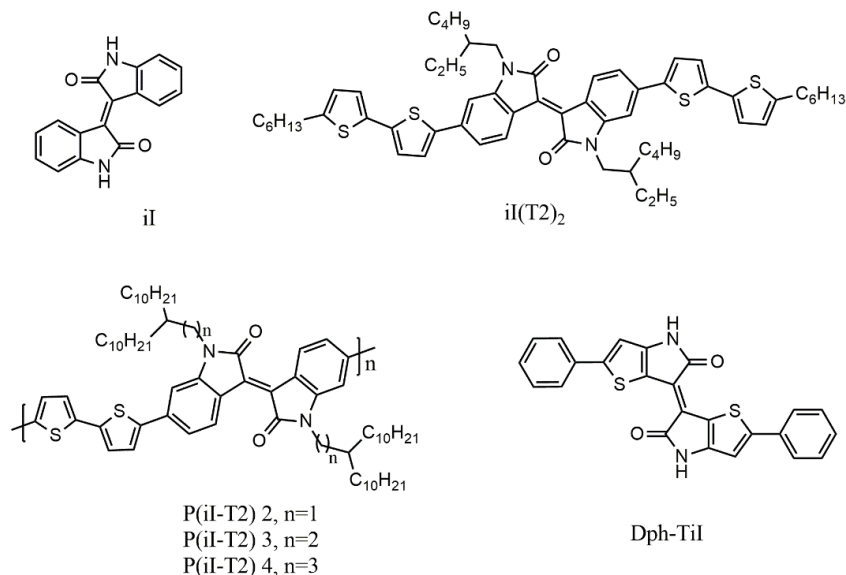


Figure 5.1 Molecular structure of il , $iI(T2)_2$, $P(iI-T2)_{2,3,4}$ and $Dph-Til$.

5.1 Thermal properties of $iI(T2)_2$

In solid-state, $iI(T2)_2$ derivatives consist of a blue-black dark powder which is composed of long single crystal needles with a length about hundreds of microns (Figure 5.2a) when observed by POM. The thermal behavior of the compound was studied by TGA and DSC. The TGA curve (Figure 5.2b) shows that the compound doesn't decompose until 320-330 °C, suggesting a good thermal stability under N₂. The polymorphism of $iI(T2)_2$ was investigated by DSC at different temperature rates and a typical thermogram recorded at 5° C/min on heating and cooling is given in Figure 5.2c. The DSC trace upon heating shows a sharp endothermic peak at around 183°C ($\Delta H \approx 38 \text{ J g}^{-1}$), which corresponds to the melting point of the single-crystalline $iI(T2)_2$ needles to isotropic liquid phase. On cooling, the compound crystallizes at 164°C with a significant hysteresis (about 20°C) characteristic of the crystallization of large molecular derivatives.

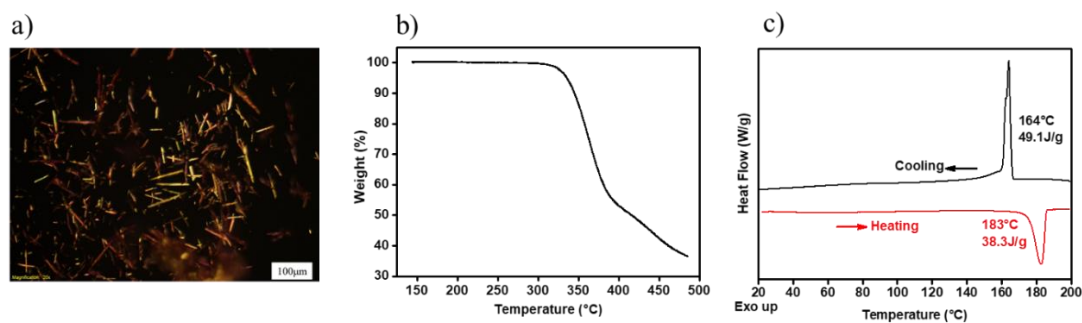


Figure 5.2 a) $iI(T2)_2$ powder observed with optical microscope under polarized light. b) TGA curve and c) DSC curves at a rate of $5\text{ }^\circ\text{C}/\text{min}$ of $iI(T2)_2$ compound.

5.2 Structure and morphology of $iI(T2)_2$ thin films

Thin films of $iI(T2)_2$ were prepared by spin coating on silicon substrates with SiO_2 and OTS-treated surface. The thin films on SiO_2 substrate were spin-coated at a spin rate of 3000rpm for 40 s from a 0.5 wt% chloroform solution in the glove box. For the preparation of the OTS treated surface, the substrates were further silanized following the procedures described in the literature¹⁴⁵. The films on OTS surface were spin-coated at lower spin rate (1000rpm) for 40 s from a more concentrated chloroform solution (1 wt.%) due to large propensity of the solution for dewetting on hydrophobic surfaces. The annealing of the spin-coated films was then carried out on a hot plate in the glove box. The details of sample preparation (type of substrates, annealing procedures) for all POM, GIXS and AFM characterizations and OFETs fabrication hereinafter are summarized below in [Table 5.1](#).

Table 5.1 Summary of substrate use and annealing history of spin-coated films for all POM, GIXS and AFM characterization, and OFETs fabrication hereinafter.

Sample code	Substrate	Maximum annealing temperature	Annealing history
film 0	SiO_2	RT	as-prepared
film 1		100	at 100°C for 20min
film 2		140	at $100\text{ }^\circ\text{C}$ and $140\text{ }^\circ\text{C}$ for 20 min each
film 3		160	at $100\text{ }^\circ\text{C}$, $140\text{ }^\circ\text{C}$ and $160\text{ }^\circ\text{C}$ for 20min each
film 4	OTS	160	at $100\text{ }^\circ\text{C}$, $140\text{ }^\circ\text{C}$ and $160\text{ }^\circ\text{C}$ for 20min each

5.2.1 Polarized optical microscope (POM)

The effect of the annealing on the film morphology was investigated first by POM. As shown in [Figure 5.3](#), the appearance of thin films in reflection mode under the crossed polarized light

slightly changes with the increase of annealing temperature and time. The films become brighter and brighter, indicating a progressive modification within the organic layer. As a result, the film 3, annealed for 20 min at 100 °C, 140 °C and 160 °C, presents the brightest optical texture as illustrated in [Figure 5.3d](#).

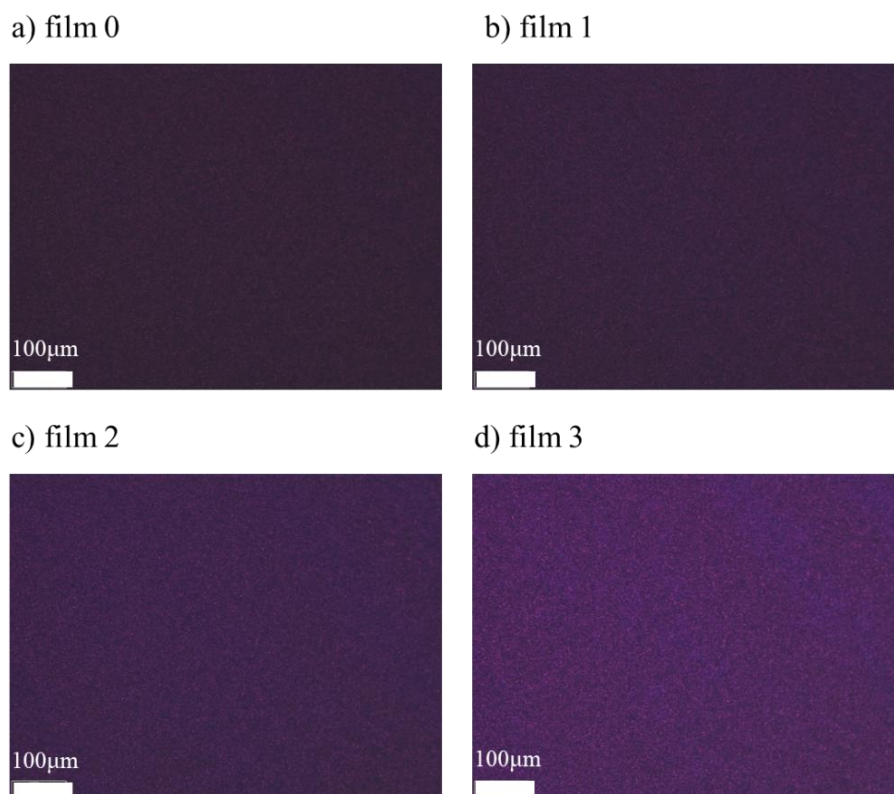


Figure 5.3 POM images of the spin-coated film on SiO₂ surface. a) film 0: as-prepared, b) film 1: annealed at 100 °C for 20 min, c) film 2: annealed at 100 °C and 140 °C for 20 min each, and d) film 3: annealed at 100 °C, 140 °C and 160 °C for 20 min each. (Note that the same light intensity was applied during all the observations)

5.2.2 Grazing incidence X-ray scattering (GIXS)

To further investigate the structure and morphology of il(T2)_2 thin films, GIXS measurements were carried out at room temperature on film 0, 1 and 2 ([Figure 5.4](#)). The GIXS patterns of the three films present similar reflections with the same spot positions, pointing out that all the films present the same crystallite phase and same oriented structure. However, the three films differ significantly in the size of the crystallites. For the as-prepared film (film 0), the average crystallite size is about few nanometers ($\sim 40\text{-}50$ Å from Scherrer equation ¹⁴⁹, see also [§2.5.1](#)) and give substantially broadened reflections spots. After annealing, the reflections spots of GIXS patterns are narrower and narrower, suggesting an important increase of the crystallite size, as for the film 2 (annealed at 140°C) in which the crystallites are larger than 20 nm. Note

that these results are consistent with the progressive changes of optical textures observed by POM for the films with the increase of annealing temperature and time.

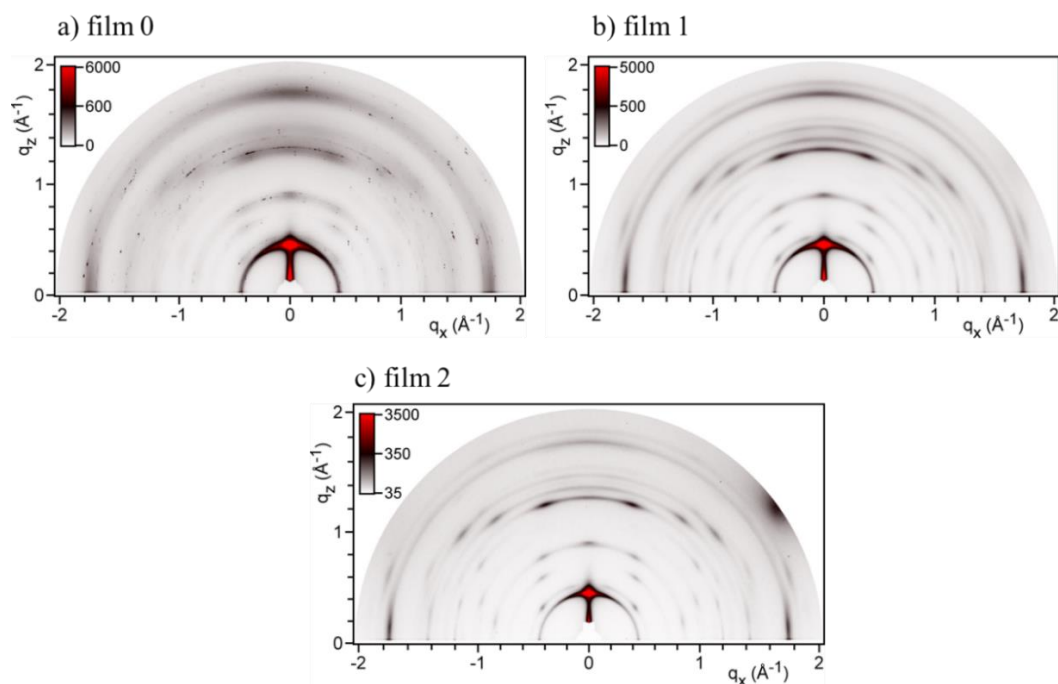


Figure 5.4 Grazing incidence X-ray scattering patterns of $il(T2)_2$ in a) film 0 (as-prepared), b) film 1 (annealed at 100 °C for 20 min), c) film 2 (annealed at 100 °C and 140 °C for 20 min each).

5.2.3 Atomic force microscope (AFM)

The morphologies of spin-coated thin films of $il(T2)_2$ before and after annealing were also analyzed by tapping mode AFM. As displayed from the topography and phase images in [Figure 5.5](#), the as-prepared spin-coated film 0 ([Figure 5.5a](#)) exhibits small crystallites with a high density of grain boundaries. These small crystallites grow to larger domains with the increase of annealing temperature and time as shown in [Figures 5.5b, c, d](#). For film 2 (annealed at 140°C), the size of crystallites can be estimated about tens of nanometers, in good agreement with the previous GIXS observations. The film 3, annealed with the highest temperature value, even presents very large domains about hundreds of nanometers, confirming the beneficial effect of the temperature on the film morphology. The analysis of the height profile of film 3 showed a well-structured surface with the presence of steps with a height about 1.8 nm (see yellow inset in [Figure 5.5d](#)). That suggests a possible orientation of molecules on the edge with the long π -conjugated backbone parallel to the surface. Unfortunately, a further description of the molecular arrangement within the film would require the complete structure resolution of the crystalline phase of $il(T2)_2$ that was not performed yet.

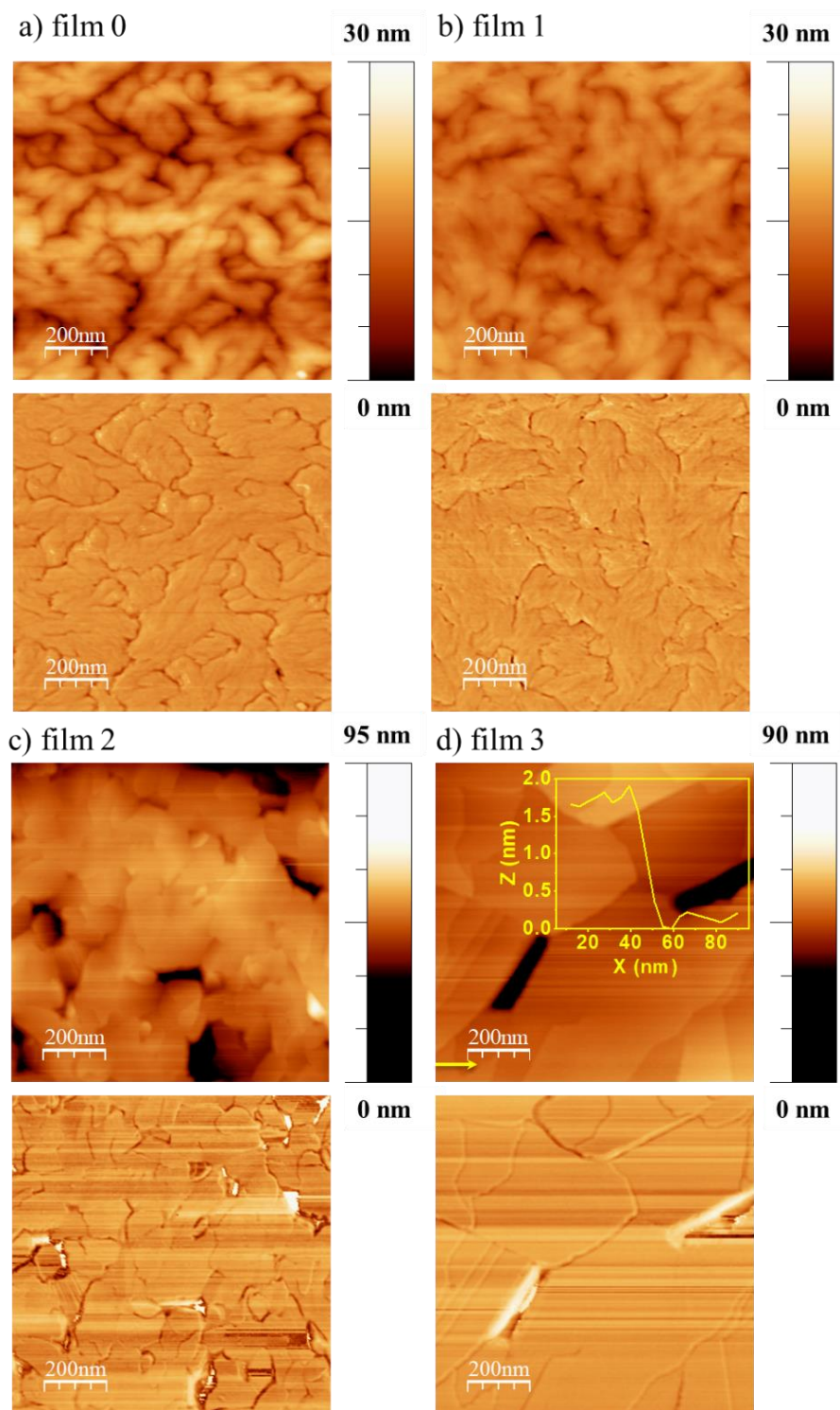


Figure 5.5 AFM topography (top) and phase (bottom) images of the spin-coated film on SiO₂ surface. a) film 0 (as-prepared), b) film 1 (annealed at 100 °C), c) film 2 (annealed at 100 °C and 140 °C) and d) film 3 (annealed at 100 °C, 140 °C and 160 °C). The yellow insets in d) show the terrace step profiles on the surface of thin film 3 along the yellow arrow.

5.3 Electronic properties of $iI(T2)_2$ thin films

The electronic properties of $iI(T2)_2$ were investigated by photoelectron spectroscopy (Figure 5.6a). This measurement was performed with fresh spin-coated thin film samples (as prepared) on a silicon wafer. A HOMO level of -5.4 eV was extracted (Reference of HOMO and LUMO level is the vacuum level (0 eV)). The optical energy gap E_g^{opt} , expressed in electronvolts, was evaluated with the onset of the absorption spectrum in chloroform (See Figure 5.6b) according to the equation given in §4.4 of chapter 4. Based on this equation and for an absorption onset of 706nm, E_g^{opt} is calculated around 1.75 eV and the LUMO level can be estimated at about -3.65eV. Note that these values are in good agreement with HOMO/LUMO levels already reported for this material and evaluated by cyclic voltammetry¹⁴⁰.

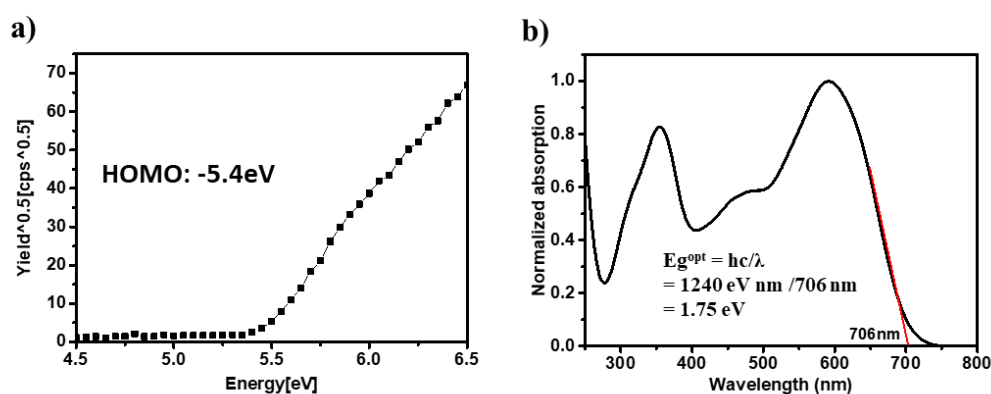


Figure 5.6 a) Photoelectron spectroscopy of $iI(T2)_2$ spin-coated thin film (as prepared); b) Absorption spectrum of $iI(T2)_2$ in chloroform and calculation of its optical band gap.

5.4 Charge transport properties of $iI(T2)_2$ thin films and annealing effect

5.4.1 Time of flight (TOF)

The charge transport properties of $iI(T2)_2$ material were investigated first by Time of Flight (TOF) technique. In TOF configuration, a thick film of 9 μm is sandwiched between transparent ITO electrodes in order to apply a continuous electric field. Then, a short laser pulse is used to photogenerate charges on one side of the sandwich cell that will move under the applied bias and create a transient photocurrent. From the lifetime of this photocurrent, electron or hole mobilities can be extracted with a simple equation given in experimental part.

Both photocurrents caused by holes and electrons drift were observed with the thick film $iI(T2)_2$, as displayed in **Figure 5.7**.

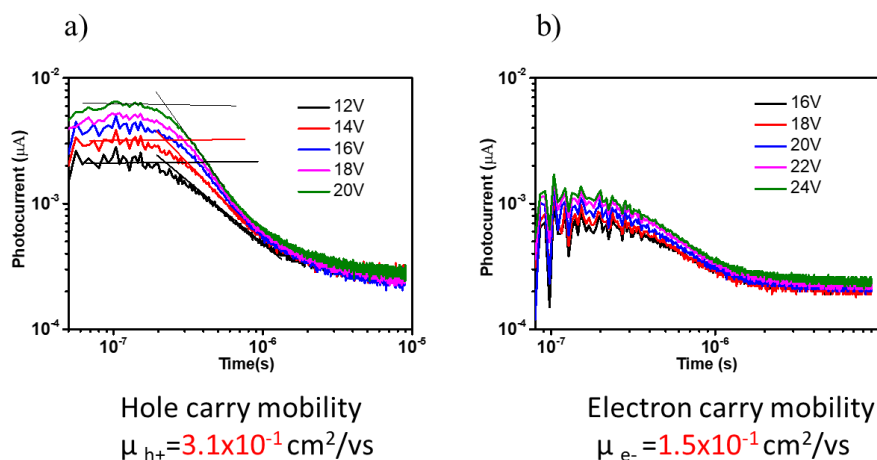


Figure 5.7 Transient photocurrent curves recorded at room temperature on $iI(T2)_2$ thick film ($9\mu\text{m}$):

a) hole mobility; b) electron mobility.

Moreover, the average electron mobility ($1.5 \times 10^{-1} \text{ cm}^2 \text{V}^{-1} \text{ s}^{-1}$) was comparable to the average hole mobility ($3.1 \times 10^{-1} \text{ cm}^2 \text{V}^{-1} \text{ s}^{-1}$), suggesting an ambipolar charge transport of $iI(T2)_2$ as already reported with other iI derivatives such as iI ²⁴⁵, $iI\text{-C6}$ ²⁴⁶, $P(iI\text{-T1})$ ²⁴⁷ and $P(iI\text{-T2})$ ¹ ²⁴⁸ (See **Figure 5.8**). Note that, the charge carrier mobilities extracted from TOF method are generally higher than that extracted from FET devices since the latter has to consider several parameters that can affect the mobility value (device geometry, contact resistance, ...).

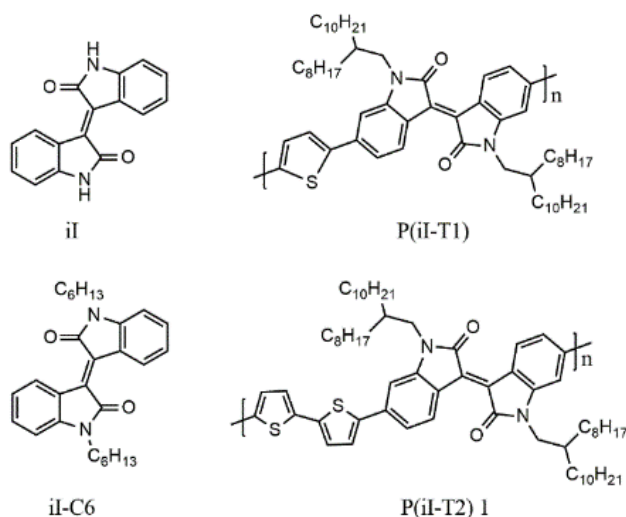


Figure 5.8 Molecular structures of iI ²⁴⁵, $iI\text{-C6}$ ²⁴⁶, $P(iI\text{-T1})$ ²⁴⁷ and $P(iI\text{-T2})$ ¹ ²⁴⁸.

5.4.2 Organic field-effect transistor (OFET)

The charge carrier mobility of $iI(T2)_2$ thin films prepared by spin coating was investigated. The effect of annealing on charge transport properties was carried out with BG/BC transistors with SiO_2 surfaces. In addition, air stability of $iI(T2)_2$ FETs on SiO_2 substrate and ambipolar properties of OTS-treated devices were also investigated.

Charge transport properties of $iI(T2)_2$ thin films in transistor configuration and annealing effect

The transistor fabrication is described in the experimental part. Considering the energy HOMO level of the material (-5.4eV, see §5.3), gold contacts are well-suited for hole injection and charge transport investigation. Figure 5.9 shows typical transfer curves and output curves of FET devices measured on films before and after gradient-temperature annealing. The devices show p-type conduction and the average hole mobilities were extracted from saturation regimes of five to ten transistors for each sample. As observed in Figure 5.10, the average hole mobility gradually increases when the annealing temperature of the film increases. This result is consistent with the previous POM, GIXS and AFM observations, showing a significant enhancement of the film morphology and the growth of crystalline domains during the annealing process. These bigger domains offer a lower density of grain boundaries and allow an easier charge flow within the transistor channel. As a result, a maximum hole mobility of $1.1 \times 10^{-2} \text{ cm}^2 \text{V}^{-1} \text{s}^{-1}$ was observed for a FET device based on film 3 (maximum annealing temperature at 160 °C) on SiO_2 surface in the glove box. The enhancement of the charge transport properties by annealing thin films of iI -based polymer derivatives was already reported by Pei and coworkers²⁴⁸. In this work, the authors showed that direct spin-coated films of P(iI -T1) polymer (See Figure 5.8) did not exhibit detectable field-effect, whereas it was measured after annealing at 150 °C for 20 min to show a hole mobility of $0.015 \text{ cm}^2 \text{V}^{-1} \text{s}^{-1}$. In addition, another work based on P(iI -T2) 1 polymer (See Figure 5.8) demonstrated that spin-coated films also displayed an increase of hole mobility from about $0.15 \text{ cm}^2 \text{V}^{-1} \text{s}^{-1}$ to $0.42 \text{ cm}^2 \text{V}^{-1} \text{s}^{-1}$ after annealing at 150 °C for 20 min.

The other device parameters such as the threshold voltage (V_{th}) or the on/off current ratios (I_{on}/I_{off}) are given in Table 5.2. In this table, we can observe that I_{on}/I_{off} increases by one order of magnitude after annealing at 160°C and the V_{th} slightly increases after the successive annealing treatments of the films. The increasing of the V_{th} can be explained by the probable alteration of the interface between the material and the bottom electrodes that can occur during

the modification of the film morphology with the temperature. Note that these transistors based on SiO₂ surfaces were also tested for n-type operation and no electron conduction was detected (no n-type characteristics).

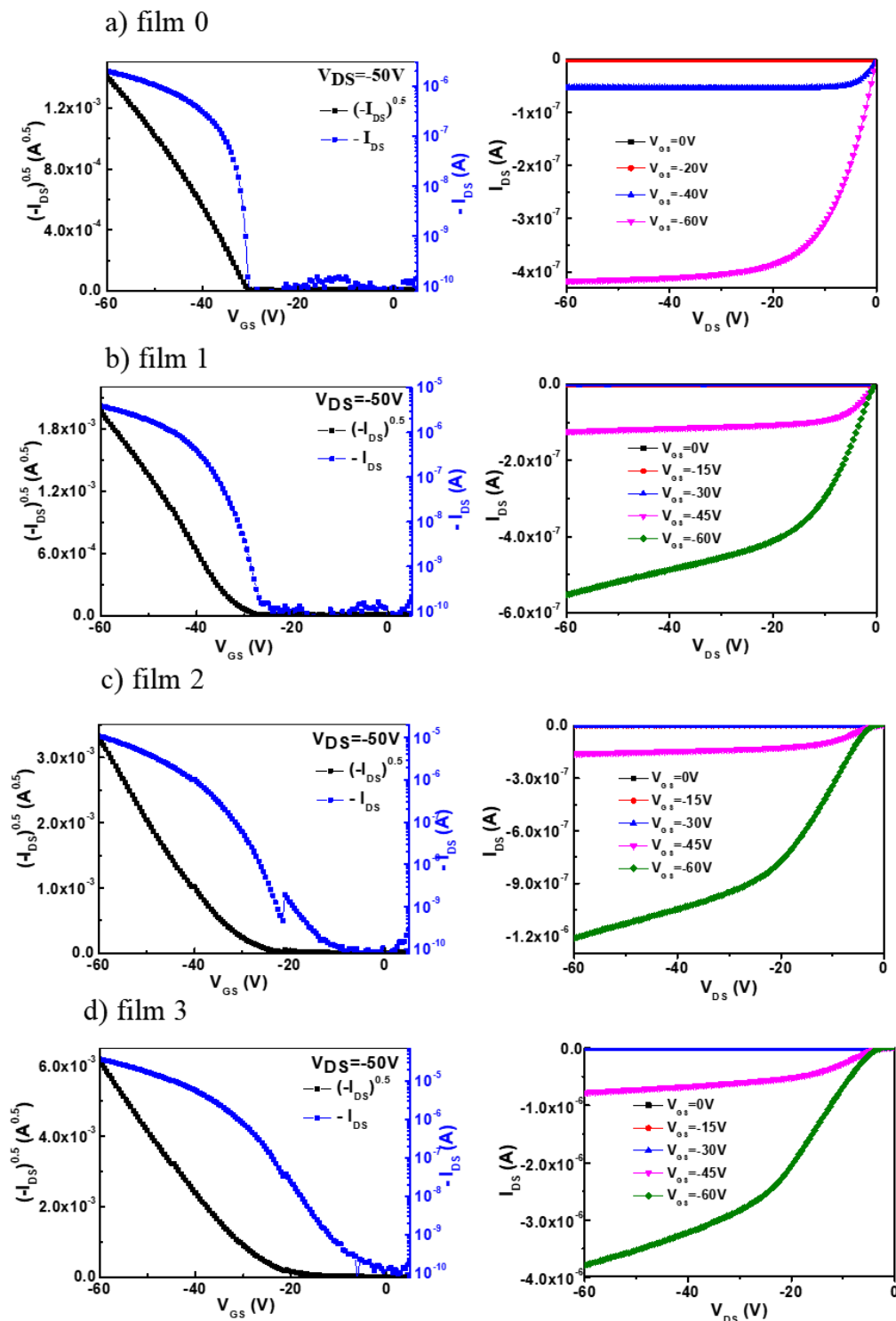


Figure 5.9 Transfer (left) and output (right) characteristics of *iI(T2)₂* OFETs on SiO₂ surface based on a) film 0 (as-prepared), b) film 1 (annealed at 100 °C), c) film 2 (annealed at 100 °C and 140 °C, and d) film 3 (annealed at 100 °C, 140 °C and 160 °C).

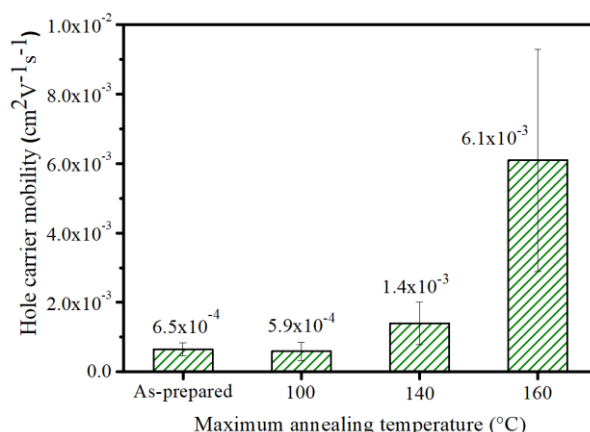


Figure 5.10 Annealing temperature dependence of hole carrier mobility of *iI(T2)₂* OFETs on SiO₂ surface. Each charge mobility value was the average value of five to ten devices.

Table 5.2 Summary of the electrical characteristics of *iI(T2)₂* OFETs.

Sample code	Maximum annealing temperature	μ_h (cm ² V ⁻¹ s ⁻¹) ^{a,b}	V_{th} (V) ^b	I_{ON}/I_{OFF} ($V_{DS}=-50V$) ^b
0	As-prepared	(6.5±1.9)X10 ⁻⁴	-(20±16)	(2.2±2.1) X10 ⁴
1	100	(5.9±2.6) X10 ⁻⁴	-(27±15)	(2.4±1.6) X10 ⁴
2	140	(1.4±0.6)X10 ⁻³	-(28±9.8)	(3.5±3.1) X10 ⁴
3	160	(6.1±3.2)X10 ⁻³	-(24±10)	(1.9±1.5) X10 ⁵

^a from saturation regime. ^b Average values based on five to ten of FET devices.

Air stability of the *iI(T2)₂* thin film transistors

The air stability of devices based on film 3 on SiO₂ presenting the highest mobility was investigated more deeply (See Table 5.2). To this end, transistors were removed from the glove box and electrical measurements were performed in ambient condition. As illustrated in Figure 5.11b, the devices still work in air but the performances are slightly affected and the hole carrier mobility decreases around one order of magnitude ($4.7 \times 10^{-4} \text{ cm}^2 \text{V}^{-1} \text{s}^{-1}$) under lower source-gate bias. However, to some extent, the devices ($4.5 \times 10^{-3} \text{ cm}^2 \text{V}^{-1} \text{s}^{-1}$) recover its original performances after the source-gate bias goes higher. Finally, the reversibility ($5.8 \times 10^{-3} \text{ cm}^2 \text{V}^{-1} \text{s}^{-1}$) of the previous device performances is observed (Figure 5.11c) by measuring again the transistors in the glove box atmosphere after ambient air condition exposure. The relatively good stability of the devices after ambient air exposure can be explained²⁴⁸ by the low-lying HOMO level of *iI(T2)₂* around -5.4eV evaluated by photoelectron spectroscopy (See Figure 5.6a). Note that similar behaviors were observed for OTFT devices based on P(*iI(T2)*) 1 (molecular structure is shown in Figure 5.8) showing also good ambient stability due to a deep HOMO level of -5.7eV²⁴⁸.

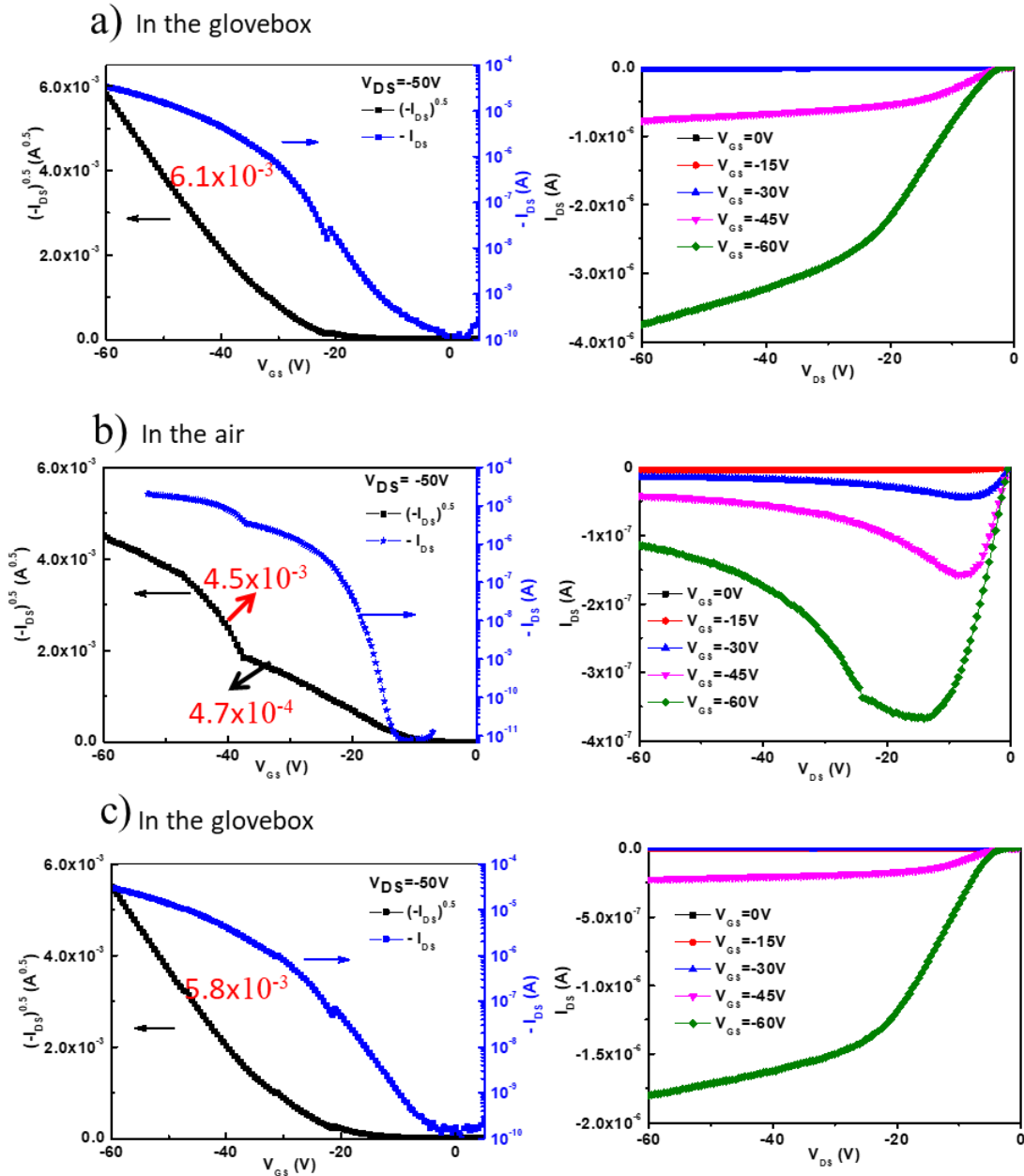


Figure 5.11 Transfer (left) and output (right) characteristics of $iI(T2)_2$ OFETs (SiO_2 surface) based on film 3 (annealed at 100 °C, 140 °C and 160 °C for 20 min each, a) under the glove box N_2 atmosphere, b) under the ambient air condition and c) under the glove box N_2 atmosphere after air exposure.

Charge transport properties of $iI(T2)_2$ thin film on OTS-treated surfaces

The charge transport properties of $iI(T2)_2$ thin films based on OTS-treated surface devices were also investigated. The preparation of the BG/BC OTS-treated transistors is described in experimental part. One of the main problems for the fabrication of such devices was the deposition of the spin-coated $iI(T2)_2$ thin film on the top of the OTS-treated surface. Indeed,

the $iI(T2)_2$ chloroform solution dewets easily during the spin coating on a hydrophobic OTS-treated substrate. As a result, the interdigitated electrodes of transistors were partially covered by the $iI(T2)_2$ thin film as displayed in [Figure 5.12](#). [Figure 5.13](#) shows typical transfer and output curves of such no-optimized FET devices measured with film 4 (See [Table 5.1](#)).

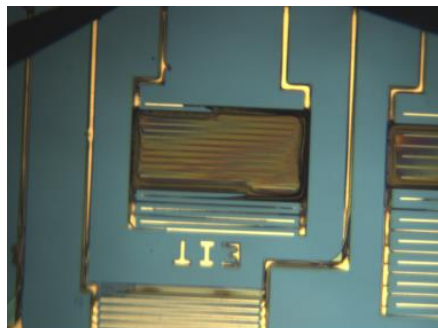


Figure 5.12 Picture of spin-coated $iI(T2)_2$ thin film on a transistor (interdigitated electrodes) with an OTS-treated surface.

On OTS surfaces, the transistors present typical p-type and n-type transfer characteristics (indicating the ambipolar conduction of the devices [Figure 5.13 a and b, left](#)). Mobilities values about $1.7 \times 10^{-4} \text{ cm}^2 \text{V}^{-1} \text{s}^{-1}$ and $1.5 \times 10^{-5} \text{ cm}^2 \text{V}^{-1} \text{s}^{-1}$ were calculated for hole and electron, respectively. The detection of the n-type conduction could be explained by the OTS surface treatment that can remove the hydroxyl groups at the SiO_2 dielectric interface which usually trap electrons and substantially affect the n-type behavior of OSCs ^{249,250}. It could also be explained by the relatively low LUMO energy level of $iI(T2)_2$ derivative (-3.65eV, see [§5.3](#), and -3.9eV ¹⁴⁰) that can allow the electron injection from the gold electrodes to the LUMO of the material. However, it should be pointed out that the unbalanced hole and electron mobilities and the not saturated output curves of the n-type characteristics in [Figure 5.13b \(right\)](#) evidence the significant mismatching of the gold work function (-5.1eV) with the LUMO level of $iI(T2)_2$ (-3.65eV/-3.9eV). Note that this preliminary results could be probably optimized, as for example by achieving continuous film on OTS surface in using other solvents such as 1,2,4-trichlorobenzene (TCB) exhibiting high boiling point ^{251,252} and higher contact angle ²⁵³.

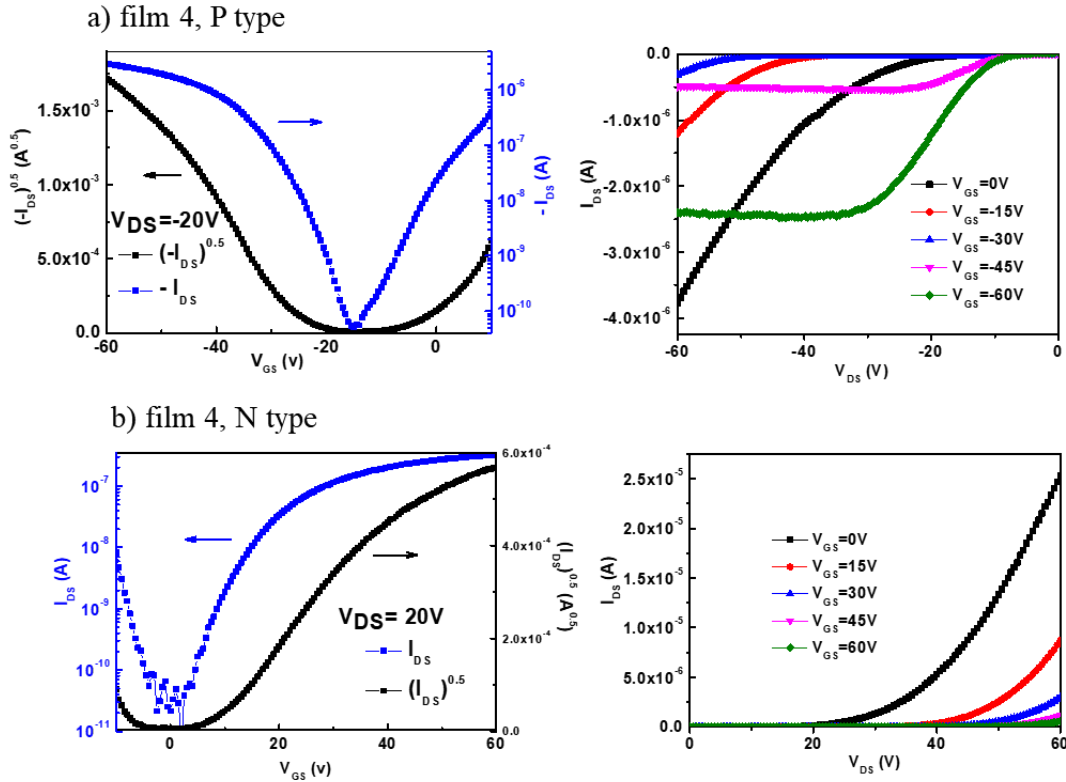


Figure 5.13 a) P-type and b) n-type transfer (left) and output (right) characteristics of $iI(T2)_2$ OFETs (OTS surface) based on film 4 (annealed at 100 °C, 140 °C and 160 °C for 20 min each).

5.5 Conclusion

In summary, charge transport properties of spin-coated thin film of isoindigo-based oligothiophenes $iI(T2)_2$ were investigated in thin film transistors configurations. The thermal properties and the effect of the annealing conditions on the film morphology was studied by Differential scanning calorimetry (DSC), Polarized optical microscope (POM), Grazing incidence X-ray scattering (GIXS) and Atomic force microscope (AFM), and demonstrated the beneficial impact of the annealing process to reduce the density of grain boundaries and improve the film structure. The film morphology/charge transport properties relationship was discussed in details and a maximum hole mobility value of $0.011 \text{ cm}^2\text{V}^{-1}\text{s}^{-1}$ was measured on the SiO_2 substrate. Moreover, a good stability of the OTFTs in air environment or after air exposure was evidenced. In addition, devices prepared with OTS-treated substrates demonstrated that an electron conduction could be also achieved, leading to ambipolar charge transport properties. This work represents the first investigation of charge carrier mobility of $iI(T2)_2$ in transistor configuration.

5.6 Experimental section

5.6.1 Materials

All materials and solvents were purchased from Sigma Aldrich and were used without further purification. $i\text{I}(\text{T}2)_2$ was synthesized by Dr. D'Aléo Anthony at Seoul (Korea).

5.6.2 TGA and DSC

Thermogravimetric analysis (TGA) and DSC were performed using TA instruments Q2000 under N_2 flow in aluminum hermetic pans. Balance purge flow and sample purge flow of N_2 were 40 ml/min and 60 ml/min respectively during the TGA analysis. The DSC traces of $i\text{I}(\text{T}2)_2$ compound on heating and cooling were recorded with a rate of 20 °C/min, 10 °C/min and 5 °C/min.

5.6.3 POM

POM was carried out using a Leica microscope equipped with a Linkam THMS 350 hot plate connected to a Linkam 93 temperature controller.

5.6.4 GIXS

The characterization of the structural properties of the spin-coated films was performed by 2D GIXS experiments at PLS-II 9A U-SAXS beamline of Pohang Accelerator Laboratory in Korea. The thin films were studied on silicon substrates and the X-rays coming from the vacuum undulator (IVU) were monochromated using Si(111) double crystals and focused on a detector consisting in a 2D CCD detector (Rayonix SX165). The distance between sample and detector was around 225 mm and the beam energy was about 11.06 keV (1.121 Å).

5.6.5 AFM

AFM experiments were carried out to examine the surface morphologies of $i\text{I}(\text{T}2)_2$ spin-coated films before and after annealing. These measurements were performed in the tapping mode, with Bruker 3100 stand alone. Tips were in silicon, associated with a resonance around 300

KHz.

5.6.6 Photoelectron spectroscopy

The HOMO level was found by measuring its work function using photoelectron spectroscopy (Riken Keiki, AC-3).

5.6.7 TOF

TOF measurements were performed in the basic configuration. The standard liquid crystal cell was purchased from Instec Inc. with gap thickness of 9 μm and transparent electrodes of indium tin oxide (ITO). Compound of $\text{iI}(\text{T}2)_2$ powder was placed near the hole of the cell and heated to the isotropic state. The sample then flowed into the cell by capillary force and the film was cooled down before using. The sample was mounted in the TOF setup using hot stage (Instec HCS302). Sample was excited by nanosecond pulses from N_2 laser at 337 nm (where the sample strongly absorbed light) and a repetition rate of 10 Hz. The excitation of the sample results in a transient photocurrent signal that is amplified and then recorded by a Tektronix TDS 5034 350 MHz digital oscilloscope. The charge mobility could be estimated via the method described in the chapter 1 (§1.3.1.2).

5.6.8 Fabrication and characterization of OFET devices

BG/BC transistors with SiO_2 surface were fabricated on silicon wafer with thermally oxidized 230nm SiO_2 layer (with capacitance $C_1 = 15 \text{ nF/cm}^2$), purchased from Fraunhofer institute for photonic microsystems. The interdigitated source and drain electrodes were 30nm Au with 10 nm high work function adhesion layer (ITO). The channel length was 2.5 μm , 5 μm , 10 μm or 20 μm , and the channel width was 10 mm. The substrates were sonicated in ethanol, acetone and chloroform successively. Then they were cleaned for 30 min in a UV-Ozone cleaner before the spin coating of $\text{iI}(\text{T}2)_2$ solution. The thin films on SiO_2 substrate surface were spin-coated at a spin rate of 3000rpm for 40 s from a 0.5 wt.% chloroform solution in the glove box.

BG/BC transistors with OTS surface were fabricated on heavily-doped Si wafer (i.e low bulk resistivity 0.01 $\Omega\cdot\text{cm}$) thermally oxidized by a 280nm-thick SiO_2 layer, purchased from MicroChemicals GmbH. SiO_2 was used here as gate dielectric (with gate capacitance $C_1 = 12 \text{ nF/cm}^2$) and the Si wafer as gate electrode in back contact. The interdigitated source and drain

electrodes were patterned by photolithography process-flow through an MJB-4 (Karl Suss) mask-aligner in vacuum contact (in collaboration with Dr. Sebastien Sanaur, CMP, Gardanne), and completed by lift-off technique in acetone overnight. Previously, a sequential thermal evaporation of a 5 nm-thick adhesion layer of Chromium and a 100 nm-thick gold layer in a vacuum chamber at 10^{-7} Torr was achieved. The channel length (L) was 5 μ m, 12.5 μ m, 25 μ m or 50 μ m, while corresponding channel width (W) was 19mm, 19mm, 18mm or 17mm respectively. The substrates were sonicated in ethanol, acetone and chloroform successively. Then they were cleaned for 30 min in a UV-Ozone cleaner. For the preparation of the OTS-treated surface, the substrates were further treated as the procedures described in the literature¹⁴⁵. The films on OTS surface were spin-coated at lower spin rate (1000rpm) for 40 s from a more concentrated chloroform solution (1 wt.%)

Current-voltage measurements of the BG/BC OFETs were collected in the glove box (N₂ environment) or in ambient atmosphere using two Keithley 2400 source units and a MS Tech probe station (MST 8000). The schematic representation and a picture of a BG/BC transistor are shown in [Figure 5.14](#).

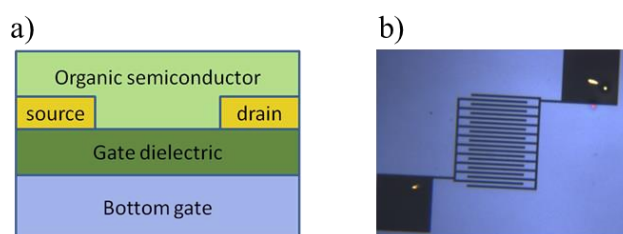


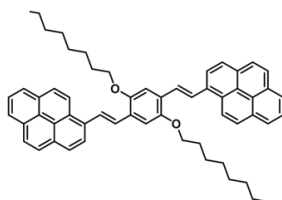
Figure 5.14 Schematic representation and the picture of a BG/BC transistor.

P-type transfer characteristics were acquired at $V_{DS} = -50$ V while V_{GS} was stepped from 5 V or 10 V to -60 V in 0.5 V increments. N-type transfer characteristics were acquired at $V_{DS} = 20$ V while V_{GS} was stepped from -10 V to 60 V in 0.5 V increments. P-type output characteristics were taken at $V_{GS} = 0$ V to -60V in 20V or 15 V increments and V_{DS} was stepped from 0 V to -60 V in 0.5 V increments. N-type output characteristics were taken at $V_{GS} = 0$ V to 60V in 15 V increments and V_{DS} was stepped from 0 V to 60 V in 0.5 V increments. Hole field-effect mobilities were calculated from the transfer characteristics in the saturation regime, using the standard method described in chapter 1 (§1.3.1.1). On/Off current ratio (I_{on}/I_{off}) was determined from the I_{DS} at $V_{GS}=0$ V (I_{off}) and $V_{GS}=-60$ V (I_{on}).

Conclusions and Perspectives

This PhD work aimed at the elaboration and characterization of organic semiconducting thin films based on different π -conjugated semiconducting materials (DAL1, BTBT, C₈-BTBT-C₈, C10-PBT and iI(T2)₂) for organic optoelectronics applications. The general goal was to optimize their fabrication methods in order to maximize their device performances of the corresponding organic optoelectronic devices (OFETs or OLEDs).

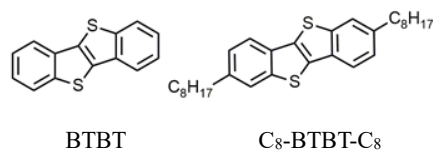
In chapter 2, we proposed an improved melt-processing method for the fabrication of crystalline organic semiconducting layers (DAL1) with millimetric single crystal monodomains. The organic films prepared by melt-processing present a much higher crystallinity than the spin-coated polycrystalline films, resulting in a hole field-effect mobility value ($5 \times 10^{-2} \text{ cm}^2\text{V}^{-1}\text{s}^{-1}$) one order of magnitude higher than spin coated thin films ($2.4 \times 10^{-3} \text{ cm}^2\text{V}^{-1}\text{s}^{-1}$). This improvement of the charge transport properties upon melt processing is accompanied by a substantial increase of the photophysical properties. The study demonstrates that the solvent-free vacuum-free melt-processing method can be utilized to fabricate high performance organic electronic and light-emitting devices. This approach is suitable for a large variety of organic semiconductors and several studies are currently in progress in our group to extend its utilization for other optoelectronics. As a consequence, this processing method should be of strong interest for future research in the field of organic electronics.



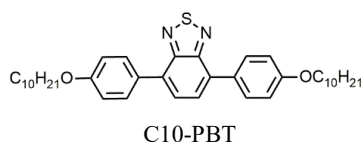
DAL1

In chapter 3, we prepared thin single crystals of unsubstituted BTBT by physical vapor transport deposition technique, and investigated for the first time its charge transport properties (maximum hole mobility value of $0.032 \text{ cm}^2\text{V}^{-1}\text{s}^{-1}$) in FET configuration. This study presents the first investigation of the FET mobility of the unsubstituted BTBT aromatic core and confirms the important role of the BTBT substitution to achieve high charge carrier mobility. On the other hand, the charge transport properties of C₈-BTBT-C₈ melt-processed thin films were also investigated by transistor, and a high mobility about $1.1 \text{ cm}^2\text{V}^{-1}\text{s}^{-1}$ was obtained, confirming once again that the solvent-free vacuum-free melt-processing method is an efficient method to fabricate high performance organic electronic devices. However, further

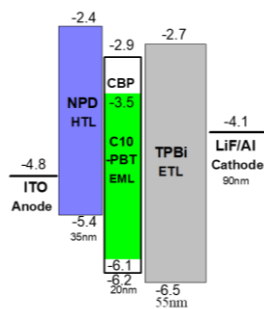
investigation of the structure of C₈-BTBT-C₈ melt-processed thin films have still to be performed in order to figure out the complete structure/property relationship of such devices.



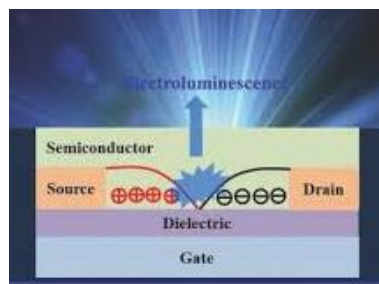
In chapter 4, we studied a new fluorescent liquid crystalline material C10-PBT. In neat film, C10-PBT presents a high PLQY about 80% after annealing, suggesting limited aggregation-induced quenching phenomena. CBP/C10-PBT blend films also show high PLQY values from 78% to 91% for concentration ranging from 70 wt% to 2 wt%, confirming that C10-PBT is not very sensitive to concentration quenching and could be a promising dye for potential light emitting devices. The OLED with CBP/6 wt% C10-PBT host/guest system as EML showed a high EQE (around 3%) which is relatively good considering the theoretical maximum EQE that could be expected with this type of fluorophore.



However, these devices, prepared by a solution deposition of the hole injection layer and emitting layer (HIL and EML), could be still optimized by using, for example, the vacuum thermal evaporation technique for the fabrication of the whole devices. A preliminary trial of an all-evaporated OLED was recently performed based on the simple OLED device structure given below; the EQE of this device based on evaporated CBP/10 wt% C10-PBT host-guest system achieved the same EQE value (2.7%) as the one based on spin-coated CBP/10 wt% C10-PBT blend film (See Figure 4.14a and b). This promising result could be obviously improved by the incorporation of hole injection layer, hole blocking layer or electron blocking layer (HIL, HBL or EBL), the optimization of the layer thicknesses, and the investigation of other layer combinations. In addition, this promising dye could be also utilized for the fabrication of other type of light emitting devices such as organic light emitting transistors (OLET, See Figure below). This study is currently in progress in collaboration with the group of Prof. Ebinazar Namdas at the University of Queensland (Australia).

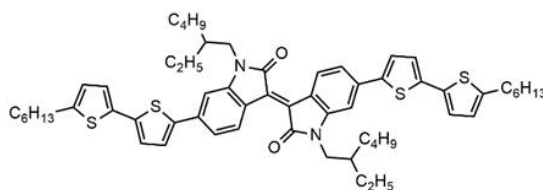


All-evaporated OLED



Organic light emitting transistor

In chapter 5, the film morphology/charge transport property relationship of isoindigo-based oligothiophenes $iI(T2)_2$ was discussed in details and a maximum hole mobility of $0.011 \text{ cm}^2\text{V}^{-1}\text{s}^{-1}$ was measured on the SiO_2 substrate, demonstrating the beneficial impact of the annealing process to reduce the density of grain boundaries, improve the film structure and thus increase the charge carrier mobility. Moreover, a good stability of the OTFTs in air environment or after air exposure was evidenced. In addition, devices prepared with OTS-treated substrates demonstrated that an electron conduction could be also achieved, leading to ambipolar charge transport properties which is essential for fabrication of organic complementary circuits.



$iI(T2)_2$

To conclude, this work definitively confirms the importance of the morphology optimization of semiconducting active layers in the field of the optoelectronics to achieve high charge transport and/or photophysical properties. More generally, we have shown that a fundamental understanding of physico-chemical aspects, notably materials processing, and the inducement of increased order and control of the solid-state structure, is critical to realize the full intrinsic potential that organic semiconductors possess. This latter point requires, in any case, an intimately integrated approach involving synthesis, phase behavior, processing, and device design.

References

- (1) Eley, D. D. Phthalocyanines as Semiconductors. *Nature* **1948**, *162* (819), 4125.
- (2) Shirakawa, H.; Louis, E. J.; MacDiarmid, A. G.; Chiang, C. K.; Heeger, A. J. Synthesis of Electrically Conducting Organic Polymers: Halogen Derivatives of Polyacetylene, (CH)_x. *Journal of the Chemical Society, Chemical Communications* **1977**, *39* (16), 578–580.
- (3) Chiang, C. K.; Fincher, C. R.; Park, Y. W.; Heeger, A. J.; Shirakawa, H.; Louis, E. J.; Gau, S. C.; MacDiarmid, A. G. Electrical Conductivity in Doped Polyacetylene. *Physical Review Letters* **1977**, *39* (17), 1098–1101.
- (4) Heeger, A.; MacDiarmid, A. G.; Shirakawa, H. The Nobel Prize in Chemistry, 2000: Conductive Polymers. *Stockholm, Sweden: Royal Swedish Academy of Sciences* **2000**.
- (5) Forrest, S. R. The Path to Ubiquitous and Low-Cost Organic Electronic Appliances on Plastic. *Nature*. 2004, pp 911–918.
- (6) Sirringhaus, H. 25th Anniversary Article: Organic Field-Effect Transistors: The Path beyond Amorphous Silicon. *Advanced Materials*. 2014, pp 1319–1335.
- (7) Siegel, A. C.; Phillips, S. T.; Dickey, M. D.; Lu, N.; Suo, Z.; Whitesides, G. M. Foldable Printed Circuit Boards on Paper Substrates. *Advanced Functional Materials* **2010**, *20* (1), 28–35.
- (8) Dong, H.; Fu, X.; Liu, J.; Wang, Z.; Hu, W. 25th Anniversary Article: Key Points for High-Mobility Organic Field-Effect Transistors. *Advanced Materials*. 2013, pp 6158–6183.
- (9) Anthopoulos, T. D.; Markham, J. P. J.; Nandas, E. B.; Samuel, I. D. W.; Lo, S. C.; Burn, P. L. Highly Efficient Single-Layer Dendrimer Light-Emitting Diodes with Balanced Charge Transport. *Applied Physics Letters* **2003**, *82* (26), 4824–4826.
- (10) Fichou, D.; Horowitz, G. Molecular and Polymer Semiconductors, Conductors, and Superconductors: Overview. In *Encyclopedia of Materials: Science and Technology*; Buschow, K. H. J., Cahn, R. W., Flemings, M. C., Ilshner, B., Kramer, E. J., Mahajan, S., Veyssi re, P. B. T.-E. of M. S. and T., Eds.; Elsevier: Oxford, 2001; pp 5748–5757.
- (11) Zaumseil, J.; Sirringhaus, H. Electron and Ambipolar Transport in Organic Field-Effect Transistors. *Chemical Reviews*. 2007, pp 1296–1323.
- (12) Blakesley, J. C.; Castro, F. A.; Kylberg, W.; Dibb, G. F. A.; Arantes, C.; Valaski, R.; Cremona, M.; Kim, J. S.; Kim, J.-S. Towards Reliable Charge-Mobility Benchmark Measurements for Organic Semiconductors. *Organic Electronics* **2014**, *15* (6), 1263–

- 1272.
- (13) Fratini, S.; Nikolka, M.; Salleo, A.; Schweicher, G.; Sirringhaus, H. Charge Transport in High-Mobility Conjugated Polymers and Molecular Semiconductors. *Nature Materials* **2020**, *19* (May), 491–502.
 - (14) Ebata, H.; Izawa, T.; Miyazaki, E.; Takimiya, K.; Ikeda, M.; Kuwabara, H.; Yui, T. Highly Soluble [1]Benzothieno[3,2-b]Benzothiophene (BTBT) Derivatives for High-Performance, Solution-Processed Organic Field-Effect Transistors. *Journal of the American Chemical Society* **2007**, *129* (51), 15732–15733.
 - (15) Alkan, M.; Yavuz, I. Intrinsic Charge-Mobility in Benzothieno[3,2-b][1]Benzothiophene (BTBT) Organic Semiconductors Is Enhanced with Long Alkyl Side-Chains. *Physical Chemistry Chemical Physics* **2018**, *20* (23), 15970–15979.
 - (16) Jurchescu, O. D.; Popinciuc, M.; Van Wees, B. J.; Palstra, T. T. M. Interface-Controlled, High-Mobility Organic Transistors. *Advanced Materials* **2007**, *19* (5), 688–692.
 - (17) Tsutsui, Y.; Schweicher, G.; Chattopadhyay, B.; Sakurai, T.; Arlin, J. B.; Ruzié, C.; Aliev, A.; Ciesielski, A.; Colella, S.; Kennedy, A. R.; et al. Charge Carrier Mobility: Unraveling Unprecedented Charge Carrier Mobility through Structure Property Relationship of Four Isomers of Didodecyl[1]Benzothieno[3,2-b][1]Benzothiophene. *Advanced Materials*. 2016, p 7291.
 - (18) Fratini, S.; Ciuchi, S.; Mayou, D.; De Laissardière, G. T.; Troisi, A. A Map of High-Mobility Molecular Semiconductors. *Nature Materials* **2017**, *16* (10), 998–1002.
 - (19) Li, J.; Zhao, Y.; Tan, H. S.; Guo, Y.; Di, C. A.; Yu, G.; Liu, Y.; Lin, M.; Lim, S. H.; Zhou, Y.; et al. A Stable Solution-Processed Polymer Semiconductor with Record High-Mobility for Printed Transistors. *Scientific Reports* **2012**, *2* (1), 754.
 - (20) Prins, P.; Grozema, F. C.; Schins, J. M.; Patil, S.; Scherf, U.; Siebbeles, L. D. A. High Intrachain Hole Mobility on Molecular Wires of Ladder-Type Poly(p-Phenylenes). *Physical Review Letters* **2006**, *96* (14), 1–4.
 - (21) Hertel, D.; Scherf, U.; Bäessler, H. Charge Carrier Mobility in a Ladder-Type Conjugated Polymer. *Advanced Materials* **1998**, *10* (14), 1119–1122.
 - (22) Botiz, I.; Stingelin, N. Influence of Molecular Conformations and Microstructure on the Optoelectronic Properties of Conjugated Polymers. *Materials* **2014**, *7* (3), 2273–2300.
 - (23) Hartmann, L.; Tremel, K.; Uttiya, S.; Crossland, E.; Ludwigs, S.; Kayunkid, N.; Vergnat, C.; Brinkmann, M. 2D Versus 3D Crystalline Order in Thin Films of Regioregular Poly(3-Hexylthiophene) Oriented by Mechanical Rubbing and Epitaxy. *Advanced Functional Materials* **2011**, *21* (21), 4047–4057.
 - (24) Ma, W.; Yan, H.; Zhou, K.; Naveed, H. B. Chapter 2 - Nanostructure of Organic Solar

- Cells. In *Micro and Nano Technologies*; Gao, F. B. T.-A. N. for S. C. and L. E. D., Ed.; Elsevier, 2019; pp 37–68.
- (25) Potscavage, W. J.; Sharma, A.; Kippelen, B. Critical Interfaces in Organic Solar Cells and Their Influence on the Open-Circuit Voltage. *Accounts of Chemical Research* **2009**, *42* (11), 1758–1767.
- (26) Fan, H.; Yang, H.; Zou, Y.; Dong, Y.; Fan, D.; Zheng, Y.; Wu, Y.; Cui, C.; Li, Y. Conjugated Side-Chains Engineering of Polymer Donor Enabling Improved Efficiency for Polymer Solar Cells. *J. Mater. Chem. A* **2020**.
- (27) Sirringhaus, H. Device Physics of Solution-Processed Organic Field-Effect Transistors. *Advanced Materials* **2005**, *17* (20), 2411–2425.
- (28) Yamagishi, M.; Takeya, J.; Tominari, Y.; Nakazawa, Y.; Kuroda, T.; Ikehata, S.; Uno, M.; Nishikawa, T.; Kawase, T. High-Mobility Double-Gate Organic Single-Crystal Transistors with Organic Crystal Gate Insulators. *Applied Physics Letters* **2007**, *90* (18), 12–15.
- (29) Tiwari, S.; Greenham, N. C. Charge Mobility Measurement Techniques in Organic Semiconductors. *Optical and Quantum Electronics* **2009**, *41* (2), 69–89.
- (30) Bredas, J. L. Mind the Gap! *Materials Horizons* **2014**, *1* (1), 17–19.
- (31) Park, S. K.; Jackson, T. N.; Anthony, J. E.; Mourey, D. A. High Mobility Solution Processed 6,13-Bis(Triisopropyl-Silylethynyl) Pentacene Organic Thin Film Transistors. *Applied Physics Letters* **2007**, *91* (6), 6–9.
- (32) Minemawari, H.; Yamada, T.; Matsui, H.; Tsutsumi, J. Y.; Haas, S.; Chiba, R.; Kumai, R.; Hasegawa, T. Inkjet Printing of Single-Crystal Films. *Nature* **2011**, *475* (7356), 364–367.
- (33) Xie, W.; Willa, K.; Wu, Y.; Häusermann, R.; Takimiya, K.; Batlogg, B.; Frisbie, C. D. Temperature-Independent Transport in High-Mobility Dinaphtho-Thieno- Thiophene (DNNT) Single Crystal Transistors. *Advanced Materials* **2013**, *25* (25), 3478–3484.
- (34) Nakayama, K.; Hirose, Y.; Soeda, J.; Yoshizumi, M.; Uemura, T.; Uno, M.; Li, W.; Kang, M. J.; Yamagishi, M.; Okada, Y.; et al. Patternable Solution-Crystallized Organic Transistors with High Charge Carrier Mobility. *Advanced Materials* **2011**, *23* (14), 1626–1629.
- (35) Iino, H.; Usui, T.; Hanna, J. Liquid Crystals for Organic Thin-Film Transistors. *Nature Communications* **2015**, *6* (1), 6828.
- (36) Iino, H.; Hanna, J. Liquid Crystalline Organic Semiconductors for Organic Transistor Applications. *Polymer Journal* **2017**, *49* (1), 23–30.
- (37) Okamoto, T.; Mitsui, C.; Yamagishi, M.; Nakahara, K.; Soeda, J.; Hirose, Y.; Miwa, K.;

- Sato, H.; Yamano, A.; Matsushita, T.; et al. V-Shaped Organic Semiconductors with Solution Processability, High Mobility, and High Thermal Durability. *Advanced Materials* **2013**, *25* (44), 6392–6397.
- (38) Mitsui, C.; Okamoto, T.; Yamagishi, M.; Tsurumi, J.; Yoshimoto, K.; Nakahara, K.; Soeda, J.; Hirose, Y.; Sato, H.; Yamano, A.; et al. High-Performance Solution-Processable N-Shaped Organic Semiconducting Materials with Stabilized Crystal Phase. *Advanced Materials* **2014**, *26* (26), 4546–4551.
- (39) Yamamura, A.; Watanabe, S.; Uno, M.; Mitani, M.; Mitsui, C.; Tsurumi, J.; Isahaya, N.; Kanaoka, Y.; Okamoto, T.; Takeya, J. Wafer-Scale, Layer-Controlled Organic Single Crystals for High-Speed Circuit Operation. *Science Advances* **2018**, *4* (2).
- (40) Jones, B. A.; Ahrens, M. J.; Yoon, M.; Facchetti, A.; Marks, T. J.; Wasielewski, M. R. High-Mobility Air-Stable n-Type Semiconductors with Processing Versatility: Dicyanoperylene-3,4:9,10-Bis(Dicarboximides)**. *Angewandte chemie* **2004**, *43*, 6363–6366.
- (41) Minder, N. A.; Ono, S.; Chen, Z.; Facchetti, A.; Morpurgo, A. F. Band-Like Electron Transport in Organic Transistors and Implication of the Molecular Structure for Performance Optimization. *Advanced Materials* **2012**, *24*, 503–508.
- (42) Chu, M.; Fan, J.-X.; Yang, S.; Liu, D.; Ng, C. F.; Dong, H.; Ren, A.-M.; Miao, Q. Halogenated Tetraazapentacenes with Electron Mobility as High as 27.8 $\text{cm}^2 \text{V}^{-1} \text{S}^{-1}$ in Solution-Processed n-Channel Organic Thin-Film Transistors. *Advanced Materials* **2018**, *30* (38), 1803467.
- (43) He, T.; Stolte, M.; Würthner, F. Air-Stable n-Channel Organic Single Crystal Field-Effect Transistors Based on Microribbons of Core-Chlorinated Naphthalene Diimide. *Advanced Materials* **2013**, *25* (48), 6951–6955.
- (44) Hou, L.; Zhang, X.; Cotella, G. F.; Carnicella, G.; Herder, M.; Schmidt, B. M.; Pätzelt, M.; Hecht, S.; Cacialli, F.; Samorì, P. Optically Switchable Organic Light-Emitting Transistors. *Nature Nanotechnology* **2019**, *14* (April), 347–353.
- (45) Jiang, H.; Hu, W. The Emergence of Organic Single-Crystal Electronics. *Angewandte Chemie - International Edition*. 2020, pp 1408–1428.
- (46) Luo, C.; Kyaw, A. K. K.; Perez, L. A.; Patel, S.; Wang, M.; Grimm, B.; Bazan, G. C.; Kramer, E. J.; Heeger, A. J. General Strategy for Self-Assembly of Highly Oriented Nanocrystalline Semiconducting Polymers with High Mobility. *Nano Letters* **2014**, *14* (5), 2764–2771.
- (47) Zhao, Z.; Yin, Z.; Chen, H.; Zheng, L.; Zhu, C.; Zhang, L.; Tan, S.; Wang, H.; Guo, Y.; Tang, Q.; et al. High-Performance, Air-Stable Field-Effect Transistors Based on

- Heteroatom-Substituted Naphthalenediimide-Benzothiadiazole Copolymers Exhibiting Ultrahigh Electron Mobility up to $8.5 \text{ cm}^2 \text{ V}^{-1} \text{ s}^{-1}$. *Advanced materials (Deerfield Beach, Fla.)* **2017**, *29* (4).
- (48) Lee, J.; Han, A.-R.; Yu, H.; Shin, T. J.; Yang, C.; Oh, J. H. Boosting the Ambipolar Performance of Solution-Processable Polymer Semiconductors via Hybrid Side-Chain Engineering. *Journal of the American Chemical Society* **2013**, *135* (25), 9540–9547.
- (49) He, G. Organic Semiconductor Electroluminescent Materials. In *Organic Optoelectronic Materials*; Li, Y., Ed.; Springer International Publishing: Cham, 2015; pp 241–302.
- (50) Pope, M.; Kallmann, H. P.; Magnante, P. Electroluminescence in Organic Crystals [16]. *The Journal of Chemical Physics* **1963**, *38* (8), 2042–2043.
- (51) Vincett, P. S.; Barlow, W. A.; Hann, R. A.; Roberts, G. G. Electrical Conduction and Low Voltage Blue Electroluminescence in Vacuum-Deposited Organic Films. *Thin Solid Films* **1982**, *94* (2), 171–183.
- (52) Tang, C. W.; VanSlyke, S. A. Organic Electroluminescent Diodes. *Applied Physics Letters* **1987**, *51* (12), 913–915.
- (53) Burroughes, J. H.; Bradley, D. D. C.; Brown, A. R.; Marks, R. N.; Mackay, K.; Friend, R. H.; Burns, P. L.; Holmes, A. B. Light-Emitting Diodes Based on Conjugated Polymers. *Nature* **1990**, *347* (6293), 539–541.
- (54) Pimputkar, S.; Speck, J. S.; DenBaars, S. P.; Nakamura, S. Prospects for LED Lighting. *Nature Photonics* **2009**, *3* (4), 180–182.
- (55) Bui, T. T.; Goubard, F.; Ibrahim-Ouali, M.; Gigmès, D.; Dumur, F. Thermally Activated Delayed Fluorescence Emitters for Deep Blue Organic Light Emitting Diodes: A Review of Recent Advances. *Applied Sciences (Switzerland)* **2018**, *8* (4).
- (56) Baldo, M. A.; O'Brien, D. F.; You, Y.; Shoustikov, A.; Sibley, S.; Thompson, M. E.; Forrest, S. R. Highly Efficient Phosphorescent Emission from Organic Electroluminescent Devices. *Nature* **1998**, *395* (6698), 151–154.
- (57) Cebrián, C.; Mauro, M. Recent Advances in Phosphorescent Platinum Complexes for Organic Light-Emitting Diodes. *Beilstein Journal of Organic Chemistry*. 2018, pp 1459–1481.
- (58) Kim, H. U.; Park, H. J.; Jang, J.-H.; Song, W.; Jung, I. H.; Lee, J. Y.; Hwang, D.-H. Green Phosphorescent Homoleptic Iridium (III) Complexes for Highly Efficient Organic Light-Emitting Diodes. *Dyes and Pigments* **2018**, *156*, 395–402.
- (59) Jang, J.-H.; Park, H. J.; Park, J. Y.; Kim, H. U.; Hwang, D.-H. Orange Phosphorescent Ir(III) Complexes Consisting of Substituted 2-Phenylbenzothiazole for Solution-

- Processed Organic Light-Emitting Diodes. *Organic Electronics* **2018**, *60*, 31–37.
- (60) Lakowicz, J. R. *Principles of Fluorescence Spectroscopy*; 2006.
- (61) Feng, H.-T.; Zeng, J.; Yin, P.-A.; Wang, X.-D.; Peng, Q.; Zhao, Z.; Lam, J. W. Y.; Tang, B. Z. Tuning Molecular Emission of Organic Emitters from Fluorescence to Phosphorescence through Push-Pull Electronic Effects. *Nature Communications* **2020**, *11* (1), 2617.
- (62) Uoyama, H.; Goushi, K.; Shizu, K.; Nomura, H.; Adachi, C. Highly Efficient Organic Light-Emitting Diodes from Delayed Fluorescence. *Nature* **2012**, *492* (7428), 234–238.
- (63) Data, P.; Takeda, Y. Recent Advancements in and the Future of Organic Emitters: TADF- and RTP-Active Multifunctional Organic Materials. *Chemistry – An Asian Journal* **2019**, *14* (10), 1613–1636.
- (64) Endo, A.; Ogasawara, M.; Takahashi, A.; Yokoyama, D.; Kato, Y.; Adachi, C. Thermally Activated Delayed Fluorescence from Sn⁴⁺–Porphyrin Complexes and Their Application to Organic Light Emitting Diodes — A Novel Mechanism for Electroluminescence. *Advanced Materials* **2009**, *21* (47), 4802–4806.
- (65) Goushi, K.; Yoshida, K.; Sato, K.; Adachi, C. Organic Light-Emitting Diodes Employing Efficient Reverse Intersystem Crossing for Triplet-to-Singlet State Conversion. *Nature Photonics* **2012**, *6* (4), 253–258.
- (66) Rogowski, R. Z.; Dzwilewski, A.; Kemerink, M.; Darhuber, A. A. Solution Processing of Semiconducting Organic Molecules for Tailored Charge Transport Properties. *The Journal of Physical Chemistry C* **2011**, *115* (23), 11758–11762.
- (67) Diemer, P. J.; Lyle, C. R.; Mei, Y.; Sutton, C.; Payne, M. M.; Anthony, J. E.; Coropceanu, V.; Brédas, J.-L.; Jurchescu, O. D. Vibration-Assisted Crystallization Improves Organic/Dielectric Interface in Organic Thin-Film Transistors. *Advanced Materials* **2013**, *25* (48), 6956–6962.
- (68) Kim, D. H.; Lee, D. Y.; Lee, H. S.; Lee, W. H.; Kim, Y. H.; Han, J. I.; Cho, K. High-Mobility Organic Transistors Based on Single-Crystalline Microribbons of Triisopropylsilylethynyl Pentacene via Solution-Phase Self-Assembly. *Advanced Materials* **2007**, *19* (5), 678–682.
- (69) Chen, J.; Tee, C. K.; Shtein, M.; Martin, D. C.; Anthony, J. Controlled Solution Deposition and Systematic Study of Charge-Transport Anisotropy in Single Crystal and Single-Crystal Textured TIPS Pentacene Thin Films. *Organic Electronics* **2009**, *10* (4), 696–703.
- (70) Li, X.; Kjellander, B. K. C.; Anthony, J. E.; Bastiaansen, C. W. M.; Broer, D. J.; Gelinck, G. H. Azeotropic Binary Solvent Mixtures for Preparation of Organic Single Crystals.

- Advanced Functional Materials* **2009**, *19* (22), 3610–3617.
- (71) Gu, X.; Shaw, L.; Gu, K.; Toney, M. F.; Bao, Z. The Meniscus-Guided Deposition of Semiconducting Polymers. *Nature Communications* **2018**, *9* (1), 534.
- (72) Diao, Y.; Shaw, L.; Bao, Z.; Mannsfeld, S. C. B. Morphology Control Strategies for Solution-Processed Organic Semiconductor Thin Films. *Energy Environ. Sci.* **2014**, *7* (7), 2145–2159.
- (73) Nam, S.; Jeong, Y. J.; Jung, J.; Kim, S. H.; Ahn, J.; Shin, K.; Jang, J. Direct Printing of Soluble Acene Crystal Stripes by a Programmed Dip-Coating Process for Organic Field-Effect Transistor Applications. *Journal of Materials Chemistry C* **2018**, *6* (4), 799–807.
- (74) Sanchez-Herencia, A. J. Water Based Colloidal Processing of Ceramic Laminates. *Key Engineering Materials* **2007**, *333*, 39–48.
- (75) Chen, C. Y.; Chang, H. W.; Chang, Y. F.; Chang, B. J.; Lin, Y. S.; Jian, P. S.; Yeh, H. C.; Chien, H. T.; Chen, E. C.; Chao, Y. C.; et al. Continuous Blade Coating for Multi-Layer Large-Area Organic Light-Emitting Diode and Solar Cell. *Journal of Applied Physics* **2011**, *110* (9), 094501.
- (76) Tseng, S. R.; Meng, H. F.; Lee, K. C.; Horng, S. F. Multilayer Polymer Light-Emitting Diodes by Blade Coating Method. *Applied Physics Letters* **2008**, *93* (15), 2006–2009.
- (77) Krebs, F. C. Fabrication and Processing of Polymer Solar Cells: A Review of Printing and Coating Techniques. *Solar Energy Materials and Solar Cells* **2009**, *93* (4), 394–412.
- (78) Xiong, K.; Hou, L.; Wu, M.; Huo, Y.; Mo, W.; Yuan, Y.; Sun, S.; Xu, W.; Wang, E. From Spin Coating to Doctor Blading: A Systematic Study on the Photovoltaic Performance of an Isoindigo-Based Polymer. *Solar Energy Materials and Solar Cells* **2015**, *132*, 252–259.
- (79) Mens, R.; Adriaensens, P.; Lutsen, L.; Swinnen, A.; Bertho, S.; Ruttens, B.; D’Haen, J.; Manca, J.; Cleij, T.; Vanderzande, D.; et al. NMR Study of the Nanomorphology in Thin Films of Polymer Blends Used in Organic PV Devices: MDMO-PPV/PCBM. *Journal of Polymer Science, Part A: Polymer Chemistry* **2008**, *46* (1), 138–145.
- (80) Hellstrom, S. L. Basic Models of Spin Coating. *Coursework for Physics 210, Stanford University.* **2007**.
- (81) Chang, J. F.; Sun, B.; Breiby, D. W.; Nielsen, M. M.; Sölling, T. I.; Giles, M.; McCulloch, I.; Sirringhaus, H. Enhanced Mobility of Poly(3-Hexylthiophene) Transistors by Spin-Coating from High-Boiling-Point Solvents. *Chemistry of Materials* **2004**, *16* (23), 4772–4776.
- (82) McCulloch, I.; Heeney, M.; Bailey, C.; Genevicius, K.; MacDonald, I.; Shkunov, M.;

- Sparrowe, D.; Tierney, S.; Wagner, R.; Zhang, W.; et al. Liquid-Crystalline Semiconducting Polymers with High Charge-Carrier Mobility. *Nature Materials* **2006**, *5* (4), 328–333.
- (83) Yuan, Y.; Giri, G.; Ayzner, A. L.; Zoombelt, A. P.; Mannsfeld, S. C. B.; Chen, J.; Nordlund, D.; Toney, M. F.; Huang, J.; Bao, Z. Ultra-High Mobility Transparent Organic Thin Film Transistors Grown by an off-Centre Spin-Coating Method. *Nature Communications* **2014**, *5* (1), 3005.
- (84) Wu, C. C.; Sturm, J. C.; Register, R. A.; Thompson, M. E. Integrated Three-Color Organic Light-Emitting Devices. *Applied Physics Letters* **1996**, *69* (21), 3117–3119.
- (85) Gu, G.; Forrest, S. R. Design of Flat-Panel Displays Based on Organic Light-Emitting Devices. *IEEE Journal on Selected Topics in Quantum Electronics* **1998**, *4* (1), 83–99.
- (86) Lan, L.; Zou, J.; Jiang, C.; Liu, B.; Wang, L.; Peng, J. Inkjet Printing for Electroluminescent Devices: Emissive Materials, Film Formation, and Display Prototypes. *Frontiers of Optoelectronics*. 2017, pp 329–352.
- (87) Krebs, F. C. Fabrication and Processing of Polymer Solar Cells: A Review of Printing and Coating Techniques. *Solar Energy Materials and Solar Cells*. 2009.
- (88) Singh, M.; Haverinen, H. M.; Dhagat, P.; Jabbour, G. E. Inkjet Printing-Process and Its Applications. *Advanced Materials* **2010**, *22* (6), 673–685.
- (89) Yin, Z. P.; Huang, Y. A.; Bu, N. Bin; Wang, X. M.; Xiong, Y. L. Inkjet Printing for Flexible Electronics: Materials, Processes and Equipments. *Chinese Science Bulletin*. 2010, pp 3383–3407.
- (90) Molina-Lopez, F.; Gao, T. Z.; Kraft, U.; Zhu, C.; Öhlund, T.; Pfattner, R.; Feig, V. R.; Kim, Y.; Wang, S.; Yun, Y.; et al. Inkjet-Printed Stretchable and Low Voltage Synaptic Transistor Array. *Nature Communications* **2019**, *10* (1), 1–10.
- (91) Mandal, S.; Noh, Y. Y. Printed Organic Thin-Film Transistor-Based Integrated Circuits. *Semiconductor Science and Technology*. 2015, p 064003.
- (92) Hösel, M.; Angmo, D.; Søndergaard, R. R.; dos Reis Benatto, G. A.; Carlé, J. E.; Jørgensen, M.; Krebs, F. C. High-Volume Processed, ITO-Free Superstrates and Substrates for Roll-to-Roll Development of Organic Electronics. *Advanced Science* **2014**, *1* (1).
- (93) Huang, Q.; Zhu, Y. Printing Conductive Nanomaterials for Flexible and Stretchable Electronics: A Review of Materials, Processes, and Applications. *Advanced Materials Technologies*. 2019.
- (94) Gu, X.; Zhou, Y.; Gu, K.; Kurosawa, T.; Guo, Y.; Li, Y.; Lin, H.; Schroeder, B. C.; Yan, H.; Molina-Lopez, F.; et al. Roll-to-Roll Printed Large-Area All-Polymer Solar Cells

- with 5% Efficiency Based on a Low Crystallinity Conjugated Polymer Blend. *Advanced Energy Materials* **2017**, 7 (14), 1–13.
- (95) Voigt, M. M.; Cuite, A.; Chung, D. Y.; Khan, R. U. A.; Campbell, A. J.; Bradley, D. D. C.; Meng, F.; Steinke, J. H. G.; Tierney, S.; McCulloch, L.; et al. Polymer Field-Effect Transistors Fabricated by the Sequential Gravure Printing of Polythiophene, Two Insulator Layers, and a Metal Ink Gate. *Advanced Functional Materials* **2010**, 20 (2), 239–246.
- (96) Søndergaard, R. R.; Hösel, M.; Krebs, F. C. Roll-to-Roll Fabrication of Large Area Functional Organic Materials. *Journal of Polymer Science, Part B: Polymer Physics*. 2013, pp 16–34.
- (97) Galagan, Y.; de Vries, I. G.; Langen, A. P.; Andriessen, R.; Verhees, W. J. H.; Veenstra, S. C.; Kroon, J. M. Technology Development for Roll-to-Roll Production of Organic Photovoltaics. *Chemical Engineering and Processing: Process Intensification* **2011**, 50 (5–6), 454–461.
- (98) Sykes, M. E. Circumventing the Tradeoff between Optical Absorption and Exciton Diffusion in Organic Photovoltaics By. **2015**.
- (99) Usta, H.; Kim, D.; Ozdemir, R.; Zorlu, Y.; Kim, S.; Ruiz Delgado, M. C.; Harbuzaru, A.; Kim, S.; Demirel, G.; Hong, J.; et al. High Electron Mobility in [1]Benzothieno[3,2-b][1]Benzothiophene-Based Field-Effect Transistors: Toward n-Type BTBTs. *Chemistry of Materials* **2019**, 31 (14), 5254–5263.
- (100) Amin, A. Y.; Khassanov, A.; Reuter, K.; Meyer-friedrichsen, T.; Halik, M. Low-Voltage OFET with C13-BTBT Semiconductor Layer. *Journal of the American Chemical Society* **2012**, 134 (40), 16548–16550.
- (101) Kim, B. J.; Miyamoto, Y.; Ma, B.; Fréchet, J. M. J. Photocrosslinkable Polythiophenes for Efficient, Thermally Stable, Organic Photovoltaics. *Advanced Functional Materials* **2009**.
- (102) Shtein, M.; Mapel, J.; Benziger, J. B.; Forrest, S. R. Effects of Film Morphology and Gate Dielectric Surface Preparation on the Electrical Characteristics of Organic-Vapor-Phase-Deposited Pentacene Thin-Film Transistors. *Applied Physics Letters* **2002**, 81 (2), 268–270.
- (103) Ye, X.; Liu, Y.; Guo, Q.; Han, Q.; Ge, C.; Cui, S.; Zhang, L.; Tao, X. 1D versus 2D Cocrystals Growth via Microspacing In-Air Sublimation. *Nature Communications* **2019**, 10 (1).
- (104) Liu, X.; Su, X.; Livache, C.; Chamoreau, L. M.; Sanaur, S.; Sosa-Vargas, L.; Ribierre, J. C.; Kreher, D.; Lhuillier, E.; Lacaze, E.; et al. Investigation of Charge Transport

- Properties of [1]Benzothieno[3,2-b][1]-Benzothiophene Single-Crystals in Field-Effect Transistor Configuration. *Organic Electronics* **2020**, 78 (December 2019), 2–8.
- (105) Maunoury, J. C.; Howse, J. R.; Turner, M. L. Melt-Processing of Conjugated Liquid Crystals: A Simple Route to Fabricate OFETs. *Advanced Materials* **2007**, 19 (6), 805–809.
- (106) Kim, A.; Jang, K. S.; Kim, J.; Won, J. C.; Yi, M. H.; Kim, H.; Yoon, D. K.; Shin, T. J.; Lee, M. H.; Ka, J. W.; et al. Solvent-Free Directed Patterning of a Highly Ordered Liquid Crystalline Organic Semiconductor via Template-Assisted Self-Assembly for Organic Transistors. *Advanced Materials* **2013**, 25 (43), 6219–6225.
- (107) Ribierre, J. C.; Li, Z.; Liu, X.; Lacaze, E.; Heinrich, B.; Méry, S.; Sleczkowski, P.; Xiao, Y.; Lafolet, F.; Hashizume, D.; et al. A Solvent-Free and Vacuum-Free Melt-Processing Method to Fabricate Organic Semiconducting Layers with Large Crystal Size for Organic Electronic Applications. *Journal of Materials Chemistry C* **2019**, 7 (11), 3190–3198.
- (108) Lee, T.-W.; Noh, T.; Shin, H.-W.; Kwon, O.; Park, J.-J.; Choi, B.-K.; Kim, M.-S.; Shin, D. W.; Kim, Y.-R. Characteristics of Solution-Processed Small-Molecule Organic Films and Light-Emitting Diodes Compared with Their Vacuum-Deposited Counterparts. *Advanced Functional Materials* **2009**, 19 (10), 1625–1630.
- (109) Shibata, M.; Sakai, Y.; Yokoyama, D. Advantages and Disadvantages of Vacuum-Deposited and Spin-Coated Amorphous Organic Semiconductor Films for Organic Light-Emitting Diodes. *J. Mater. Chem. C* **2015**, 3 (42), 11178–11191.
- (110) Schweicher, G.; Garbay, G.; Jouclas, R.; Vibert, F.; Devaux, F.; Geerts, Y. H. Molecular Semiconductors for Logic Operations: Dead-End or Bright Future? *Advanced Materials* **2020**, 32 (10), 1905909.
- (111) Liu, C.; Huang, K.; Park, W. T.; Li, M.; Yang, T.; Liu, X.; Liang, L.; Minari, T.; Noh, Y. Y. A Unified Understanding of Charge Transport in Organic Semiconductors: The Importance of Attenuated Delocalization for the Carriers. *Materials Horizons* **2017**, 4 (4), 608–618.
- (112) Kus, M.; Alic, T. Y.; Kirbiyik, C.; Baslak, C.; Kara, K.; Kara, D. A. Chapter 24 - Synthesis of Nanoparticles. In *Micro and Nano Technologies*; Mustansar Hussain, C. B. T.-H. of N. for I. A., Ed.; Elsevier, 2018; pp 392–429.
- (113) Kepler, R. G. Charge Carrier Production and Mobility in Anthracene Crystals. *Phys. Rev.* **1960**, 119 (4), 1226–1229.
- (114) LeBlanc, O. H. Hole and Electron Drift Mobilities in Anthracene. *The Journal of Chemical Physics* **1960**, 33 (2), 626.

- (115) Horowitz, G.; Delannoy, P. Charge Transport in Semiconducting Oligothiophenes. In *Handbook of Oligo- and Polythiophenes*; John Wiley & Sons, Ltd, 2007; pp 283–316.
- (116) Li, Q. *Self-Organized Organic Semiconductors: From Materials to Device Applications*; John Wiley & Sons, 2011.
- (117) Cho, S.; Kim, K.; Kim, T.; Park, H.; Kim, J.-M.; Lee, S.; Kang, Y.; Chang, K.; Kim, C. High-Contrast Imaging of Cholesterol Crystals in Rabbit Arteries Ex Vivo Using LED-Based Polarization Microscopy. *Sensors (Basel, Switzerland)* **2018**, *18* (4), 1258.
- (118) Yuan, Q.; Mannsfeld, S. C. B.; Tang, M. L.; Roberts, M.; Toney, M. F.; DeLongchamp, D. M.; Bao, Z. Microstructure of Oligofluorene Asymmetric Derivatives in Organic Thin Film Transistors. *Chemistry of Materials* **2008**, *20* (8), 2763–2772.
- (119) Fritz, S. E.; Martin, S. M.; Frisbie, C. D.; Ward, M. D.; Toney, M. F. Structural Characterization of a Pentacene Monolayer on an Amorphous SiO₂ Substrate with Grazing Incidence X-Ray Diffraction. *Journal of the American Chemical Society* **2004**, *126* (13), 4084–4085.
- (120) Mannsfeld, S. C. B.; Tang, M. L.; Bao, Z. Thin Film Structure of Triisopropylsilylethynyl-Functionalized Pentacene and Tetraceno[2,3-b]Thiophene from Grazing Incidence X-Ray Diffraction. *Advanced Materials* **2011**, *23* (1), 127–131.
- (121) Yuan, Q.; Mannsfeld, S. C. B.; Tang, M. L.; Toney, M. F.; Lüning, J.; Bao, Z. Thin Film Structure of Tetraceno[2,3-b]Thiophene Characterized by Grazing Incidence X-Ray Scattering and Near-Edge X-Ray Absorption Fine Structure Analysis. *Journal of the American Chemical Society* **2008**, *130* (11), 3502–3508.
- (122) Widjonarko, N. Introduction to Advanced X-Ray Diffraction Techniques for Polymeric Thin Films. *Coatings* **2016**, *6*, 54.
- (123) Knoll, W.; Advincula, R. C. *Functional Polymer Films, 2 Volume Set*; John Wiley & Sons, 2013.
- (124) Mannsfeld, S. C. B.; Virkar, A.; Reese, C.; Toney, M. F.; Bao, Z. Precise Structure of Pentacene Monolayers on Amorphous Silicon Oxide and Relation to Charge Transport. *Advanced Materials* **2009**, *21* (22), 2294–2298.
- (125) Binnig, G.; Quate, C. F.; Gerber, C. Atomic Force Microscope. *Phys. Rev. Lett.* **1986**, *56* (9), 930–933.
- (126) Dufrêne, Y. F.; Ando, T.; Garcia, R.; Alsteens, D.; Martinez-Martin, D.; Engel, A.; Gerber, C.; Müller, D. J. Imaging Modes of Atomic Force Microscopy for Application in Molecular and Cell Biology. *Nature Nanotechnology* **2017**, *12* (4), 295–307.
- (127) Wang, D.; Russell, T. P. Advances in Atomic Force Microscopy for Probing Polymer Structure and Properties. *Macromolecules*. 2018, pp 3–24.

- (128) Schönherr, H.; Vancso, G. J.; Schönherr, H.; Vancso, G. J. Atomic Force Microscopy in Practice. In *Scanning Force Microscopy of Polymers*; 2010; pp 25–75.
- (129) Schönherr, H.; Vancso, G. J.; Schönherr, H.; Vancso, G. J. Physical Principles of Scanning Probe Microscopy Imaging. In *Scanning Force Microscopy of Polymers*; 2010; pp 3–24.
- (130) Zhong, Q.; Inniss, D.; Kjoller, K.; Elings, V. B. Fractured Polymer/Silica Fiber Surface Studied by Tapping Mode Atomic Force Microscopy. *Surface Science Letters* **1993**, *290* (1), L688–L692.
- (131) Asmatulu, R.; Khan, W. S. Chapter 13 - Characterization of Electrospun Nanofibers. In *Synthesis and Applications of Electrospun Nanofibers*; Asmatulu, R., Khan, W. S., Eds.; Micro and Nano Technologies; Elsevier, 2019; pp 257–281.
- (132) Schmitz, I.; Schreiner, M.; Friedbacher, G.; Grasserbauer, M. Tapping-Mode AFM in Comparison to Contact-Mode AFM as a Tool for in Situ Investigations of Surface Reactions with Reference to Glass Corrosion. *Analytical Chemistry* **1997**, *69* (6), 1012–1018.
- (133) Prater, C. B.; Maivald, P. G.; Kjoller, K. J.; Heaton, M. G. Tappingmode Imaging Applications and Technology. *Digital Instruments Nanonotes, Santa Barbara, California, USA* **1995**.
- (134) Levitsky, I. A.; Kishikawa, K.; Eichhorn, S. H.; Swager, T. M. Exciton Coupling and Dipolar Correlations in a Columnar Liquid Crystal: Photophysics of a Bent-Rod Hexacatenar Mesogen. *Journal of the American Chemical Society* **2000**, *122* (11), 2474–2479.
- (135) Yuan, W. Z.; Lu, P.; Chen, S.; Lam, J. W. Y.; Wang, Z.; Liu, Y.; Kwok, H. S.; Ma, Y.; Tang, B. Z. Changing the Behavior of Chromophores from Aggregation-Caused Quenching to Aggregation-Induced Emission: Development of Highly Efficient Light Emitters in the Solid State. *Advanced Materials* **2010**, *22* (19), 2159–2163.
- (136) Dou, L.; Liu, Y.; Hong, Z.; Li, G.; Yang, Y. Low-Bandgap near-IR Conjugated Polymers/Molecules for Organic Electronics. *Chemical reviews* **2015**, *115* (23), 12633–12665.
- (137) Zhao, Y.; Guo, Y.; Liu, Y. 25th Anniversary Article: Recent Advances in n-Type and Ambipolar Organic Field-Effect Transistors. *Advanced Materials* **2013**, *25* (38), 5372–5391.
- (138) Janssen, R. A. J.; Nelson, J. Factors Limiting Device Efficiency in Organic Photovoltaics. *Advanced Materials* **2013**, *25* (13), 1847–1858.
- (139) Wang, E.; Mammo, W.; Andersson, M. R. 25th Anniversary Article: Isoindigo-Based

- Polymers and Small Molecules for Bulk Heterojunction Solar Cells and Field Effect Transistors. *Advanced Materials* **2014**, *26* (12), 1801–1826.
- (140) Mei, J.; Graham, K. R.; Stalder, R.; Reynolds, J. R. Synthesis of Isoindigo-Based Oligothiophenes for Molecular Bulk Heterojunction Solar Cells. *Organic Letters* **2010**, *12* (4), 660–663.
- (141) Nagamatsu, S.; Takashima, W.; Kaneto, K.; Yoshida, Y.; Tanigaki, N.; Yase, K. Polymer Field-Effect Transistors by a Drawing Method. *Applied Physics Letters* **2004**, *84* (23), 4608–4610.
- (142) Shtein, M.; Peumans, P.; Benziger, J. B.; Forrest, S. R. Direct, Mask- and Solvent-Free Printing of Molecular Organic Semiconductors. *Advanced Materials* **2004**, *16* (18), 1615–1620.
- (143) Matsushima, T.; Sandanayaka, A. S. D.; Esaki, Y.; Adachi, C. Vacuum-and-Solvent-Free Fabrication of Organic Semiconductor Layers for Field-Effect Transistors. *Scientific Reports* **2015**, *5* (1), 14547.
- (144) Kéna-Cohen, S.; Forrest, S. R. Room-Temperature Polariton Lasing in an Organic Single-Crystal Microcavity. *Nature Photonics* **2010**, *4* (6), 371–375.
- (145) Lessel, M.; Baumchen, O.; Klos, M.; Hähl, H.; Fetzer, R.; Paulus, M.; Seemann, R.; Jacobs, K. Self-Assembled Silane Monolayers: An Efficient Step-by-Step Recipe for High-Quality, Low Energy Surfaces. *Surface and Interface Analysis* **2015**, *47* (5), 557–564.
- (146) Ribierre, J.-C.; Zhao, L.; Inoue, M.; Schwartz, P.-O.; Kim, J.-H.; Yoshida, K.; Sandanayaka, A. S. D.; Nakanotani, H.; Mager, L.; Méry, S.; et al. Low Threshold Amplified Spontaneous Emission and Ambipolar Charge Transport in Non-Volatile Liquid Fluorene Derivatives. *Chem. Commun.* **2016**, *52* (15), 3103–3106.
- (147) Kim, J.-H.; Inoue, M.; Zhao, L.; Komino, T.; Seo, S.; Ribierre, J.-C.; Adachi, C. Tunable and Flexible Solvent-Free Liquid Organic Distributed Feedback Lasers. *Applied Physics Letters* **2015**, *106* (5), 53302.
- (148) Ribierre, J. C.; Aoyama, T.; Kobayashi, T.; Sassa, T.; Muto, T.; Wada, T. Influence of the Liquid Carbazole Concentration on Charge Trapping in C60 Sensitized Photorefractive Polymers. *Journal of Applied Physics* **2007**, *102* (3), 33106.
- (149) Smilgies, D.-M. Scherrer Grain-Size Analysis Adapted to Grazing-Incidence Scattering with Area Detectors. Erratum. *Journal of Applied Crystallography* **2013**, *46* (1), 286.
- (150) Deng, J.; Xu, Y.; Liu, L.; Feng, C.; Tang, J.; Gao, Y.; Wang, Y.; Yang, B.; Lu, P.; Yang, W.; et al. An Ambipolar Organic Field-Effect Transistor Based on an AIE-Active Single Crystal with a High Mobility Level of $2.0 \text{ cm}^2 \text{ V}^{-1} \text{ s}^{-1}$. *Chem. Commun.* **2016**, *52*

- (11), 2370–2373.
- (151) Deng, J.; Tang, J.; Xu, Y.; Liu, L.; Wang, Y.; Xie, Z.; Ma, Y. Cyano-Substituted Oligo(p-Phenylene Vinylene) Single-Crystal with Balanced Hole and Electron Injection and Transport for Ambipolar Field-Effect Transistors. *Phys. Chem. Chem. Phys.* **2015**, *17* (5), 3421–3425.
- (152) Szafranek, B. N.; Fiori, G.; Schall, D.; Neumaier, D.; Kurz, H. Current Saturation and Voltage Gain in Bilayer Graphene Field Effect Transistors. *Nano Letters* **2012**, *12* (3), 1324–1328.
- (153) Gundlach, D. J.; Zhou, L.; Nichols, J. A.; Jackson, T. N.; Necliudov, P. V.; Shur, M. S. An Experimental Study of Contact Effects in Organic Thin Film Transistors. *Journal of Applied Physics* **2006**, *100* (2), 024509.
- (154) Qiu, L.; Xu, Q.; Chen, M.; Wang, X.; Wang, X.; Zhang, G. Low-Temperature Melt Processed Polymer Blend for Organic Thin-Film Transistors. *J. Mater. Chem.* **2012**, *22* (36), 18887–18892.
- (155) Liu, C.; Xu, Y.; Noh, Y. Y. Contact Engineering in Organic Field-Effect Transistors. *Materials Today* **2015**, *18* (2), 79–96.
- (156) Davidson-Hall, T.; Kajiyama, Y.; Aziz, H. Organic Light Emitting Device Materials for Displays. In *Materials for Solid State Lighting and Displays*; John Wiley & Sons, Ltd, 2016; pp 183–230.
- (157) Baldo, M. A.; Adachi, C.; Forrest, S. R. Transient Analysis of Organic Electrophosphorescence. II. Transient Analysis of Triplet-Triplet Annihilation. *Physical Review B* **2000**, *62* (16), 10967–10977.
- (158) Namdas, E. B.; Ruseckas, A.; Samuel, I. D. W.; Lo, S.-C.; Burn, P. L. Triplet Exciton Diffusion in Fac-Tris(2-Phenylpyridine) Iridium(III)-Cored Electroluminescent Dendrimers. *Applied Physics Letters* **2005**, *86* (9), 91104.
- (159) Shin, H.-Y.; Woo, J. H.; Gwon, M. J.; Barthelemy, M.; Vomir, M.; Muto, T.; Takaishi, K.; Uchiyama, M.; Hashizume, D.; Aoyama, T.; et al. Exciton Diffusion in Near-Infrared Absorbing Solution-Processed Organic Thin Films. *Physical Chemistry Chemical Physics* **2013**, *15* (8), 2867–2872.
- (160) Hedley, G. J.; Ruseckas, A.; Samuel, I. D. W. Light Harvesting for Organic Photovoltaics. *Chemical Reviews*. 2017.
- (161) Scully, S. R.; McGehee, M. D. Effects of Optical Interference and Energy Transfer on Exciton Diffusion Length Measurements in Organic Semiconductors. *Journal of Applied Physics* **2006**, *100* (3), 034907.
- (162) Lin, J. D. A.; Mikhnenko, O. V.; Chen, J.; Masri, Z.; Ruseckas, A.; Mikhailovsky, A.;

- Raab, R. P.; Liu, J.; Blom, P. W. M.; Loi, M. A.; et al. Systematic Study of Exciton Diffusion Length in Organic Semiconductors by Six Experimental Methods. *Materials Horizons* **2014**.
- (163) Shaw, P. E.; Ruseckas, A.; Samuel, I. D. W. Exciton Diffusion Measurements in Poly(3-Hexylthiophene). *Advanced Materials* **2008**, *20* (18), 3516–3520.
- (164) Markov, D. E.; Amsterdam, E.; Blom, P. W. M.; Sieval, A. B.; Hummelen, J. C. Accurate Measurement of the Exciton Diffusion Length in a Conjugated Polymer Using a Heterostructure with a Side-Chain Cross-Linked Fullerene Layer. *Journal of Physical Chemistry A* **2005**, *109* (24), 5266–5274.
- (165) Ribierre, J. C.; Ruseckas, A.; Samuel, I. D. W.; Barcena, H. S.; Burn, P. L. Influence of the Dendron Chemical Structure on the Photophysical Properties of Bisfluorene-Cored Dendrimers. *Journal of Chemical Physics* **2008**, *128* (20), 204703.
- (166) Ruseckas, A.; Ribierre, J. C.; Shaw, P. E.; Staton, S. V.; Burn, P. L.; Samuel, I. D. W. Singlet Energy Transfer and Singlet-Singlet Annihilation in Light-Emitting Blends of Organic Semiconductors. *Applied Physics Letters* **2009**, *95* (18), 183305.
- (167) Stevens, M. A.; Silva, C.; Russell, D. M.; Friend, R. H. Exciton Dissociation Mechanisms in the Polymeric Semiconductors Poly(9,9-Dioctylfluorene) and Poly(9,9-Dioctylfluorene-Co-Benzothiadiazole). *Physical Review B - Condensed Matter and Materials Physics* **2001**, *63* (16), 165213.
- (168) Lunt, R. R.; Giebink, N. C.; Belak, A. A.; Benziger, J. B.; Forrest, S. R. Exciton Diffusion Lengths of Organic Semiconductor Thin Films Measured by Spectrally Resolved Photoluminescence Quenching. *Journal of Applied Physics* **2009**, *105* (5), 053711.
- (169) Lunt, R. R.; Benziger, J. B.; Forrest, S. R. Relationship between Crystalline Order and Exciton Diffusion Length in Molecular Organic Semiconductors. *Advanced Materials* **2010**, *22* (11), 1233–1236.
- (170) Mullenbach, T. K.; McGarry, K. A.; Luhman, W. A.; Douglas, C. J.; Holmes, R. J. Connecting Molecular Structure and Exciton Diffusion Length in Rubrene Derivatives. *Advanced Materials* **2013**, *25* (27), 3689–3693.
- (171) Lelaidier, T.; Leoni, T.; Ranguis, A.; D'Aléo, A.; Fages, F.; Becker, C. Adsorption and Growth of Bis-Pyrene Molecular Layers on Au(111) Studied by STM. *The Journal of Physical Chemistry C* **2017**, *121* (13), 7214–7220.
- (172) Takimiya, K.; Osaka, I.; Mori, T.; Nakano, M. Organic Semiconductors Based on [1]Benzothieno[3,2- B][1]Benzothiophene Substructure. *Accounts of Chemical Research* **2014**, *47* (5), 1493–1502.

- (173) Takimiya, K.; Ebata, H.; Sakamoto, K.; Izawa, T.; Otsubo, T.; Kunugi, Y. 2,7-Diphenyl[1]Benzothieno[3,2-b]Benzothiophene, A New Organic Semiconductor for Air-Stable Organic Field-Effect Transistors with Mobilities up to $2.0 \text{ cm}^2 \text{ V}^{-1} \text{ s}^{-1}$. *Journal of the American Chemical Society* **2006**, *128* (39), 12604–12605.
- (174) Roche, G. H.; Tsai, Y.-T.; Clevers, S.; Thuau, D.; Castet, F.; Geerts, Y. H.; Moreau, J. J. E.; Wantz, G.; Dautel, O. J. The Role of H-Bonds in the Solid State Organization of [1]Benzothieno[3,2-b][1]Benzothiophene (BTBT) Structures: Bis(Hydroxy-Hexyl)-BTBT, as a Functional Derivative Offering Efficient Air Stable Organic Field Effect Transistors (OFETs). *J. Mater. Chem. C* **2016**, *4* (28), 6742–6749.
- (175) Roche, G. H.; Thuau, D.; Valvin, P.; Clevers, S.; Tjoutis, T.; Chambon, S.; Flot, D.; Geerts, Y. H.; Moreau, J. J. E.; Wantz, G.; et al. π -Conjugated Organosilica Semiconductors: Toward Robust Organic Electronics. *Advanced Electronic Materials* **2017**, *3* (9), 1700218.
- (176) Amin, A. Y.; Khassanov, A.; Reuter, K.; Meyer-Friedrichsen, T.; Halik, M. Low-Voltage Organic Field Effect Transistors with a 2-Tridecyl[1] Benzothieno[3,2-b][1]Benzothiophene Semiconductor Layer. *Journal of the American Chemical Society* **2012**.
- (177) Minemawari, H.; Tanaka, M.; Tsuzuki, S.; Inoue, S.; Yamada, T.; Kumai, R.; Shimoi, Y.; Hasegawa, T. Enhanced Layered-Herringbone Packing Due to Long Alkyl Chain Substitution in Solution-Processable Organic Semiconductors. *Chemistry of Materials* **2017**, *29* (3), 1245–1254.
- (178) Alkan, M.; Yavuz, I. Intrinsic Charge-Mobility in Benzothieno[3,2-b][1]Benzothiophene (BTBT) Organic Semiconductors Is Enhanced with Long Alkyl Side-Chains. *Physical Chemistry Chemical Physics* **2018**, *20* (23), 15970–15979.
- (179) Wang, C.; Abbas, M.; Wantz, G.; Kawabata, K.; Takimiya, K. “Heavy-Atom Effects” in the Parent [1]Benzochalcogenopheno[3,2-b][1]Benzochalcogenophene System. *Journal of Materials Chemistry C* **2020**.
- (180) Ebata, H.; Miyazaki, E.; Yamamoto, T.; Takimiya, K. Synthesis, Properties, and Structures of Benzo[1,2-b:4,5-b']Bis[b] Benzothiophene and Benzo[1,2-b:4,5-b']Bis[b]Benzoselenophene. *Organic Letters* **2007**, *9* (22), 4499–4502.
- (181) Laudise, R. .; Kloc, C.; Simpkins, P. .; Siegrist, T. Physical Vapor Growth of Organic Semiconductors. *Journal of Crystal Growth* **1998**, *187* (3–4), 449–454.
- (182) Briseno, A. L.; Tseng, R. J.; Ling, M.-M.; Falcao, E. H. L.; Yang, Y.; Wudl, F.; Bao, Z. High-Performance Organic Single-Crystal Transistors on Flexible Substrates. *Advanced Materials* **2006**, *18* (17), 2320–2324.

- (183) Vyas, V. S.; Gutzler, R.; Nuss, J.; Kern, K.; Lotsch, B. V. Optical Gap in Herringbone and π -Stacked Crystals of [1]Benzothieno[3,2-b]Benzothiophene and Its Brominated Derivative. *CrystEngComm* **2014**, *16* (32), 7389–7392.
- (184) Lhuillier, E.; Ithurria, S.; Descamps-Mandine, A.; Douillard, T.; Castaing, R.; Xu, X. Z.; Taberna, P. L.; Simon, P.; Aubin, H.; Dubertret, B. Investigating the N- and p-Type Electrolytic Charging of Colloidal Nanoplatelets. *Journal of Physical Chemistry C* **2015**, *119* (38), 21795–21799.
- (185) Lhuillier, E.; Pedetti, S.; Ithurria, S.; Heuclin, H.; Nadal, B.; Robin, A.; Patriarche, G.; Lequeux, N.; Dubertret, B. Electrolyte-Gated Field Effect Transistor to Probe the Surface Defects and Morphology in Films of Thick CdSe Colloidal Nanoplatelets. *ACS Nano* **2014**, *8* (4), 3813–3820.
- (186) Shankar, K.; Jackson, T. N. Morphology and Electrical Transport in Pentacene Films on Silylated Oxide Surfaces. *Journal of Materials Research* **2004**, *19* (7), 2003–2007.
- (187) Seo, H. S.; Jang, Y. S.; Zhang, Y.; Syed Abthagir, P.; Choi, J. H. Fabrication and Characterization of Pentacene-Based Transistors with a Room-Temperature Mobility of 1.25 cm^2/Vs . *Organic Electronics: physics, materials, applications* **2008**, *9* (4), 432–438.
- (188) Goldmann, C.; Gundlach, D. J.; Batlogg, B. Evidence of Water-Related Discrete Trap State Formation in Pentacene Single-Crystal Field-Effect Transistors. *Applied Physics Letters* **2006**, *88* (6), 63501.
- (189) Jurchescu, O. D.; Baas, J.; Palstra, T. T. M. Electronic Transport Properties of Pentacene Single Crystals upon Exposure to Air. *Applied Physics Letters* **2005**, *87* (5), 052102.
- (190) Shimotani, H.; Asanuma, H.; Takeya, J.; Iwasa, Y. Electrolyte-Gated Charge Accumulation in Organic Single Crystals. *Applied Physics Letters* **2006**, *89* (20), 203501.
- (191) Panzer, M. J.; Frisbie, C. D. Polymer Electrolyte-Gated Organic Field-Effect Transistors: Low-Voltage, High-Current Switches for Organic Electronics and Testbeds for Probing Electrical Transport at High Charge Carrier Density. *Journal of the American Chemical Society* **2007**, *129* (20), 6599–6607.
- (192) Wan, J.; Li, Y.; Ulbrandt, J. G.; Smilgies, D.-M.; Hollin, J.; Whalley, A. C.; Headrick, R. L. Transient Phases during Fast Crystallization of Organic Thin Films from Solution. *APL Materials* **2016**, *4* (1), 016103.
- (193) Kobayashi, H.; Kobayashi, N.; Hosoi, S.; Koshitani, N.; Murakami, D.; Shirasawa, R.; Kudo, Y.; Hobara, D.; Tokita, Y.; Itabashi, M. Hopping and Band Mobilities of Pentacene, Rubrene, and 2,7-Dioctyl[1] Benzothieno[3,2-b][1]Benzothiophene (C8-

- BTBT) from First Principle Calculations. *Journal of Chemical Physics* **2013**, *139* (1).
- (194) Izawa, T.; Miyazaki, E.; Takimiya, K. Molecular Ordering of High-Performance Soluble Molecular Semiconductors and Re-Evaluation of Their Field-Effect Transistor Characteristics. *Advanced Materials* **2008**, *20* (18), 3388–3392.
- (195) Saito, M.; Osaka, I.; Miyazaki, E.; Takimiya, K.; Kuwabara, H.; Ikeda, M. One-Step Synthesis of [1]Benzothieno[3,2-b][1]Benzothiophene from o-Chlorobenzaldehyde. *Tetrahedron Letters* **2011**, *52* (2), 285–288.
- (196) Dolomanov, O. V.; Bourhis, L. J.; Gildea, R. J.; Howard, J. A. K.; Puschmann, H. J. OLEX2: A Complete Structure Solution, Refinement and General All Round Good Thing Olex2. *Journal of Applied Crystallography* **2009**, *42* (2), 339–341.
- (197) Sheldrick, G. M. SHELXT--Integrated Space-Group and Crystal-Structure Determination. *Acta Crystallographica Section A* **2015**, *71* (1), 3–8.
- (198) Sheldrick, G. M. Crystal Structure Refinement with SHELXL. *Acta Crystallographica Section C* **2015**, *71* (1), 3–8.
- (199) Sergeev, S.; Pisula, W.; Geerts, Y. H. Discotic Liquid Crystals: A New Generation of Organic Semiconductors. *Chemical Society Reviews* **2007**, *36* (12), 1902–1929.
- (200) Wang, Y.; Shi, J.; Chen, J.; Zhu, W.; Baranoff, E. Recent Progress in Luminescent Liquid Crystal Materials: Design, Properties and Application for Linearly Polarised Emission. *Journal of Materials Chemistry C* **2015**, *3* (31), 7993–8005.
- (201) Luo, J.; Xie, Z.; Lam, J. W. Y.; Cheng, L.; Chen, H.; Qiu, C.; Kwok, H. S.; Zhan, X.; Liu, Y.; Zhu, D.; et al. Aggregation-Induced Emission of 1-Methyl-1, 2, 3, 4, 5-Pentaphenylsilole. *Chemical communications* **2001**, No. 18, 1740–1741.
- (202) Hong, Y.; Lam, J. W. Y.; Tang, B. Z. Aggregation-Induced Emission. *Chemical Society Reviews* **2011**, *40* (11), 5361–5388.
- (203) Yoon, S.-J.; Kim, J. H.; Kim, K. S.; Chung, J. W.; Heinrich, B.; Mathevet, F.; Kim, P.; Donnio, B.; Attias, A.-J.; Kim, D.; et al. Mesomorphic Organization and Thermochromic Luminescence of Dicyanodistyrylbenzene-Based Phasmidic Molecular Disks: Uniaxially Aligned Hexagonal Columnar Liquid Crystals at Room Temperature with Enhanced Fluorescence Emission and Semiconductivity. *Advanced Functional Materials* **2012**, *22* (1), 61–69.
- (204) Huang, D.; Prehm, M.; Gao, H.; Cheng, X.; Liu, Y.; Tschierske, C. Synthesis and Self-Assembly of Luminescent Hexacatenar Molecules Incorporating a 4, 7-Diphenyl-2, 1, 3-Benzothiadiazole Core. *RSC advances* **2016**, *6* (26), 21387–21395.
- (205) Lin, L.; Guo, H.; Fang, X.; Yang, F. Novel AIE Columnar Liquid Crystals: The Influence of the Number of Diphenylacrylonitrile Groups on the Mesomorphic and

- Fluorescence Properties. *RSC advances* **2017**, 7 (33), 20172–20177.
- (206) Wu, X.; Xie, G.; Cabry, C. P.; Xu, X.; Cowling, S. J.; Bruce, D. W.; Zhu, W.; Baranoff, E.; Wang, Y. Linearly Polarized Electroluminescence from Ionic Iridium Complex-Based Metallomesogens: The Effect of Aliphatic-Chain on Their Photophysical Properties. *Journal of Materials Chemistry C* **2018**, 6 (13), 3298–3309.
- (207) Mei, J.; Hong, Y.; Lam, J. W. Y.; Qin, A.; Tang, Y.; Tang, B. Z. Aggregation-Induced Emission: The Whole Is More Brilliant than the Parts. *Advanced Materials* **2014**, 26 (31), 5429–5479.
- (208) Wang, Y.; Liao, Y.; Cabry, C. P.; Zhou, D.; Xie, G.; Qu, Z.; Bruce, D. W.; Zhu, W. Highly Efficient Blueish-Green Fluorescent OLEDs Based on AIE Liquid Crystal Molecules: From Ingenious Molecular Design to Multifunction Materials. *J. Mater. Chem. C* **2017**, 5 (16), 3999–4008.
- (209) Cheng, Z.; Zang, Y.; Li, Y.; Li, B.; Hu, C.; Li, H.; Yang, Y. A Chiral Luminescent Liquid Crystal with a Tolane Unit. *Liquid Crystals* **2016**, 43 (6), 777–782.
- (210) Schultz, A.; Diele, S.; Laschat, S.; Nimtz, M. Novel Columnar Tetraphenylethenes via McMurry Coupling. *Advanced Functional Materials* **2001**, 11 (6), 441–446.
- (211) Heiskanen, J. P.; Vivo, P.; Saari, N. M.; Hukka, T. I.; Kastinen, T.; Kaunisto, K.; Lemmetyinen, H. J.; Hormi, O. E. O. Synthesis of Benzothiadiazole Derivatives by Applying C–C Cross-Couplings. *The Journal of Organic Chemistry* **2016**, 81 (4), 1535–1546.
- (212) Xu, Z.; Du, H.; Yin, M.; Wang, B.; Zhao, J.; Xie, Y. Benzothiadiazole, Hexylthiophen and Alkoxy Benzene Based Solution Processable Copolymer: Effect of the Electron Withdrawing Substituents (Fluorine Atoms) on Electrochemical, Optical and Electrochromic Properties. *Organic Electronics* **2018**, 61, 1–9.
- (213) Kim, H. S.; Park, S. R.; Suh, M. C. Concentration Quenching Behavior of Thermally Activated Delayed Fluorescence in a Solid Film. *Journal of Physical Chemistry C* **2017**, 121 (26), 13986–13997.
- (214) Kim, D. H.; D'Aléo, A.; Chen, X. K.; Sandanayaka, A. D. S.; Yao, D.; Zhao, L.; Komino, T.; Zaborova, E.; Canard, G.; Tsuchiya, Y.; et al. High-Efficiency Electroluminescence and Amplified Spontaneous Emission from a Thermally Activated Delayed Fluorescent near-Infrared Emitter. *Nature Photonics* **2018**, 12 (2), 98–104.
- (215) Martínez-Martínez, V.; Lim, J.; Bañuelos, J.; López-Arbeloa, I.; Miljanić, O. Š. Strong Intramolecular Charge Transfer Emission in Benzobisoxazole Cruciforms: Solvatochromic Dyes as Polarity Indicators. *Physical Chemistry Chemical Physics* **2013**, 15 (41), 18023–18029.

- (216) Ye, H.; Kim, D. H.; Chen, X.; Sandanayaka, A. S. D.; Kim, J. U.; Zaborova, E.; Canard, G.; Tsuchiya, Y.; Choi, E. Y.; Wu, J. W.; et al. Near-Infrared Electroluminescence and Low Threshold Amplified Spontaneous Emission above 800 Nm from a Thermally Activated Delayed Fluorescent Emitter. *Chemistry of Materials* **2018**, *30* (19), 6702–6710.
- (217) Greenham, N. C.; Samuel, I. D. W.; Hayes, G. R.; Phillips, R. T.; Kessener, Y. A. R. R.; Moratti, S. C.; Holmes, A. B.; Friend, R. H. Measurement of Absolute Photoluminescence Quantum Efficiencies in Conjugated Polymers. *Chemical Physics Letters* **1995**, *241* (1–2), 89–96.
- (218) Mattoussi, H.; Murata, H.; Merritt, C. D.; Iizumi, Y.; Kido, J.; Kafafi, Z. H. Photoluminescence Quantum Yield of Pure and Molecularly Doped Organic Solid Films. *Journal of Applied Physics* **1999**, *86* (5), 2642–2650.
- (219) Lakowicz, J. R. *Principles of Fluorescence Spectroscopy*; 2006.
- (220) Matsushima, T.; Qin, C.; Goushi, K.; Bencheikh, F.; Komino, T.; Leyden, M.; Sandanayaka, A. S. D.; Adachi, C. Enhanced Electroluminescence from Organic Light-Emitting Diodes with an Organic–Inorganic Perovskite Host Layer. *Advanced Materials* **2018**, *30* (38), 1–7.
- (221) Suzuki, K.; Seno, A.; Tanabe, H.; Ueno, K. New Host Materials for Blue Emitters. *Synthetic Metals* **2004**, *143* (1), 89–96.
- (222) Zhang, Q.; Kuwabara, H.; Potscavage, W. J.; Huang, S.; Hatae, Y.; Shibata, T.; Adachi, C. Anthraquinone-Based Intramolecular Charge-Transfer Compounds: Computational Molecular Design, Thermally Activated Delayed Fluorescence, and Highly Efficient Red Electroluminescence. *Journal of the American Chemical Society* **2014**, *136* (52), 18070–18081.
- (223) Kawamura, Y.; Yamamoto, H.; Goushi, K.; Sasabe, H.; Adachi, C.; Yoshizaki, H. Ultraviolet Amplified Spontaneous Emission from Thin Films of 4,4'-Bis(9-Carbazolyl)-2,2'-Biphenyl and the Derivatives. *Applied Physics Letters* **2004**, *84* (15), 2724–2726.
- (224) Zhao, L.; Komino, T.; Inoue, M.; Kim, J. H.; Ribierre, J. C.; Adachi, C. Horizontal Molecular Orientation in Solution-Processed Organic Light-Emitting Diodes. *Applied Physics Letters* **2015**, *106* (6), 063301.
- (225) Yang, Y.; Nakamichi, T.; Yoshioka, H.; Yahiro, M.; Era, M.; Watanabe, H.; Cui, Y.; Oki, Y.; Qian, G. Spectral-Resolving Capable and Integratable Multilayered Conductive Films via an Inkjet Method. *Journal of Materials Chemistry C* **2013**, *1* (9), 1739–1744.
- (226) Sobus, J.; Bencheikh, F.; Mamada, M.; Wawrzinek, R.; Ribierre, J. C.; Adachi, C.; Lo,

- S. C.; Namdas, E. B. High Performance P- and n-Type Light-Emitting Field-Effect Transistors Employing Thermally Activated Delayed Fluorescence. *Advanced Functional Materials* **2018**, 28 (28).
- (227) Park, W. J.; Lee, Y.; Kim, J. Y.; Yoon, D. W.; Kim, J.; Chae, S. H.; Kim, H.; Lee, G.; Shim, S.; Yang, J. H.; et al. Effective Thermally Activated Delayed Fluorescence Emitter and Its Performance in OLED Device. *Synthetic Metals* **2015**.
- (228) Seki, S.; Sawada, Y.; Nishide, T. Indium-Tin-Oxide Thin Films Prepared by Dip-Coating of Indium Diacetate Monohydroxide and Tin Dichloride. *Thin Solid Films* **2001**.
- (229) Brown, T. M.; Kim, J. S.; Friend, R. H.; Cacialli, F.; Daik, R.; Feast, W. J. Built-in Field Electroabsorption Spectroscopy of Polymer Light-Emitting Diodes Incorporating a Doped Poly(3,4-Ethylene Dioxothiophene) Hole Injection Layer. *Applied Physics Letters* **1999**, 75 (12), 1679–1681.
- (230) Jenekhe, S. A.; Zhang, X.; Chen, X. L.; Choong, V.-E.; Gao, Y.; Hsieh, B. R. Finite Size Effects on Electroluminescence of Nanoscale Semiconducting Polymer Heterojunctions. *Chemistry of Materials* **1997**, 9 (2), 409–412.
- (231) Strukelj, M.; Papadimitrakopoulos, F.; Miller, T. M.; Rothberg, L. J. Design and Application of Electron-Transporting Organic Materials. *Science* **1995**, 267 (5206), 1969–1972.
- (232) Greenham, N. C.; Moratti, S. C.; Bradley, D. D. C.; Friend, R. H.; Holmes, A. B. Efficient Light-Emitting Diodes Based on Polymers with High Electron Affinities. *Nature* **1993**.
- (233) Liehm, P.; Murawski, C.; Furno, M.; Lüssem, B.; Leo, K.; Gather, M. C. Comparing the Emissive Dipole Orientation of Two Similar Phosphorescent Green Emitter Molecules in Highly Efficient Organic Light-Emitting Diodes. *Applied Physics Letters* **2012**, 101 (25), 4–8.
- (234) Kim, K. H.; Moon, C. K.; Lee, J. H.; Kim, S. Y.; Kim, J. J. Highly Efficient Organic Light-Emitting Diodes with Phosphorescent Emitters Having High Quantum Yield and Horizontal Orientation of Transition Dipole Moments. *Advanced Materials* **2014**, 26 (23), 3844–3847.
- (235) Frischeisen, J.; Yokoyama, D.; Endo, A.; Adachi, C.; Brütting, W. Increased Light Outcoupling Efficiency in Dye-Doped Small Molecule Organic Light-Emitting Diodes with Horizontally Oriented Emitters. *Organic Electronics* **2011**, 12 (5), 809–817.
- (236) Zhao, L.; Komino, T.; Inoue, M.; Kim, J. H.; Ribierre, J. C.; Adachi, C. Horizontal Molecular Orientation in Solution-Processed Organic Light-Emitting Diodes. *Applied Physics Letters* **2015**.

- (237) Lee, S. Y.; Yasuda, T.; Komiyama, H.; Lee, J.; Adachi, C. Thermally Activated Delayed Fluorescence Polymers for Efficient Solution-Processed Organic Light-Emitting Diodes. *Advanced Materials* **2016**, *28* (21), 4019–4024.
- (238) Svensson, M.; Zhang, F.; Veenstra, S. C.; Verhees, W. J. H.; Hummelen, J. C.; Kroon, J. M.; Inganäs, O.; Andersson, M. R. High-Performance Polymer Solar Cells of an Alternating Polyfluorene Copolymer and a Fullerene Derivative. *Advanced Materials* **2003**, *15* (12), 988–991.
- (239) Wang, E.; Hou, L.; Wang, Z.; Hellström, S.; Zhang, F.; Inganäs, O.; Andersson, M. R. An Easily Synthesized Blue Polymer for High-Performance Polymer Solar Cells. *Advanced Materials* **2010**, *22* (46), 5240–5244.
- (240) Zou, Y.; Najari, A.; Berrouard, P.; Beaupré, S.; Réda Aïch, B.; Tao, Y.; Leclerc, M. A Thieno [3, 4-c] Pyrrole-4, 6-Dione-Based Copolymer for Efficient Solar Cells. *Journal of the American Chemical Society* **2010**, *132* (15), 5330–5331.
- (241) Randell, N. M.; Kelly, T. L. Recent Advances in Isoindigo-Inspired Organic Semiconductors. *Chemical Record* **2019**, *19* (6), 973–988.
- (242) Lei, T.; Dou, J. H.; Pei, J. Influence of Alkyl Chain Branching Positions on the Hole Mobilities of Polymer Thin-Film Transistors. *Advanced Materials* **2012**, *24* (48), 6457–6461.
- (243) Yoo, D.; Hasegawa, T.; Ashizawa, M.; Kawamoto, T.; Masunaga, H.; Hikima, T.; Matsumoto, H.; Mori, T. N-Unsubstituted Thienoisindigos: Preparation, Molecular Packing and Ambipolar Organic Field-Effect Transistors. *Journal of Materials Chemistry C* **2017**, *5* (10), 2509–2512.
- (244) Graham, K. R.; Stalder, R.; Wieruszewski, P. M.; Patel, D. G.; Salazar, D. H.; Reynolds, J. R. Tailor-Made Additives for Morphology Control in Molecular Bulk-Heterojunction Photovoltaics. *ACS Applied Materials and Interfaces* **2013**, *5* (1), 63–71.
- (245) Ashizawa, M.; Masuda, N.; Higashino, T.; Kadoya, T.; Kawamoto, T.; Matsumoto, H.; Mori, T. Ambipolar Organic Transistors Based on Isoindigo Derivatives. *Organic Electronics* **2016**, *35*, 95–100.
- (246) Hasegawa, T.; Ashizawa, M.; Matsumoto, H. Design and Structure-Property Relationship of Benzothienoisindigo in Organic Field Effect Transistors. *RSC Advances* **2015**, *5* (75), 61035–61043.
- (247) Randell, N. M.; Radford, C. L.; Yang, J.; Quinn, J.; Hou, D.; Li, Y.; Kelly, T. L. Effect of Acceptor Unit Length and Planarity on the Optoelectronic Properties of Isoindigo-Thiophene Donor-Acceptor Polymers. *Chemistry of Materials* **2018**, *30* (14), 4864–4873.

- (248) Lei, T.; Cao, Y.; Fan, Y.; Liu, C.-J.; Yuan, S.-C.; Pei, J. High-Performance Air-Stable Organic Field-Effect Transistors: Isoindigo-Based Conjugated Polymers. *Journal of the American Chemical Society* **2011**, *133* (16), 6099–6101.
- (249) Chua, L.; Zaumseil, J.; Chang, J.; Ou, E. C. General Observation of N-Type Field-Effect Behaviour in Organic Semiconductors_JZ.Pdf. *Nature* **2005**, *434* (March), 194–199.
- (250) Cho, S.; Seo, J. H.; Kim, G. H.; Kim, J. Y.; Woo, H. Y. Observation of Ambipolar Field-Effect Behavior in Donor-Acceptor Conjugated Copolymers. *Journal of Materials Chemistry* **2012**, *22* (39), 21238–21241.
- (251) Majewski, L. A.; Kingsley, J. W.; Balocco, C.; Song, A. M. Influence of Processing Conditions on the Stability of Poly(3-Hexylthiophene)-Based Field-Effect Transistors. *Applied Physics Letters* **2006**, *88* (22), 1–4.
- (252) Chang, J. F.; Clark, J.; Zhao, N.; Sirringhaus, H.; Breiby, D. W.; Andreasen, J. W.; Nielsen, M. M.; Giles, M.; Heeney, M.; McCulloch, I. Molecular-Weight Dependence of Interchain Polaron Delocalization and Exciton Bandwidth in High-Mobility Conjugated Polymers. *Physical Review B - Condensed Matter and Materials Physics* **2006**, *74* (11), 1–12.
- (253) Lei, T.; Cao, Y.; Zhou, X.; Peng, Y.; Bian, J.; Pei, J. Systematic Investigation of Isoindigo-Based Polymeric Field-Effect Transistors: Design Strategy and Impact of Polymer Symmetry and Backbone Curvature. *Chemistry of Materials* **2012**, *24* (10), 1762–1770.